



HAL
open science

Development of a microfluidic device based on Deterministic Lateral Displacement (DLD) for biological sample preparation, towards the extraction of extracellular vesicles

Eloïse Pariset

► To cite this version:

Eloïse Pariset. Development of a microfluidic device based on Deterministic Lateral Displacement (DLD) for biological sample preparation, towards the extraction of extracellular vesicles. Biological Physics [physics.bio-ph]. Université Grenoble Alpes, 2018. English. NNT : 2018GREAY027 . tel-01978865

HAL Id: tel-01978865

<https://theses.hal.science/tel-01978865>

Submitted on 11 Jan 2019

HAL is a multi-disciplinary open access archive for the deposit and dissemination of scientific research documents, whether they are published or not. The documents may come from teaching and research institutions in France or abroad, or from public or private research centers.

L'archive ouverte pluridisciplinaire **HAL**, est destinée au dépôt et à la diffusion de documents scientifiques de niveau recherche, publiés ou non, émanant des établissements d'enseignement et de recherche français ou étrangers, des laboratoires publics ou privés.

THÈSE

Pour obtenir le grade de

DOCTEUR DE LA COMMUNAUTE UNIVERSITE GRENOBLE ALPES

Spécialité : **Physique Appliquée**

Arrêté ministériel : 25 mai 2016

Présentée par

Eloïse PARISET

Thèse dirigée par **Vincent AGACHE**, Directeur de Recherche,
CEA - Leti

préparée au sein du **CEA Leti (DTBS)**
en collaboration avec le laboratoire du **Professeur Scott Manalis**,
MIT, Koch Institute for Integrative Cancer Research
dans l'**École Doctorale de Physique**

Développement d'un dispositif microfluidique de Déplacement Latéral Déterministe (DLD) pour la préparation d'échantillons biologiques, en vue de l'extraction de vésicules extracellulaires

Thèse soutenue publiquement le **1^{er} octobre 2018**
devant le jury composé de :

M. Rémy SADOUL

Professeur, Grenoble Institut Neurosciences, Examineur, Président

M. Charles BAROUD

Professeur, Pasteur – Polytechnique, Rapporteur

M. Jean-Louis VIOVY

Professeur, Institut Curie, Rapporteur

Mme Mathilde REYSSAT

Maitre de Conférences, ESPCI Paris, Examinatrice

M. Vincent AGACHE

Ingénieur-Chercheur, CEA-Leti, Directeur de thèse

Mme Aurélie THUAIRE

Ingénieur-Chercheur, CEA-Leti, Invitée

M. Scott MANALIS

Professeur, Koch Institute for Integrative Cancer Research, MIT, Invité



"When you're following your energy and doing what you want all the time, the distinction between work and play dissolves."

— Shakti Gawain

Contents

Remerciements

Glossary

Definition of DLD Geometrical Parameters

Table of implemented DLD Devices

Introduction

1 Literature Review	23
1.1 Extracellular Vesicles: Structure and Functions	23
1.1.1 Introduction	23
1.1.2 Physiological Functions	29
1.1.3 Diagnostic and Therapeutic Potential	32
1.1.4 Current Challenges in EV Research	35
1.2 Standard Characterization Techniques	36
1.2.1 Size and Morphology Characterization	37
1.2.2 Composition Characterization	43
1.3 Isolation Techniques	46
1.3.1 Density-based Isolation	48
1.3.2 Affinity Capture-based Isolation	50
1.3.3 Surface Electric Charge-based Isolation	51
1.3.4 Size-based Isolation	52
1.3.5 Emerging Microfluidics Isolation Techniques	53
1.4 Deterministic Lateral Displacement (DLD) Separation	58
1.4.1 Separation Principle	58
1.4.2 Predictive Models to anticipate Critical Diameters	59
1.4.3 Design Improvements to increase Separation Efficiency	70
1.4.4 Biological Applications of DLD Separation	71
2 Development of DLD Devices	75
2.1 Finite Element Modeling of DLD Separation	75
2.2 Influence of the Pillar Shape: Numerical Study	77

2.3	Anisotropy Effect and Impact on DLD Separation	79
2.3.1	Definition and Illustration of Anisotropy in DLD arrays of Elongated Pillars	80
2.3.2	Parametric Study of the Anisotropy Magnitude	81
2.3.3	Impact of Anisotropy on Particle Trajectory	83
2.3.4	Multi-Separation DLD Designs	86
2.4	Implemented DLD Designs	87
2.4.1	Version 1	88
2.4.2	Version 2: Improvements	91
2.4.3	Version 3: Exploratory Designs	95
2.5	Fabrication of DLD Devices	99
2.5.1	Fabrication Process Flow: Version 1	99
2.5.2	Fabrication Process Flow: Improvements	101
2.6	Packaging	102
3	Validation of DLD Separation with Beads	107
3.1	Experimental Section	107
3.2	Characterization of our DLD Devices	108
3.2.1	Determination of the Critical Diameters	108
3.2.2	Determination of the Recovery Yield	111
3.2.3	Focus on “Nano-DLDs”	111
3.3	Influence of the Pillar Shape	119
3.4	Influence of a New Parameter: the Channel Width	121
3.4.1	Multiple Critical Diameters in DLD Arrays	121
3.4.2	Influence of the Channel Width on the Intermediary Mode	125
3.4.3	Prediction of the Critical Diameters with the Intermediary Mode Effect	128
3.5	New Separation Phenomena with Exploratory Designs	131
3.5.1	DLD Concentration	131
3.5.2	Multi-Separation with Elongated Pillars	131
4	DLD Purification of Biological Samples	137
4.1	Isolation of Bacteria in Blood Samples	137
4.1.1	Validation of Blood Purification	138
4.1.2	Validation of Bacteria Recovery	142
4.2	Extraction of Extracellular Vesicles from Cell Culture Media	148
4.2.1	Standard Ultracentrifugation and Limitations	148
4.2.2	Alternative Standard Isolation Protocols	159
4.2.3	Comparison of the three Isolation Protocols	161
4.2.4	Microfluidic Extraction of Extracellular Vesicles including DLD	163
5	Multi-DLD Platforms for Complex Samples	177
5.1	Connection of DLD Modules: Presentation of the Problem	177

5.2	Solution n°1: Droplet-based Platform	180
5.2.1	Experimental Section	180
5.2.2	Droplet T-Junctions as Pressure Controllers at DLD Outlets	181
5.2.3	Possible Droplet Platforms	183
5.2.4	Predictive Model to Apply Optimized Input Pressures	186
5.3	Solution n°2: Transient Flexible Chambers	192
5.3.1	Experimental Section	193
5.3.2	Two-Stage Separation Principle	195
5.3.3	Validation of the Two-Stage Fractionation with Beads	199
5.3.4	Application to the isolation of Bacteria from Blood Samples	202

Conclusion

Bibliography

Appendix

A	Appendix	245
A.1	Appendix 1: Exosomal functions for different biofluids	245
A.2	Appendix 2: Cancer-specific EV biomarkers	247
A.3	Appendix 3: Overview of clinical trials for EV-based therapies	251
A.4	Appendix 4: DLD chip surface treatments	251
A.5	Appendix 5: DLD trajectory of fluorescent beads	254
A.6	Appendix 6: Protocol for RBC fixation with glutaraldehyde	270
A.7	Appendix 7: THP-1 cell differentiation protocol	272
A.8	Appendix 8: Transmission electron microscopy sample preparation	272

List of Publications and Patents

Remerciements

C'est le coeur un peu lourd que j'écris ces lignes. Achever ce manuscrit signifie aussi m'envoler à plus de 9 000 kilomètres de toutes les personnes qui ont énormément compté pour moi durant ces trois dernières années...

Je souhaiterais tout d'abord remercier Claude VAUCHIER, Béatrice ICARD et Séverine VIGNOUD de m'avoir donné la chance d'intégrer leur laboratoire.

Mes remerciements ensuite à l'ensemble des membres du jury pour leur implication dans l'évaluation de cette thèse. Un grand merci à M. Rémy SADOUL, président du jury, ainsi qu'aux rapporteurs, M. Charles BAROUD et M. Jean-Louis VIOVY, pour leur analyse approfondie de ce manuscrit, et l'apport significatif de l'ensemble de leurs commentaires. Merci enfin à Mme Mathilde REYSSAT d'avoir accepté d'examiner ces travaux, trois ans après l'évaluation de mon stage de fin d'études de l'ESPCI Paris. Je tiens à exprimer ma profonde gratitude envers chaque membre du jury pour les discussions passionnantes partagées au cours de la soutenance.

Je remercie mon directeur de thèse, Vincent AGACHE, pour l'échange constant et particulièrement prolifique de nos idées, pour son ouverture à chacune de mes propositions et la confiance qu'il m'a accordée. Un immense merci à mon encadrante, Aurélie THUAIRE, dont le soutien sans faille m'a permis d'aborder chaque difficulté avec sérénité. Merci à celui que je considère comme mon mentor, Jean BERTHIER, j'espère sincèrement que nos chemins se croiseront à nouveau à l'avenir.

I want to thank Professor Scott Manalis for the opportunity he gave me to conduct experiments in his laboratory at MIT, in the Koch Institute for Integrative Cancer Research. This enlightening and inspiring experience was the starting point for my american journey to NASA... I also would like to thank all the incredibly talented people I had the chance to meet at MIT. Thank you to Bashar, the daily sunshine of the lab. Thank you to Teemu, who was at the same time an amazing science and gym teacher! Thank you to Georgios for his time and all the helpful comments on our Scientific Reports paper.

Merci à Nathalie DUSSERT-ROSSET, qui a su traiter toutes ces missions avec une efficacité remarquable !

J'aimerais maintenant remercier certaines personnes sans qui ces travaux n'auraient pu voir le jour. Merci au très talentueux François BOIZOT, je t'aurais bien pris dans mes bagages pour la suite de mes aventures !! Merci à Catherine PUDDA pour ton implication hors normes, j'espère que le mot "DLD" ne te rappellera pas de trop mauvais souvenirs... Merci à Frédéric REVOL-CAVALIER, le meilleur expérimentateur que j'ai eu la chance de rencontrer. Même si tout n'était pas gagné au départ, je suis fière des résultats que l'on a su tirer ensemble de nos manips de DLD ! Merci à Yves FOUILLET pour toute l'expertise microfluidique dont j'ai pu profiter dès mon arrivée. Merci à Nicolas VERPLANCK, sans tes conseils de standardisation je serais sans doute encore en train de tester mes tout premiers designs ! Merci à Mathilde MENNETEAU et

Camille ECHAMPARD, pour l'aide immense que vous m'avez apportée à des moments critiques de la thèse. Merci à Pierre MARCOUX pour ton initiation à la microbiologie, j'aurai été formée par un grand maître du domaine ! Merci infiniment à Simon SACCHET pour ta patience à l'usinage de centaines de micropiliers ! Merci à Thomas BORDY, mon rayon de soleil grenoblois ! Merci à Myriam CUBIZOLLES, Remco DEN DULK, Manuel ALESSIO, Guillaume NONGLATON, Martine COCHET, Marie-Line COSNIER, quelle chance d'avoir pu travailler avec vous ! Merci aux collègues qui ont avant tout été des amis extraordinaires, Patricia et Charly.

Une énorme pensée pour ma famille. Voir la fierté dans les yeux de sa maman est sans doute le meilleur carburant pour se surpasser dans la vie !

Beaucoup d'émotions au souvenir de tous les éclats de rire partagés avec les personnes exceptionnelles que cette thèse m'a permis de rencontrer... Charlotte, mon binôme de thèse (mon Tic pour qui je resterai le Tac), Emeric et Prisca, la meilleure team de la travée 102, Roxane et ses rires qu'on doit entendre jusque sur Mars, Guillaume et nos "points de thèse" improvisés sur la montée de la Bastille, Thomas et les traumatismes d'espaces insécables qu'il aura causés sur moi, Aurélie la pire cascadeuse de tous les temps, Thibault (arrêtez de vous moquer), Emilie et Morgane, mes co-bureaux adorées, Mélissa (que j'ai tellement embêtée avec mes bactéries !!), Perrine, notre petite maman à tous, et les inoubliables "anciens", Vivian, David, Hadrien, Céline, Maxime, Claire, Julien.

Enfin comment exprimer ma reconnaissance envers celui pour qui j'aurais souhaité que cette rédaction ne s'arrête pas ! Giacomo, ton nom devrait apparaître dès la première page de ce manuscrit, tant tu auras contribué sur tous les plans à la réussite de ce projet. Mon "Expert LaTeX", je me souviendrai de ta patience devant mes listes de soucis de compilation, de nos éclats de rire au comptage dans le manuscrit de l'apparition du mot "DLD", de ton écoute infaillible à la dixième répétition de la soutenance, de ta présence à chacune des étapes de cette aventure, et de tout ce qu'elle m'a apporté. Tu es une personne formidable et je souhaite que ce manuscrit soit le nôtre, tout comme les superbes souvenirs qui y resteront associés.

Glossary

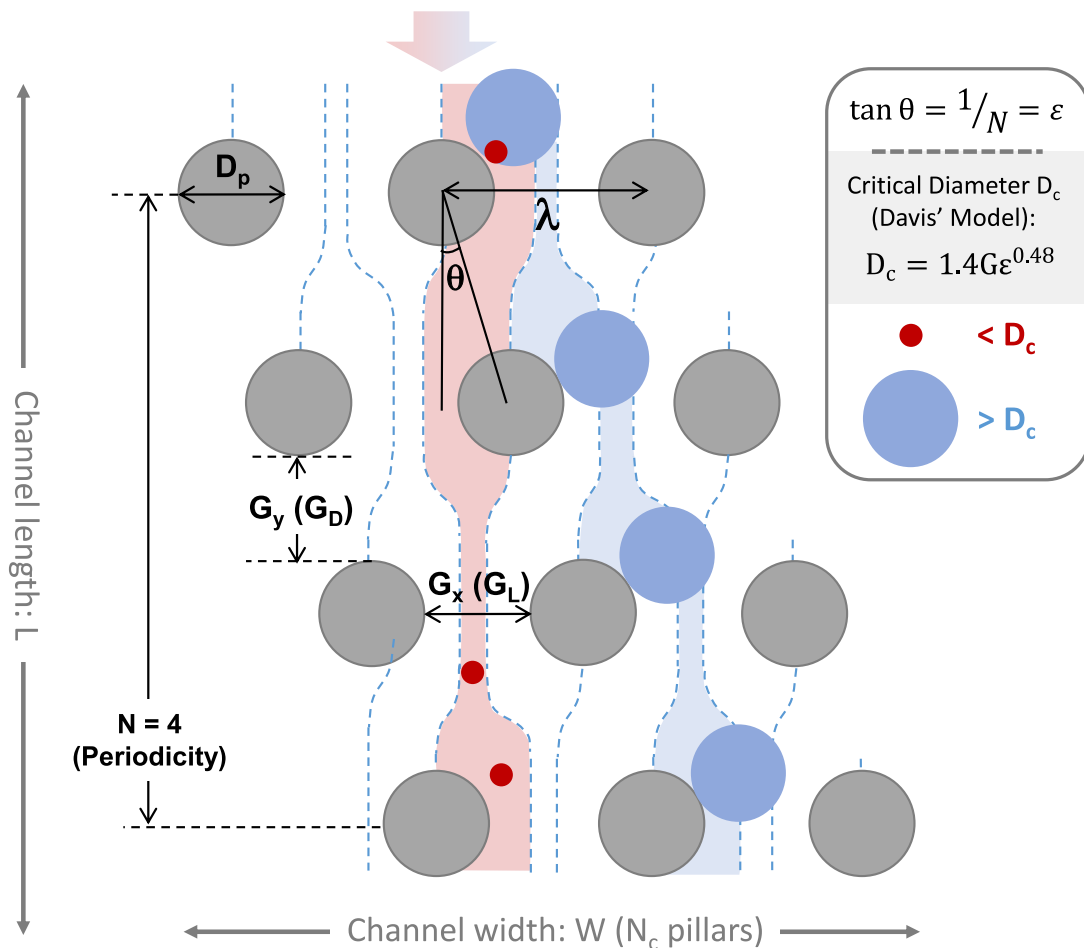
AB	Apoptotic Body
ADP	Adenosine DiPhosphate
AF4	Asymmetrical-Flow Field-Flow Fractionation
AFM	Atomic Force Microscopy
AIEX	AnIon EXchange
Alix	ALG-2 interacting protein X
ALK	Anaplastic Lymphoma Kinase
APC	Antigen-Presenting Cell
ARF	ADP Ribosylation Factor
BSA	Bovine Serum Albumin
CaI	Calcium Ionophore
CCD	Charge-Coupled Device
CMOS	Complementary MetalOxide Semiconductor
CNS	Central Nervous System
COC	Cyclic Olefin Copolymer
CTC	Circulating Tumor Cell
CTE	Chronic Traumatic Encephalopathy
DC	Dendritic Cell
DLD	Deterministic Lateral Displacement
DLS	Dynamic Light Scattering
DNA	DeoxyriboNucleic Acid
DOE	Design Of Experiments
E. coli	Escherichia coli
EDTA	EthyleneDiamine Tetraacetic Acid
EGFR	Epidermal Growth Factor Receptor
ELISA	Enzyme-Linked Immunosorbent Assay

ELLSA	Enzyme-Linked Lectin-Specific Assay
EM	Electron Microscopy
EPDM	Ethylene Propylene Diene Monomere
ESCRT	Endosomal Sorting Complex Required for Transport
EV	Extracellular Vesicle
EXO	EXOsome
FBS	Fetal Bovine Serum
FC	Flow Cytometry
FCB	Fluidic Circuit Board
FITC	Fluorescein IsoThioCyanate
FLS	Forward Light Scatter
GFP	Green Fluorescent Protein
GP	GlycoProtein
GTA	GluTarAldehyde
HDL	High-Density Lipoprotein
HIV	Human Immunodeficiency Virus
HSP	Heat Shock Protein
IDT	InterDigital Transducer
IFN	InterFeroN
ILV	IntraLuminal Vesicle
IP	Immune-affinity Purification
ISEV	International Society for Extracellular Vesicles
LAMP	Lysosome-Associated Membrane Protein
LPS	LipoPolySaccharide
M0	Unpolarized Macrophage
M1	Pro-inflammatory Macrophage
M2	Anti-inflammatory Macrophage
MAR	Mass Accumulation Rate

MDSC	Myeloid-Derived Suppressor Cell
MFCs	Microfluidic Flow Control System
MFGE	Milk Fat Globule-Epidermal growth factor
MHC	Major Histocompatibility Complex
miRNA	MicroRNA
MMP	Matrix MetalloProteinase
mRNA	Messenger RNA
MV	MicroVesicle
MVB	Multi-Vesicular Body
NK	Natural Killer
NMR	Nuclear Magnetic Resonance
NTA	Nanoparticle Tracking Analysis
PBMC	Peripheral Blood Mononuclear Cell
PBS	Phosphate Buffered Saline
PCR	Polymerase Chain Reaction
PDMS	PolyDiMethylSiloxane
PLT	PLaTelet
POC	Point-Of-Care
PROSPR	PRotein Organic Solvent PRecipitation
PSA	Prostate Specific Antigen
qRT-PCR	Quantitative Reverse Transcription PCR
RAB	RAS-related protein in Brain
RAS	Retrovirus-Associated DNA Sequences
RBC	Red Blood Cell
RFP	Red Fluorescent Protein
RIE	Reactive Ion Etching
RInSE	Rapid Inertial Solution Exchange
RNA	RiboNucleic Acid
RPS	Resistive Pulse Sensing
RS	Raman Spectroscopy

RT-PCR	Reverse Transcription PCR
SAXS	Small-Angle X-ray Scattering
SDS-PAGE	Sodium Dodecyl Sulfate - Polyacrylamide Gel Electrophoresis
SEC	Size Exclusion Chromatography
SEM	Scanning Electron Microscopy
SERS	Surface Enhanced Raman Spectroscopy
SIRS	Systemic Inflammatory Response Syndrome
SLS	Side Light Scatter
SMR	Suspended Microchannel Resonator
SMV	Shedding MicroVesicle
SNR	Suspended Nanochannel Resonator
SPR	Surface Plasmon Resonance
SSAW	Standing Surface Acoustic Waves
SV	Synaptic Vesicle
TEM	Transmission Electron Microscopy
TFF	Tangential-Flow Filtration
TfR	Transferrin Receptor
TRPS	Tunable Resistive Pulse Sensing
TSA	Tryptic Soy Agar
Tsg	Tumor Susceptibility Gene
UC	UltraCentrifugation
VFC	Vesicle Flow Cytometer
Vn	Venceremin peptide
WB	Western Blotting

Definition of DLD Geometrical Parameters



Schematic representation of a DLD pillar array, where D_p is the pillar diameter, θ is the slant angle, G_y (G_D) is the downstream gap, G_x (G_L) is the lateral gap, λ is the center-to-center pillar distance, N is the array period, ϵ is the shift fraction, L is the channel length, W is the channel width, N_c is the number of pillars in the channel width and D_c is the critical diameter.

Table of implemented DLD Devices

Group 1	1	2	3			
Pillar Shape	Circles	Circles	Circles			
Pillar Size D_p (μm)	1	2	3			
Downstream Gap G_x (μm)	1	2	3			
Lateral Gap G_y (μm)	1	2	3			
Channel Width (μm)	360	360	360			
Slant Angle θ ($^\circ$)	0.6	0.6	0.6			
Periodicity N	100	100	100			
Length (μm)	44000	44000	44000			
D_c Davis (μm)	0.15	0.31	0.46			
D_c Inglis (μm)	0.12	0.24	0.35			
Group 2	1	2	3	4	5	6
Pillar Shape	Circles	Circles	Circles	Triangles	Hexagons	I-shaped
Pillar Size D_p (μm)	5	9	9	9	9	9
Downstream Gap G_x (μm)	5	9	4.5	9	9	9
Lateral Gap G_y (μm)	5	9	9	9	9	9
Channel Width (μm)	1100	1100	1100	1100	1100	1100
Slant Angle θ ($^\circ$)	1.4	1.9	1.9	1.9	1.9	1.9
Periodicity N	40	30	30	30	30	30
Length (μm)	44000	44000	44000	44000	44000	44000
D_c Davis (μm)	1.2	2.5	2.5	2.5	2.5	2.5
D_c Inglis (μm)	0.9	2.0	2.0	2.0	2.0	2.0
Group 3	1	2	3	4	5	6
Pillar Shape	Circles	Circles	Circles	Circles	Circles	Circles
Pillar Size D_p (μm)	11	15	20	30	11	15
Downstream Gap G_x (μm)	11	15	20	30	5.5	7.5
Lateral Gap G_y (μm)	11	15	20	30	11	15
Channel Width (μm)	2500	2500	2500	2500	2500	2500
Slant Angle θ ($^\circ$)	3.8	3.8	3.8	3.8	3.8	3.8
Periodicity N	15	15	15	15	15	15
Length (μm)	44000	44000	44000	44000	44000	44000
D_c Davis (μm)	4	6	8	11	4	6
D_c Inglis (μm)	4	5	6	9	4	5

Introduction

In addition to soluble molecules, extracellular vesicles (EVs) of varying sizes – typically from the nanometer to the micrometer range – are released by cells as a means of intercellular communication. Over the past decades, a large amount of work has been oriented towards identifying the cargo components of EVs and understanding their physiological functions. One of the significant milestones in EV research was the discovery of protected and targeted transfer of encapsulated RNA by EVs between cells, which induces functional responses (Valadi *et al.*, *Nature Cell Biology*, 2007). EV action can occur across both short and long distances, as they circulate in most biological fluids. Among the different EV subpopulations, exosomes in particular have attracted attention owing to their endocytic origin. Since they reflect the phenotypic state of their parent cells, EVs have great diagnostic and prognostic potential. In particular, new perspectives are offered by EVs for noninvasive early liquid biopsy. Indeed, several significant advantages make them remarkable biomarkers: their high concentration in all biofluids (unlike circulating tumor cells), their stability (compared to soluble biomarkers) and their universality, since they are secreted by a wide variety of parent cell types (Sun *et al.*, *Anal. Chim. Acta.*, 2018).

However, one of the main obstacles in the clinical use of EVs is the need for a consistent method to isolate a pure and undamaged EV subpopulation from unprocessed biofluids. This extraction is particularly challenging due to the small dimensions and high heterogeneity of EV populations. Across all available isolation technologies – such as ultracentrifugation, precipitation, chromatography and magnetic capture – none can simultaneously address the issues of purity, speed, cost, efficiency, sample volume, and concentration. The need for reproducible and standardized isolation protocols is identified as one of the primary bottlenecks for EV studies by the International Society for Extracellular Vesicles (ISEV) (Witwer *et al.*, *J. Extracell. Vesicles*, 2017).

In this context, microfluidic technologies have the potential to enhance the performance of sample preparation with respect to cost, time, and sample volume. Microfluidics opens new perspectives towards point-of-care diagnostics, with strong potential for miniaturization, integration, and automation. Thus, during the past few years, innovative microfluidic-based separation technologies have emerged from the need for routine clinical-grade EV isolation solutions (Contreras-Naranjo *et al.*, *Lab Chip*, 2017).

Among the most promising sample preparation technologies for EV purification, Deterministic Lateral Displacement (DLD) has the advantage of preserving the integrity of the sample through passive and label-free separation. DLD fractionates differently-sized particle subpopulations thanks to the slanted orientation of pillar arrays in a microfluidic channel. The ability to fine-tune the separation diameter by simply altering design parameters in the pillar array makes this a highly versatile technology. As a result, DLD has been extensively implemented for biotechnology applications, ranging from the extraction of circulating tumor cells (Karabacak *et al.*, *Nat. Protoc.*, 2014) to the extraction of exosomes from purified EV samples (Wunsch *et al.*, *Nat. Nanotechnol.*, 2016). However, the complete microfluidic extraction of EVs from unprocessed biofluids has not yet been successfully performed.

This thesis aims to provide new technological improvements that make DLD separation more predictive, efficient, and easy-to-integrate. The goal is to be able to extract and characterize EVs with minimal sample manipulation. In order to achieve this goal, new DLD designs were implemented based on preliminary

numerical modeling. Adjusting the classical DLD configuration enabled to increase the separation capacity, reduce clogging issues, eliminate performance-limiting contributions (e.g. side walls effects), and integrate additional functions to DLD separation – such as concentration, particle capture and solvent exchange. After experimental optimization with microbeads, the DLD devices were implemented for purification of unprocessed biofluids, including human blood samples and cell culture media. A cascade of serially connected DLD steps was used to purify complex samples over a wide range of particle sizes. However, technical enhancements on the connections between consecutive devices were necessary to improve the performance of the individual DLDs or the performance of the entire system. These technical enhancements were then leveraged to implement a multi-step protocol with limited sample manipulation for EV extraction from cell culture media, combining DLD purification (to deplete large contaminants) and magnetic capture (to collect target EV subpopulations). This approach is particularly relevant for direct integration of sample preparation to downstream sample analysis and opens new perspectives towards an all-in-one diagnostics solution based on EV extraction and identification.

This manuscript is organized in five chapters. The first chapter provides an overview of recent advances in EV research and diagnostic potential. A focus is made on the potential of DLD to improve EV isolation with respect to up-to-date technologies. The second chapter presents the innovations carried out on the design of new DLD devices, focusing on numerical and technological developments. The third chapter then describes the preliminary characterization of our proposed components, followed by the adjustment of predictive models based on this characterization. The fourth chapter is then dedicated to demonstrating the potential of these devices for biological applications, beginning with the isolation of *E. coli* bacteria from human blood samples (for sepsis diagnostics) and moving to the extraction of EVs. The purification of multi-component biofluids highlights the need for several sequential DLD steps. This motivates the final chapter, which provides two complementary approaches to maximize the performance of DLD separations in a cascaded configuration: biphasic droplet microfluidics to encapsulate DLD-sorted particles at each purification step, and an automated platform with integrated sample collection and injection between DLD stages. Beyond the issue of EV extraction, the technical innovations proposed in this manuscript could be extended to benefit any applications requiring successive microfluidic steps operated both automatically and independently.

Les vésicules extracellulaires (ou “EVs”), constituent un moyen important de communication intercellulaire. Ces vésicules sont délimitées par une membrane lipidique et présentent une grande hétérogénéité, avec des diamètres variant typiquement de la dizaine de nanomètres à la centaine de micromètres. Au cours des vingt dernières années, de nombreux travaux se sont penchés sur le contenu des EVs et la compréhension de leurs fonctions physiologiques. La découverte de l’encapsulation d’ARN par les EVs et de leur transfert entre les cellules, ainsi que des réponses fonctionnelles associées, est apparue comme une étape décisive de la recherche sur les EVs (*Valadi et al., Nature Cell Biology, 2007*). Grâce à leur circulation dans la plupart des fluides biologiques, l’action des EVs est effective à la fois à longue et courte distances. Parmi les différentes sous-populations d’EVs, les exosomes attirent une attention toute particulière, en raison de leur origine endocytaire. En effet, leur composition reflète celle de la cellule émettrice, ce qui leur confère un fort potentiel de diagnostic. En particulier, les exosomes ouvrent de nouvelles perspectives de biopsie liquide non invasive. Plusieurs avantages en font des biomarqueurs particulièrement intéressants : leur forte concentration dans la plupart des biofluides (en comparaison avec les cellules tumorales circulantes), leur stabilité (contrairement aux biomarqueurs solubles), et leur universalité, puisqu’ils sont sécrétés par une large gamme de types cellulaires (*Sun et al., Anal. Chim. Acta., 2018*).

Cependant, un des principaux obstacles actuels à l’utilisation clinique des exosomes est la nécessité d’une méthode robuste d’isolement de sous-populations d’EVs pures et intègres, à partir de biofluides complexes. L’extraction des EVs est particulièrement délicate en raison de leur faible dimension et de leur grande hétérogénéité. Aucune des technologies d’isolement actuellement disponibles – telles que l’ultracentrifugation, la précipitation, la chromatographie et la capture magnétique – ne permet d’assurer de bonnes performances à la fois en termes de pureté, de rapidité, de coût, d’efficacité, de volume et de concentration. La nécessité de protocoles d’isolement reproductibles et standardisés a été identifiée en 2017 par la Société Internationale pour les Vésicules Extracellulaires (ISEV) comme l’un des principaux enjeux de la recherche sur les EVs (*Witwer et al., J. Extracell. Vesicles, 2017*).

Dans ce contexte, les technologies microfluidiques apparaissent comme particulièrement prometteuses pour améliorer les performances de l’isolement des EVs selon des critères de coût, de durée du protocole et de volume d’échantillon. La microfluidique ouvre également de nouvelles perspectives pour le diagnostic point-of-care, en apportant davantage de miniaturisation, d’intégration et d’automatisation. Ainsi, de nombreuses techniques innovantes de préparation d’échantillon microfluidique ont émergé au cours des dernières années pour tenter d’adresser la problématique d’isolement de routine d’échantillons d’EVs dans un contexte clinique (*Contreras-Naranjo et al., Lab Chip, 2017*).

Parmi les technologies microfluidiques les plus prometteuses pour la purification d’EVs, la technique de Déplacement Latéral Déterministe (DLD) présente l’avantage de préserver l’intégrité de l’échantillon via une séparation passive et sans marquage. Cette technique met en oeuvre un réseau de piliers micrométriques, qui oriente les particules de l’échantillon, en fonction de leur taille, dans un canal microfluidique. Il s’agit d’une technologie particulièrement versatile puisque le diamètre de séparation est simplement déterminé par les paramètres géométriques du réseau de piliers (espace entre piliers, angle d’orientation, forme des piliers, etc...). Ainsi, le principe de DLD a été largement exploité pour différentes applications en biotechnologie, allant de l’extraction de cellules tumorales circulantes (*Karabacak et al., Nat. Protoc., 2014*).

à l'extraction d'exosomes à partir d'échantillons purifiés d'EVs (*Wunsch et al., Nat. Nanotechnol., 2016*). Cependant, l'extraction complète d'EVs à partir de biofluides non purifiés n'a pour le moment pas pu être réalisée, et requiert de nombreux développements technologiques supplémentaires.

Les travaux de thèse présentés ici apportent de nouvelles améliorations à la séparation par DLD standard, afin de la rendre mieux prédictible, plus efficace et plus facilement intégrable. L'objectif est de proposer une technique d'extraction des EVs à partir d'échantillons non purifiés, qui soit automatisée et intégrée, de façon à limiter les étapes de manipulation d'échantillon. Pour atteindre cet objectif, des designs innovants de DLD ont été mis en oeuvre sur la base de modélisations numériques. Ces développements ont permis d'augmenter la capacité de séparation, de réduire le phénomène de colmatage entre les piliers, d'éliminer les effets perturbateurs du tri (comme les effets de bord du canal), et d'intégrer des fonctions microfluidiques complémentaires au tri par DLD – telles que la concentration et la capture de particules, ou encore le changement de solvant. Nos dispositifs de DLD ont été préalablement validés avec des microbilles modèles, puis implémentés pour la purification d'échantillons de sang humain et de milieu de culture cellulaire. La nécessité de mise en cascade de plusieurs dispositifs de DLD complémentaires, connectés en série, a été démontrée pour la purification d'échantillons complexes présentant une large gamme de tailles de particules. Plusieurs solutions technologiques ont été proposées pour adresser cette problématique, en améliorant les performances de chaque étape de DLD dans la configuration en série. Ces développements ont ensuite été exploités pour proposer un protocole microfluidique complet, permettant d'extraire de façon automatisée une sous-populations d'EVs à partir de milieu de culture, grâce à l'intégration d'une étape de DLD à une étape de capture magnétique. Cette approche ouvre également des perspectives plus larges pour la connexion microfluidique de l'étape de préparation d'échantillon à l'étape de caractérisation dans une approche de diagnostic toute intégrée, basée sur l'extraction et l'identification des EVs.

Ce manuscrit est organisé en cinq chapitres. Le premier chapitre présente un état de l'art des avancées récentes de la recherche sur les EVs et de leur potentiel pour des applications de diagnostic. Les techniques standards et microfluidiques d'extraction des EVs sont également présentées, avec un focus sur le potentiel de la technologie de DLD pour l'amélioration des performances de cette extraction. Le deuxième chapitre présente les innovations apportées par nos dispositifs de DLD, sur la base de développements numériques et technologiques. Le troisième chapitre regroupe les caractérisations préliminaires de nos dispositifs de DLD, à partir desquelles un nouveau modèle prédictif a pu être proposé pour la détermination du diamètre de séparation par DLD. Le quatrième chapitre est dédié à l'application de ces dispositifs pour des problématiques biologiques concrètes ; en commençant par l'isolement de bactéries *E. coli* à partir d'échantillons de sang humain (en vue du diagnostic du sepsis), pour ensuite adresser l'application visée d'extraction des EVs. La purification de biofluides complexes présentant différents types de composants biologiques nécessite généralement la mise en cascade de plusieurs étapes de DLD. C'est pourquoi le dernier chapitre traite de deux approches complémentaires pour maximiser les performances des dispositifs de DLD en cascade : l'encapsulation des particules triées en sortie de chaque module de DLD par une microfluidique biphasique ; et le contrôle de chambres flexibles intermédiaires, permettant la collecte et l'injection de l'échantillon entre chaque étape. Au-delà de la problématique d'extraction des EVs, les innovations technologiques présentées ici peuvent être étendues à toute application nécessitant l'opération automatique et indépendante de plusieurs étapes microfluidiques successives.

Literature Review

Introduction: Literature Review

- In this Chapter, the structure and functions of extracellular vesicles (EVs) will be presented, before focusing on their strong diagnostic and therapeutic potential.
- Then, standard isolation and characterization techniques applied to EVs will be reviewed, with a focus on the related limitations.
- We will show how microfluidics can overpass some of these limitations and review the current demonstrations of EV isolation through microfluidic technologies.
- One of these microfluidic isolation techniques, called Deterministic Lateral Displacement (DLD), will be specifically considered as a promising label-free, passive, modular and easy-to-implement method to extract EVs from complex samples.
- Existing theoretical and experimental developments in the field of DLD separation will be reviewed, with a focus on ongoing improvements to optimize the efficiency of particle sorting.
- Biological applications of the DLD purification will be presented, including some reported results towards the extraction of EVs and nanoparticles.

1.1 Extracellular Vesicles: Structure and Functions

1.1.1 Introduction

In pluricellular organisms, communication between cells is ensured either through direct interaction or through exchange of extracellular molecules, such as proteins, peptides, lipids, hormones, growth factors, cytokines and nucleotides. These molecules are secreted by an emitting cell and activate intracellular signaling and modifications of the recipient cell physiological state. Eukaryotes use an additional intercellular communication pathway: the exchanged small molecules can be encapsulated in membrane vesicles that are released by cells in their extracellular environment and circulate in most biological fluids [1]. These extracellular vesicles (EVs) have been extensively studied over the past decade because of their significant (patho)physiological functions. In 2011 was started an **International Society for Extracellular Vesicles (ISEV)** composed of over 1,000 members in order to standardize EV research. Figure 1.1 shows the extremely fast literature growth in this field [2].

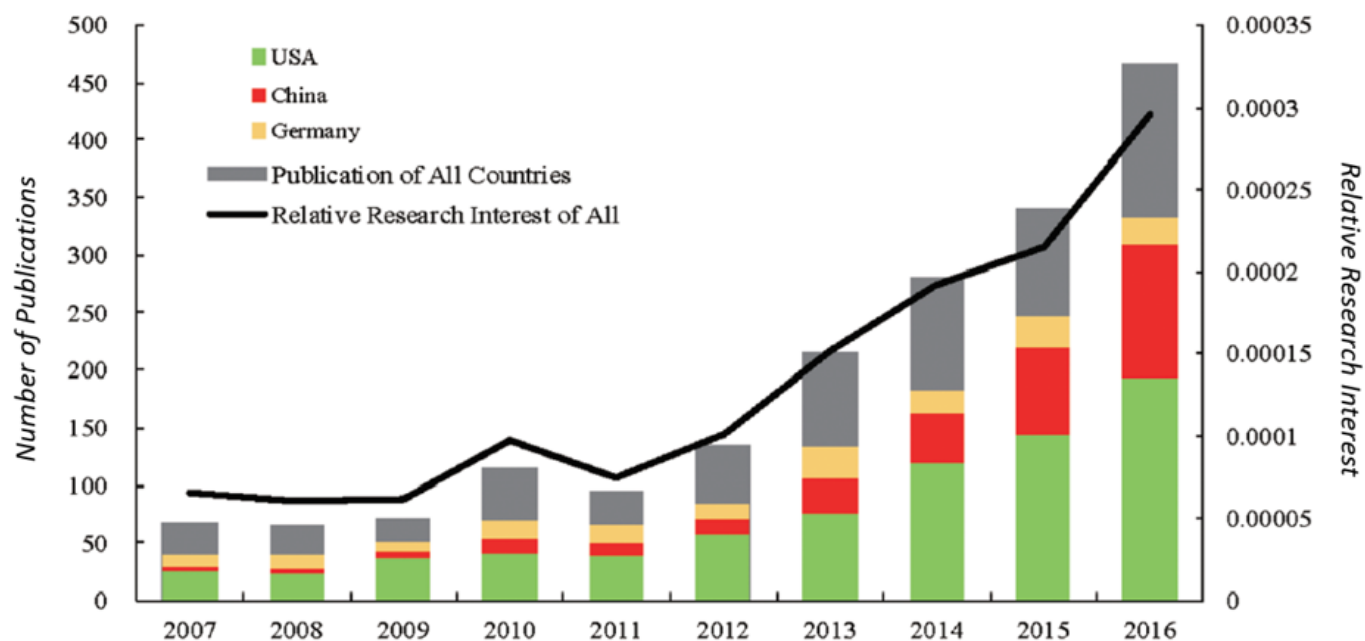


Figure 1.1: Number of publications on EV research worldwide and for the top 3 countries, and worldwide relative research interest [2].

Discovery

Observed for the first time in 1946 by Chargaff and West [3], EVs were initially considered as “platelet dusts” originating from cell death [4]. In 1983, Pan et al. [5] showed that some EVs were released by multi-vesicular bodies (MVBs) as a mechanism to eliminate plasma membrane proteins during reticulocyte maturation. Immunologists were the first to take a deep interest in EVs in 1996, evidencing that EVs isolated from B lymphocytes present antigens and induce an immune response [6].

Classes of Extracellular Vesicles

EVs are defined by a spherical lipid bilayer and contain hydrophilic soluble components from their emitting cell [7], such as RNA, proteins, lipids, sugars, enzymes, metabolites and DNA [8] (fig. 1.2).

Among the different species transported by EVs, the most exciting component is **functional RNA**, that can be translated by recipient cells and modify their phenotype. In 2006-2007, the transport of mRNAs and miRNAs by EVs was first demonstrated [9, 10]. Moreover, translation of the encapsulated mRNAs into proteins in target cells evidenced an efficient transfer of the genetic information through EVs [11, 12].

In addition to RNA, some EVs were also shown to transport **short DNA sequences** [13, 14, 15, 8] and proteins, that are related to the EV biogenesis pathway, the cell stimuli (surface topography, activation, oxygen rate...) and the isolation technique.

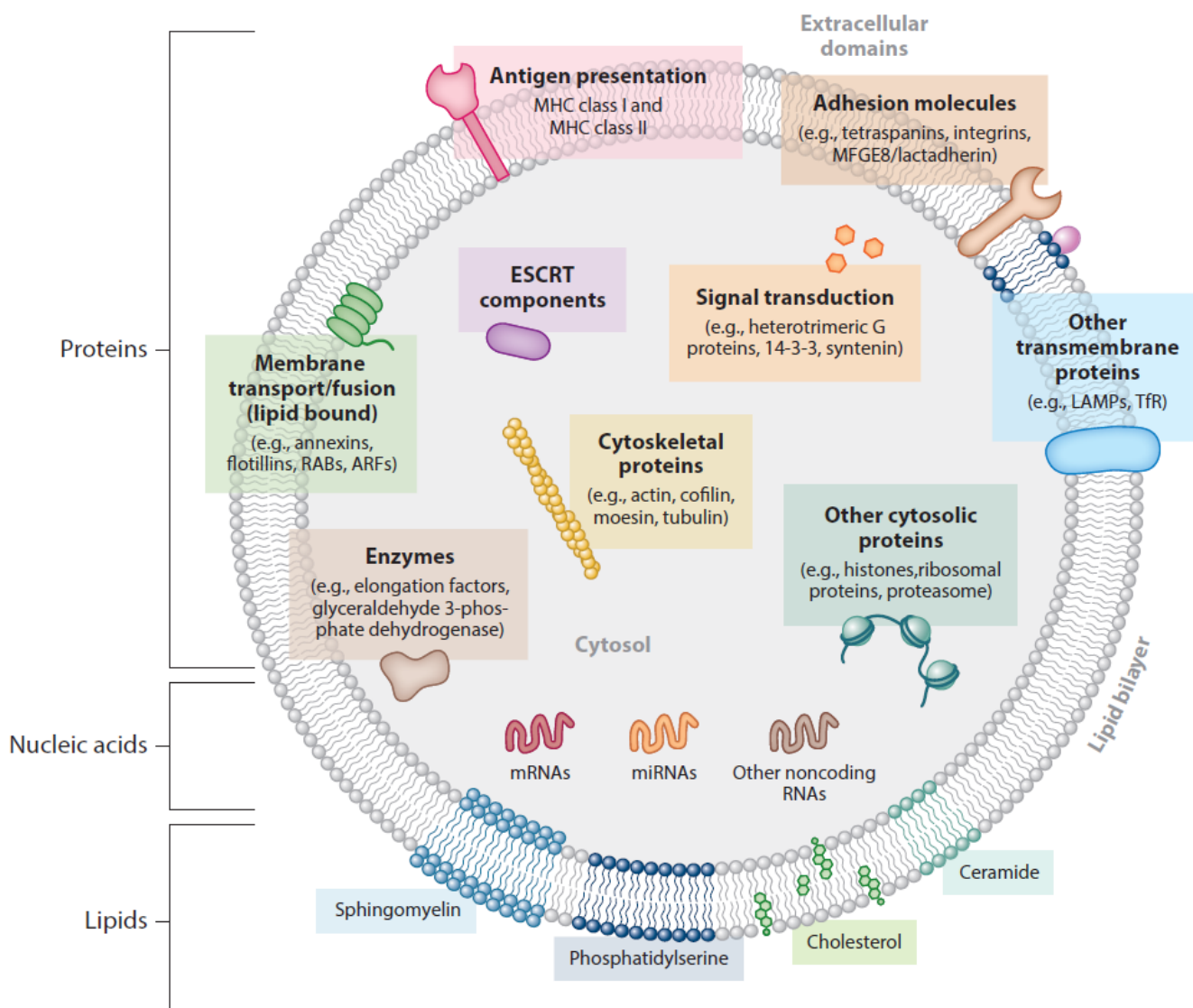


Figure 1.2: Overview of EV composition [16]. Some components can be present only in some EV subtypes and not in all types of EVs. Abbreviations: ARF = ADP ribosylation factor, ESCRT = endosomal sorting complex required for transport, LAMP = lysosome-associated membrane protein, MHC = major histocompatibility complex, MFGE8 = milk fat globule-epidermal growth factor 8, RAB = RAS-related protein in brain, TfR = transferrin receptor.

Concerning the **lipid membrane** of EVs, its composition influences the formation, function and stability of the vesicles [17]. Higher concentrations in sphingolipids and disaturated lipids (such as cholesterol) were found in EV membranes compared to cell membranes, which makes EVs more rigid [18, 19]. As a result, EVs display high stability in different extracellular environments, with very promising applications for use as new drug delivery vehicles [20, 21]. EV membranes also display higher phosphatidylserine

concentrations compared to cell membranes, which was proved to make their internalization by recipient cells easier [22].

The **concentration** of released EVs depends on the emitting cell type, its physiological state and external stimulations from the extracellular microenvironment [23]. Stimuli such as hypoxic conditions [24], acidic microenvironment [19] and calcium ionophore stimulation [10] are usually used to increase the concentration of released EVs. In this last case, increasing the intracellular calcium concentration was shown to enhance the secretion of EVs [25]. These external stimuli not only affect the number of secreted EVs, but they also modify their composition. Other extracellular microenvironment conditions reported to affect the EV composition are inflammatory signals [26, 27], oncogenic signals [28, 29], hypoxia [30, 31] and acidic conditions [19].

Several online databases provide a list of the different EV components:

- [miRandola](#) for EV miRNAs
- [Vesiclepedia](#), [EVpedia](#) and [ExoCarta](#) for proteins, nucleic acids and lipids transported by EVs

EVs can be broadly classified into three different categories according to their biogenesis pathway: **exosomes**, **ectosomes or shedding microvesicles (SMVs)**, **apoptotic bodies (ABs)**.

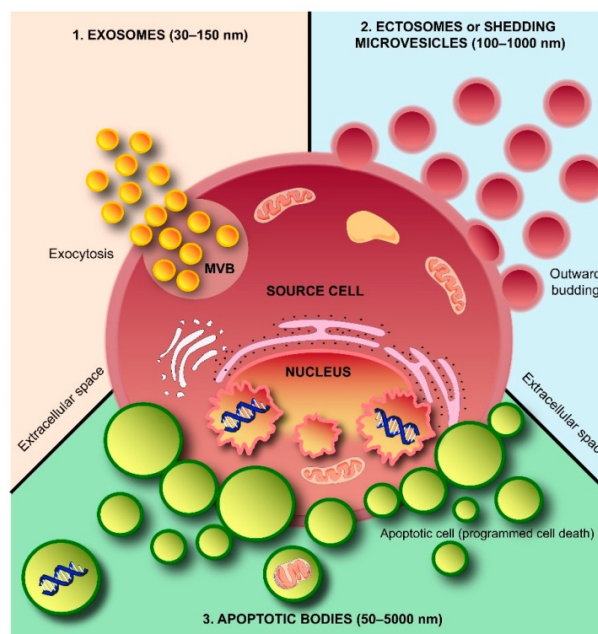


Figure 1.3: Schematic representation of the three types of EVs: exosomes, ectosomes or shedding microvesicles and apoptotic bodies [32].

The release pathway of each EV subtype is represented in fig. 1.3: exosomes originate from exocytosis, SMVs form through budding of the plasma membrane and ABs are generated during cell apoptosis to eliminate cell debris.

SMVs are large vesicles with diameters between 100 nm and 1000 nm. The composition of SMVs has been less studied than the one of exosomes, but some molecules seem to be enriched according to the cell type, such as matrix metalloproteinases (MMPs), glycoproteins (GPIb, GPIIb-IIIa, P-selectin) and integrins (Mac-1) [32]. ABs display diameters from 50 nm up to 5000 nm. They are involved in the encapsulation and elimination of cellular debris. Characteristics for these three EV populations are summarized in table 1.1.

Table 1.1: Subclasses of Extracellular Vesicles, adapted from [33], [34] and [35].

	Exosomes	Shedding Microvesicles	Apoptotic Bodies
Biogenesis	Fusion between multivesicular bodies and plasma membrane	Direct budding from plasma membrane	Cell apoptosis
Diameters	30 nm - 100 nm	100 nm - 1000 nm	50 nm - 5000 nm
Sedim.	100,000 g	10,000 g	1,000 g up to 100,000 g
Biomarkers	Proteins involved in MVB formation (Alix and Tsg101), chaperones (Hcs70 and Hsp90), presenting molecules (MHCI and MHCII), tetraspanins (CD63, CD9, CD81)	Integrins, glycoproteins, phosphoproteins, selectins, proteins involved in plasma membrane budding (AARDC1 and Tsg101), proteins that regulate cytoskeleton remodeling (GTP-binding protein ARF6), CD40 ligand	DNA-binding histones, phosphatidylserine
Content	RNA, DNA, cytoplasmic and membrane proteins	RNA, DNA, cytoplasmic and membrane proteins	Nuclear fractions, cell organelles
Main reference	They et al., Curr. Protoc. Cell Biol., Chapter 3 (2006) [36]	Heijnen et al., Blood, 94 (1999) [37]	They et al., J. Immunol., 166 (2001) [38]

Focus on Exosomes

Exosomes are generated from the inner endosomal compartments of the cells, called multivesicular bodies (MVBs). In 1985 [39], it was demonstrated that MVBs can either follow a degradative pathway through lysosomes, or fuse with the plasma membrane to release their content in the extracellular environment. The content of MVBs is called "intraluminal vesicles (ILVs)". When ILVs are released into the extracellular space, they are then referred to as "exosomes".

Exosomes convey some specific protein types that stem from the endocytic pathway and the plasma membrane, which are clearly different from the proteins found in apoptotic membrane vesicles [38]. Biological markers of exosomes are complex to define because exosomes come from intermediate intracellular compartments that are not identified by a specific biomarker themselves, unlike other intracellular compartments (for example, the protein composition of MVBs evolves during maturation) [23]. Pseudo-markers for exosomes have been identified, such as proteins required for the formation of MVBs (Alix and Tsg101), chaperones (Hcs70 and Hsp90), presentation molecules (MHCI and MHCII) and tetraspanins (CD63, CD9, CD81) [40, 41, 7]. However, tetraspanins have also been found in ABs and SMVs [29, 42]. A recent

proteomic study of heterogeneous EV populations showed differences in the concentration level of five proteins, according to the EV subtype [43].

The size of exosomes is determined by the dimension of the internal vesicles of MVBs where they are formed, which ranges from 30 nm to 100 nm. The density of exosomes was shown to be in the range 1.13-1.19 g/mL, depending on the intravesicular protein enrichment [44].

Therefore, according to the literature, exosomes are supposed to verify the three following characteristics:

- Display diameters between 30 nm and 100 nm, with a characteristic asymmetry of the size distribution that is right-skewed to larger dimensions [45].
- Present characteristic proteins.
- Originate from the fusion of multivesicular endosomes with the plasma membrane.

However, recent ISEV meetings have mentioned that [46]:

- Exosome diameters can reach up to 250 nm.
- Other types of EVs also display exosomal proteins, such as tetraspanins.
- EVs identical to exosomes can stem directly from the plasma membrane.

In conclusion, **reliably identifying the type of EVs that is being handled is challenging and the ISEV strongly recommends to use the general term "extracellular vesicles" in publications.**

Mechanisms of Action of Extracellular Vesicles

EVs interact with recipient cells according to three possible mechanisms [33]:

- Adhesion of the vesicle on the recipient cell surface through interactions between a vesicle ligand and a cell receptor.
- Interaction between target cell receptors and soluble ligands that are cleaved from EV membrane proteins.
- Internalization of the vesicle into endocytic compartments of the recipient cell through endocytosis or membrane fusion.

Each of them requires an initial interaction between specific receptors on the EV and the plasma membrane of the recipient cell [16]. After internalization, in order for EV components to be degraded and influence the recipient cell physiology, fusion with the plasma membrane and with the membrane of endocytic compartments is necessary, which was demonstrated through fluorescent labelling [47, 19]. Another study [48] also showed that EVs enter endosomes and then move along microtubules.

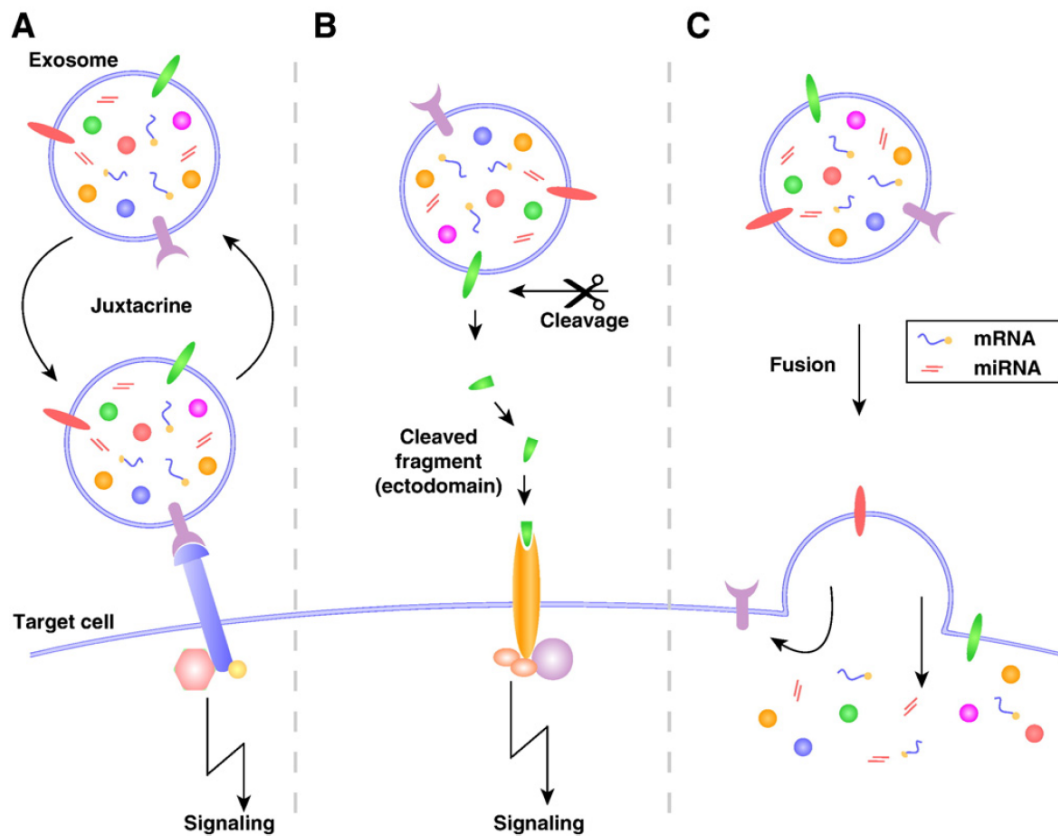


Figure 1.4: Illustration of the three mechanisms of interaction between EVs and recipient cells: A. intracellular signaling activation through interactions between EV membrane proteins and target cell receptors. B. intracellular signaling activation by a soluble ligand cleaved from an EV membrane protein. C. EV fusion with the target cell membrane and release of EV molecules. [41]

1.1.2 Physiological Functions

El Andaloussi et al. classified EV physiological functions into four categories [35]:

- Stem cell phenotype modulation and maintenance [9]
- Tissue repair [49]
- Blood coagulation [50]
- Immune surveillance [51]

Yanez-Mo et al. [1] reviewed in 2015 the numerous reported physiological functions of EVs according to their biofluid origin. A summary table is proposed in Appendix 1.

Role in Immunity

The adaptative immune system enables protection against specific pathogens, with an enhanced response after an initial presentation of the antigen, thanks to the immunological memory. B cells and T cells are the main lymphocytes of the adaptative immune system. "Non-self" antigens are recognized by receptors on antigen-presenting cells (APCs). Antigen-specific receptors on B cells interact with the foreign antigen and process it in order to display it on major histocompatibility complexes (MHC class II), that activate helper T cells, also known as CD4⁺ T cells. After activation, helper T cells secrete cytokines that trigger the secretion of antibodies from other immune cells and recruit macrophages, neutrophils and other lymphocytes. This process is illustrated on fig. 1.5. In addition to this activation way, cytotoxic T cells (also known as CD8⁺ T cells) can also be activated by the cells presenting MHC class I molecules associated with foreign antigens in order to kill the infectious agents.

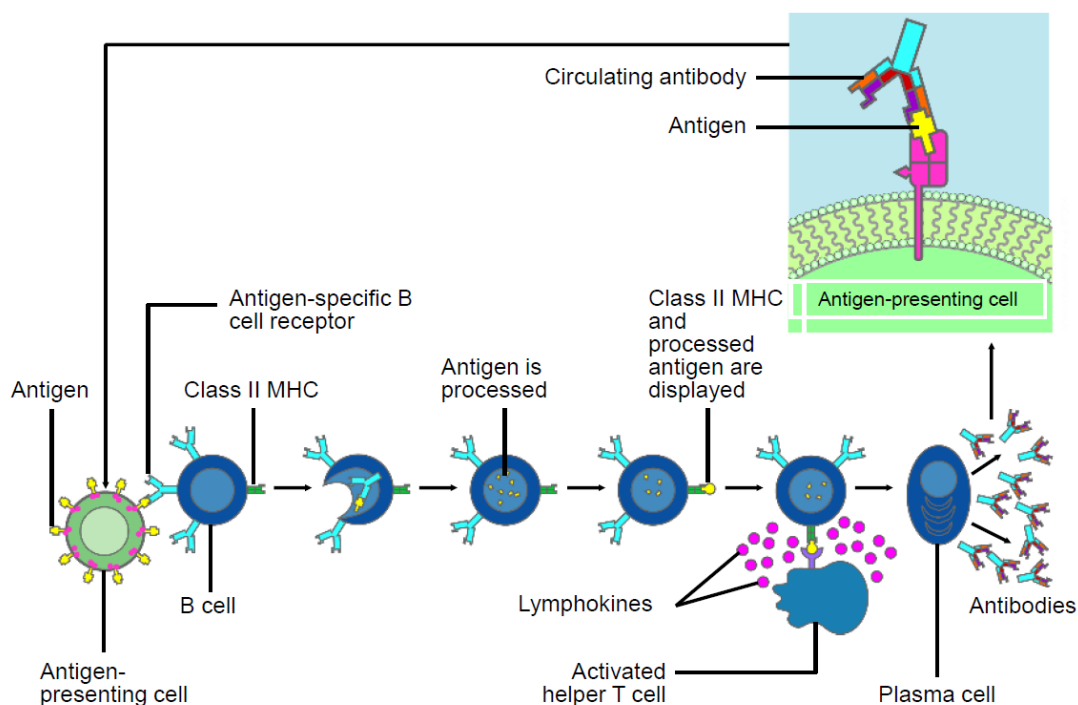


Figure 1.5: General view of the activation process of B cells to make antibodies, from BME344 course at Northwestern University, Evan Scott, 2015.

EVs participate in this immunity process through four different ways:

- Carry antigens that are recognized by APCs: Antigens presented by exosomes can be either transmembrane proteins from the donor cell surface or internal proteins from the donor cell endosomal compartments. Activation of T-cells was demonstrated by exosomes from cultured tumour cell lines [52], bacteria-infected macrophages [53] and virus-infected endothelial cells [54].

- Present peptide-MHC complexes directly:
 - Dendritic cells (DC) release exosomes with MHC class I molecules on their surface [55, 56, 57, 58].
 - Exosomes secreted by APCs present MHC class II molecules. However, they need to be captured by recipient dendritic cells (DCs) to activate helper T-cells[59].
- Induce transformation of target cells into immune APCs [60].
- Present proteins that have an immuno-suppressive effect through different action modes: activation of T cell apoptosis [61], inhibition of T cell proliferation [62], decrease of the cytotoxicity of natural killer (NK) and cytotoxic T cells [63, 64], inhibition of the differentiation into DCs [65] and generation of myeloid-derived suppressor cells (MDSCs) [66]. This tolerogenic effect is very promising to promote graft survival [67], reduce inflammation [68] and allergy responses[69].

Role in Neurobiology

EVs are secreted by both neuronal and glia cells in the Central Nervous System (CNS) [70, 71, 72]. Neural presynaptic terminals produce both synaptic vesicles (SVs) and EVs [73]. SVs are 35 to 55 nm vesicles [74] that release neurotransmitters at the synapse by calcium-triggered fusion with the presynaptic plasma membrane [75]. Since 2006 [71], EVs emerge as a new synaptic vesicle type, that is secreted by the axon to transport not only neurotransmitters but also RNAs, proteins and lipids [76]. In addition to this molecular exchange, EVs have several roles in the CNS:

- Myelination of axons to increase signal conduction velocity [77]
- Plasticity of the synapses [78]
- Activation of synapses [79]
- Supply of neurotrophic factors [80]
- Activation and spread of neuroinflammatory responses [81]
- Neurodegeneration through protein disposal [82]
- Natural therapeutic effect after neurological disorders by promoting angiogenesis and neurogenesis [83]

Neuronal EVs have been shown to transport pathogenic proteins and deregulated miRNAs that participate in neurodegenerative diseases, such as prion, Alzheimer's, Parkinson's, Huntington's diseases and amyotrophic lateral sclerosis [84, 85]. More broadly, Janas et al.[73] raised the question if deficient EV transport could be implied in all types of synaptopathy. Recently, new exosomal biomarkers were presented as specifically related to neurodegenerative disorders [86]. Therefore, accurately understanding EV functions in neurodegenerative diseases could lead to new diagnostic and therapeutic solutions.

1.1.3 Diagnostic and Therapeutic Potential

In tumor biology

Standard tissue biopsy is painful, life-threatening and requires enough sample material, which can be a problem for example in pancreatic cancer [87, 88]. Moreover, strong intra-tumor heterogeneity and instability makes tissue biopsy-based diagnosis very difficult [89]. Therefore, **noninvasive diagnostic methods** are required to detect cancer in the earliest stages of tumor progression, personalize and follow treatments and detect the emergence of resistances to treatments [90]. Current cancer diagnosis suffers from the lack of specific biomarkers and the concentration variability of known biomarkers, which leads to numerous false-positive cases and over-treatment problems [91].

Liquid biopsy can be based on three types of tumor-derived objects in body fluids: circulating tumor cells (CTCs), cell-free DNA/RNA and EVs. Tumor-derived EVs have several advantages over CTCs and nucleic acids for liquid biopsy applications: EVs display higher stability, they enable protein analysis in addition to sequencing (like CTCs) and their concentration is much higher than CTC levels in body fluids (about 10^9 /mL for EVs [92] vs 10-100/mL for CTCs [93] in blood). Moreover, EVs are secreted from the first stages of the metastatic development, much sooner than the first possible detection of CTCs in body fluids [94].

EV exchange contributes to cancer spreading from malignant cancer cells through multiple mechanisms [95, 96, 97, 98, 99]:

- Tumor growth through cell proliferation [100, 101, 102, 103, 104, 105, 106, 107].
- Tumorigenesis through transformation of stem cells [108, 109, 110, 111, 112], increase in the metastatic potential of less malignant tumor cells [113, 114], activation of myofibroblasts [115] or degradation of the extracellular matrix [116, 117].
- Angiogenesis through migration stimulation and tubule formation in endothelial cells [118, 119, 120, 121, 122, 123, 124, 125, 126] and the activation of cancer-associated fibroblasts [127].
- Drug resistance spreading from cancer cells [128, 129, 130, 131, 132], from cancer-associated fibroblasts [133] and from stromal cells [134, 106], removal of chemotherapy drugs [135] and modulation of therapeutic antibodies binding [136].
- Suppression of the antitumor immune response [137, 138, 139] through apoptosis of cytotoxic T lymphocytes [140, 141, 142], suppression of the immune response of dendritic cells [143, 144] and regulation of tumor-associated macrophages [145, 146].
- Preparation of pre-metastatic niches in distant tissues [147, 101, 148, 149, 150, 151, 152, 153, 154], especially across the blood-brain-barrier [155, 156] and in the bone marrow [157].
- Matrix remodelling by metalloproteinases transported by tumor-derived EVs [158].
- Cancer-associated thrombosis through the formation of neutrophil extracellular traps [159].
- Inflammation that contributes to cancer progression [160].

Cancerous EVs flow through the blood circulation to reach distant organs. For example, melanoma-released EVs injected through the tail vein of naive mice reached the lungs, spleen, bone marrow and liver [161]. The circulation of EVs is responsible for the increase in vessel leakiness, the increase in metastases and the neoplastic growth through recruitment of bone marrow-derived cells. Moreover, breast cancer EVs were shown to promote the colonization of distant tissues through activation of the mesenchymal-to-epithelial transition [113].

Johan Skog et al. at Massachusetts General Hospital (MGH) published in 2008 the first demonstration that tumor mutations influence the RNA content of EVs, which can be used diagnostically [162]. **Several specific miRNA, lipid or protein biomarkers have been identified in EVs according to the cancer type** [163]. They are reported in Appendix 2.

The amount of EVs in body fluids was shown to be a diagnostic tool itself, called “Liquid Tumor Mass Diagnosis” by Cappello et al. [164]. Indeed, **the level of circulating EVs is related to the tumor progression**, which enables cancer diagnosis without the need for specific biomarkers [165, 166, 167, 168, 169, 170, 171]. All the available studies show an increase in EV concentrations with tumor progression, through different quantification techniques, such as immunocapture-based ELISA, protein quantification, Nanoparticle Tracking Analysis or flow cytometry. **Now standardized techniques should be developed to reliably quantify the level of EVs in body fluids for clinical applications.**

From Skog’s research at MGH was founded a company called **Exosome Diagnostics** (USA, MA) to commercialize exosomal RNA-based diagnostic tests from plasma samples. Their exoRNeasy kit can be purchased from QIAGEN and enables isolation of total EV RNA for further sequencing analysis in order to detect and measure levels of genes related to cancer and other diseases. The isolation of EV RNA is performed through two successive steps: the capture of EVs from prefiltered plasma in a membrane affinity spin column and the lysis of bound EVs with specialized buffers for RNA extraction. Four liquid biopsy tests using this RNA extraction technology are already available to detect prostate cancer (ExoDx Prostate IntelliScore) or lung cancer (ExoDx Lung ALK, Lung T790M and Lung EGFR).

Exosomics (Italy) also provides EV-RNA and DNA extraction kits for liquid biopsy and cancer screening. First, the isolation of EVs from up to 7 mL of complex biofluids can be performed through two different technology: the “SeleCTEV” technology that capture EVs with a peptide-affinity method, and the “SoRTEV” technology with immuno-affinity beads coated with specific antibodies against EV surface antigens. After isolation of EVs, EV-RNA and DNA is extracted with proprietary reagents. Exosomics also commercializes analytical assays, based on ELISA or PCR platforms.

Caris Life Sciences (USA and Switzerland) also developed an immunocapture technology called “**Cari-some**” to capture blood EVs on coated beads and detect specific surface antigens with fluorescently labelled antibodies. A first test is already available for prostate cancer diagnosis and displays better sensitivity and specificity compared to standard PSA test.

Finally, **Exosome Sciences** is developing an Enzyme-Linked Lectin-Specific Assay (ELLSA) to isolate exosomal biomarkers, such as TauSome, that could be the first non-invasive biomarker of Chronic Traumatic Encephalopathy (CTE).

EVs are also considered as potential biomarkers in chemotherapy treatments, for example by measuring

the mRNA levels in EVs, which reflect the level in parental cells and allow evaluation of the treatment efficiency [172].

As pointed out by Zocco et al. [173], the two main challenges in the development of EV-based diagnostic technologies, such as those mentioned above are the ability to:

- Standardize and simplify EV isolation from undiluted body fluids.
- Detect the entire panel of EV biomarkers with high sensitivity and specificity.
- Collect undamaged vesicles in a non-destructive way to further study the structural and physical properties of EVs in addition to proteomic and sequencing analysis.

In infectious diseases

EVs are also exploited by viruses to spread infections [174, 175]. In particular, several mechanisms are used in the context of virus infection [176, 177, 178]:

- The use of exosomal release pathway for the production of viral particles
- The transport of viral mRNA, miRNA and proteins by exosomes
- The release of viruses together with exosomes to escape immune surveillance
- The modulation of exosomal release by virus proteins acting on the infected cell.

Ellwanger et al. [177] recently reported a critical review for the particular case of HIV infections. An increase in the concentration of plasma exosomes was recently demonstrated for HIV-positive subjects compared to controls, as well as an increase in the exosomal Notch4 protein [179]. This study opens new perspectives towards the understanding of the relationship between exosomal cargo and HIV disease, that could lead to the identification of new biomarkers and therapeutics. Moreover, DeMarino et al. [180] showed that antiretroviral therapy result in the loading of viral components (RNAs and proteins) in EVs in HIV-1 infected patients. Therefore, better understanding of EV functions in HIV disease would enable to avoid negative effects of EV transport.

In diabetes

Pancreatic beta cells contribute to glucose homeostasis and play a key role in the development of diabetes. EVs secreted by pancreatic beta cells contribute to the progression of diabetes by transporting the heat shock protein Hsp90 into endothelial cells [181]. In type 1 diabetes, it was shown that EVs generate autoimmunity through T-cell proliferation, leading to the destruction of the insulin-secreting cells in the pancreas [182, 183, 184]. Therefore, EVs emerge as promising biomarkers for type 1 diabetes. In particular, seven specific EV miRNAs were found to be markers of type 1 diabetes [185]. In type 2 diabetes, EVs from adipose tissues, skeletal muscles and hepatocytes participate in the resistance to insulin by transporting functional proteins and RNAs [186, 187].

In arthritis

EVs have several roles in arthritis (both rheumatoid arthritis and osteoarthritis) [188, 189]:

- Inflammation through antigen presentation and activation of the immune system
- Destruction of the extracellular matrix, damaging cartilage
- Delivery of miRNAs

EVs are potential biomarkers in rheumatoid arthritis, with two reported specific markers: the membrane citrullinated protein [190, 191] and miRNA-155 [192].

Therapeutic Potential

EVs have natural therapeutic effects by driving **tissue regeneration** through four different mechanisms:

- Induction of angiogenesis in endothelial cells [193]
- Suppression of apoptosis and stimulation of cell proliferation [194]
- Delivery of immunomodulatory signals [195] for immunotherapy [33]
- Recruitment or reprogramming of cells required for tissue regeneration [9, 196, 197]

In addition, four different EV-based strategies can be implemented to **prevent cancer spreading** [198]:

- Inhibit EV production by multi-vesicular bodies (MVBs) [199]
- Inhibit EV release [200, 161]
- Inhibit EV uptake by recipient cells [201, 202]
- Modify specific EV components that contribute to disease spreading [203]

Furthermore, the ability of EVs to transport various RNA species makes them particularly interesting as **drug delivery vehicles** [9, 204, 193, 205, 206, 207]. In particular, it was shown that EVs not only transport mRNAs, but they also deliver them into target cells for translation into proteins [10, 162], which is dynamically regulated in EVs by several proteins [208, 209]. The use of EVs as delivery vectors presents several advantages: they are naturally biocompatible and immunologically inert, they can be patient-derived and they are able to cross major biological barriers such as the blood-brain barrier [210, 211].

Appendix 3 reports completed and running clinical trials for EV-based therapeutic strategies.

1.1.4 Current Challenges in EV Research

According to Kalra et al. [32], several challenges have to be overcome in order to better understand EV functions and potential:

- EV nomenclature needs standardization to avoid confusion between the different types of EVs, which are very complex to precisely identify.

- Robust isolation protocols need to be implemented and standardized, especially for diagnostic and therapeutic applications.
- Isolation techniques need to be improved in order to separate the different EV subpopulations.
- Interactions between the different types of EVs need to be better evaluated in order to know if excluded EV subtypes display the same functions.
- The biogenesis pathway of EVs have to be better understood. In particular, it is still unknown if cargo packaging into EVs follows a selective or a random process.
- Further studies are required to know how the EV concentration influences their functions.
- Evaluation of the life time of EVs is needed.
- The mechanism of communication between EVs and target cells is still unclear, while it is fundamental for therapeutic developments.

Since 2010, the EV-TRACK consortium gathers 95 participants from 38 institutions to evaluate more than 1250 publications on EV research, that are centralized on the EV-TRACK website [212]. Since their creation in 2011, the ISEV regularly publishes recommendations to meet the "**minimal experimental requirements**" when reporting scientific studies on EVs [213, 214, 215].

The main ISEV recommendations are summarized below:

- Provide an analysis of the protein composition of the EV preparation. Identification and relative quantification of several proteins (at least 3) is required since no single specific marker has been identified so far to prove the presence of EVs.
- At least two different methods should be implemented to characterize the heterogeneity of EVs. In particular, size distribution measurement techniques should be compared to microscopy observations since a single size characterization does not differentiate vesicles from other particle types of similar sizes.
- When action of specific vesicular proteins or RNA species is demonstrated, it is necessary to verify that these components come from EVs and are not soluble molecules co-isolated with EVs.

In order to apply all these recommendations, **robust isolation and characterization techniques** are required to isolate pure EV samples and provide complete analysis of the exosomal signature. In this context, the Cancer-ID project (<https://www.cancer-id.eu/>) was launched in 2015 in the Netherlands by 6 universities in collaboration with 22 companies to fully characterize tumor-derived EVs for clinical applications, thanks to many different combined techniques. Standard available characterization and isolation techniques are presented in the next section, as well as emerging technologies, that provide improvements to overcome current limitations of standard technologies.

1.2 Standard Characterization Techniques

Two categories of EV properties can be characterized by standard techniques: the size and morphology of EVs, and their internal and surface protein composition. An excellent review recently reported all the

standard and emerging techniques to characterize EVs [216].

1.2.1 Size and Morphology Characterization

Electron Microscopy

Electron microscopy (EM) enables to obtain images of EVs with a resolution on the order of the nanometer. The images are obtained either by transmission of the electron beam through the sample (transmission electron microscopy TEM) or by inelastic diffusion and scattering of the electron beam on the sample surface (scanning electron microscopy SEM). TEM is the most common EM technique for EV characterization owing to its better resolution, but SEM can also provide interesting complementary information as better 3D images of the particles surface can be obtained. As EM observations are performed in vacuum, EVs have first to be fixed and dehydrated before observation. The most common sample preparation protocol consists of the deposition of a liquid sample drop on the grid followed by fixation and dehydration by a chemical treatment with paraformaldehyde [217] or glutaraldehyde [36] (fig. 1.6 a). The pellet containing EVs at the end of the differential centrifugation protocol can also be fixed directly and sectioned in ultrathin slices [218]. Even if this second protocol is more laborious than the first one, the risk of adhesion problems of some vesicles on the grid is avoided and the concentration of EVs is increased. Cryogenic freezing before EM observations is a growing preparation technique to replace fixation steps by chemical treatments that are responsible for size and morphology artefacts. Indeed, the observed cup-shaped structure of EVs was not recovered when cryogenic preparation was implemented instead of chemical fixation [36]. However, alterations of the natural size and structure of the vesicles can still happen in cryo-TEM because of the limited width of the frozen layer (usually on the order of a few hundreds of nanometers), that squeezes larger vesicles and makes them appear wider. Moreover, the high intensity of the electron beam can be responsible for EVs damages [219] (fig. 1.6 b). Specific surface biomarkers can be stained by immunogold particles in order to detect subpopulations of EVs, as reported by Melo et al. [220] who specifically imaged EVs from breast cancer cells expressing CD9 biomarkers on their surface.

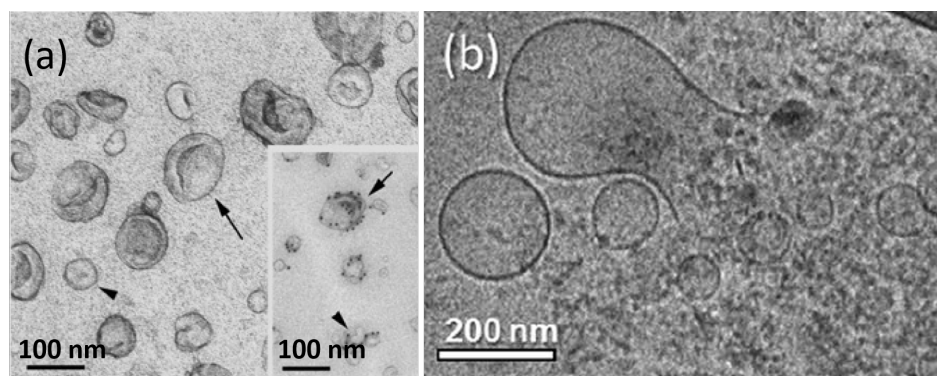


Figure 1.6: (a) Typical TEM observations of the cup-shaped structure of EVs after chemical fixation. Insert: Labeling of surface exosomal MHC class II antigens with coated 10 nm-gold particles [36]. (b) TEM observations of EVs after cryogenic fixation and membrane breakage of the vesicles [219]

Atomic Force Microscopy

Atomic force microscopy (AFM) is another widely used imaging technique to obtain surface topography of EVs by scanning the sample surface with a vibrating cantilever tip. Fixation of the vesicles on a very flat surface is required before imaging by AFM. In most cases, mica surfaces coated with antibodies specific for EVs surface biomarkers are implemented for AFM imaging, which also enables to detect subpopulations of EVs [221]. Fixation and dehydration steps in the preparation protocol may alter the morphology of the EVs, this is why liquid mode was reported to be preferred for EVs characterization by AFM than air-tapping mode [222] (fig. 1.7). Whitehead et al. [223] compared the stiffness of malignant and non-malignant cell line EVs by PeakForce tapping AFM, but deformability measurements may be questionable when considering impacts of fixation on the stiffness of such small-sized vesicles.

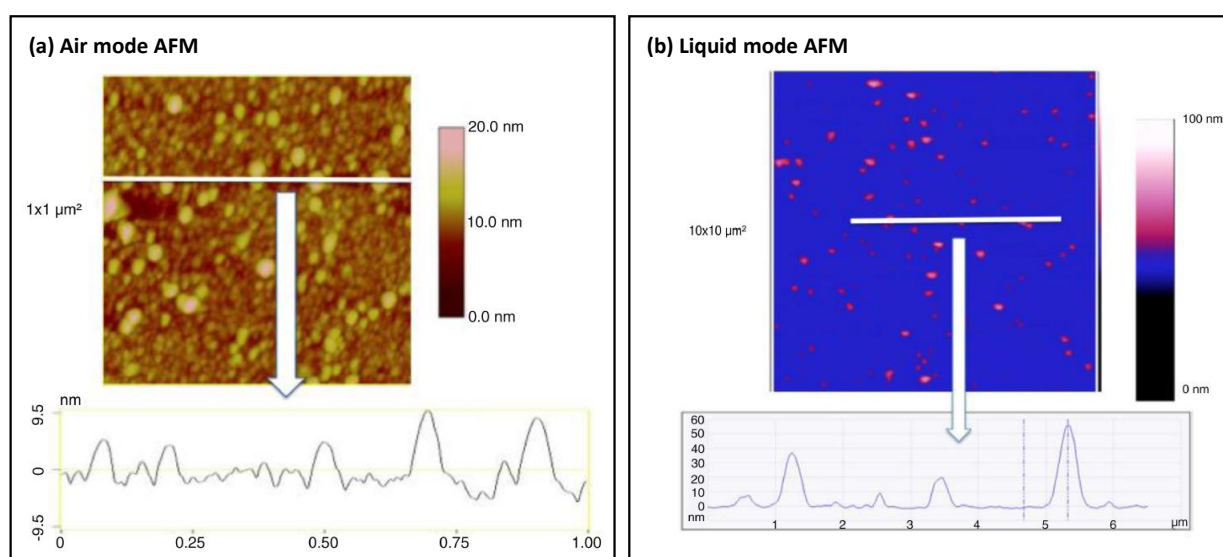


Figure 1.7: (a) AFM image in air mode of breast cancer cell-derived EVs and corresponding cross-section histogram (b) AFM image in liquid mode of breast cancer cell-derived EVs and corresponding cross-section histogram: the obtained EV size range is up to 10 times higher in liquid mode compared to air mode [222]

Dynamic Light Scattering

Dynamic light scattering (DLS) makes use of the light scattering of a laser beam by diffusing particles submitted to Brownian motion, in order to determine their size. Indeed, the measured variations of the scattered intensity is directly related to the size of the particles. Thanks to a mathematical algorithm, the average diameter of the particles can be calculated, assuming a spherical shape. Moreover, most DLS instruments also measure the zeta potential of charged particles by applying an electric field and measuring the migration velocity. Although this technique is rapid and convenient, it is not well adapted to heterogeneous samples such as EVs and post-treatment models only apply to a single or several well-resolved monodisperse population(s). Indeed, when a polydisperse sample is processed, the corresponding

size distribution may be biased towards large particles as the intensity of the scattered light increases with the particle size [224]. The shifting of the size distribution towards larger diameter for EVs populations was observed by van der Pol et al. [225] and this bias can even make small vesicles undetectable. This is why a preliminary sample preparation is necessary to fractionate EVs samples into different sized subpopulations.

Nanoparticle Tracking Analysis

Nanoparticle tracking analysis (NTA) is a particle tracking method to determine both the size distribution and the concentration of particles down to 50 nm. In addition to the measurement of the scattered intensity of a laser beam, the mean velocity of each individual particle is determined with the Stokes-Einstein equation from the Brownian motion recorded by a CCD camera. As with DLS, the zeta potential can also be measured by applying an electric field across the sample. Because of its convenience and fast processing, NTA is the most widely used method to characterize the size and concentration of EVs, even if the detection limit of the microscope makes the analysis impossible under 50 nm. In fluorescent mode (f-NTA), the resolution limit can be improved by fluorescently labelling specific vesicles that present a target surface biomarker [225]. NTA characterization requires the isolation of EVs from other contaminants of similar sizes as they present the same Brownian motion and cannot be distinguished with this technique. Moreover, data processing from NTA instruments is still laborious and time and storage capacity is required to analyze the video data after each measurement. The main limitation of this characterization technique is the dependence of the obtained concentration and size distribution on the chosen detection parameters, such as the camera level (combination of the shutter time and the camera gain) and detection threshold (minimum intensity required to be assigned as a particle). Maas et al. [226] demonstrated the effect of these parameters on the calculated concentration, while fig. 1.8 shows how the detection threshold influences the obtained size histogram for the same EV sample.

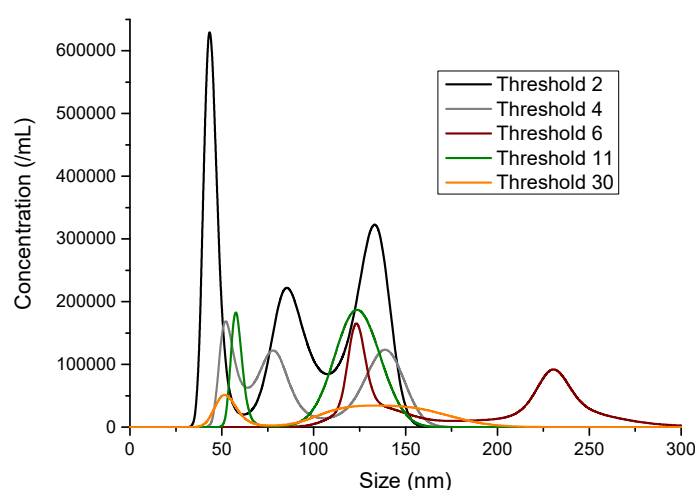


Figure 1.8: Influence of the detection threshold for NTA measurements (with a fixed camera level) of an EV sample extracted through differential centrifugation from THP-1 cell culture media.

Tunable Resistive Pulse Sensing

Tunable resistive pulse sensing (TRPS) is an impedance-based flow cytometry technique that uses the Coulter principle to determine the number of particles and their size distribution based on individual particle measurements. An ionic current is created by a transmembrane voltage across a nanopore between two electrolyte solutions. When particles flow through the membrane, a current decrease is measured according to the particle size, which enables to characterize the size distribution of the sample. The nanopore size has to be small enough to detect particles since the sensitivity of RPS instruments depends on the ratio between the particles size and the pore diameter, that should range from 0.1 and 0.7 [227]. Therefore, in order to measure an entire EVs population, several RPS devices have to be cascaded with different detection limits. Maas et al. highlighted the influence of the pore size on the measured particle concentration [226]. According to their pore dimensions, RPS instruments can measure particles from 50 nm to 10 μm [228] and recent developments have shown further improvements in the measurement stability and sensitivity [229], even if the detection limit still has to be reduced in order to analyze all the vesicles sizes. The main issue when using RPS for EV characterization is the passage of several particles simultaneously in the pore (that are detected as one single large particle), and the risk of pore clogging or sticking of proteins on the pore surface. Indeed, as the determination of the particle size is dependent on the pore diameter, any change in the nanopore size with adhesion of contaminants is responsible for measurement errors. This is why a careful sample preparation step has to be performed before RPS detection in order to remove large contaminants and proteins, as well as adapted dilutions. Moreover, several calibrations have to be done regularly to precisely know the pore dimensions at each time, and this process severely increases the measurement time. RPS has the advantage of being easily combined with other characterization techniques like DLS, fluorescence flow cytometry or Raman spectroscopy. Moreover, zeta potential and surface charge can also be determined from RPS measurements thanks to analytical descriptions of the dependence of particle size and position with the pore dimensions and the measured resistance shift [230]. RPS instruments are commercially-available, like the qNano instrument from Izon Science Ltd. This equipment enables to characterize particles from 40 nm to 10 μm , thanks to a tunable pore size with a polyurethane membrane that can be mechanically stretched. TRPS and NTA were recently compared by Akers et al [231]. This study showed that NTA detected more EVs inferior to 150 nm, while TRPS was better at detecting larger EVs.

Other Methods

Thanks to micromechanical resonators with integrated microfluidic channels (a concept that was pioneered at MIT by Prof. Scott Manalis' group), EVs can be individually analyzed in flow in a label-free and non-destructive way. Measurement of the buoyant mass of single particles is performed from the recording of the resonance frequency shift of a hollow cantilever while particles are flowing in a buried fluidic channel [232] (fig. 1.9 a). This technology is known as "**Suspended Microchannel Resonator**" (SMR), or SNR for the nanometric version of the sensor. Among the various possible applications offered by this characterization principle recent developments showed the determination of drug sensitivity of cancer cells from their mass accumulation rate (MAR) [233, 234], the measurement of single-cell growth rates with serial arrays of SMRs [235] and the RNA sequencing of single cells throughout the cell cycle with trap arrays [236]. In addition to mass measurements, information on the deformability of single particles can

be obtained from their passage time through channel constrictions [237]. Density can also be measured from the buoyant mass of the particle in two successive fluids of different densities [238]. By reducing the dimensions of the device and driving the sensor at the onset of nonlinearity, a mass resolution down to 0.85 attogram could be achieved [239], enabling the extraction of size histograms of exosomes (fig. 1.9). At CEA Leti, the concept of SMRs has been adapted to plate resonators that do not require vacuum packaging [240], in the perspective of weighing nanometer-sized individual particles [241].

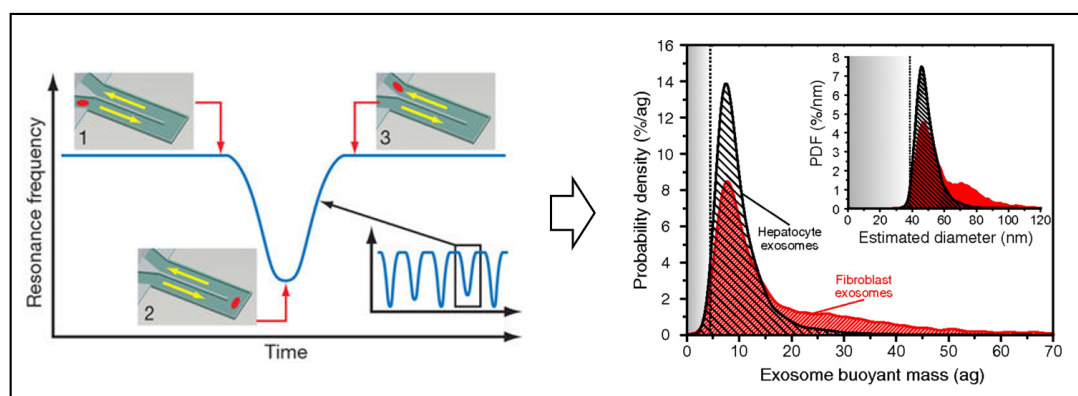


Figure 1.9: Cantilever sensors developed at MIT by Scott Manalis Group: principle of buoyant mass measurement [242] and application to the weighing of hepatocyte and fibroblast exosomes, with corresponding size histograms from estimated density [239].

Raman spectroscopy (RS) enables to identify the molecular composition of samples by studying the inelastic scattering of a laser light. Indeed, the wavelength of the scattered light is related to the energy loss or gain due to molecular vibrational transitions. Therefore, RS is a very interesting technique to characterize the biochemical composition of EVs without any labelling requirement. Even if RS can only give information on populations of multiple EVs and leads to complex spectra, it is an interesting tool to compare several EV populations [243, 244], especially with Surface Enhanced Raman Spectroscopy (SERS) [245]. For example, RS has recently demonstrated promising diagnosis applications with specific spectral signatures for normal and cancer cell derived EV populations [246, 247].

Excitation with light illumination on a surface is able to generate surface electromagnetic signals called **surface plasmons**. The wavelength of the optical transmission peak depends on the refractive index and composition of the illuminated surface. This phenomenon can be implemented to detect EVs [248] when surface plasmons are generated and wavelength shifts are detected with an antibodies-coated surface that captures flowing EVs. Im et al. [249] developed a nano-plasmonic exosome assay system called nPLEX that makes use of the Surface Plasmon Resonance (SPR) phenomenon to detect and quantify captured EVs in an array of nanoholes in a 200 nm-thick Au film. Indeed, SPR enables to quantify the captured EVs since the amount of transmitted wavelength shifting is related to the adsorbed molecular mass density. This device is very promising for EV detection with a detection limit 10^4 -fold higher than western blotting and 10^2 -fold larger than ELISA assay from sample volumes as low as 1 μ L [250].

Small-angle X-ray scattering (SAXS) is a measurement of elastic scattering radiations of X-ray photons. Unlike crystallography that collects scattering radiations at wide angles to get information on the atomic structure, SAXS uses low angles scattering radiations. From the scattering intensity curve as a function of scattering angles, structural information on the phospholipid bilayer and the transmembrane proteins can be obtained, as well as global size and shape characterization for EVs smaller than 100 nm. For example, size and molecular composition of neuron synaptic vesicles were obtained from SAXS measurements by Castorph et al. [251].

Table 1.2: Main advantages and limitations of the EV characterization techniques described above.

Technique	Advantages	Limitations
TEM	Morphological study Possible visual differentiation between EVs of interest and other particles of similar size	Bulky and time-consuming technique to obtain statistical results Possible alteration of EVs due to the fixation step (chemical or cryogenic)
AFM	Both structural and biological information by selecting EVs presenting target antigens on a coated surface	Time-consuming Requires to engineer effective coated surfaces Possible alteration of EV shape and stiffness when attached to the surface
DLS	Fast and easy handling on a large number of EVs Measures both size and zeta potential	Measurements are biased in heterogeneous samples Requires adapted sample dilutions
NTA	Fast analysis of a large number of EVs Measures both size and concentration	Unconvenient handling to avoid air bubbles in the fluidic circuit High dependence of the results on the chosen detection parameters and sample dilution
TRPS	Fast and easy handling on a large number of EVs Measures size, concentration and zeta potential	Analysis of heterogeneous EV populations requires several successive measurements with different pore sizes Measurements are biased by potential pore clogging Requires adapted sample dilutions
SMR/SNR	Only method that weights particles Potential additional information on density and stiffness, single particle analysis	Time-consuming handling and process to analyze a high number of EVs Requires effective upstream sample preparation to avoid clogging issues in the fluidic channel by heterogeneous EV populations
RS	Biochemical characterization	Limited information on the analyzed EVs
SPR	Detection of specific target EVs that are captured on a coated surface	Limited information on the analyzed EVs (concentration only) Small analysis volume Requires surface functionalization
SAXS	Structural information on the EV membrane	Complex interpretation of obtained SAXS data Limited information on the analyzed EVs

* TEM = Transmission Electron Microscopy, AFM = Atomic Force Microscopy, DLS = Dynamic Light Scattering, NTA = Nanoparticle Tracking Analysis, TRPS = Tunable Resistive Pulse Sensing, SMR/SNR = Suspended Micro-/Nanochannel Resonator, RS = Raman Spectroscopy, SPR = Surface Plasmon Resonance, SAXS = Small Angle X-ray Scattering

1.2.2 Composition Characterization

Flow Cytometry

Flow cytometry was originally developed for cell characterization by recording the scattered and fluorescence intensities when single particles flow in front of a laser beam. Flow focusing enables to generate a continuous flow with individual particles that successively enter the detection volume. This technique can perform quantification of surface EV proteins by attaching them to fluorescent antibodies and measuring up to nine fluorescence signals at the same time. However, it cannot distinguish EVs from fluorescently labelled protein aggregates [252]. Recently, Stoner et al. [253] have proposed a new high sensitivity flow cytometer, called Vesicle Flow Cytometer (VFC) to specifically increase the fluorescent signal associated to EVs. A comparative study showed that VFC counted two to three times less EVs than NTA and TRPS, possibly because VFC enables not to count protein aggregates or other particles of similar sizes [231]. In addition, Apogee Flow Systems now commercializes a specific micro flow cytometer dedicated to the detection of nanometer-sized particles, such as EVs or protein aggregates. A comparative study showed that conventional flow cytometry gave 300-fold lower EV concentrations compared to NTA and TRPS measurements, while the dedicated Apogee A50 Micro cytometer gave a 15-fold underestimation of the EV concentration [254].

In addition to the characterization of surface proteins, flow cytometry also gives information on the size and morphology of particles thanks to two detectors that record at the same time the intensity of forward light scatter (FLS) and side light scatter (SLS). Current developments try to decrease the detection limit to better detect EVs by using membrane fluorescent intercalating dyes [255]. However, even for vesicles larger than the detection limit, there is a large uncertainty in the particles diameter because of the uncertainty for the refractive indices of EVs. Indeed, as the EVs refractive index is known to be between 1.36 and 1.45, this corresponds to a 5.5-fold uncertainty in sizes [256]. Moreover, similarly to what was reported for Resistive Pulse Sensing (RPS), “swarm signals” may happen when several vesicles are contained in the detection volume at the same time [256]. In this case, several small vesicles, that would not scatter sufficient signal intensity to be detected alone, are measured as one larger vesicle, and adapted sample dilutions are required.

Fluorescence Microscopy

Fluorescence microscopy enables to explore EVs function in normal physiological states since it can be performed *in vivo*. EVs are tracked thanks to lipophilic fluorescent dyes that can be inserted in the lipid bilayer of the vesicles or with a fluorescent molecule that interacts specifically with surface biomarkers. The most common dyes for CD63 surface biomarker are lipophilic carbocyanines, the green fluorescent protein (GFP) or the red fluorescent protein (RFP). Suetsugu et al. [257] used the GFP dye for cancer-cell-derived EVs *in vivo* in cancer mouse models in order to follow the role of EVs in tumor growth and metastasis. This study was complemented with observations of vesicle exchange between tumor cells in living mouse and the role of this exchange in the increase of the metastatic properties of the receiving cells [258]. In addition, fluorescence microscopy can be used as a characterization tool to determine the concentration of EVs, by assuming that all the vesicles are stained by a fluorescent dye.

Western Blotting

Western blotting is useful to verify the presence of proteins that are known to be transported or presented on the surface of the EVs [165]. The most commonly investigated proteins are surface markers such as tetrasparins (CD9, CD63, CD81 and CD82) and Major Histocompatibility Complex (MHC) molecules, but also cytosolic proteins and cytoskeletal proteins. After lysis of the vesicles, the proteins are separated by gel electrophoresis (usually SDS-PAGE, Sodium Dodecyl Sulfate - Polyacrylamide Gel Electrophoresis) and transferred to a membrane before being stained with specific antibodies. Western blotting needs a very careful purification of EVs because proteins coming from contaminants cannot be distinguished from EVs proteins. This is why the detection with Western blotting of proteins known to be presented by EVs is not sufficient to prove the presence of the vesicles in the sample.

ELISA

Enzyme-linked immunosorbent assay (ELISA) is another technique to detect surface and internal proteins of lysed EVs with high sensitivity and possible quantification of the protein content [259]. After immobilization of the proteins on a solid surface, detection antibodies are added. Two strategies can be used to observe the presence of the targeted proteins: either the detection antibody is covalently linked to an enzyme or it is detected by a secondary antibody that is linked to an enzyme. When the enzyme's substrate is added, a color change is observed because of the induced enzymatic reaction. Several commercially available ELISA kits are adapted to the analysis of EVs proteins, such as specific ELISA kits from System Biosciences. However, it is still hard to find specific antibodies for each existing EVs subcategory.

Bradford Assay

When a quantification of the total protein content of the EVs is required, the Bradford assay can be implemented. This protein quantification may also be used to quantify the total amount of isolated EVs [260]. With this technique, the detection is not specific to a particular antigen, but it quantifies the total amount of proteins after EV lysis. It is a colorimetric protein assay that is based on the color shift of the Coomassie Brilliant Blue dye. The Coomassie Reagent is mixed with the sample and the absorbance is measured with a spectrophotometer set to 595 nm after 10 minutes of incubation at room temperature. When the dye binds to proteins, its color shifts from red to blue as it forms a complex with the bound proteins. According to the intensity of the blue color, it is possible to estimate the amount of proteins that are present in the sample [261]. However, very careful purification of EVs is required before performing this assay since all protein contaminants are also detected at the same time as EVs proteins.

Molecular Profiling

Molecular profiling techniques for EVs characterization include mass spectrometry [262] and RNA profiling with quantitative reverse transcription polymerase chain reaction (qRT-PCR) or bioanalyzers, that use electrophoresis and flow cytometry to measure the size and quantity of genetic material and proteins [263, 264]. These techniques enable to profile the transported proteins and RNA fragments, including short sequences like miRNA and mRNA and longer sequences. Commercially-available kits enable to isolate

specifically RNA and proteins from EV samples. An “Exosome Proteomics Service” is proposed by System Biosciences to perform mass spectrometry of the protein content of EVs from raw biofluid samples.

RNA Sequencing

Detecting specific mutations in EV-RNA is a key approach for diagnostic applications. Quantitative RT-PCR is usually used for such low concentrations in nucleic acids, but it requires to know them in advance, which is not adapted to most EV applications, where specific mutations need to be identified. For example, mutations in glioma tumor-derived exosomes were detected and quantified with droplet digital PCR [265].

Table 1.3: Characteristics of the main classical EV characterization techniques

Technique	Information	Volume	Measurement time	Reference
SEM	Size, morphology	~ μL	Hours	Sharma et al., 2010 [266]
TEM	Size, morphology	~ μL	Hours	Van Der Pol et al., 2012 [34]
AFM	Size, morphology, mechanical deformability	~ 10 μl	Hours	Sharma et al., 2010 [266]
DLS	Size, zeta potential	> 20 μl	Minutes	Sokolova et al., 2011 [267]
NTA	Size, zeta potential, concentration	~ 100 μl	Minutes	Dragovic et al., 2011 [268]
TRPS	Size, zeta potential, concentration	~ 100 μl	Minutes	Maas et al., 2014 [269]
SMR/SNR	Mass, density, deformability of single particles	~ 100 μl	Hours	Olcum et al., 2014 [239]
RS	Comparison of molecular compositions	~ μL	Minutes	Gualerzi et al., 2017 [244]
SPR	High sensitivity quantification	~ μL	Hours	Im et al., 2014 [249]
SAXS	Structural information	~ μL	Minutes	Castorph et al., 2010 [251]
FC	Size, morphology, concentration, surface markers	~ 100 μl	Seconds	Robert et al., 2009 [270]
FM	Dynamic physiological functions	NA	Hours	Zomer et al., 2015 [258]
WB	Surface and internal targeted proteins (no quantification)	15 μl per lane	> 12 hours (overnight incub.)	Logozzi et al., 2009 [165]
ELISA	Surface and internal targeted proteins (quantification)	100 μl per well	> 12 hours (overnight incub.)	Yoshioka et al., 2014 [259]
BA	Total protein content (quantification)	100 μl	10 min	He et al., 2014 [260]

* SEM = Scanning Electron Microscopy, TEM = Transmission Electron Microscopy, AFM = Atomic Force Microscopy, DLS = Dynamic Light Scattering, NTA = Nanoparticle Tracking Analysis, TRPS = Tunable Resistive Pulse Sensing, SMR/SNR = Suspended Micro-/Nanochannel Resonator, RS = Raman Spectroscopy, SPR = Surface Plasmon Resonance, SAXS = Small Angle X-ray Scattering, FC = Fluorescence Cytometry, FM = Fluorescence Microscopy, WB = Western Blot, ELISA = Enzyme-Linked ImmunoSorbent Assay, BA = Bradford Assay

1.3 Isolation Techniques

In order to isolate EVs, all of their physical and membrane biochemical properties can be exploited. These properties range from proteins expressed at the EV outer membrane, surface membrane electrical charges, size and density. One should bear in mind the particular properties that these biological objects display, beginning with their size, which can have a huge impact on technical issues for isolation. Experimenters have the choice between several technical methods in order to isolate EVs. A comparison of the main EV isolation techniques is given in table 1.4.

Table 1.4: Comparison of the main standard isolation techniques for EV preparation

Method	Principle	Time	Advantages	Drawbacks
Differential centrifugation	Density	~5h	Large sample volume High recovery yield	Time-consuming Expensive equipment Alteration of EV structure Co-isolation of contaminants
Density gradient separation	Density	~5h	High recovery yield EV subpopulations	Time-consuming Small sample volume Co-isolation of contaminants
Ultrafiltration	Size	~2h	Fast Easy procedure Good portability Low cost No specific equipment	Co-isolation of contaminants Low recovery yield Small sample volume Alteration of EV structure
Size exclusion chromatography	Size	~1h	High purity	Small sample volume Low recovery yield Alteration of EV structure
Polymeric-based precipitation	Solubility	~1h	Fast Easy procedure Highly scalable	Co-isolation of contaminants Interference with unknown polymers Alteration of EV structure
Immunoaffinity capture	Membrane antigens	~5h	EV subpopulations High purity Easy procedure	Small sample volume Low recovery yield High reagent cost Need to identify EV markers Alteration of EV structure

The different available techniques to isolate EVs have already been described in several comprehensive reviews [271, 272, 273, 274, 275, 276, 277, 46, 278, 279, 280, 281]. In order to clarify the advantages and disadvantages of each method here are reviewed the different isolation strategies and the associated EV properties enabling the separation. All the different types of EV isolation techniques are summarized in fig. 1.10 and were reported in our review paper [282].

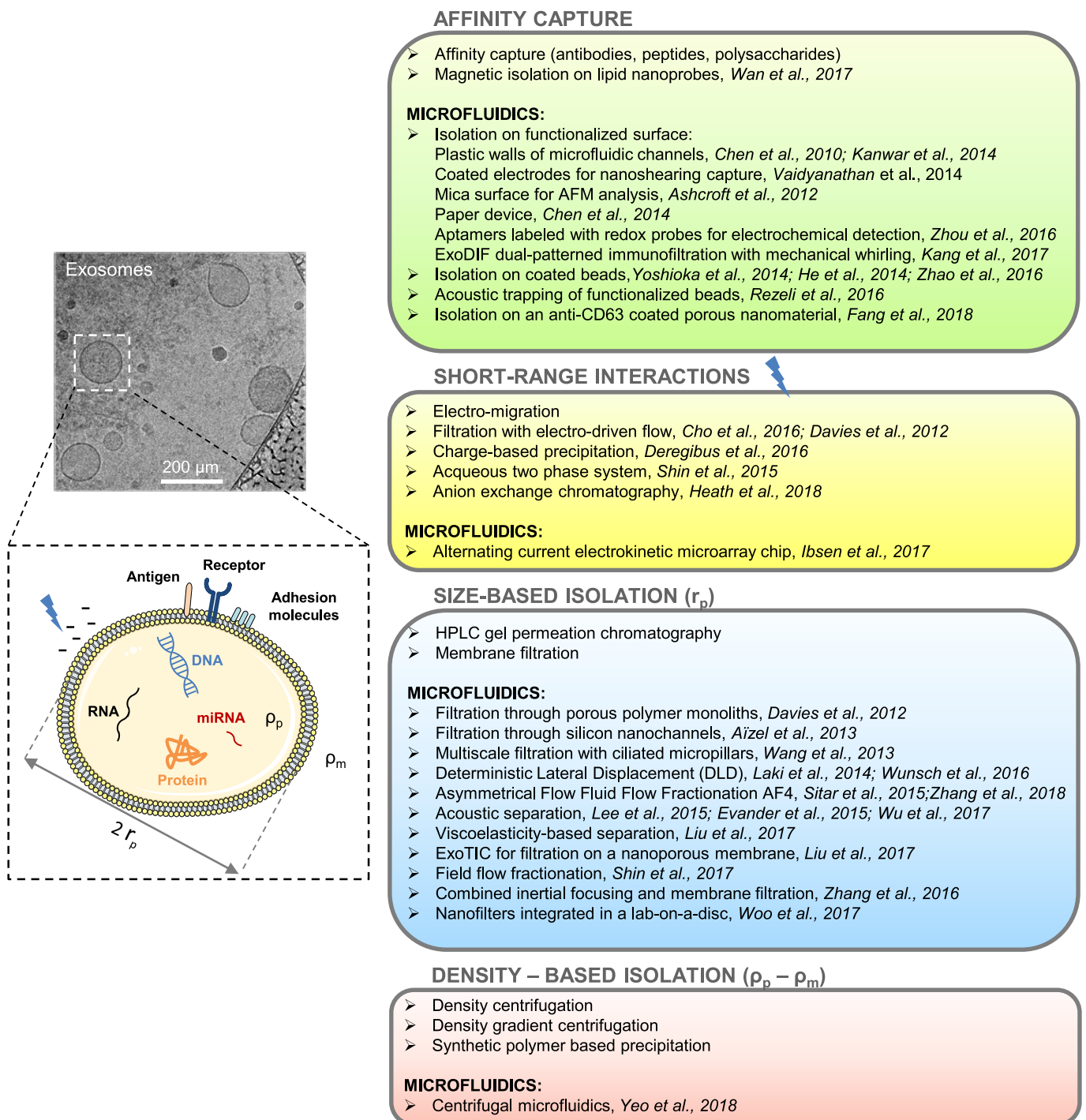


Figure 1.10: Representation of the different EV properties that can be used to isolate them. Exosomes from THP-1 cells are exemplified by a transmission electron microscopy image [282].

1.3.1 Density-based Isolation

From the physical point of view the simple way to isolate vesicles is to **centrifuge** them in order to accelerate the natural sedimentation rate of particles based on their difference of density compared to their surrounding media. In the stationary state, the equilibrium between the Stokes' (viscous) and the buoyancy's force enables to obtain the time needed to pellet particles of size r_p and density ρ_p suspended in a medium of density ρ_m and viscosity η when the rotation is performed at an angular speed ω . The time to pellet the particles will be related to R_0 the distance of the surface of liquid in the centrifuge tube and R_t the distance of the tube bottom from the rotation axis.

$$t = \frac{9\eta}{2r_p^2\omega^2\Delta\rho} \ln\left(\frac{R_t}{R_0}\right) \quad (1.1)$$

From this equation we can estimate the increase of time necessary to pellet exosomes compared to what is required to pellet cells. Taking a ratio of 100 between the size of cells (around 10 μm) and exosomes (around 100 nm) and acceleration 100 times higher for exosomes (1,000g to 100,000g for example) we obtain a **ratio of 100 between the duration requested for exosome sedimentation compared to cells, transforming a process of a few minutes into a process of a few hours**. This illustrates one of the main drawbacks of this method which is the time to pellet EVs. Despite this issue, differential centrifugation is the most common method to purify EVs from body fluids and cell media. The protocol generally consists of successive centrifugation steps with increasing centrifugal forces in order to first remove contaminants that are larger than the vesicles and then pellet EVs by ultracentrifugation [36]. However, even with a given protocol, the isolation efficiency strongly depends on the rotor type (fixed or swinging), on the pelleting efficiency (rotor k-factor) and on the viscosity of the biofluid [283]. The influence of these different parameters makes the isolation protocol difficult to generalize from one laboratory to another [284]. Figure 1.11 presents the different reported protocols to isolate each EV subtype by differential centrifugation.

	Exosomes	Microvesicles	Apoptotic bodies	Oncosomes
Size	40–120 nm	100 nm–1 μm	50 nm–2 μm	1–10 μm
Differential centrifugation and filtration steps	<ol style="list-style-type: none"> 1. 300 $\times g$, 10 min 2. 2,000 $\times g$, 10 min 3. Filtration (0.1, 0.22 or 0.8 μm) 4. 100,000–120,000 $\times g$, 1.5–2 hours (Théry et al. 2009, Rani et al. 2011, Tauro et al. 2012)	<ol style="list-style-type: none"> 1. 300 $\times g$, 10 min 2. 2,000 $\times g$, 10 min 3. Filtration 0.8; 1.0 μm (optional) 4. 10–20,000 $\times g$, 30 min (Heijnen et al. 1999, Palmisano et al. 2012)	<ol style="list-style-type: none"> 1. 300 $\times g$, 10 min 2. 2,000 $\times g$, 20 min Comment: Apoptotic bodies are also present in 10,000 and 100,000 $\times g$ fractions (Théry et al. 2001, Crescitelli et al. 2013)	<ol style="list-style-type: none"> 1. 2,800 $\times g$, 10 min 2. 10,000 $\times g$, 30 min, Comment: Alternatively filtration through 0.2 μm with centrifugation 30 s, 8000 $\times g$ – oncosomes are captured by the filter (Morello et al. 2013)
Additional purification	<ol style="list-style-type: none"> 1. Multiple dilutions in PBS and centrifugations 100,000 $\times g$, 70 min 2. sucrose cushion (Rani et al. 2011) 			
Fraction in density gradient	1.07–1.18 g/ml (Heijnen et al. 1999, Théry et al. 2001, Keller et al. 2009, Tauro et al. 2012)	Unspecified	1.24–1.28 g/ml (Théry et al. 2001)	Unspecified

Figure 1.11: Different centrifugation-based isolation protocols for each EV subtype [279].

In terms of isolation efficiency, because centrifugation separates particles by density, the recovered pellet contains both EVs and smaller contaminants with similar density, such as viruses, proteins, protein aggregates and cellular debris. Moreover, the high centrifugal forces could possibly lead to damaged vesicles [285], which is problematic when the isolated vesicles are recovered for diagnosis or therapeutic purposes. In order to decrease protein contamination, an additional sucrose gradient step can be added [286], which however does not separate EVs from high-density lipoproteins (HDLs) with similar densities [287]. Numerous commercial kits use **precipitation reagents** to reduce the centrifugal force needed to isolate EVs. This technique is based on the decrease of vesicles' solubility in presence of a polymer that captures particles between 60 and 150 nm. This "polymer net" is then removed by a low-speed centrifugation step while EVs are recovered in the pellet. These kits enable the isolation of vesicles with a very low number of processing steps, from any biofluid, and they do not require the use of a complex and expensive equipment. Figure 1.12 reports the different commercially available kits to isolate EVs [288].

Company	Kit name	Sample source	Input sample	Protocol time
ThermoFisher Scientific	Total Exosome Isolation (source specific)	Cell culture media, plasma, serum, urine	1–10 ml cell culture media; 0.1–1 ml plasma or serum; 0.8–5 ml urine	~14 h cell culture media; ~2 h plasma; ~1.5 h serum; ~2.5 h urine
	Total Exosome Isolation (Bio Fluids)	Amniotic fluid, ascites, cerebrospinal fluid, milk, saliva	0.2–1 ml	~4 h
Qiagen	exoEasy Maxi	Cell culture media, plasma, serum	16 ml for cell culture media; 4 ml plasma or serum	~30 min
Exiqon	miRCURY™ Exosome Isolation	Cell culture media, cerebrospinal fluid, plasma, serum, urine	1–10 ml cell culture media; 0.5–1.4 ml plasma or serum; 1 ml cerebrospinal fluid; 2–5 ml urine	~2 h
System Biosciences	ExoQuick	Serum, ascites	0.25 ml	~1.5 h serum; ~13 h ascites
	ExoQuick-TC	Cell culture media, cerebrospinal fluid, urine	5–10 ml	~13 h
BioVision	Exosome Isolation	Cell culture media, plasma, serum, urine	2–4 ml cell culture media; 0.1–0.5 ml plasma or serum; 5–20 ml urine	~2 h
	Exosome Isolation (Bio Fluids)	Amniotic fluid, breast milk, bronchoalveolar lavage, cerebrospinal fluid, gastrointestinal fluid, inflammatory fluid, lymph fluid, saliva	0.5–2 ml	~40 min
Cell Guidance Systems	Exo-spin™	Cell culture media, plasma, serum, saliva, urine	1–50 ml cell culture media, urine, saliva; 0.5 ml plasma or serum	~3 h cell culture media, urine, saliva; ~2 h plasma or serum
Norgen Biotek Corporation	Exosome Purification	Cell culture media, plasma, serum, urine	5–35 ml ^a cell culture media; 0.05–10 ml ^a plasma or serum; 0.25–30 ml ^a urine	~45 min cell culture media; ~30 min plasma, serum, urine
101Bio	PureExo [®] Exosome Isolation	Cell culture media, plasma, serum	2–4 ml cell culture media; 0.1–0.5 ml plasma or serum	~2 h
Izon Science	qEV Size Exclusion Column	Cell culture media, plasma, saliva, serum, urine	0.1–0.5 ml	~20 min

^a Volume depending on the kit format (mini, midi, maxi).

Figure 1.12: Commercially-available EV isolation kits [288] (the protocol time given for qEV size exclusion columns does not include the cleaning time of about 1 to 2 hours when reused).

Even if the RNA and protein recovery rates have been shown to be higher with these commercial kits compared to chromatography, ultracentrifugation or immuno-affinity based separations [289], this result is likely related to the lower purity of the samples isolated with these types of isolation kits [290]. Moreover, EVs were observed to be more damaged after isolation with polymeric precipitation in comparison to differential centrifugation [291]. Helwa et al. [292] recently compared differential centrifugation and three polymer-based precipitation kits (ExoQuick, Total Exosome Isolation Reagent and miRCURY). They confirmed a higher EV yield and protein recovery with the commercial kits compared to differential centrifugation. However, the miRNA concentration was strongly different from one kit to another, which confirms that results can hardly be compared between studies using different isolation protocols. The main issue encountered with these precipitation-based isolation techniques is the lack of knowledge about the polymeric content of these solutions and its potential influence on the biological activities of EVs. In 2015, a Protein Organic Solvent Precipitation (PROSPR) technique was proposed to precipitate soluble plasma proteins in cold acetone, while EVs remain in suspension [293]. This enables to remove protein contaminants before isolating EVs through classical centrifugation or filtration.

1.3.2 Affinity Capture-based Isolation

Affinity-based purification allows the selective capture of particles that present a specific biomarker, thanks to the interaction of EV surface proteins with antibodies, peptides or polysaccharides. For immune-affinity purification (IP), the standard exosomal surface markers that could be used are members of the tetrasparin family, such as CD9, CD41, CD63 and CD81, or membrane phosphatidylserine (PS).

Wako Chemicals (USA) commercializes a MagCapture Exosome Isolation Kit based on affinity capture of EVs by magnetic beads coated with PS-binding proteins. However, this kit cannot be used with plasma treated with chelating agents, such as EDTA or citric acid. **Norgen Biotek** (Canada) commercializes EV isolation kits that use a silicon carbide resin to interact with EV membrane proteins. Membrane-based affinity binding is implemented in the exoEasy kit available from **Qiagen** (Germany) and the MACSPlex Exosome Kit from **Miltenyi Biotec** (USA). This last kit has been experimentally used for some of our developments and will be described in details later in Chapter 4.

Immunological purification gives higher purity and a higher recovery rate when compared to a differential centrifugation strategy [294] and vesicle-bead complexes are particularly useful for downstream analysis like flow cytometry [36]. However the drawback of this method is the need to have first identified a molecular target to perform the isolation. Because the classification of EVs is still in its infancy [295], it may be necessary to use a label-free method to isolate and study these objects. Moreover, proteins, cells and cell debris presenting the same antigen as the targeted EV biomarker may also be captured on the beads and degrade the sample purity and this multi-step process is time-consuming. In order to cope with the specificity of the capture towards a given biomarker, a surfactant-free latex bead strategy that leads to a covalent bond between EVs and beads has been developed [22]. However, elution of EVs from this type of beads appeared to be very difficult.

Immunological purification reached a new stage of maturity when the first microfluidic device for

the isolation of EVs was developed by Chen et al. in 2010 [296]. They developed a PDMS chip with an anti-CD63 antibody coating using herringbone grooves in the channel to increase the capture surface of the chip. The injected samples have to be first separated from the main contaminants (leukocytes and platelets) precluding the use of whole blood samples, but the authors were able to show the capture of CD63-positive EVs from blood serum and cell culture supernatant. As an example, from the same 400 μl serum volume, more than seven times more RNA was extracted from the captured EVs for glioblastoma multiform patient serum than for normal serum, opening up the possibility for using immuno-based devices for new biomarkers discovery in cancer. As compared with the magnetic bead-based immuno separation, this method has the advantage of being a single-step technique, with a process time inferior to one hour, but it is limited to low volume samples because of the slow flow rate that is required to optimize diffusion and capture of vesicles in the channel (about $10 \mu\text{l min}^{-1}$). In 2014 [297], the same group reported a paper-based device with the capture of vesicles through immunoaffinity between EV surface biomarkers and coated anti-CD63 antibodies or annexin V using a biotin-avidin immobilization strategy. On the surface of the porous cellulose membranes, polystyrene holes were designed to enable the deposition of a 5 μl sample in each hole. When compared to the immuno-based chip reported in 2010 [296], this device was able to extract twice as much RNA per unit volume of serum, with 5 times less sample needed. The anti-CD63 coated membranes were also implemented for the isolation of vesicles from aqueous humor samples to relate the morphological structure of EVs to the development of glaucoma. For such applications, the very low sample volume needed to isolate EVs is a significant advantage of this device.

Polysaccharides, like heparin, coated on beads have been used to isolate EVs from filtrated biofluids with higher protein purity when compared to ultracentrifugation (UC) and similar RNA extraction yields to sucrose gradient, UC and polymeric precipitation [298]. However, for some RNA species, concentrations were significantly lower after heparin-affinity isolation and sucrose gradient, suggesting that the surface proteins targeted by polysaccharides are not presented by all the EV populations. Peptide-coated beads can also be used to isolate EVs with targeted surface proteins, like heat shock proteins, after low-speed centrifugation and filtration. For example, EV isolation with the venteremin (Vn) peptide showed similar performances as UC with standard laboratory equipments and a reduced processing time [299]. This method was shown to provide an easy to handle approach to obtain proteomic analysis of EVs [300].

1.3.3 Surface Electric Charge-based Isolation

Recently, a new electro-migration configuration, combined with filtration through nanoporous membranes was reported, in order to isolate EVs according to both their surface electrical charge and their size [301]. In this device, an electric field is applied across a 30-nm pore membrane. As in the device developed by Davies et al. [302], the separation relies on the fact that EVs migrate more than other particles contained in the processed whole blood. Moreover, the nanoporous membranes placed on both upper and lower channel walls enable selective elimination of deviated particles smaller than the pores size, while retaining vesicles that are larger than this critical size. The main advantage is the short processing time needed to isolate vesicles from an important sample volume (1 mL of sample can be processed in 30 minutes). The purified EV samples were compared to ultracentrifugation and polymeric precipitation isolation techniques. It was

found that the developed microfluidic technique leads to higher vesicle recovery than ultracentrifugation, but also higher impurity concentration [301]. When compared to a commercial kit, this system shows higher vesicle recovery and also better purity [301]. Therefore, the developed electro-filtration device is a rapid technique to isolate vesicles from unprocessed blood with a very good recovery rate and an acceptable purity.

Heath et al. [303] recently proposed to use anion exchange (AIEX) chromatography for charge-based isolation of EVs. This technique uses the negative surface charge of EVs to bind them to a positively charged chromatographic matrix. The attached EVs are then eluted with a specific mobile phase. The yield, purity and size distribution of collected EVs were compared to those obtained with ultracentrifugation and tangential-flow filtration (TFF). AIEX chromatography demonstrated similar performances as ultracentrifugation and better purity compared to TFF.

1.3.4 Size-based Isolation

Size-based isolation is often combined with density-based isolation when **ultrafiltration** through membrane filters is used as a complement to differential centrifugation, either before ultracentrifugation to remove large particles or after ultracentrifugation to separate EVs from smaller proteins. Adding an ultrafiltration step to the ultracentrifugation protocol enables to increase the purity of the isolated vesicles [304]. Commercially-available ultrafiltration columns have already been widely used to isolate EVs from biofluids [305] or culture cell media [306]. However, the recovery rate may decrease due to the trapping of EVs in the nano- or micropores of the membrane, which also leads to clogging issues. Moreover, the high shear-stress applied through the membrane pores may alter the integrity of the vesicles by deforming or even breaking up the processed EVs. In order to limit EV damage, the applied forces have to be reduced. Gravity can be used as driven force [218] but is particularly time-consuming. When EVs are retained on the filter, sample contaminations usually occur with some adherent proteins. Using a low-protein binding filter with a hydrophilized polyvinylidene difluoride membrane enabled [307] to limit protein contamination of EVs isolated from urine samples, but it was not possible to avoid contamination from all urine adherent proteins.

Size exclusion chromatography (SEC) can separate EVs into several fractions of different size ranges. While passing through the filtration column, the trajectory of the particles is directly related to their sizes, making larger particles elute before smaller fractions. Commercially-available columns, such as **qEV columns from IZON**, were used to efficiently fractionate EV samples after centrifugation steps [217], and have been implemented for some of our own experiments (which will be presented in details in Chapter IV). Therefore, SEC cannot be used as a single-step process to isolate EVs from raw biofluids or cell culture media, but it usually only fractionates EVs isolated from centrifugation or ultrafiltration techniques. SEC can also purify EV samples by separating the vesicles from protein contaminations [308, 309]. Moreover, SEC is often followed by an ultracentrifugation step in order to concentrate the isolated fractions of EVs. As mentioned for ultrafiltration, pushing EVs through the filtration column may disturb the integrity of the vesicles and induce clogging issues.

In a very interesting review, Saenz-Cuesta et al. [310] compared several standard EV isolation protocols in order to find the easiest technique to implement in an hospital environment. They report that all the different isolation techniques could be implemented in hospital except ultracentrifugation, which requires equipments that are usually not available. However, **no current technique enables to obtain at the same time high EV concentration, high purity, EV integrity, a specific selection of exosomes, time efficiency and low cost.** Kalra et al. [32] reported the current general problems related to the isolation of EVs:

- The lack of purity in isolated samples, that contain protein aggregates, viruses and other aggregated biomolecules.
- Sample loss and damaging during the isolation step because of high centrifugal, mechanical forces and multi-steps protocols.
- The need for standardization of isolation protocols to enable comparison between all emerging new results on EV functions and use.

For these reasons, novel isolation techniques are emerging, trying to make **EV sample preparation fast, cost-effective, portable, with high recovery yield, easy procedure and without damaging the vesicles.**

1.3.5 Emerging Microfluidics Isolation Techniques

Since 2010 [296], microfluidic devices have emerged to enable the isolation of EVs from reduced sample volumes and to avoid the need for costly equipments. Moreover, miniaturized isolation systems are promising for point-of-care (POC) acquisition and diagnosis. Figure 1.13 reports the advantages and limitations of both conventional and microfluidic isolation technologies [272].

Separation technologies		Advantages	Disadvantages
Conventional technologies	Ultracentrifugation	Most commonly used and well developed	Time consuming and low purity
	Immunomagnetic beads	Higher purity, great for standard analysis method	Separate exosomes with targeted proteins only
	Commercial kits	Easy to use No need of expensive equipment	Contamination by undisclosed chemicals
Microfluidics	Size-based microfluidics	Size uniformity to separated exosomes Avoid the contamination of non-exosomal proteins and other EV subtypes	Complicated photolithography fabrication
	Immunoaffinity-based microfluidic separation	Sample efficiency Fast separation	Separate exosomes with targeted proteins only
	Dynamic microfluidics	On-chip detection Simple microchannel structure Controllable process. Specific separation Size uniformity High purity	Related physical knowledge needed for operation

Figure 1.13: Comparison of conventional and microfluidic technologies for EV isolation [272]

Thanks to on chip immunological isolation, fully integrated microfluidic systems have been developed recently to enable both extraction and characterization of EVs with minimized sample manipulation steps. At the same time, size-based microfluidic isolation techniques have emerged, with the advantage of being label-free. After reviewing the different immuno-affinity based microfluidic systems we will focus on the size-based microfluidic isolation methods.

Immuno-based Microfluidic Devices

Capture of EVs on functionalized beads within microfluidic channels has been widely exploited to combine immuno-based isolation to on-chip characterization. The first-reported integrated system proposed to characterize EVs was based on a miniaturized NMR system with a microfluidic filtration step followed by capture of EVs with functionalized magnetic beads [311, 312]. Captured EVs on magnetic beads can also be detected optically with fluorescently-labelled antibodies after concentration of the beads with a magnet [260, 313]. Microfluidic mixing of the coated beads and the vesicles improves interaction efficiency and enables lower processing times compared to standard overnight protocols.

In the platform developed by Jeong et al. [314], the antibody detection of captured EVs on magnetic beads was not optical but electrical. Indeed, targeting antibodies were attached to an oxidizing enzyme that generates an electrical current in the presence of a specific chromogenic electron mediator. Therefore, from the recorded electrical signal amplitude, it was possible to determine the relative quantity of presented surface proteins for EVs from different cell lines.

Alternatively, Dudani et al. [315] used immunological isolation on functionalized beads and size-dependent behavior of particles in microfluidic channels to detect isolated EVs with on-chip flow cytometry in their RInSE (Rapid Inertial Solution Exchange) device. Captured 20 μm -beads with isolated EVs were focused in a central microfluidic flow while smaller contaminants - that were not captured by the functionalized beads - did not have sufficient inertial lift to be focused in the centerline of the channel. This method allowed the specific detection of EVs exposed on the beads surface with a flow cytometry laser beam focused in the central output channel.

Size-based Microfluidic Methods

Other microfluidic techniques offer the possibility to perform **label-free isolation of unaltered EVs**. Both active and passive size-based microfluidic techniques are presented in this section. Active isolation techniques have the advantage of being less impacted by the strong diffusive behavior of nanoparticles, such as EVs, while passive techniques are much easier to implement and display a flowing environment closer to the physiological environment of the vesicles.

Acoustic standing waves can be applied in microfluidic channels to create a size-dependent force that allows particle separation. When a particle is placed in a standing pressure wave, the scattering of the wave leads to a radiative force acting on the particle that takes the following form [316]:

$$F_{rad} = 4\pi \Phi(\bar{K}, \bar{\rho}) k r_p^3 E_{ac} \sin(2kx) \quad (1.2)$$

Where Φ is the contrast factor depending on the ratio of compressibility and density between the particle and the medium (this contrast factor is positive for EVs), \bar{K} is the compressibility ratio, $\bar{\rho}$ is the density ratio, k is the wave number, r_p is the particle radius and E_{ac} is the acoustic energy density. As this relation shows, the size of the effective area of the radiative force is related to its wavelength $\lambda = 2w$ and independently the force intensity is related to the acoustic energy and the volume of the particle. We can evaluate the time τ that the particle will take to move along a distance w , by equating the radiating force and the drag force from the Stokes-Einstein relation (which is proportional to r_p):

$$\tau = \frac{w^2 \eta}{E_{ac} r_p^2} \quad (1.3)$$

This equation shows that if a sample (composed of different sized particles) is introduced near an anti-node, larger particles will be directed towards a node much more rapidly than smaller ones, enabling the selection of small particles like EVs in the central streamline. During this process, diffusion occurs with a characteristic time given by $\tau = w^2/D$, where D is the Stokes-Einstein diffusion coefficient. For 100 nm-particles, the diffusion time is about 60 times larger than the acoustic time defined above to move along the same distance w . For example, it only takes 40 s to displace 100 nm-particles along a distance $w = 100 \mu\text{m}$ with an acoustic energy density $E_{ac} = 100 \text{J/m}^3$, while 40 min are required to diffusively cross the same distance. This demonstrates that diffusion does not impede the acoustic separation process.

The first demonstration of EV separation with acoustic forces was published in 2015 by Hakho Lee group from Massachusetts General Hospital [317]. By applying standing surface acoustic waves (SSAW) thanks to a pair of interdigitated transducer (IDT) electrodes, the sample is focused in the centerline of the channel at the channel input. Large vesicles are deviated from the centerline towards the pressure nodes near the channel walls, while small particles stay in the centerline. Three output channels allow the recovery of small particles in the center outlet and large particles in the two side outlets. The size cutoff from which particles are deviated by the ultrasound field can be tuned by changing the device settings (input acoustic power and flow rate). In this work, the size cutoff was set to 300 nm and NTA measurements confirmed the separation of two EV subpopulations around this applied cutoff diameter. Moreover, western blot assays showed a higher concentration of exosomal markers in the center output channel and a majority of microvesicle markers in the side channels, which confirms that the size-based separation of EVs is efficient in this acoustic separation system in order to decipher different small particle populations.

While this first demonstration was performed on isolated and concentrated EVs from centrifuged cell culture media, Wu et al. [318] recently achieved isolation of exosomes from whole blood thanks to two cascaded acoustic devices in order to first remove blood cells and then extract exosomes from microvesicles and apoptotic bodies (fig. 1.14).

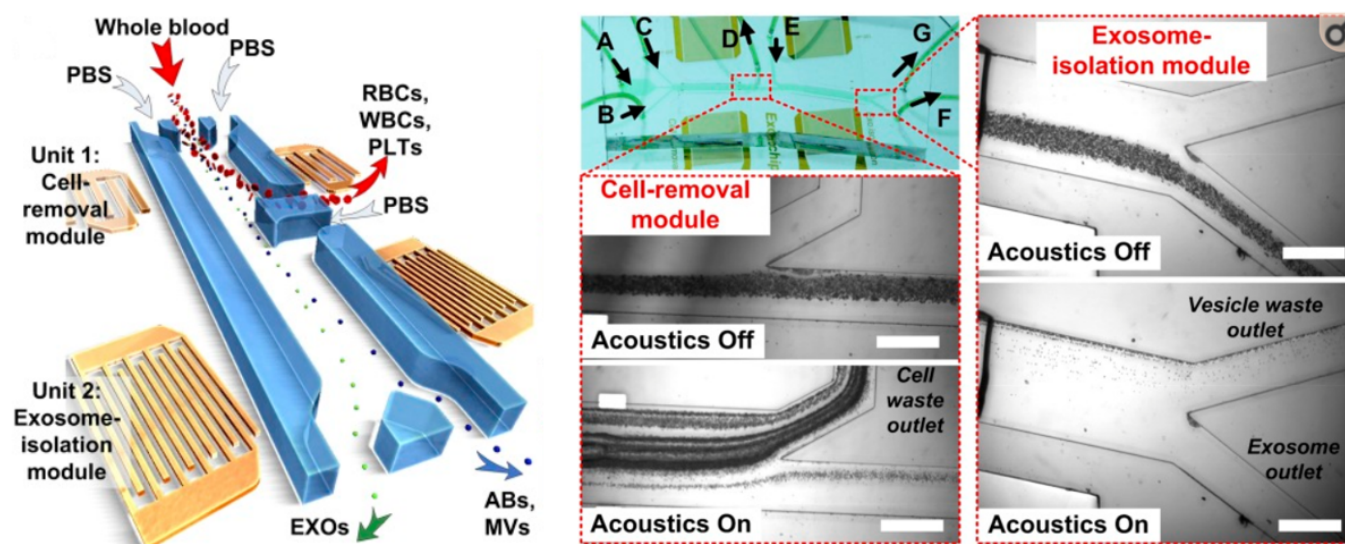


Figure 1.14: Left: Schematic representation of the acoustic separation device with one first unit to remove blood cells (RBCs, WBCs, PLTs) and a second unit to isolate exosomes (EXOs) from apoptotic bodies (ABs) and microvesicles (MVs). Right: Optical images of both separation zones (cell-removal module and exosome-isolation module) when acoustics is off or on [318].

Asymmetrical-flow field-flow fractionation (AF4) is a passive separation technique based on the differences between diffusion coefficients of particles according to their sizes. The AF4 channel contains a porous bottom plate that enables the formation of a perpendicular cross-flow in the channel. Because of this cross-flow, particles are carried out towards the membrane, whose pores are smaller than the particle size. In steady state, the concentration profile of particles perpendicular to the membrane is associated to a characteristic length D/U , where D is the diffusion coefficient and U is the transversal velocity. As the diffusion coefficient is related to the particle size, we can see in this method that both U and D could be used to carry the fractionation. The larger diffusion coefficient of small particles gives higher concentration in the centerline. As the elution flow velocity v has a parabolic profile, smaller particles elute from the microfluidic channel more rapidly than larger ones (fig. 1.15). This method has been used to separate EVs according to their size [319], with the processed EVs prepared from a purchased lyophilized exosome standard. The authors were able to separate two particle populations, with an average size of 23 nm for the first population and 135 nm for the second population, according to dynamic light scattering (DLS) measurements. Both subpopulations had a broad distribution, owing to the high heterogeneity of EV samples. Even if protein impurities between 20 and 100 nm were still observed by TEM in the processed samples, this technique is promising.

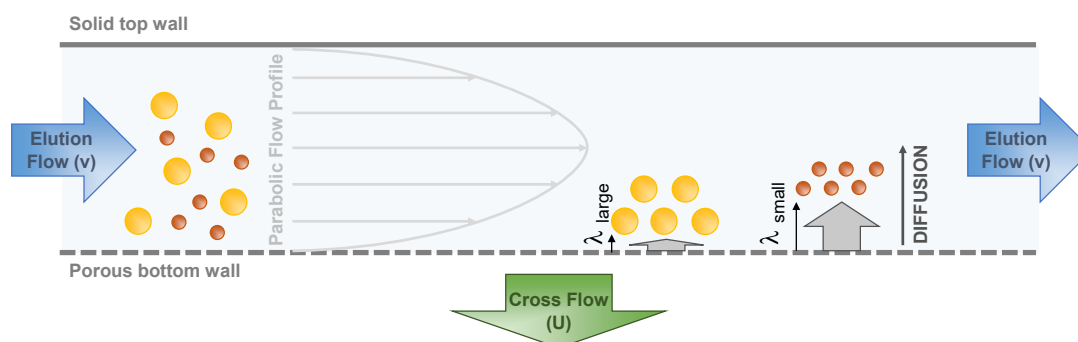


Figure 1.15: Schematic representation of the section of the AF4 channel showing the parabolic velocity profile of the principal flow with the field flow perpendicular to it, adapted from Muller et al., 2014 [320]. Faster diffusing particles (small ones) are eluted earlier by the faster central streamlines compared to larger ones staying near the accumulating wall.

Since its first reference in 2004 [321], **deterministic lateral displacement (DLD)** has emerged as a highly promising microfluidic technique for size-based separation of biological particles, including EVs [322]. DLD is a passive and label-free separation technique with high potential for both micrometer- and nanometer-sized particles [323]. DLD separation is performed in an array of regularly disposed pillars to orient the fluid path in a microfluidic channel. When particles are injected in the DLD channel, their trajectory is determined by their position relative to the different streamlines. Particles larger than a cutoff diameter - also known as critical diameter - are deviated along the pillar rows, while smaller particles remain in the channel axis. This enables to recover two separated particle populations around the critical diameter in two different output channels. Based on the presented literature review, this technology was selected to isolate EVs from complex biofluids for several reasons:

- Use of microfluidics enables to handle small sample volumes, save processing time and develop a portable system for point-of-care diagnosis applications. It also allows direct integration of the characterization step on the same miniaturized platform.
- No external forces are applied on the vesicles, which limits artificial modifications and damage of the EV physiological properties.
- Label-free isolation enables to isolate the entire EV population, with no need to anticipate the specific EV biomarkers we are looking for.
- The same technology can be implemented to separate a large range of particle sizes, from the nanometer to the micrometer scale, which is well appropriate to complex biofluids that contain many different particle scales.
- The separation efficiency does not depend on the flow rate in the laminar regime, which strongly simplifies the fluidic control and optimization when compared to other microfluidic separation techniques (such as AF4).

This technology and its applications are presented in details in the next section.

1.4 Deterministic Lateral Displacement (DLD) Separation

1.4.1 Separation Principle

DLD is a microfluidic particle-separation technique that uses the bifurcation of a laminar flow around an array of regularly arranged pillars. Each pillar row is laterally shifted when compared to the previous row by a distance $\delta\lambda$ where λ is the center-to-center distance between two adjacent pillars. When the fluid emerges from an inter-pillar spacing, the obstacle that is encountered by the fluid in the next row induces bifurcations around the obstacle. Let us take ϕ as the total fluid flux going through the gap, $\epsilon\phi$ is the stream quantity deviated by the obstacle, where ϵ is equal to $\delta\lambda/\lambda$. Therefore, the total flow that is contained between two adjacent pillars can be divided into $\delta\lambda/\lambda$ lanes. At each row, the lanes are deviated to the next position with respect to pillars. Thanks to the low Reynolds number, the streams in each lane do not cross or mix. After $N = 1/\epsilon = \lambda/\delta\lambda$ rows, the lanes go back to their original position. This process is described by fig. 1.16 for $\epsilon = 1/3$ [321].

Particles with radius smaller than the lane width follow the streamlines and have a global straight path. These particles actually cross the column of obstacles every N rows, when they pass from the first lane to the last lane (from lane 1 to lane 3 in fig. 1.16). This motion is called the “**zigzag mode**”. In contrast, larger particles are deviated by the pillar array. Indeed, in this case the particle is too large to stay in the lane 1 or 3 and it is bumped towards the lane 2 (fig. 1.16). This transport pattern is called the “**displacement mode**”. The **critical diameter** D_c defines the particle size between the zigzag and the displacement modes. It is thus twice the width of the first lane next to the pillars. Several models have been proposed to anticipate the value of the critical diameter according to the geometrical parameters of the pillar array.

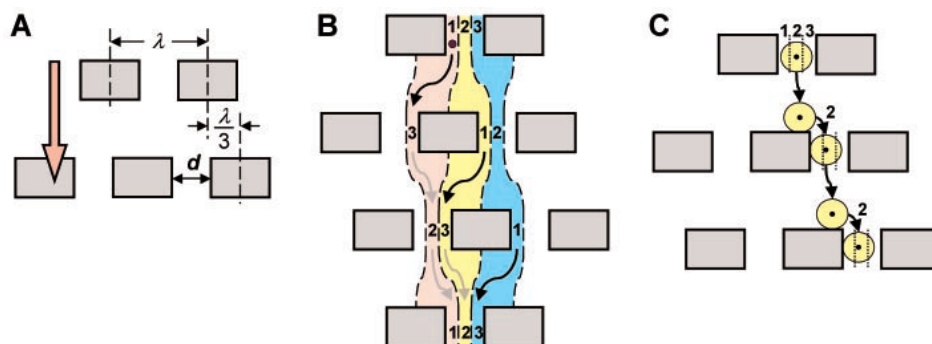


Figure 1.16: (A) Definition of the pillar array (B) Repartition of the three fluid streams (red, yellow and blue): lane 1 at the first obstacle becomes lane 3 at the second row, lane 3 becomes lane 2 at the third row, and so on. Particles with radius smaller than the first lane width follow the streamline and stay in the same lane. (C) Particles with radius larger than the first lane width follow the streamline passing through the particle’s center, so these particles are displaced from one lane to the next one [321].

1.4.2 Predictive Models to anticipate Critical Diameters

Inglis' Model

Inglis et al. [324] determined the width of the critical lane described in the previous section from Huang et al. [321] in order to find a model for the critical diameter. The lane width is not the same for central streamlines and for streamlines that are next to the pillars. Indeed, the fluid flux is the same in each lane but the average flow velocity is smaller in tangential lanes compared to central lanes, which leads to a wider lane next to the pillars. The lane width can be written as $\beta = \eta G \epsilon$, where η takes into account the non-uniform flow through the inter-pillar spacing and G is the gap between two adjacent pillars. This expression gives the critical diameter $D_c = 2\beta = 2\eta G \epsilon$. In this model, there are three main hypotheses:

- Low Reynolds number flow
- Infinitely tall pillars
- Infinitely large and long DLD channel

We know that the fluid flux in a lane is ϵ times the total flux between two adjacent posts. Inglis et al. [325] determined the coefficient η from this expression, by integrating the flow profile $u(x)$ along the width of the first streamline (fig. 1.17 a): $\int_0^\beta u(x) dx = \epsilon \int_0^G u(x) dx$. This calculation leads to the following expression for D_c/G :

$$D_c/G = Re \left(1 + 2w + \frac{1}{2w} \right) \text{ where } w = \left(\frac{1}{8} - \frac{\epsilon}{4} + \sqrt{\frac{\epsilon}{16}(\epsilon - 1)} \right)^{1/3} \left(-\frac{1}{2} - \frac{i\sqrt{3}}{2} \right) \quad (1.4)$$

Davis' Model

In his thesis [326], Davis developed an **empirical model** for the critical diameter, based on the obtained data of displaced or zigzag trajectories for model microbeads (fig. 1.17 b). The best matching model is given by this relationship:

$$D_c = 1.4G\epsilon^{0.48} \quad (1.5)$$

A comparison between the predicted normalized critical diameters (critical diameter / inter-pillar gap) according to Inglis' and Davis' models is given in fig. 1.17 (b) for typical shift fraction (ϵ) values. Similar evolutions of D_c/G are found in both cases, with an increasing critical diameter for increasing shift fraction (larger slant angle). It is noticed that Inglis' model gives values for D_c/G up to 20% lower than those predicted by Davis' model. This is mainly due to the approximation of the parabolic flow profile between pillars in the Inglis' model, while Davis' model is based on experimental data.

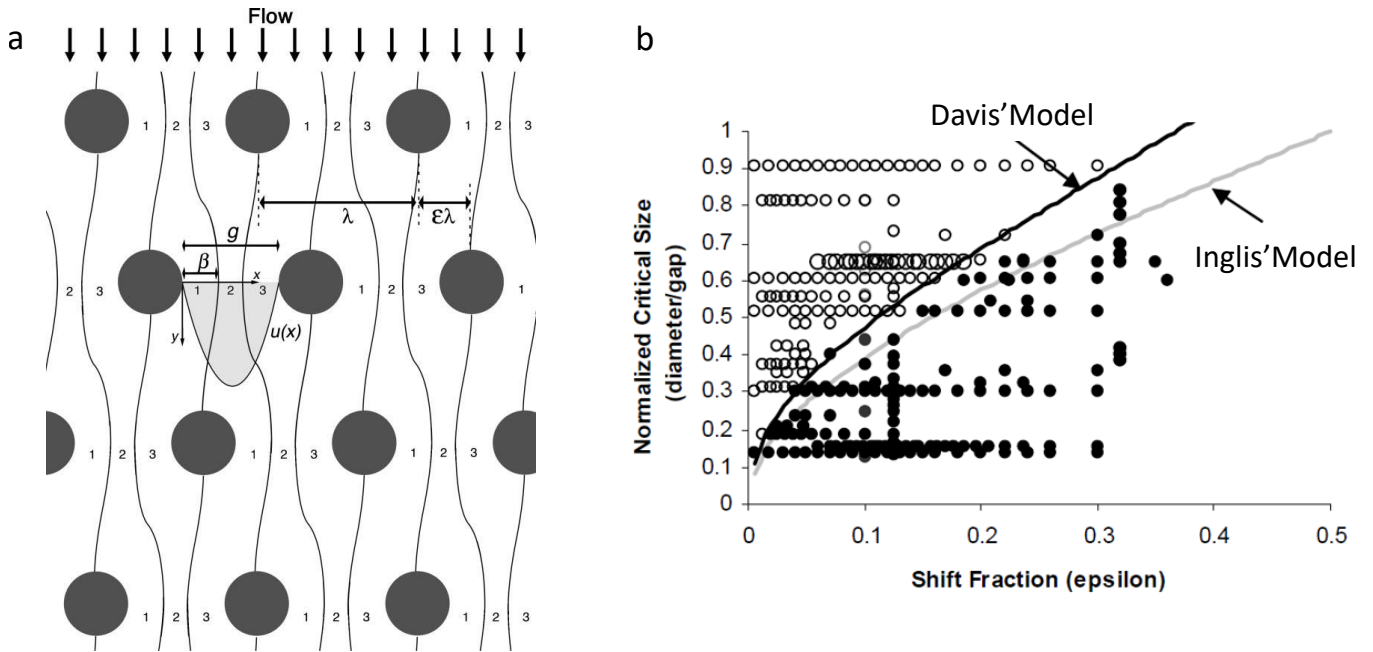


Figure 1.17: a) Top view diagram of the streamlines in the DLD array, with associated geometrical parameters, reprinted from [325]. b) Experimental data of the displaced and straight particles as a function of the shift fraction (open circles = displaced particles, filled circles = straight particles) and comparison between Davis’ experimental model (based on the represented experimental data) and Inglis’ parabolic theory, reprinted from [326].

Mixed Motion

In addition to the zigzag and the displacement modes, a third trajectory mode was numerically and experimentally observed for **intermediate particle sizes** [327]. An asymmetric distribution of the flow lane width was described through 2D flow field simulations, with the first lane having a smaller width than the last one (lane 1 thinner than lane 3 in fig. 1.16). This asymmetry is caused by the oblique distribution of the pillar array and it is responsible for a third trajectory mode called “mixed motion”. Particles in mixed motion are deviated along an angle between the zigzag and the displacement trajectories. The mixed motion is observed for intermediate sized particles because they approach the stagnation point of the obstacles, which slows down the particle velocity. When they reach a pillar stagnation point, particles are subjected to non-deterministic displacement (Brownian motion), and their trajectory is a non-predicted mixing of zigzag and displacement motions.

The existence of three trajectory modes leads to **two critical diameters**: the first one $d_{f,1}$ corresponds to the width of the first flow lane and it determines the transition between the zigzag and the mixed modes. The second critical diameter $d_{f,c}$ determines the transition between the mixed and the displacement modes. Therefore, particles in mixed motion have diameters between $d_{f,1}$ and $d_{f,c}$. The first critical diameter has been determined previously by the Inglis’ model, according to the flow lane width next to pillars. However,

the second critical diameter was shown not to be correlated with any flow lane width and no analytic expression was proposed to the best of our knowledge, but this critical value was shown to be related to the asymmetry of the flow lane distribution. It was determined through 3D particle flow simulations and was found to be about 1.5 times $d_{f,1}$ [327].

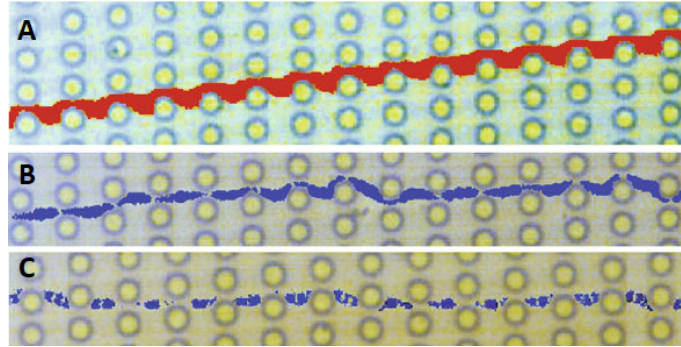


Figure 1.18: Experimental observation of the three trajectory modes with particles in displacement mode (A), mixed motion (B) and zigzag mode (C) [327].

Multidirectional Motion

When $1/\epsilon = \lambda/\delta\lambda$ is not an integer, two particular modes are observed for the particles' trajectory in addition to the zigzag and the displacement modes. In this case, the shift fraction ϵ can be written as M/N , where M is an integer that is not a divisor of N . Similarly to the case where $1/\epsilon = 1/N$ is an integer, the rational shift fraction M/N also leads to a division of the gap between adjacent posts into N flow lanes with the same amount of liquid flux. However, instead of being deviated from one flow lane to the next one, large particles are deviated along M flow lanes. Long et al. [328] studied the effect of rational shift fractions on the trajectory of particles in a simplified DLD model, where all the flow lanes have the same width λ/N and the pillars are considered as pointlike obstacles. They identified four different trajectory modes according to the particle dimension relative to the flow lane width.

Influence of the Flow Rate

Huang et al. [321] showed the influence of the flow speed on the transition between the zigzag and the displacement modes. At low flow speeds, the Brownian motion of the particles makes them seem larger than their real size with respect to the lane width. This leads to a transition that is smoother than the transition for higher flow speeds that display smaller diffusion lengths. This phenomenon is illustrated in fig. 1.19 (a), where two different flow rates were applied to inject the same bead mixture.

Dinceau et al. [329] recently explored high-Reynolds regimes for DLD devices, with a Reynolds number ranging from 10 to 60. As represented in fig. 1.19 (b), the formation of microvortices behind the pillars at high Reynolds number induces a decrease in the critical diameter. Lubbersen et al. [330] took advantage of these vortices to improve the separation efficiency with Reynolds numbers ranging from 2 to 34. Therefore,

different critical diameters could be obtained with the same device by simply changing the injection flow rate.

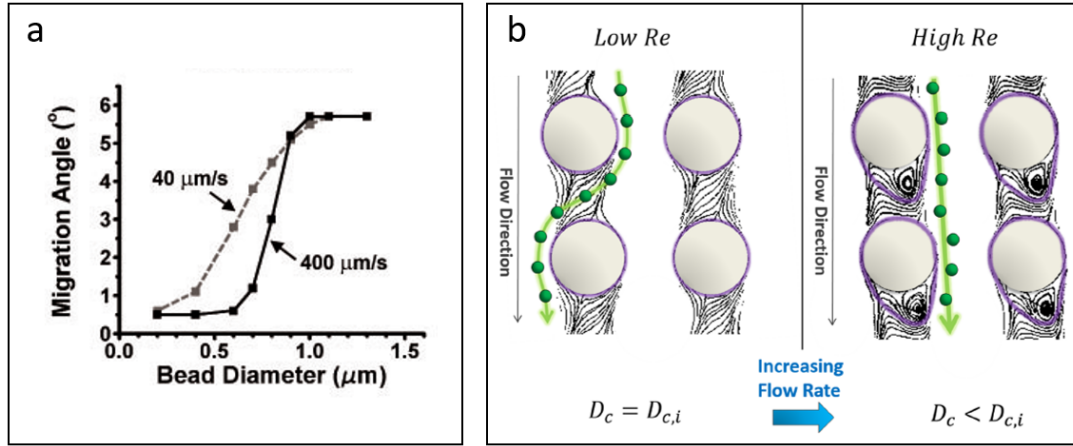


Figure 1.19: a) Influence of the flow speed on the transition between the zigzag and the displacement modes, reprinted from [321]. b) Resulting changes in the streamline distribution and critical diameter when increasing the Reynolds number, reprinted from [329].

Influence of the Fluid Viscosity

The theory developed by Inglis et al. [324] to predict the critical diameter value was extended by D'Avino [331] in the case of non-Newtonian fluids. From numerical simulations, the inter-pillar velocity profile was computed for two types of non-Newtonian fluids (with a power-law model or a Bird-Carreau model). When compared to the velocity field obtained with Newtonian fluids, a lower maximum and flat profile was obtained with non-Newtonian fluids. The effect of shear-thinning in non-Newtonian fluids induced a decrease in the critical diameter. A new model was proposed for the critical diameter, according to the fluid shear-thinning n , for an array periodicity N_{post} varying from 2 to 8.

Impact of Particle Diffusion

As DLD relies on a deterministic process instead of a diffusive process, particle diffusion should be avoided in order not to disturb the deterministic separation process. The diffusion length can be simply computed as $d = \sqrt{D_{diff} \frac{l}{v}}$, where $D_{diff} = \frac{k_B T}{3\pi\mu D_p}$, μ is the dynamic viscosity, D_p is the particle diameter, l is the complete length of the DLD device and v is the average speed in the device. The influence of diffusion was shown to be responsible for some deviations from the Inglis' model for the separation of small particles in DLD devices [332]. Therefore, the deterministic prediction of particle trajectory is valid only when particles are too large to experience a significant diffusion process.

Heller and Bruus [333] introduced the diffusion and size dispersion in a predictive model for the critical diameter. They experimentally shown that the critical diameter can be more than 3 times larger for particle

dimensions strongly affected by Brownian motion, since small diffusive particles rarely meet the pillars. Moreover, two critical sizes were defined in the DLD system: a small particle diameter d_1 below which diffusion dominates and a large particle diameter d_2 above which the deterministic separation happens.

An advection-diffusion model was proposed by Cerbelli [334] to take into account at the same time the particle-obstacle interactions, particle-induced flow modifications and diffusivity along the DLD channel. An interesting conclusion of this work was the fact that **nanoscale DLD devices still efficiently separate diffusive nanoparticles since the effective diffusivity parameters controlling dispersion scale lower than linearly with the particle diffusivity.**

Evaluation of the Shear Stress

Davis [326] evaluated the shear stress that is experienced by particles while flowing through the pillar array. Particles experience the largest shear stress between the gaps, where the flow speeds up because of the narrow path. The shear stress can be written as $\tau = \mu\gamma$, where μ is the dynamic viscosity of the fluid and γ is the shear rate. We can approximate the inter-pillar spacing as a single infinitely long channel of width G . In this channel, the pressure can be written as a uniform drop along the total length. After solving the Stokes' equation at low Reynolds number for the steady state solution and neglecting the depth dimension (because the channel depth is far wider than the gap G), we get the maximum shear rate at the channel wall, calculated from the parabolic velocity profile across the channel width:

$$\gamma = \frac{dv_y}{dx} = \frac{4v_{max}}{G} \quad (1.6)$$

For example, for a speed of 2 mm/s and a gap of 10 μm , this corresponds to a shear stress of 0.8 Pa. **This is the same order of magnitude as the shear stress experienced in large arteries (0.3 Pa), but it is well below the shear stress experienced in capillaries (10 Pa) [335].** The applied shear stress was also recently numerically investigated for different pillar shapes and Reynolds numbers by Rangharajan et al. [336].

In particular, more information can be found on forces applied on RBCs and resulting deformations in several numerical studies [337, 338].

Influence of the Particle Shape and Deformability

When DLD is applied to the separation of biological particles, the deformability of these particles has to be taken into account to model their trajectory into the pillar array. Indeed, deformable particles show an apparent size that is dependent on the fluid velocity, which is a different behavior from rigid particles. Moreover, for non-isotropic particle shapes, the effective size is dependent on the orientation of the particles in the pillar array.

Quek et al. [339] used the immersed boundary method [340] to simulate the trajectory of deformable particles in DLD arrays by computing the elastic forces applied on the particle membrane at successive time steps. This numerical study showed a third type of trajectory, in addition to the classical zigzag and displacement modes, for large deformable particles, called the "**dispersive mode**". This trajectory mode is represented in fig. 1.20 (c). The dispersive mode is obtained when the particles are larger than approximately half the gap size between adjacent pillars. In this case, the plugging effect makes the fluid flow bend either upward or downward, which is increased when the slant angle is sufficiently large and when the particles are sufficiently deformable. As the dispersive path is totally unpredictable, these large deformable particles follow a random trajectory that limits the sorting ability of the device.

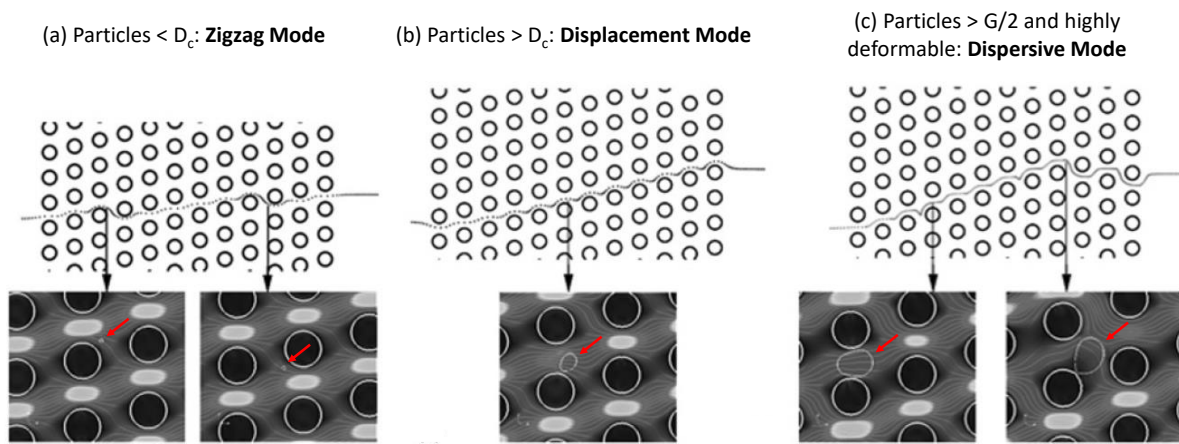


Figure 1.20: Plots of the streamlines and center of mass of particles migrating through a DLD array for (a) the zigzag trajectory (b) the displacement trajectory and (c) the dispersive trajectory. The red arrows show the position of the particles in each case, reprinted from [339].

Krueger et al. [341] performed three-dimensional immersed-boundary-finite-element-lattice-Boltzmann simulations (lattice-Boltzmann method for the fluid phase, finite-element method for the membrane dynamics and immersed-boundary method for the bidirectional fluid-membrane coupling) in order to model the separation of **deformable red blood cells (RBCs)** in DLD devices. The deformability of RBCs was described by the capillary number Ca , which is the ratio of viscous stress to characteristic membrane stress: $Ca = \frac{p l r}{K_s}$, where p is the applied pressure gradient, l is the gap length scale ($l = \sqrt{GH}$, G the inter-pillar spacing and H the channel height), r is the in-plane radius of the RBCs and K_s is the in-plane shear elasticity of the RBCs. The RBC trajectory was studied for different row shift values (d) and for different RBC deformabilities (Ca) (fig. 1.21). The transition between the zigzag and the displacement modes was modeled as: $d(\mu\text{m}) = 2.9 + 5.4e^{-1.72Ca}$. This study shows that deformability-based separation could be performed with DLD devices since, for a same device geometry, two particles with different Capillary numbers can follow different trajectory modes.

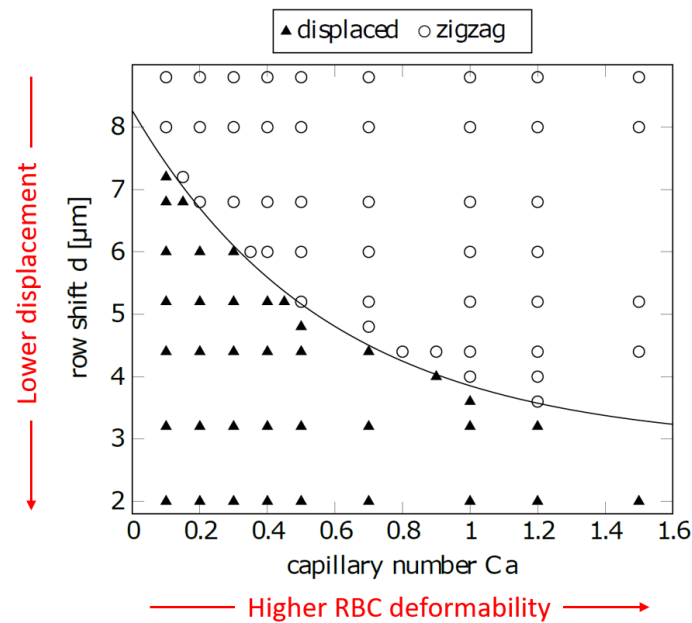


Figure 1.21: Representation of the trajectory mode (displaced or zigzag) of RBCs as a function of the row shift d and the capillary number Ca (for an inter-pillar spacing $G = 12 \mu\text{m}$) [341].

Zhang et al. [342] modeled the **deformability of RBCs** in different pillar shapes. They employed the dissipative particle dynamics (DPD) method to model the microfluidic flow and a bead-spring model with a ring-like structure to represent the suspended particles. Friction forces (dissipative and random DPD forces) were implemented for the particle-fluid coupling. They numerically demonstrated that RBCs deform differently according to the pillar shape (fig. 1.22).

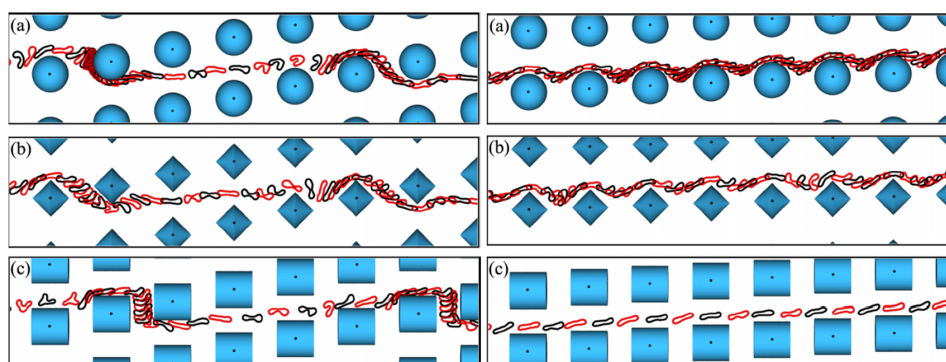


Figure 1.22: Numerical Simulation of the trajectory and the deformation of RBCs in arrays of circular, diamond and square pillars in the zigzag mode (left) and in the displacement mode (right) [342].

Recently, a design optimization problem was reported to identify the optimal pillar shape to differentiate

RBCs with different deformability characteristics, in particular according to the viscosity contrast between the inner fluid of the cells and their extracellular media [343]. The pillar cross section was parameterized and optimal designs were extracted from simulations of the cell flows through a 2D device in order to perform efficient RBC sorting for medical diagnostic applications, such as malaria detection.

In addition to non-spherical RBCs, other particle shapes were studied by Fu et al. [344], such as different **polygonal particles**. Based on numerical simulations, they showed a strong influence of the particle shape on their trajectory and adapted the pillar geometries to optimize the separation efficiency of each particle shape.

Influence of the Pillar Shape

Different pillar shapes have been studied to optimize the sorting efficiency, reduce clogging and increase the flow rate through the DLD devices.

Pillar shapes with different **protrusion and groove structures** have been studied experimentally by Ranjan et al. [345]. These pillar shapes are particularly interesting for the separation of non-spherical particles since they enable to constraint the orientation of the particles through rotational movements and thus improve the separation efficiency. This phenomenon was named the "containment effect". For each pillar shape, the quality of the separation was assessed through a "separation index" with 3 μm -spherical beads (supposed to follow a zigzag trajectory in the studied array for cylindrical pillars). It was observed that the separation of the beads was affected by the pillar shape, with the smallest separation index for circular pillars [345]. Inertial forces are supposed to be responsible for these observed separation differences. Indeed, when the fluid stream is expanded and contracted by the groove structure of the pillars, the particles are subjected to changes in velocity and they are ejected by the generated inertial forces, leading to a transverse migration of the particles.

As the **I-shaped design** has the largest protrusion and grooved structure, it also shows the largest separation index. This pillar shape generates a mechanical torque that can be applied to non-spherical biological objects. This effect is favorable to prevent the particles from escaping the direction of the pillar array and to direct the particles in their largest dimension in order to increase the separation efficiency. Examples of applications with this I-shape structure are presented in fig. 1.23. This I-shaped structure was implemented by Au et al. [346] to specifically remove small clusters of circulating tumor cells (CTCs) after a first removal of the largest CTC cluster with cylindrical pillars.

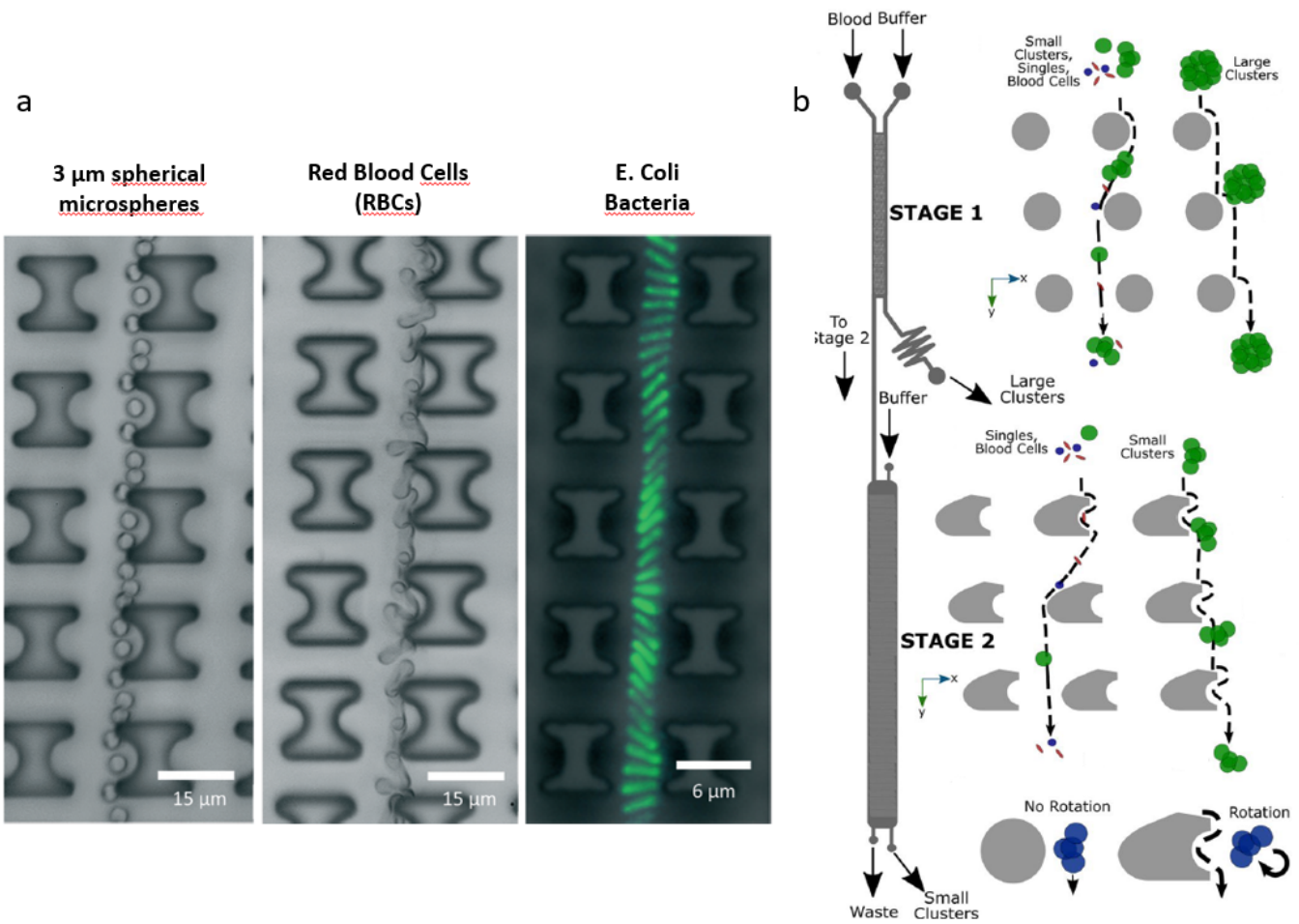


Figure 1.23: a) Trajectory in an I-shape pillar array of 3 μm spherical microspheres, RBCs and, E. coli bacteria, reprinted from [345]. b) Representation of the two-stage cluster separation device, with a first stage of cylindrical pillars to deviate the largest clusters and a second stage of asymmetric pillars to remove small clusters, reprinted from [346].

Simulations were performed by Wei et al. [347] to propose a general formula for predicting the critical diameter whatever the post shape implemented in the DLD device. From the empirical formula proposed by Davis [326] for cylindrical pillars, Wei et al. [347] introduced a new shape factor α to generalize the formula for five different pillar shapes: circles, rectangles, I-shape, octagons and hexagons. The ratio of sub-channel widths η was defined as a key parameter to determine the flow gradient shape and thus the critical diameter of the DLD device. Indeed, simulations confirmed that rectangular and I-shaped pillars have the same critical diameter (and they present the same ratio of sub-channel widths). However, even if octagonal and hexagonal pillars have the same ratio of sub-channel widths, they present slight differences in the critical diameters. This suggests that it would be more appropriate to characterize pillars by the sub-channel area instead of the ratio of sub-channel widths.

Zhang et al. [342] generalized the formula proposed by Wei et al. [347] to anticipate the critical diameter for three pillar shapes: circles, diamonds and squares. They combined the effects of the deformability of non-isotropic RBCs and those of the pillar shapes to model the trajectory and the orientation of cells in different DLD geometries. Two dimensionless parameters were introduced to take the pillar shape into account in the predictive formula for D_c :

$$D_c = \alpha G \epsilon^\beta \quad (1.7)$$

Where G is the inter-pillar spacing, ϵ is the array shift fraction and α and β are dimensionless parameters that depend on the shape and the arrangement of the pillars.

We have compared the values obtained for the critical diameter with circular and rectangular pillars according to the models given by Zang [342] and Wei [347] respectively. Good agreement was found in both cases:

Tilt ratio ϵ	1/5		1/8		1/10	
	Zhang et al.	Wei et al.	Zhang et al.	Wei et al.	Zhang et al.	Wei et al.
Circular	6.5 μm	6.5 μm	5.2 μm	5.1 μm	4.6 μm	4.6 μm
Rectangular	4.6 μm	4.2 μm	3.3 μm	3.1 μm	2.9 μm	2.7 μm

Figure 1.24: Comparison of the obtained critical diameter with circular and rectangular pillars according to Zang's and Wei's models.

When the pillar shape is asymmetric, the orientation of the pillar in the microchannel influences the critical diameter. This is the case for triangular pillars, for which the critical diameter is different when the particles are displaced by the vertex of the triangle or when they are deviated by the flat edge of the triangle, because the stream widths are different at these two positions [348]. Moreover, when particles are displaced by the vertex of the triangles, the fluid flux is shifted towards the vertex and the stream width along this edge is reduced. In this orientation, the critical size is smaller compared with the one that is obtained with cylindrical pillars of similar distribution [349]. The shift of the velocity profile between two adjacent triangular pillars is compared to cylindrical pillars in fig. 1.25.

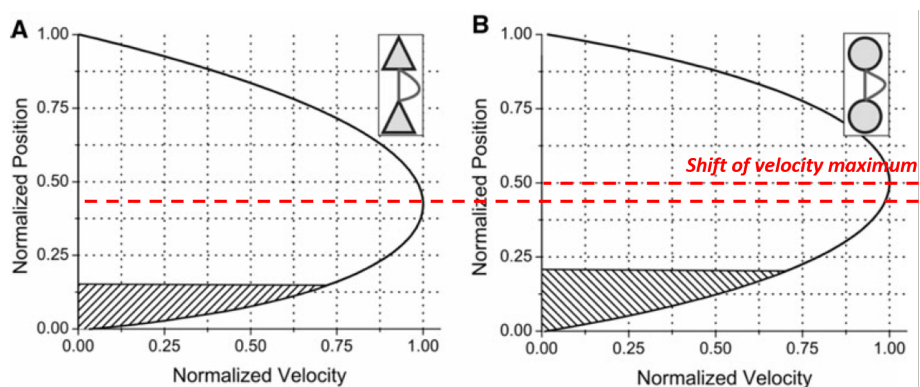


Figure 1.25: Numerical simulated flow profiles for DLD arrays with triangular (a) and circular (b) pillars [349].

From the velocity profile of the fluid flow between two adjacent triangular or cylindrical pillars, Louterback et al. [349] implemented the method developed by Inglis et al. [324] to compute the critical diameters as a function of the slant angle for both pillar geometries (fig. 1.26 A). A decrease is observed for the critical diameter with triangular pillars compared with cylindrical pillars, which has a main advantage: it allows to increase the gap size for a given slant angle and for the same critical diameter, which reduces clogging problems and increases throughput. The ratio of the gap size for triangular and cylindrical pillars for a fixed critical diameter is given in fig. 1.26 B as a function of the slant angle. These numerical studies clearly show that triangular pillars enable to increase the inter-pillar gap for the same separation diameter.

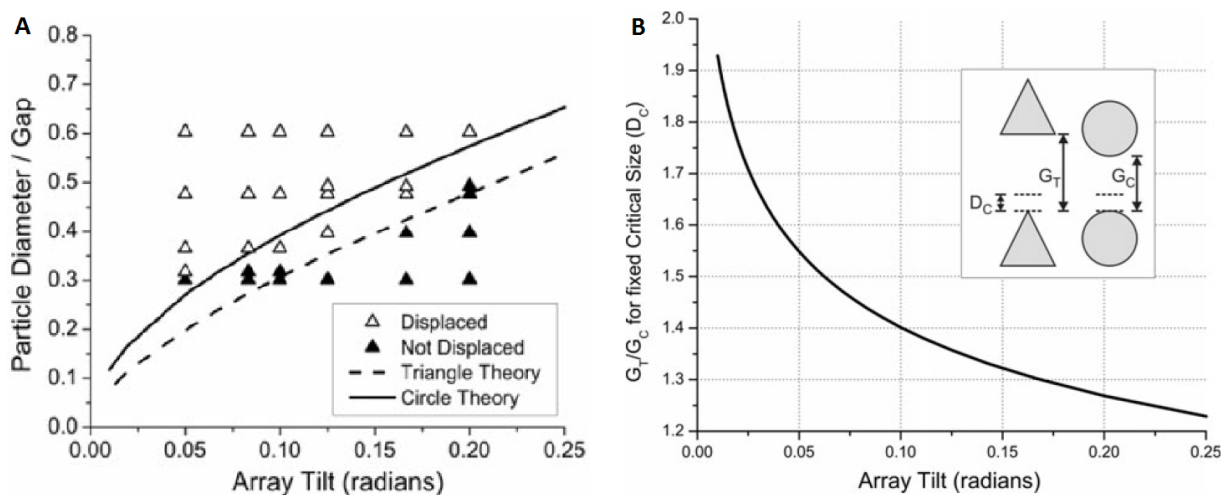


Figure 1.26: (A) Critical particle sizes normalized to gap width for triangular and cylindrical pillars according to the slant angle (triangular symbols = experimental data with triangular pillars, solid and dashed lines = theoretical predictions) (B) Ratio of inter-pillar gaps for triangular (G_T) and cylindric (G_C) pillar arrays for a fixed critical diameter (D_C) according to the array slant angle [349].

In conclusion, "classical" Inglis' and Davis' models have to be adapted to each pillar shape since the flow field and particle behavior strongly depend on the pillar geometry. Non-rigid particles are also strongly influenced by the flow rate and local fields applied near the pillars. In this case, the critical diameter is dependent not only on the geometrical parameters of the pillars, but it also relies on the deformability and the shape of the particles. This makes predictions of the sorting through DLD devices more complex, but it also enables new opportunities to sort particles according to parameters complementary to their size, such as deformability and shape.

Two pillar shapes were identified as particularly interesting from this state-of-the-art: the triangular shape that enables to decrease the critical diameter for a given inter-pillar spacing compared to circular pillars, and the I shape that improves the separation efficiency for anisotropic or deformable particles.

1.4.3 Design Improvements to increase Separation Efficiency

Optimize the Pillar Shape and Array Geometry

A topology optimization technique was implemented by Hyun et al. [350] to define a pillar shape with the highest inter-pillar spacing (to minimize clogging) for a given critical diameter. In addition, airfoil obstacles were shown to better separate soft biological samples [351]. In addition to the pillar shape, the array geometry was optimized to reduce clogging issues, increase throughput and simplify the fabrication process with a sieve-based lateral displacement structure [352].

Reduce Clogging

Clogging issues were avoided by using deposited water droplets to replace rigid pillars [353]. Then, particles were injected in an immiscible oil phase and separated by the droplet pillars. This new concept also presents the advantage to enable fully renewable and reconfigurable DLD designs.

Maximize Particle Concentration

Concentration of particles was achieved with the DLD technology, at the same time as separation, thanks to a mirror-symmetric channel design [354]. Thanks to this geometry, up to 50 fold concentrations of 10 μm beads and Jurkat cells were demonstrated.

Combine DLD with other Complementary Forces

Improvements of the DLD separation efficiency were demonstrated by combining DLD with dielectrophoresis [355] or ionic surrounding media [356]. Moreover, gravity can be used as the driving force to inject particles in the DLD device [357, 358] and pillars can be replaced by a force field generated by a set of interdigital transducers [359].

1.4.4 Biological Applications of DLD Separation

The DLD technology is particularly relevant to the isolation of biological particles since it addresses many different size ranges, in a label-free and non-damaging way. It has been recently applied to the isolation of several types of biological particles for various applications. They are summarized in table 1.5.

Table 1.5: Biological applications of DLD separation

Application	Performances	Reference
Blood components	Fractionation of blood components with a deviation of 99.6 % of all WBCs while 99 % of RBCs are not deviated	Davis et al., 2006 [360]
	Plasma extraction from whole blood at a flow rate of $0.4 \mu\text{l min}^{-1}$	
	Characterization of platelet activation from the exit position of platelets following thrombin and temperature-induced activation	Inglis et al., 2008 [361]
	Ten-fold enrichment of leukocytes from whole blood at a flow rate of $115 \mu\text{l min}^{-1}$ with 6 parallel DLD devices	Inglis et al., 2011 [362]
	Separation of RBCs with different morphologies and deformabilities with different exit positions for discocytes, echinocytes and stomatocytes	Beech et al., 2012 [363]
	100 % deviation of RBCs from 10x-diluted blood samples at a flow rate of $0.2 \mu\text{l min}^{-1}$ with I-shaped pillars	Zeming et al., 2013 [364]
	Separation of blood components according to both size and deformability following treatment with glutaraldehyde	Holmes et al., 2014 [365]
	Isolation of WBCs from whole blood with a purity of 72 % and a separation efficiency of 99.8 % at $30 \mu\text{l min}^{-1}$ followed by lysis of WBCs for virological extraction with ultra-sharp nanoblade arrays	Choi et al., 2015 [366]
	Automated preparation of human leukocytes for flow cytometry with a recovery rate of 88 % for WBCs and removal of more than 99.9 % of RBCs with a mirrored design to increase throughput	Civin et al., 2016 [367]
	Study of RBC behavior in DLD devices with different viscosity contrasts between the intracellular fluid and suspending medium	Henry et al., 2016 [368]
	Asymmetrical gaps to enhance deviation of RBCs	Zeming et al., 2016 [369]
	Isolation of WBCs from whole blood at a flow rate of $140 \mu\text{l min}^{-1}$ with a ridge DLD pattern	Kim et al., 2016 [370]
	DLD slanted and asymmetric lattices to isolate leukocytes and monocytes from 5x-diluted blood sample	Yamada et al., 2017 [371]
	Isolation of 80 % of the injected leukocytes suspended in PBS and encapsulation in an oil solution to measure protease activity of single leukocytes	Jing et al., 2016 [372]
	Leukocyte enrichment from plateletpheresis donation with a T-cell recovery of 80 % and a platelet depletion of 87 % (two-fold improvement of the recovery yield compared to standard Ficoll and magnetic isolation)	Campos-Gonzalez et al., 2018 [373]

Table 1.6: Biological applications of DLD separation

Application	Performances	Reference
Tissue engineering	Deviation of more than 97 % of epithelial cells from epithelial cells at a flow rate of 200 $\mu\text{l min}^{-1}$	Green et al., 2009 [374]
Circulating Tumor Cells (CTCs)	Deviation of more than 85 % of CTCs at a flow rate of 10 ml min^{-1} from a 20x-diluted blood solution spiked with CTCs at 106/mL	Loutherback et al., 2012 [375]
	Characterization of the isolation efficiency for different flow rates and types of CTCs spiked at 10 ⁴ /mL in a 10x-diluted blood solution	Liu et al., 2013 [376]
	Isolation of CTCs from blood samples of tumor-bearing mice at 7 $\mu\text{l min}^{-1}$	Okano et al., 2015 [377]
	Antigen-independent extraction of CTCs in a CTC-iChip with combination of both DLD (for RBC removal) and magnetophoresis (for elimination of labeled leukocytes) from human blood samples	Karabacak et al., 2014 [378]
	Multiplexing of the CTC-iChip purification to achieve debulking of blood samples at 15-20 million cells per second	Fachin et al., 2017 [379]
	Separation of single CTCs from clusters of CTCs with a combination of two DLD separation steps to deviate large and small clusters of CTCs at 10 $\mu\text{l min}^{-1}$	Au et al., 2017 [346]
	Isolation of platelet-covered CTCs with a combination of DLD to remove free platelets and a herringbone immunocoated chip to capture platelet-covered CTCs in blood from patients with breast cancer and melanoma	Jiang et al., 2017 [380]
Parasite extraction	Isolation of African trypanosomes from 20x-diluted blood samples at 60 nl min^{-1}	Holm et al., 2011 [381]
Spore extraction	Isolation of 99 % of fungal spores from a suspension at 4.10 ⁶ spores/mL	Inglis et al., 2010 [382]
Fractionation of PBMCs, RBCs and Evs	Deviation of RBCs and PBMCs from a suspension of isolated EVs, RBCs and PBMCs	Laki et al., 2014 [383]
Bacteria purification	Separation of cultured human bacterial pathogens <i>Streptococcus pneumoniae</i> according to three morphological types: single cocci, diplococci and chains	Beech et al., 2018 [384]
Droplet sorting	Gravity-driven flow of droplets in an array of pillars created with macroscopic LEGO pegs	Bowman et al., 2012 [385]
Separation of main and satellite droplets	DLD device connected to a microfluidic droplet generator to separate main (~60 μm in diameter) and satellite (1-30 μm in diameter) water-in-oil droplets	Tottori et al., 2017 [386]
Protein detection	PDMS DLD device with micrometric pillars to isolate albumin and polymer vesicles attached to microbeads to reduce diffusion issues with nanometer-sized components	Zeming et al., 2018 [387]
Extracellular vesicles purification	Nano-DLD arrays with inter-pillar spacings down to 25 nm to displace isolated exosomes down to 20 nm	Wunsch et al., 2016 [388]

This review of the DLD biological applications confirms the high potential of this technology to perform passive and portable sample preparation on a wide range of particle sizes. However, very limited demonstrations of this emerging technology have been reported with extracellular vesicles (EVs). Fractionation of EVs with nano-sized pillars has been reported after standard purification of the entire EV population [388], but now it would be interesting to develop a **completely automated and portable DLD-based sample preparation device, without any need for other bulky and time-consuming isolation techniques.**

Chapter Summary: Literature Review

- Extracellular vesicles (EVs) have recently generated a growing interest because of their high potential as liquid biopsy biomarkers and therapeutic agents.
- Standardization of the EV isolation protocols is required to produce clinical-grade vesicles and preserve integrity and functions of EV biomarkers.
- Isolation and characterization of EVs is complex because of the small size and high heterogeneity of EV samples.
- Microfluidic-based isolation techniques generally enable faster and easier preparation from lower sample volumes, as well as integration of both isolation and characterization steps with the same portable device. Cheap and portable instruments can be developed for point-of-care diagnostics with high multiplexing power by exploiting new separation phenomena offered by the microscale properties.
- Deterministic Lateral Displacement (DLD) was selected for the microfluidic isolation of EVs since it is a passive, label-free and highly modular technique.
- Several predictive models enable to anticipate the separation diameter of DLD devices. However, refinements are required to take into account the pillar shape, fluid flow rate, particle diffusion, shape and deformability. Design improvements can also enable to reduce clogging issues, improve separation efficiency and concentrate particles while sorting them.
- DLD has already been implemented for different biological applications, such as the separation of blood components, isolation of circulating tumor cells, sorting of droplets and fractionation of exosomes. However, the extraction of EVs directly from a complex biofluid has never been demonstrated so far with the DLD technology.

Résumé du Chapitre : Etat de l'Art

- Les vésicules extracellulaires (EVs) ont récemment fait l'objet d'un grand intérêt scientifique en raison de leur fort potentiel en tant qu'agents thérapeutiques et biomarqueurs en biopsie liquide.
- La standardisation des protocoles d'isolement des EVs est indispensable à l'utilisation clinique des vésicules, de même que la préservation de l'intégrité et des fonctions de ces biomarqueurs.
- La faible dimension et l'hétérogénéité des populations d'EVs rendent leur isolement et leur caractérisation particulièrement complexes.
- Les techniques d'isolement microfluidiques apportent des solutions pour une préparation d'échantillon plus rapide et plus simple, à partir de plus faibles volumes d'échantillon, ainsi qu'une plus grande intégration des étapes d'isolement et de caractérisation dans un même dispositif. Les nouvelles propriétés de séparation qu'offre la microfluidique permettent l'émergence d'instruments portables et à bas coût pour des applications de diagnostic point-of-care.
- La technique de Déplacement Latéral Déterministe (DLD) a été identifiée comme un moyen particulièrement adapté à l'extraction microfluidique des EVs, puisqu'il s'agit d'une technique passive, sans marquage, présentant une grande versatilité.
- Plusieurs modèles prédictifs sont communément utilisés pour anticiper le diamètre de séparation des dispositifs de DLD en fonction de leurs paramètres géométriques. Cependant, des améliorations restent nécessaires pour prendre en compte à la fois la forme des piliers, le débit d'injection de l'échantillon, la diffusion des particules, ainsi que leur forme et leur déformabilité. Des améliorations du design sont aussi requises pour adresser les problématiques de colmatage entre les piliers, améliorer l'efficacité de séparation et permettre la concentration des particules au cours du tri.
- La technologie de DLD a déjà été implémentée pour différentes applications biologiques, telles que la séparation de composants du sang, l'isolement de cellules tumorales circulantes, le tri de gouttes, et le fractionnement d'échantillons d'EVs purifiés. Cependant, des développements supplémentaires sont encore requis pour réussir à réaliser l'extraction complète d'EVs directement à partir d'un biofluide complexe par un système microfluidique de DLD.

Development of DLD Devices

Introduction: Development of DLD Devices

- In Chapter 1, DLD has been identified as a sample preparation technology with high potential for the isolation of EVs in a portable, cost-effective, label-free and non-damaging way.
- In this Chapter, our numerical simulation work will be presented to identify design rules optimizing the efficiency of DLD sorting.
- Based on this preliminary study, the selected DLD designs will be described, as well as their silicon-based fabrication process, performed in the cleanroom facilities at CEA-Leti.
- Our packaging solution will also be presented to ensure convenient plug-and-play fluidic connections to DLD chips.

2.1 Finite Element Modeling of DLD Separation

In order to optimize the DLD designs, we first numerically model the separation of particles according to the geometry of the micropillar array. To that purpose, we use the COMSOL Multiphysics software in single-phase laminar regime with the “particle tracing” module. In order to simplify our numerical model and decrease the computing duration, we make the following assumptions:

- Spherical and non-deformable particles (which is not valid for real biological particles).
- No modification of the flow pattern by the particles, which means that the particle trajectory is weakly coupled to the hydrodynamics. Note that this assumption may fail with highly concentrated samples, like whole blood.
- No interaction between particles and channel surfaces (pillars and walls).
- 2D study (since the channel height is experimentally at least 6 times higher than the inter-pillar spacing).

Our COMSOL model first computes the hydrodynamics of the carrier fluid. Then the particle trajectory is computed by solving the Newton equation, taking into account inertia, gravity and drag force. Moreover, refinements are added to the “Particle Tracing” module, in order to take into account wall-exclusion effects, that induce DLD sorting. Indeed, the particle position should not only be determined by its barycenter, but also by its envelope. Therefore, we have set up a rebound condition on any solid boundary — in our

case the pillars and channel walls — based on the distance from the particle barycenter to the wall, so that the particle envelope does not intersect the wall surface. The distance from a point of the computational domain to the boundary is given by the signed distance function $d(x)$ and verifies the Eikonal equation [389]:

$$|\nabla d(x)| = 1 \quad (2.1)$$

The Eikonal equation requires that the distance to the walls function $d(x)$ is differentiable at the walls. This restriction stems from the remark that the distance function on the boundary is:

$$\nabla d(x)|_{\partial\Omega} = n(x) \quad (2.2)$$

where n is the inward normal to the boundary Ω . The normal unit vector on pillars with sharp edge is not defined, and this induces a singularity. The introduction of rounded edges solves this problem.

Once the wall-distance map is calculated, the steric effect of the particles can be implemented. Indeed, the particle contacts the wall when $d(x)$ is equal to the particle radius and its velocity is directed towards the wall. Upon contact, a rebound condition on the velocity of the particle \vec{V}_p is set up, where \vec{n} is a unit vector orthogonal to the pillar and \vec{t} is a unit vector tangent to the pillar:

$$\begin{cases} \vec{n} \cdot \vec{V}_{p,rebond} = -\vec{n} \cdot \vec{V}_p \\ \vec{t} \cdot \vec{V}_{p,rebond} = \vec{t} \cdot \vec{V}_p \end{cases} \quad (2.3)$$

fig. 2.1 shows that inducing the steric effect in our model is required to properly model the separation of particles through DLD.

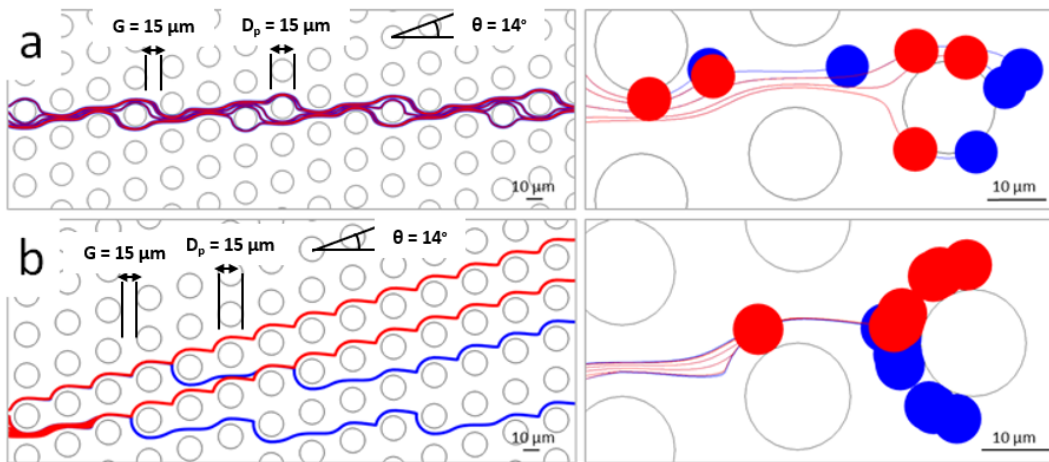


Figure 2.1: Trajectory of 7 μm (blue) and 7.2 μm (red) particles moving around an array of circular pillars without (a) or with (b) the rebound conditions. The geometrical characteristics of the pillar array are represented: inter-pillar spacing (G) = 15 μm , pillar diameter (D_p) = 15 μm , slant angle (θ) = 14°.

In order to validate our numerical model, the obtained critical diameters (defined as the smallest particle diameter for which a displacement mode is observed) were compared to Davis’ and Inglis’ models. Figure 2.2 (a) shows **good agreement of our numerical results with Davis’ model, while Inglis’ model is shifted towards smaller critical diameters**. This suggests that Inglis’ assumption of a parabolic flow profile between adjacent pillars does not exactly match the experimental and numerical results. In this case, refinements should be considered to take into account the anisotropy induced by the slanted pillar array.

2.2 Influence of the Pillar Shape: Numerical Study

The number of geometrical parameters that describe the pillars are numerous: shape, orientation, spacing and period number. With our numerical model, we numerically investigate the influence of the pillar shape and orientation for a fixed pillar width of $15\ \mu\text{m}$ and an inter-pillar spacing of $10\ \mu\text{m}$. **Five pillar geometries are considered: circles, hexagons, octagons and triangles, with two orientations for hexagons and triangles**. Figure 2.2 (b) shows that both the shape and the orientation of pillars influence the critical diameter.

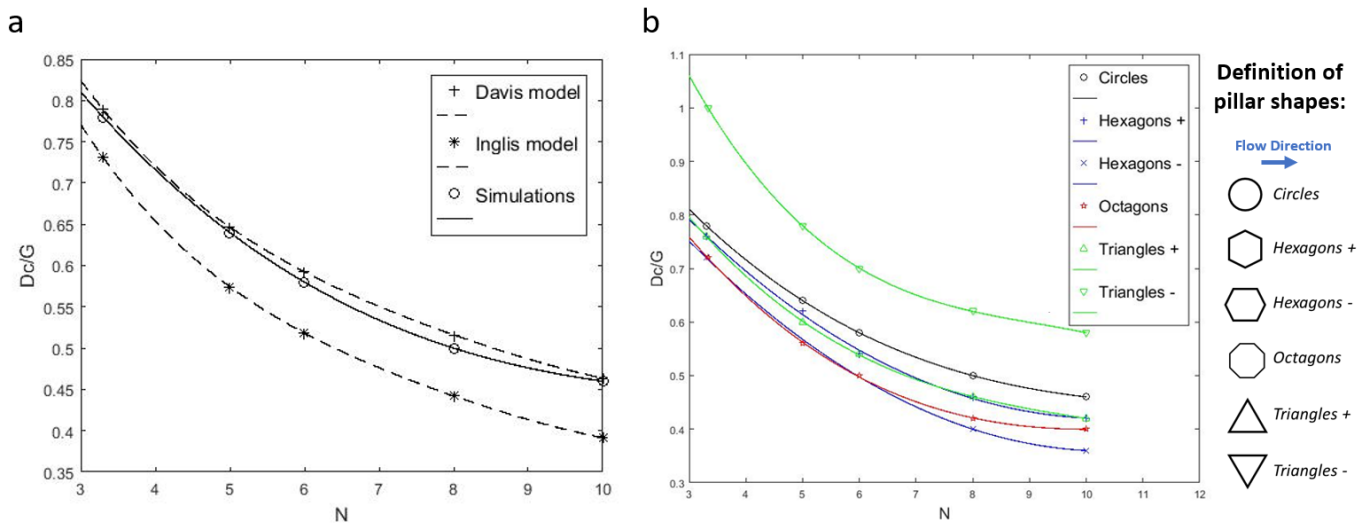


Figure 2.2: a) Comparison of the normalized critical diameters (D_c/G , where G is the inter-pillar spacing), for our model, Davis’ and Inglis’ models, for different values of array periodicity N . b) Diagram of the normalized critical diameter (D_c/G) for pillars with different shapes and orientations relative to the flow direction.

The effect of the pillar orientation is represented in fig. 2.3 with a flow going from the left to the right side. When compared to a vertical pillar edge, it is shown that the critical diameter decreases with a positive slope of the pillar edge, as the streamlines are directed upwards ($D_{c1} < D_{c2}$ on fig. 2.3 a,b), while it increases with a negative slope, as the streamlines are directed downwards ($D_{c3} < D_{c2}$ on fig. 2.3 b,c). This result is in agreement with fig. 2.2 (b) that shows higher critical diameters for triangles (-) compared to triangles (+).

The stall line is defined as the limit streamline that is stopped at a stagnation point on the left edge of a pillar (red point on fig. 2.3 (d) and (e)). Above the stall line, streamlines flow above the pillar, while below the stall line, streamlines flow below the pillar. Therefore, the position of the stall line and the stagnation point defines the value of the critical diameter.

Even with the small N value that is considered ($N = 3.3$), the stagnation point is always located at the top-half section of the pillars (fig. 2.3 (d) and (e)). Therefore, only this section influences the D_c value. Since the positive-slope triangles (triangles (+)) and hexagons (+) pillars have the same slope for the left edge (120° -slope), hexagons (+) pillars have similar D_c values as triangles (+) (fig. 2.2 b).

When considering the hexagon - pillar shape, the stagnation point is located on the flat left edge of the pillar for all the studied N values (from 3 to 10). When considering the octagon pillar shape, the stagnation point is located on the flat surface of the left edge for small N values, but it is located on the positive-slope edge for N values superior to 7. This explains the evolution of the ratio D_c/G with N for octagonal pillars: octagons behave like hexagons - pillars for small N values (stagnation point on a flat edge) and they behave like hexagons (+) and triangles (+) pillars for larger N values (stagnation point on a positive-slope edge). This transition is clearly observed in fig. 2.2 (b) for N values around 7-8.

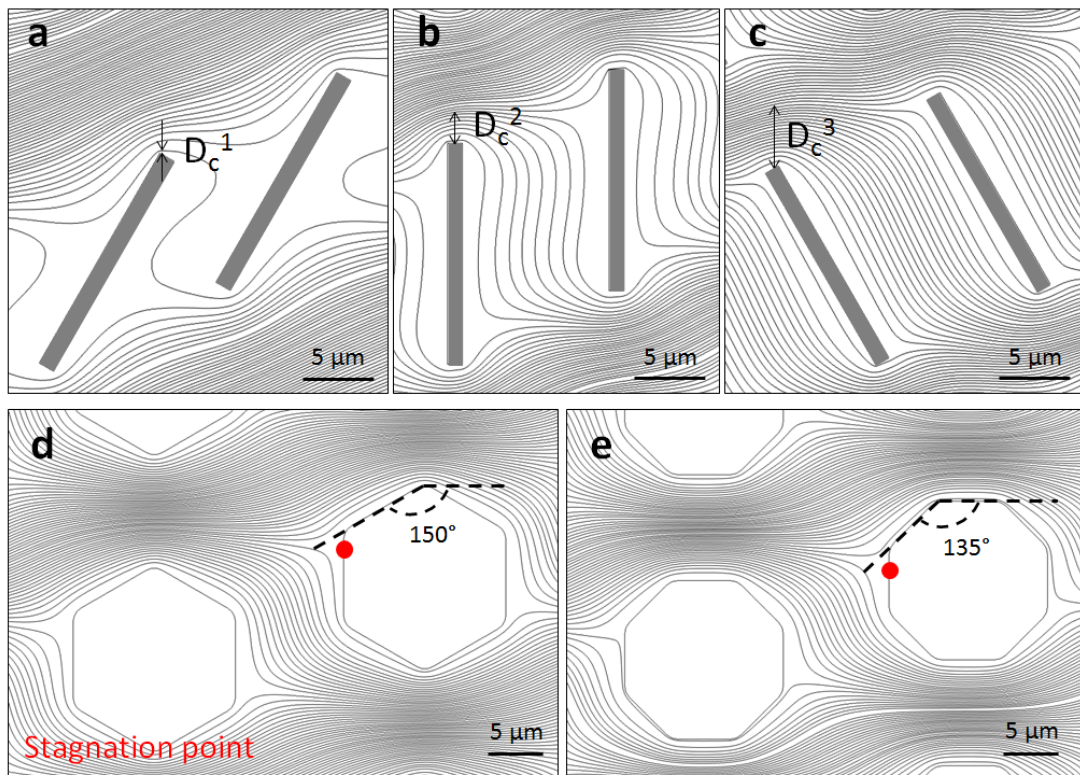


Figure 2.3: Comparison of the streamline distribution around rectangular pillars with three different orientations (a-c), hexagonal (d) and octagonal (e) pillars, with $N = 3.3$.

The generalized Davis' model proposed by Zhang et al. [390] was used to find the α and β parameters with our pillar shapes in the following formula (with $\epsilon = 1/N$):

$$D_c = \alpha G \epsilon^\beta \quad (2.4)$$

Both α and β parameters were obtained for each pillar shape from our numerical simulations:

Pillar Shape	Circle	Hex. +	Hex. -	Oct.	Tri. +	Tri. -
α	1.4	1.4	1.4	1.4	1.4	1.1
β	0.48	0.54	0.60	0.53	0.54	0.49

Figure 2.4: Values of the fitting parameters α and β for each studied pillar shape.

As suggested by Zhang et al. [390], we confirm that the α parameter is the same as in the Davis' formula for all the geometries, except for inverted triangles. Therefore, the α parameter seems to represent the orientation of the pillar edge that is encountered by the stall line. The β parameter is a characteristic of each pillar shape with a decrease in β when the slope of the pillar edge increases.

This new predictive model for D_c enables to choose the most appropriate pillar shapes to decrease the separation diameter while maintaining inter-pillar spacings as high as possible (and reduce clogging issues).

2.3 Anisotropy Effect and Impact on DLD Separation

In addition to the geometrical parameters of the pillar array, a phenomenon called "anisotropy" also influences the separation of particles in DLD devices. Anisotropy is induced by the **asymmetry of the oblique DLD pillar array** and is characterized by a symmetry breaking of the flow lane distribution. Recently, anisotropy was defined by Vernekar et al. [391] as the "tendency of an array to induce a pressure gradient along the lateral axis". Therefore, the magnitude of anisotropy can be quantified by measuring the **lateral pressure gradient along the channel width**. We will use this definition of anisotropy (expressed in Pa/mm) in the following sections.

The anisotropy effect was proved to change the critical diameter and induce unexpected particle trajectories [391]. Experimentally, asymmetrical DLD lattice patterns were exploited to increase the separation efficiency of red blood cells [369].

As the DLD anisotropy effect appears to be a key parameter to optimize particle separation, the influence of several geometrical parameters on the anisotropy magnitude is explored here. In particular, **the pillar orientation is shown to be a dominant factor that has not been considered so far**. The influence of the anisotropy effect on the particle trajectory is illustrated in this section and provides perspectives for tunable multi-separation DLD devices.

2.3.1 Definition and Illustration of Anisotropy in DLD arrays of Elongated Pillars

From our numerical simulations, it is observed that slanted elongated pillars induce streamline bending in the direction of the oriented pillars (fig. 2.5). Anisotropy is quantified from our numerical simulations as the lateral pressure gradient along the channel width (fig. 2.6).

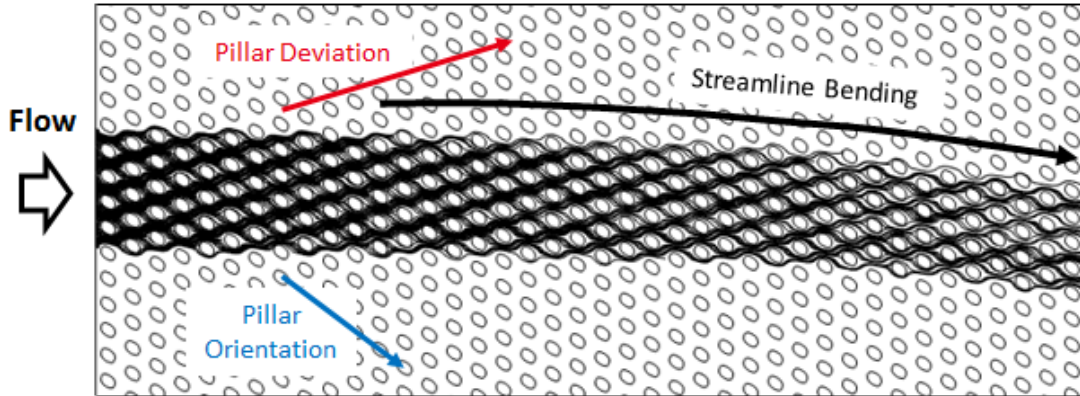


Figure 2.5: Downward bending of streamlines in an array of downward-oriented ellipsoidal pillars.

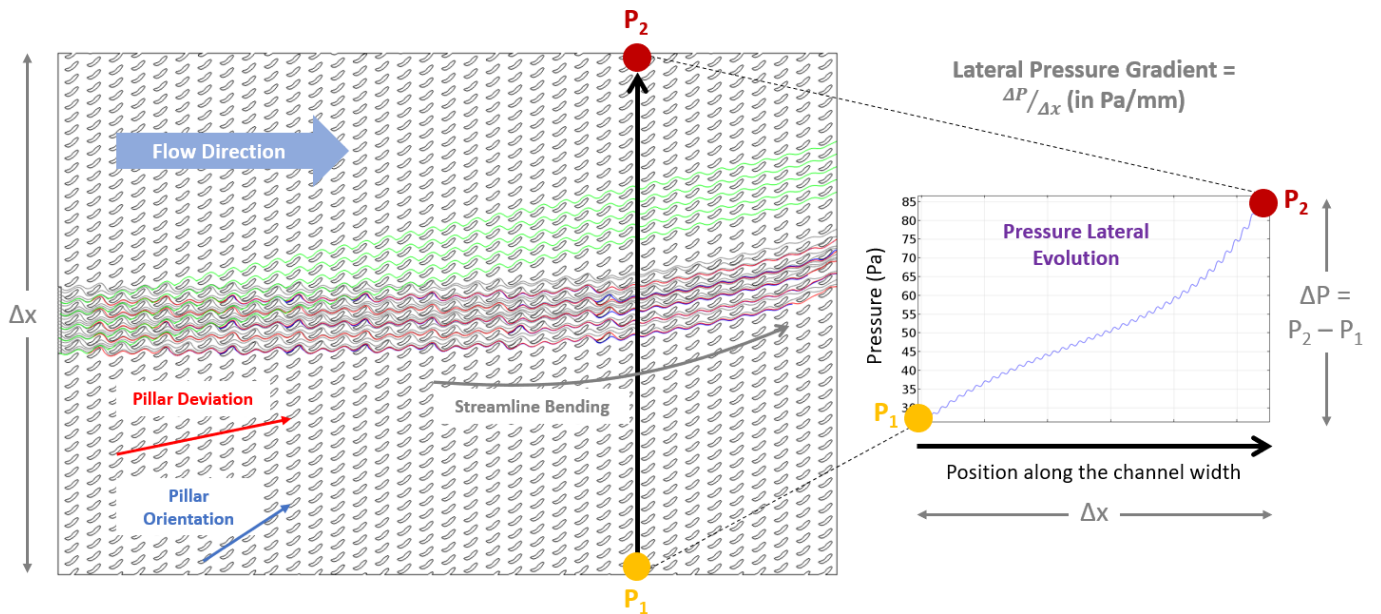


Figure 2.6: Upward bending of streamlines in an array of upward-oriented elongated pillars. Representation of our quantification method for anisotropy: anisotropy is defined as the lateral pressure gradient along the channel width. In the shown example, a bottom-up increase of the lateral pressure is observed since the elongated pillars are oriented upwards.

2.3.2 Parametric Study of the Anisotropy Magnitude

The magnitude of anisotropy is quantified according to three geometrical parameters of ellipsoidal pillars (represented in fig. 2.7): **the ratio of lateral-gap to downstream-gap (G_x/G_y)**, **the pillar slant angle (τ)** and **the array period (N)**. Two array periodicities (N=16 and N=3) are considered in our parametric study. Figure 2.7 represents the evolution of anisotropy for these two N values, according to G_x/G_y and τ . Positive τ angles (upward-oriented pillars) generate positive anisotropy, while negative τ angles (downward-oriented pillars) lead to negative anisotropy (fig. 2.8) with the same positive-oriented pillar array. Interestingly, a pillar orientation of $\tau = -6^\circ$ is required to get zero anisotropy (which compensates for the positive orientation of the pillar array).

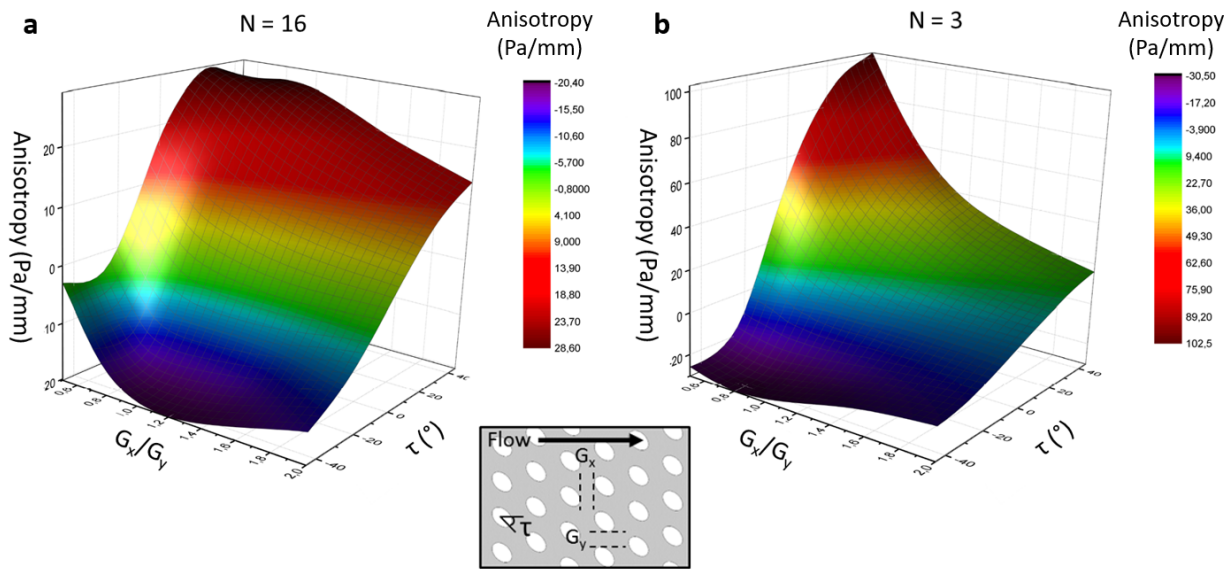


Figure 2.7: Evolution of anisotropy with the gap ratio (G_x/G_y) and the pillar slant angle (τ) for an array period N=16 (a) and N=3 (b).

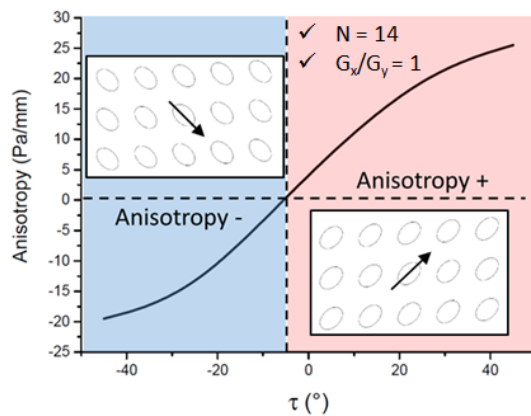


Figure 2.8: Evolution of anisotropy with the pillar orientation (τ) for $N = 14$ (or $\theta = 4^\circ$) and $G_x/G_y = 1$.

For upward-oriented pillars, anisotropy continuously grows when G_x/G_y decreases. Below a certain inter-pillar spacing ratio, anisotropy becomes constant because streamlines are confined in the displacement path (fig. 2.9 a). When the pillars are pointing downwards, the effect is different: above a certain threshold, anisotropy becomes more and more negative when the pillars get closer, but below this threshold, anisotropy increases again when decreasing the inter-pillar spacing (fig. 2.9 b).

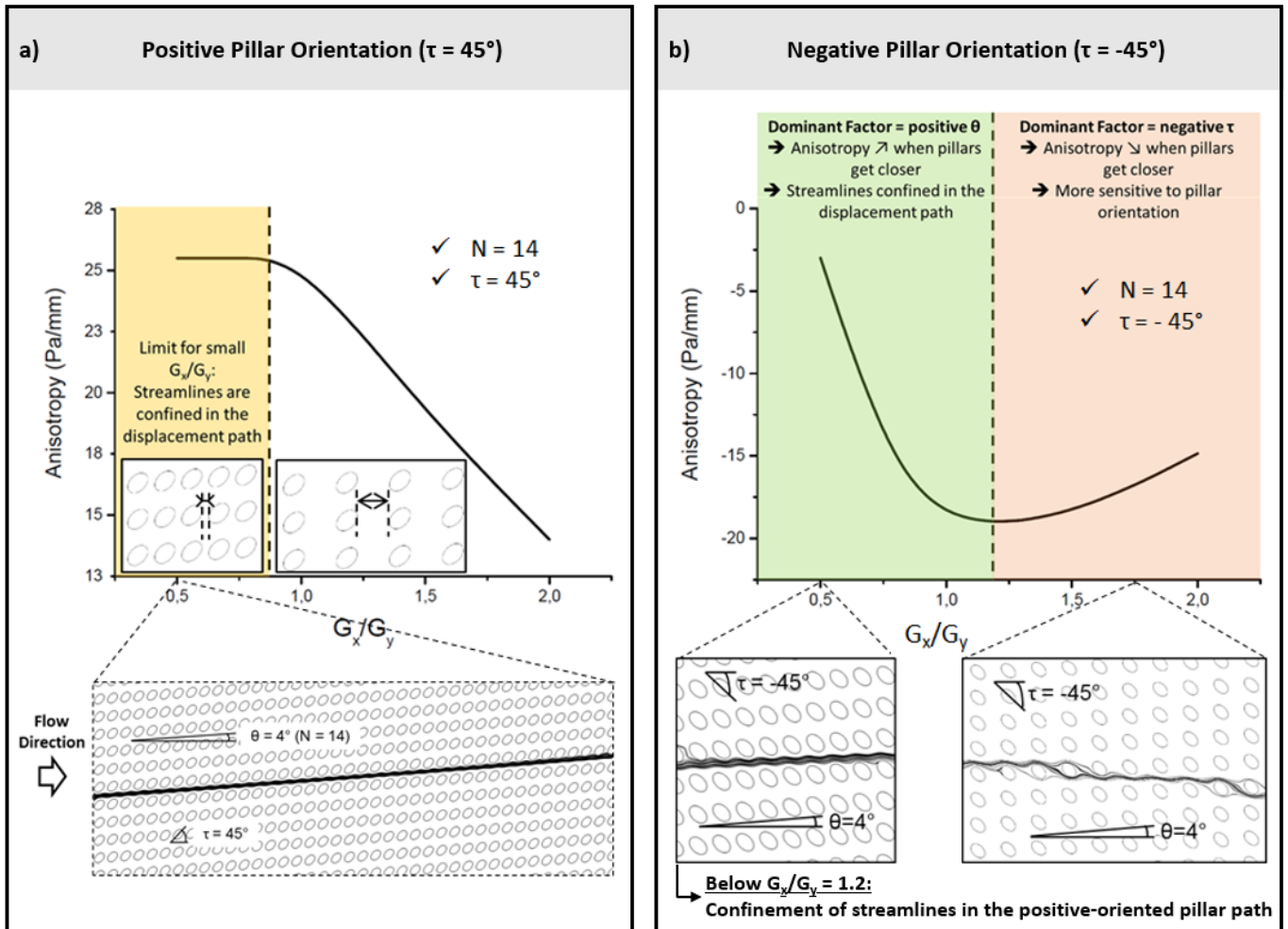


Figure 2.9: a) Evolution of anisotropy with the gap ratio G_x/G_y for $N = 14$ (or $\theta = 4^\circ$) and $\tau = 45^\circ$ (upward-oriented pillars, positive anisotropy). b) Evolution of anisotropy with the gap ratio G_x/G_y for $N = 14$ and $\tau = -45^\circ$ (downward-oriented pillars, negative anisotropy).

The reported threshold for negative τ orientations is due to the confinement of streamlines in the positive-oriented pillar path for small G_x/G_y ratios, that makes anisotropy become more positive. The position of the threshold depends on the array slant angle θ . In particular, it decreases when increasing the array slant angle (fig. 2.10).

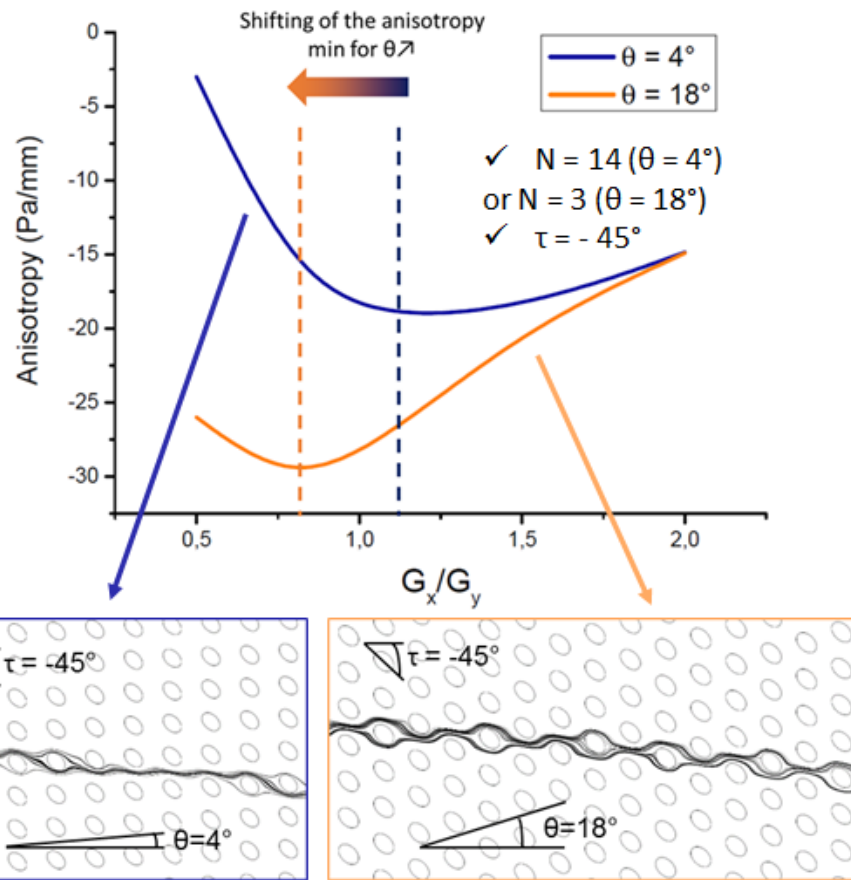


Figure 2.10: Anisotropy minimum for $\theta = 4^\circ (N = 14)$ and $\theta = 18^\circ (N = 3)$

In conclusion, the orientation of the pillars relative to the direction of the pillar array is a key parameter that influences the anisotropy magnitude:

- When pillars are oriented in the same direction as the pillar array: the anisotropy magnitude increases with the pillar orientation angle (τ) until reaching a plateau around $\tau = 45^\circ$.
- When pillars are oriented in the opposite direction to the pillar array: the anisotropy magnitude reaches a maximum negative value for a pillar orientation angle around $\tau = 45^\circ$.
- In both cases, the absolute value of the anisotropy magnitude is maximum when the lateral gap is equal to the downstream gap (inter-pillar spacing ratio G_x/G_y close to 1).

2.3.3 Impact of Anisotropy on Particle Trajectory

From the previous parametric study of the anisotropy amplitude, we select some specific values to observe the effect of anisotropy on the particle trajectory with the COMSOL numerical model presented earlier in this section.

Zero Anisotropy

In a DLD array of zero anisotropy, particles in zigzag mode have a perfectly straight path without any deviation along the channel (fig. 2.11). As mentioned earlier fig. 2.8, zero anisotropy is obtained with pillars slightly oriented downwards ($\tau = -6^\circ$). Thus, even with isotropic pillars, anisotropy is naturally induced in DLD channels because of the orientation of the pillar array.

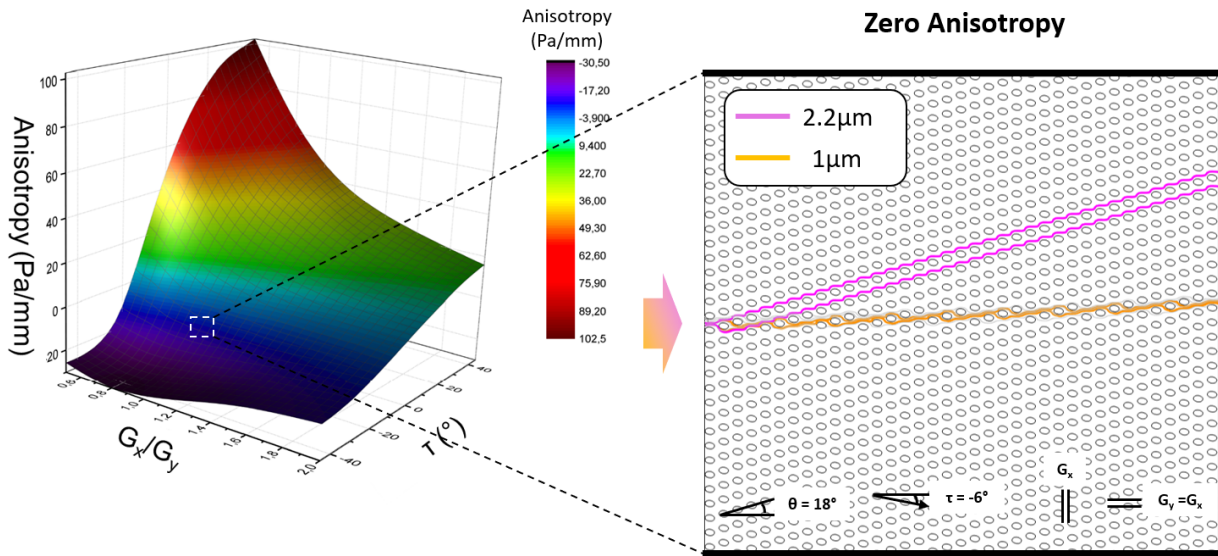


Figure 2.11: Trajectory of $1\ \mu\text{m}$ (orange) and $2.2\ \mu\text{m}$ (purple) particles in a DLD array of zero anisotropy ($\theta = 18^\circ$, $\tau = -6^\circ$ and $G_x/G_y = 1$)

Positive Anisotropy

The effect of positive anisotropy is studied with the following parameters of the DLD array: $\theta = 18^\circ$, $\tau = 45^\circ$ and $G_x/G_y = 1$. In this case, the trajectory of particles in zigzag mode is bended upwards along the DLD channel (fig. 2.12). This is undesirable because at the exit of the DLD separator, the distance between particles in displacement and in zigzag modes is decreased, which compromises the efficiency of the separation.

Negative Anisotropy

Designs with negative anisotropy are particularly promising: in this case, the separation distance between particles in zigzag and in displacement modes is increased, because the trajectory of small particles is bended downwards, according to the orientation of pillars, while larger particles are deviated by the DLD pillar array (fig. 2.13). Therefore, using ellipsoidal pillars pointing in the opposite direction compared to the pillar array is a good option to increase the separation efficiency. However, these pillars also induce an increase in the critical diameter (as observed when comparing fig. 2.12 to fig. 2.13, where $2.2\ \mu\text{m}$ particles follow a displacement trajectory with the positive pillar orientation and a zigzag trajectory with the negative pillar orientation), which means that smaller inter-pillar spacings or slant angles are required to keep the same critical diameter with negative-oriented pillars.

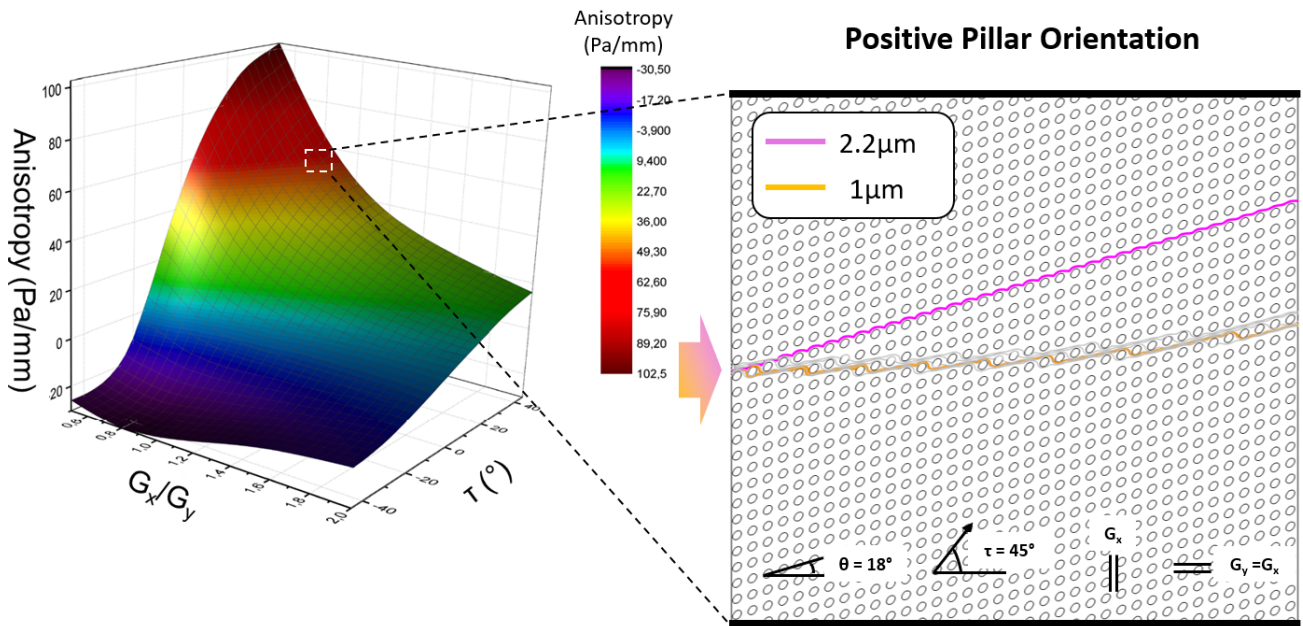


Figure 2.12: Trajectory of 1 μm (orange) and 2.2 μm (purple) particles in a DLD array of positive anisotropy ($\theta = 18^\circ$, $\tau = 45^\circ$ and $G_x/G_y = 1$). Streamlines are displayed in grey.

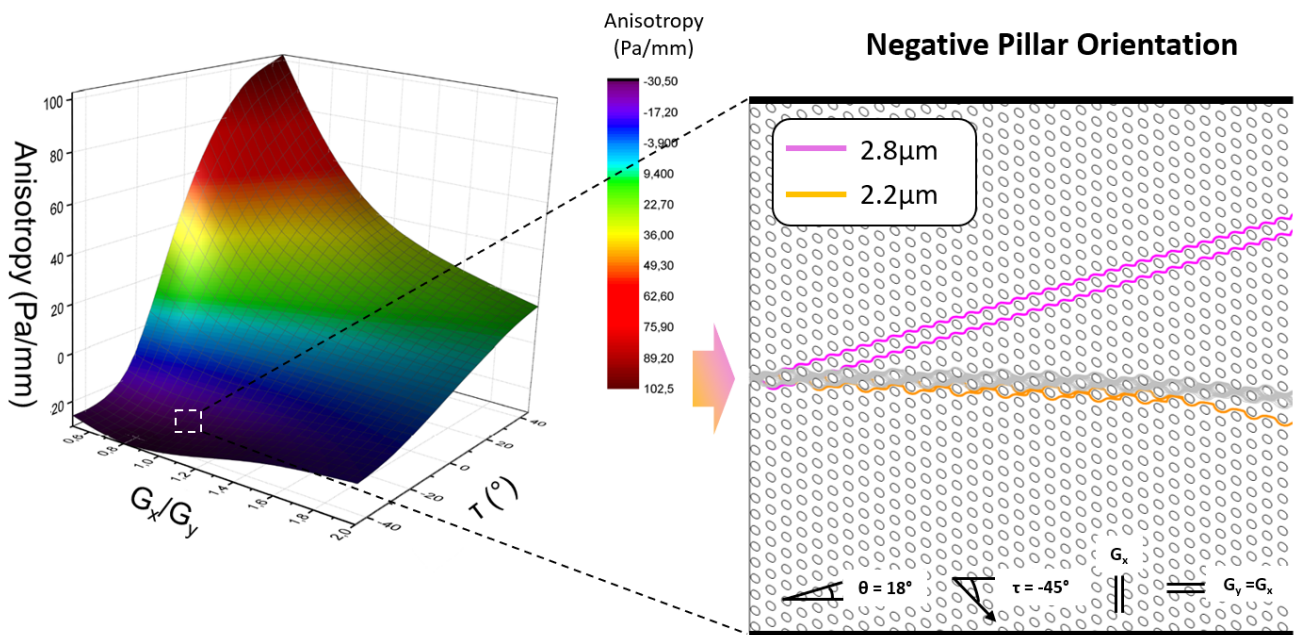


Figure 2.13: Trajectory of 2.2 μm (orange) and 2.8 μm (purple) particles in a DLD array of positive anisotropy ($\theta = 18^\circ$, $\tau = -45^\circ$ and $G_x/G_y = 1$). Streamlines are displayed in grey.

2.3.4 Multi-Separation DLD Designs

A very interesting application of negative anisotropy is the multi-separation of several particle sizes in a single DLD device. Here we take advantage of the negative bending of particle trajectory to separate several particle sizes at the same time. Indeed, DLD channels with negative anisotropy have more than two particle trajectories (zigzag and displacement). Intermediate trajectories are also observed: particles start to follow a displacement trajectory and at a specific point (called curvature point), they are re-oriented in the opposite direction, along the pillar orientation (fig. 2.14). The position of the curvature point depends on the particle size and is closer to the entrance for smaller particles. Therefore, at the channel exit, many different particle subpopulations can be collected in several output channels. More particle subpopulations can be separated with longer DLD channels.

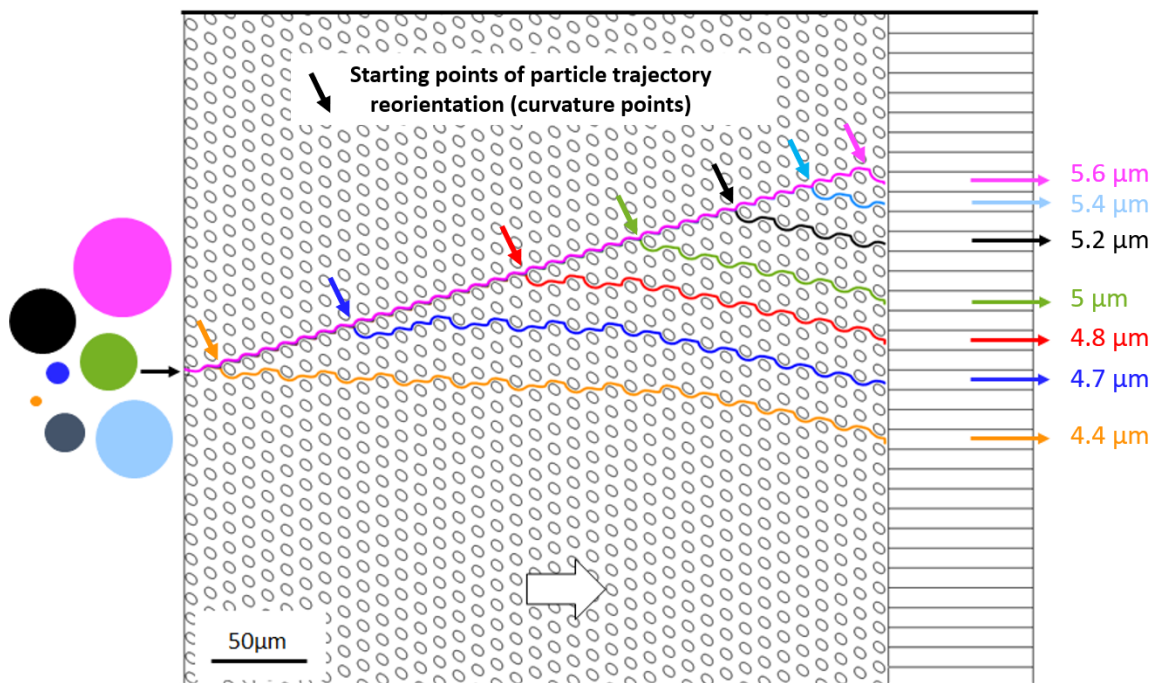


Figure 2.14: Multi-separation in a DLD array with ellipsoidal pillars ($\tau = -45^\circ$, $G = 6 \mu\text{m}$, $N = 3$)

From Davis' model [326], the predicted critical diameter with the design of fig. 2.14 ($\tau = -45^\circ$, $G = 6 \mu\text{m}$, $N = 3$) is $D_c = 5 \mu\text{m}$. In our multi-separation design, particles are separated around the critical diameter predicted by Davis' model, with only a few hundreds of nanometers between the diameters of adjacent particle subpopulations. The separation accuracy between the different particle populations is only limited by the minimum width of the output channels, which is equal to the inter-pillar spacing ($6 \mu\text{m}$ in the example of fig. 2.14). Moreover, packaging considerations have to be taken into account when a large number of output fluidic connections are required to collect each particle subpopulation. Typically, about 10 output fluidic connections can reasonably be implemented on our cartridge format, which means 10 separated particle subpopulations.

Another example is given on fig. 2.15, with a larger inter-pillar spacing ($\tau = -45^\circ$, $G = 10 \mu\text{m}$, $N = 3$). Again, the Davis' model is verified, with a separation around the predicted critical diameter ($D_c = 8.3 \mu\text{m}$).

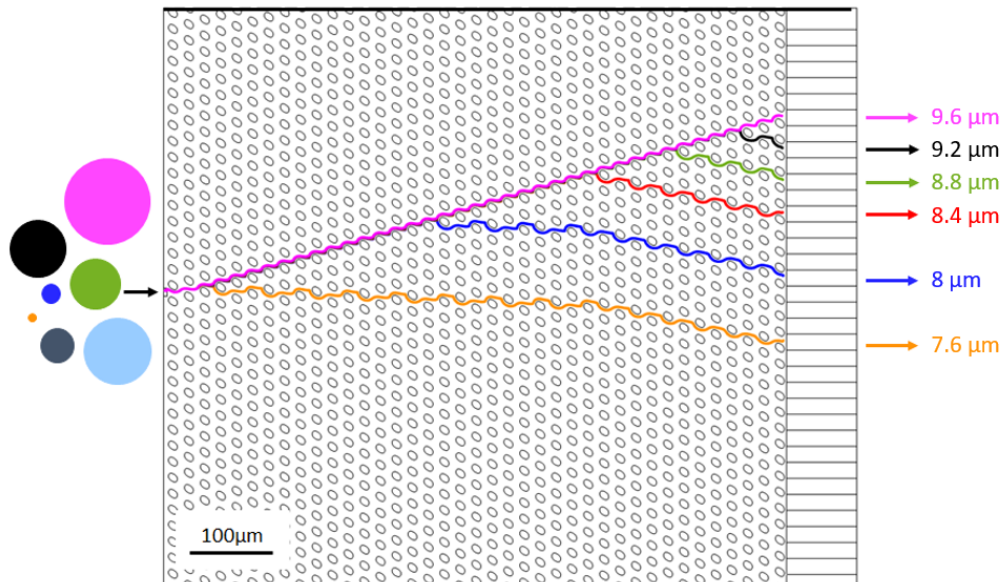


Figure 2.15: Multi-separation in a DLD array with ellipsoidal pillars ($\tau = -45^\circ$, $G = 10 \mu\text{m}$, $N = 3$)

Therefore, multi-separation DLD devices can be designed from the classical Davis' model to fractionate a large number of particle sizes in a single device. This is particularly relevant for applications that require the separation of particle subpopulations with very close sizes, such as virus or EV populations. **It can also be used as a characterization method to evaluate the polydispersity of samples**, either through direct visualization of the trajectory for fluorescent particles, or combined with downstream analysis at each outlet.

Improvements in terms of separation efficiency could be made by using other types of oriented pillar shapes (such as triangles, rectangles, etc...) in order to further increase anisotropy and separation efficiency of multiple particle populations.

2.4 Implemented DLD Designs

During my PhD project, three different versions of DLD designs have been successively implemented, corresponding to three different silicon batches. Improvements have been made between the first and the second versions, both in the design and the fabrication process. Version 3 was based on the same optimized fabrication process as version 2 to implement exploratory designs for complementary functions to DLD separation, such as concentration and buffer exchange. The three different versions will be reviewed in the following section before focusing on the corresponding fabrication process. The obtained sorting results will be presented in Chapter 3.

2.4.1 Version 1

The first version of DLD devices has been designed so as to sort a range of particle dimensions from 150 nm to 20 μm , which corresponds to typical particle sizes in the biofluids of interest (blood and cell culture media). The V1 designs have the following characteristics (geometrical parameters summarized in fig. 2.16):

- Two inlets: one inlet for the sample solution (sample inlet width = 100 μm) and the second inlet for the buffer solution (buffer inlet width = 300 μm) to carry large deviated particles
- Two pillar shapes: circles (standard) and triangles (shown to decrease the critical diameter for a given slant angle and inter-pillar spacing [349])
- Three separation zones in each DLD channel with three different slant angles but a given inter-pillar spacing along the entire channel length
- Two types of outlets: one version with two exit channels and one version with four exit channels
- The minimum channel length l required in each sorting section for large particles to be completely deviated by the pillar array: $l = L / \tan(\theta)$, where L is the channel width and θ is the slant angle of the pillar array
- Same pillar size and inter-pillar spacing
- Four pillar dimensions to sort several ranges of particle sizes: 60 μm , 20 μm , 5.5 μm and 1 μm

Design Number	1	2	3	4
Pillar Size D_p (μm)	60	20	5.5	1
Inter-Pillar Spacing G (μm)	60	20	5.5	1
Channel Width (μm)	400	400	400	400
Section 1				
Slant Angle θ ($^\circ$)	2.6	9.9	7.2	7.3
Periodicity N	22	5.7	7.9	7.8
Length (μm)	3200	572	786	785
D_c Davis (μm)	19	12	2.9	0.52
D_c Inglis (μm)	15	11	2.4	0.45
Section 2				
Slant Angle θ ($^\circ$)	2.6	4.3	3.1	3.3
Periodicity N	22	13.3	18.3	17.4
Length (μm)	3200	1334	1834	1770
D_c Davis (μm)	19	8	1.9	0.35
D_c Inglis (μm)	15	7	1.5	0.29
Section 3				
Slant Angle θ ($^\circ$)	2.6	1.1	0.5	0.9
Periodicity N	22	50	110	66.7
Length (μm)	3200	5000	11000	7143
D_c Davis (μm)	19	4	0.8	0.19
D_c Inglis (μm)	15	3	0.6	0.15

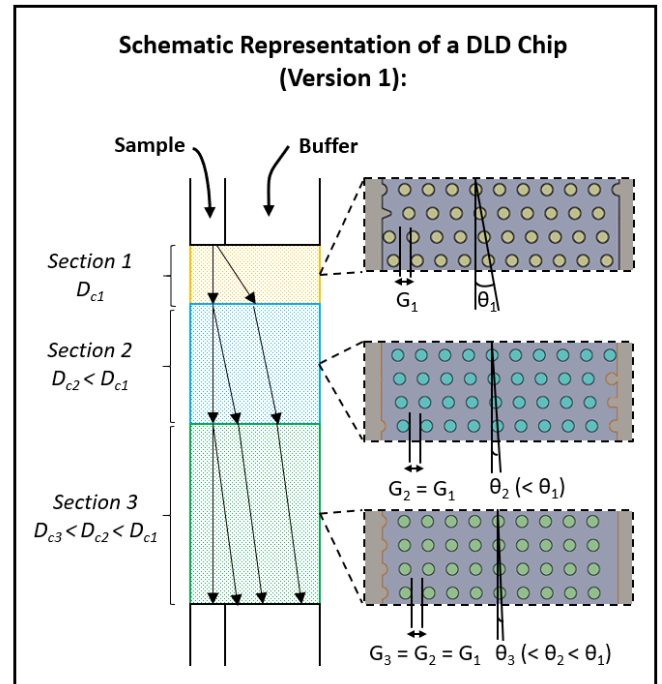


Figure 2.16: Characteristics of version 1 DLD designs. The pillar size (D_p) corresponds to the diameter for circular pillars and the height for equilateral triangular pillars.

Optical and scanning electron microscopy (SEM) images are given below for the four DLD designs:

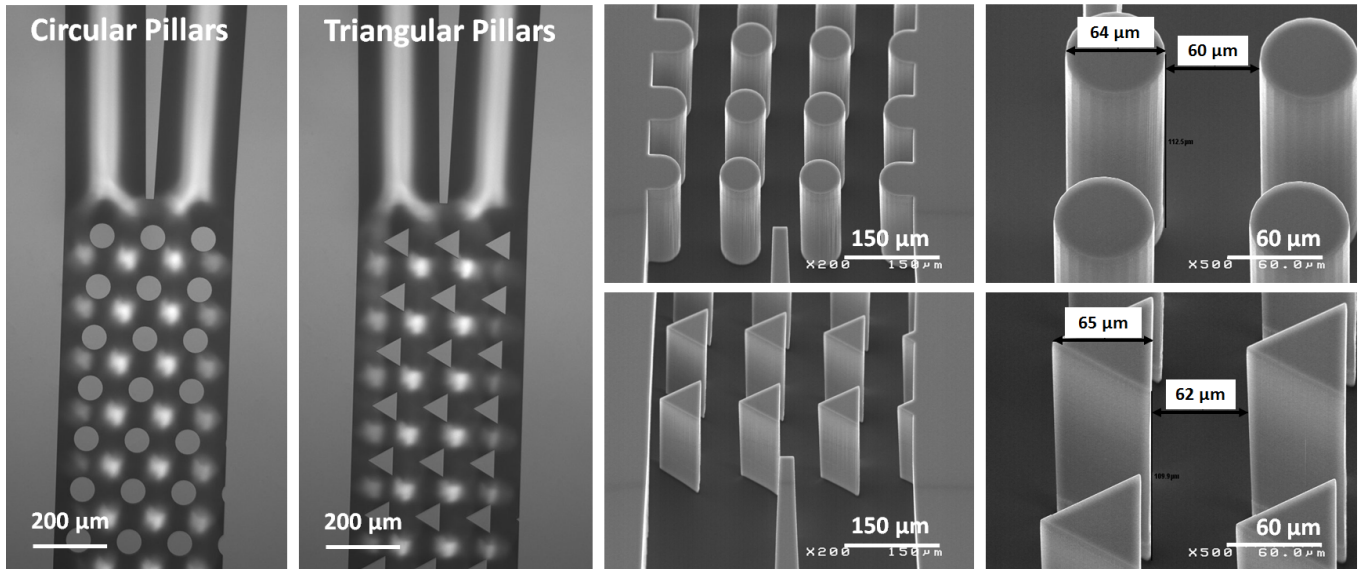


Figure 2.17: Optical and SEM images of our DLD devices: design 1 with pillar diameter (D_p) = 60 μm, inter-pillar spacing (G) = 60 μm, channel width = 400 μm

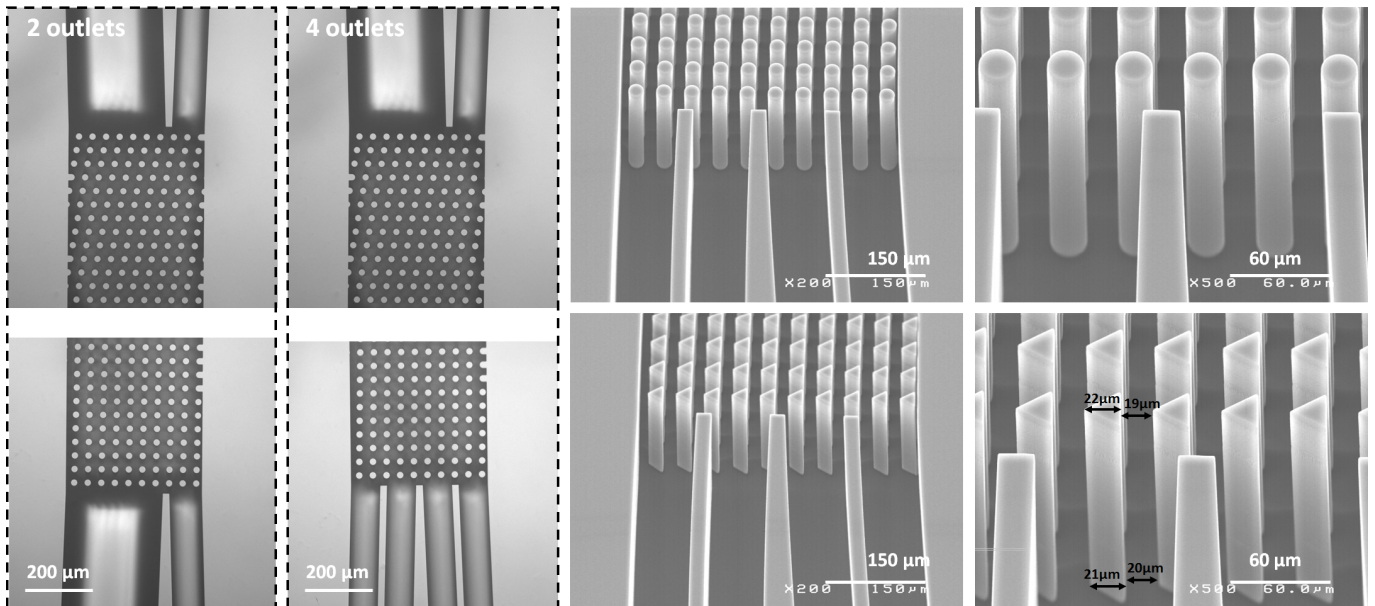


Figure 2.18: Optical and SEM images of our DLD devices: design 2 with pillar diameter (D_p) = 20 μm, inter-pillar spacing (G) = 20 μm, channel width = 400 μm.

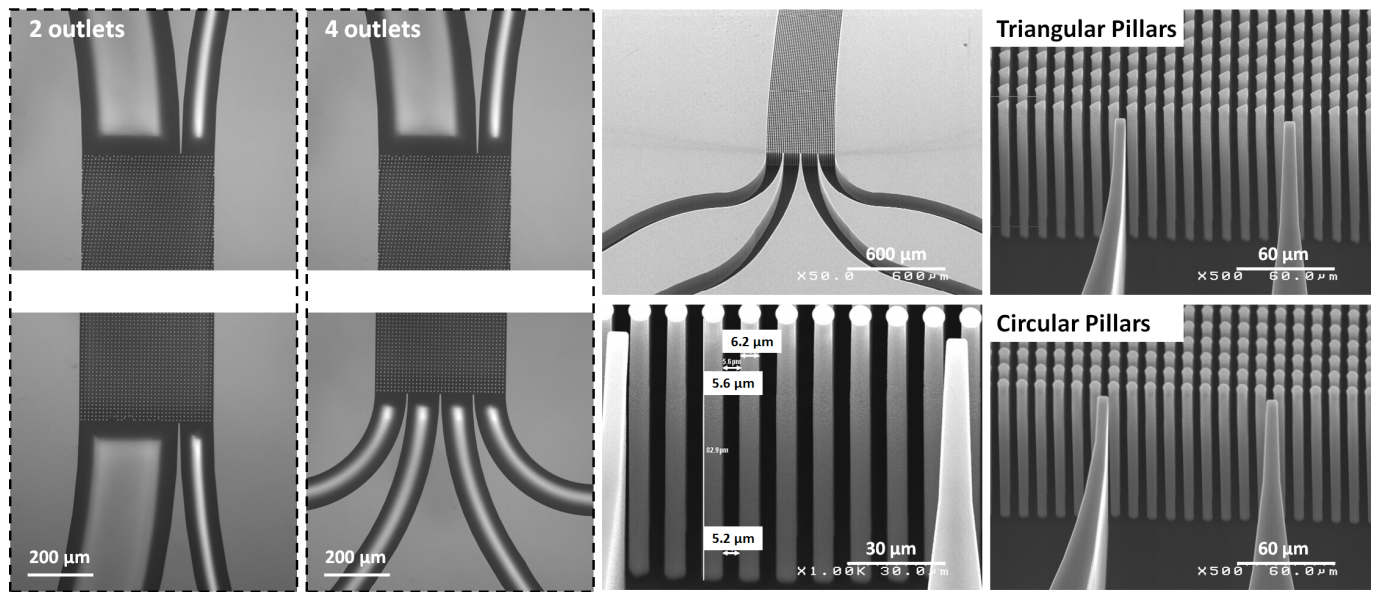


Figure 2.19: Optical and SEM images of our DLD devices: design 3 with pillar diameter (D_p) = 5.5 μm, inter-pillar spacing (G) = 5.5 μm, channel width = 400 μm.

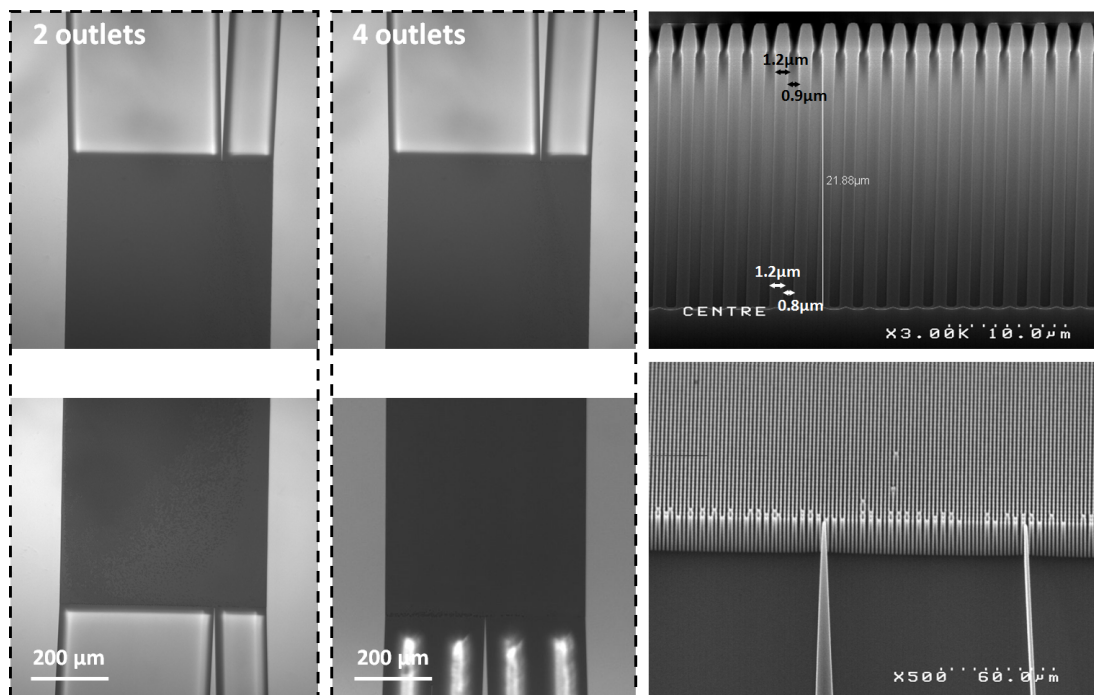


Figure 2.20: Optical and SEM images of our DLD devices: design 4 with pillar diameter (D_p) = 1 μm, inter-pillar spacing (G) = 1 μm, channel width = 400 μm.

Standardization considerations were implemented in the design phase in order to simplify the packaging of our DLD chips. This standardization was part of the H2020 European Project MFManufacturing (<http://mf-manufacturing.eu/>). The position and size of the fluidic holes were common for all the different designs (fig. 2.21). This standard footprint enables to use the same packaging solution (cartridge and holder) for any of the DLD designs.

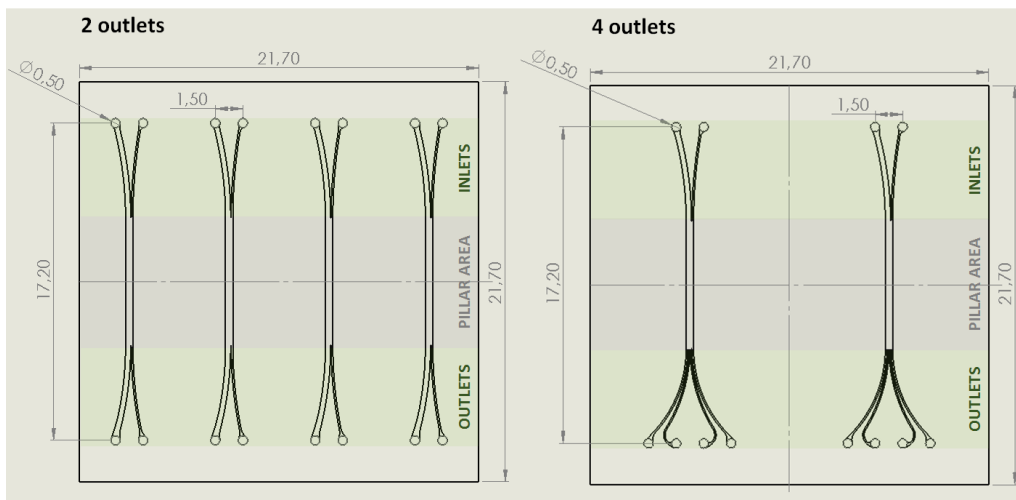


Figure 2.21: Position of the fluidic holes in the 2-outlets and 4-outlets versions of the DLD chips (measurements are given in mm).

2.4.2 Version 2: Improvements

From the experimental testing of the first designs, the following improvements have been implemented in the second version of DLD devices in order to improve the separation efficiency and reduce clogging issues (with geometrical characteristics given for the 15 designs in fig. 2.22):

- Increase the channel width to reduce the wall effects (that will be described in Chapter 3)
- Increase the channel length with the intent of increasing the separation efficiency
- Implement other pillar shapes in addition to circles and triangles: hexagons (that lead to a smaller critical diameter for the selected orientation compared to the other pillar shapes, as presented in Section 2.2 of this Chapter) and I-shaped pillars (shown to improve the deviation of RBCs [345])
- Implement asymmetrical inter-pillar spacings, with a smaller downstream gap compared with the lateral gap, shown to improve the deviation efficiency [369]
- Implement designs with only one inlet to simplify handling and pressure control at the DLD entrance. One should notice that in this case, part of the non-deviated particles are lost in the deviated outlet since they are injected in the entire channel width. The proportion of lost non-deviated particles is equal to the ratio of the deviated outlet width to the entire channel width.

- Choose equal channel widths and lengths at the inlet and outlet to avoid intrinsic imbalance of hydraulic resistances
- Add intermediary channels upstream of the DLD pillar array to reduce clogging at the DLD entrance by carrying particles towards the inter-pillar spacings
- Add intermediary channels downstream of the DLD pillar array to avoid disturbing streamlines between the pillar array and the exit
- Remove pillar portions on the channel sides to avoid particle capture between side pillars and walls

Group 1	1	2	3			
Pillar Shape	Circles	Circles	Circles			
Pillar Size D_p (μm)	1	2	3			
Downstream Gap G_x (μm)	1	2	3			
Lateral Gap G_y (μm)	1	2	3			
Channel Width (μm)	360	360	360			
Slant Angle θ ($^\circ$)	0.6	0.6	0.6			
Periodicity N	100	100	100			
Length (μm)	44000	44000	44000			
D_c Davis (μm)	0.15	0.31	0.46			
D_c Inglis (μm)	0.12	0.24	0.35			

Definition of D_p for the different pillar shapes:

Group 2	1	2	3	4	5	6
Pillar Shape	Circles	Circles	Circles	Triangles	Hexagons	I-shaped
Pillar Size D_p (μm)	5	9	9	9	9	9
Downstream Gap G_x (μm)	5	9	4.5	9	9	9
Lateral Gap G_y (μm)	5	9	9	9	9	9
Channel Width (μm)	1100	1100	1100	1100	1100	1100
Slant Angle θ ($^\circ$)	1.4	1.9	1.9	1.9	1.9	1.9
Periodicity N	40	30	30	30	30	30
Length (μm)	44000	44000	44000	44000	44000	44000
D_c Davis (μm)	1.2	2.5	2.5	2.5	2.5	2.5
D_c Inglis (μm)	0.9	2.0	2.0	2.0	2.0	2.0

Group 3	1	2	3	4	5	6
Pillar Shape	Circles	Circles	Circles	Circles	Circles	Circles
Pillar Size D_p (μm)	11	15	20	30	11	15
Downstream Gap G_x (μm)	11	15	20	30	5.5	7.5
Lateral Gap G_y (μm)	11	15	20	30	11	15
Channel Width (μm)	2500	2500	2500	2500	2500	2500
Slant Angle θ ($^\circ$)	3.8	3.8	3.8	3.8	3.8	3.8
Periodicity N	15	15	15	15	15	15
Length (μm)	44000	44000	44000	44000	44000	44000
D_c Davis (μm)	4	6	8	11	4	6
D_c Inglis (μm)	4	5	6	9	4	5

Figure 2.22: Characteristics of version 2 DLD designs and definition of the pillar size D_p for the four pillar shapes: circles, triangles, hexagons and I-shaped.

Optical and SEM images are given below for the three groups of DLD designs:

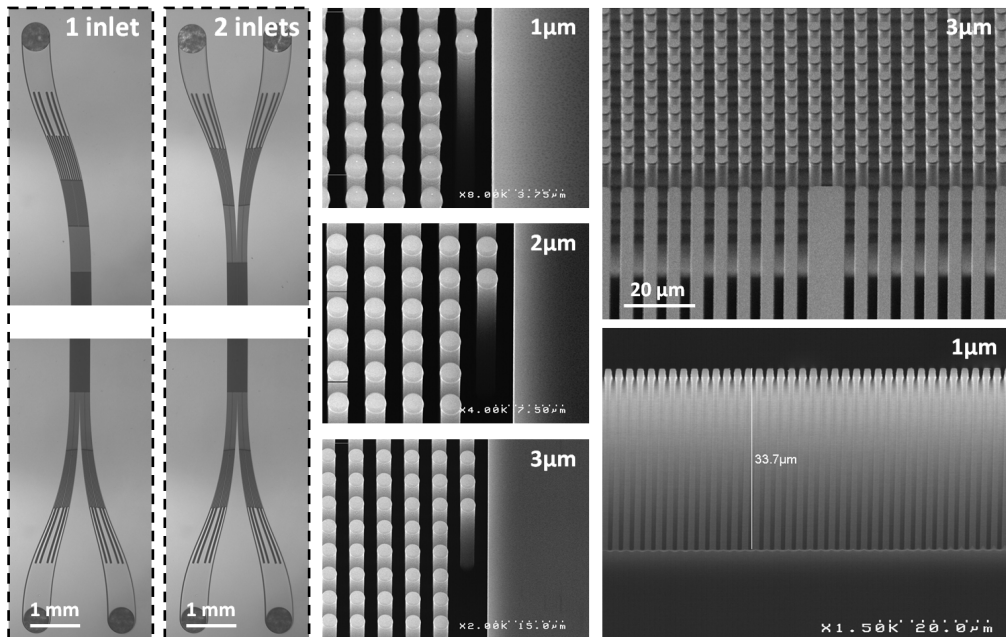


Figure 2.23: Optical and SEM images of our DLD devices: Group 1 with pillar diameters (D_p) between 1 μm and 3 μm , inter-pillar spacings (G) between 1 μm and 3 μm , channel width = 360 μm .

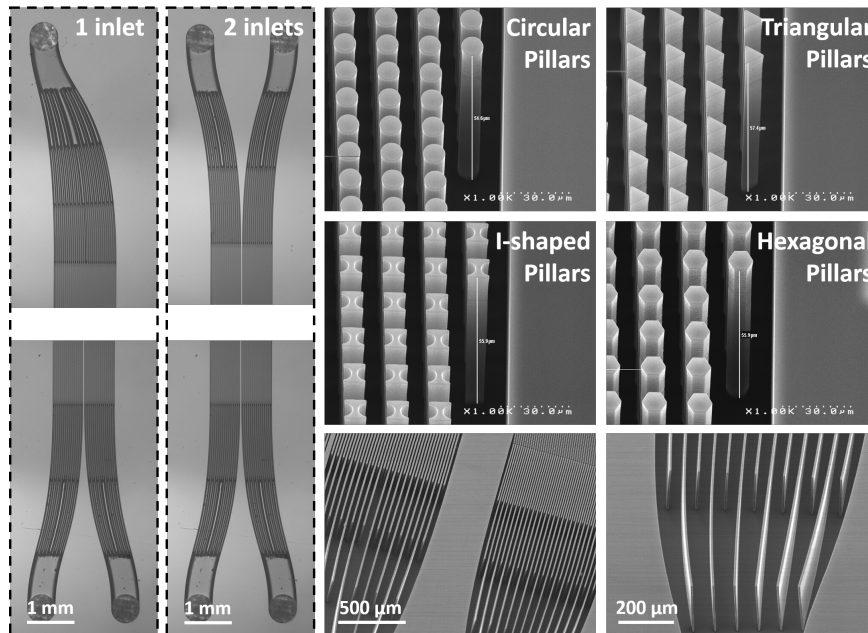


Figure 2.24: Optical and SEM images of our DLD devices: Group 2 with pillar diameters (D_p) between 5 μm and 9 μm , inter-pillar spacings (G) between 5 μm and 9 μm , channel width = 1100 μm .

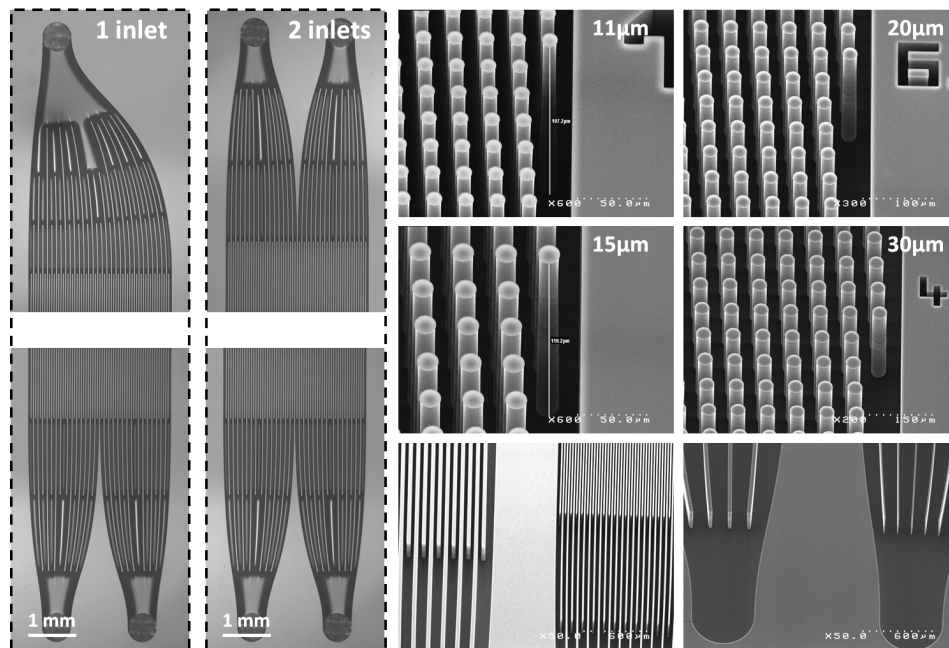


Figure 2.25: Optical and SEM images of our DLD devices: Group 3 with pillar diameters (D_p) between $11\ \mu\text{m}$ and $30\ \mu\text{m}$, inter-pillar spacings (G) between $11\ \mu\text{m}$ and $30\ \mu\text{m}$, channel width = $2500\ \mu\text{m}$.

The same standardized inlet/outlet footprints were used for the chips in the first and the second versions to simplify the packaging of the DLD chips. The standard dimensions are given below for version 2 DLD chips:

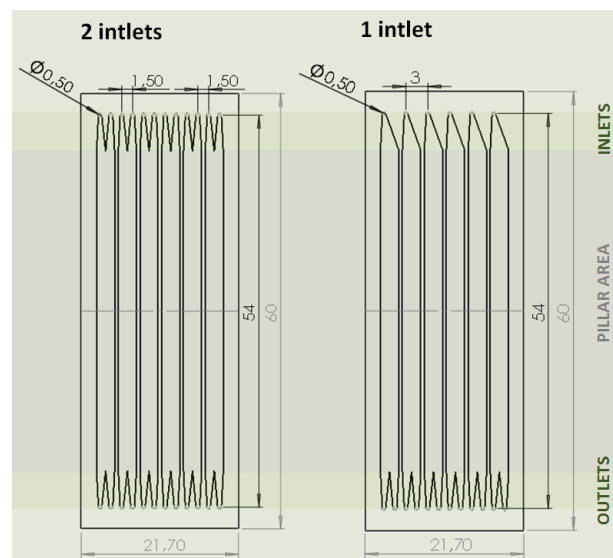


Figure 2.26: Position of the fluidic holes in the 2-inlets and 1-inlet versions of the DLD chips (measurements are given in mm).

2.4.3 Version 3: Exploratory Designs

Three types of exploratory DLD devices have been designed in order to improve the separation efficiency and the fluidic handling.

Anisotropic Devices

In order to test the anisotropic effects described in section 2.3, designs with oriented pillars have been implemented. The following parameters have been tested:

- The pillar shape: ellipses or triangles, with the geometrical characteristics defined in fig. 2.27 (a)
- The pillar orientation, defined by the angle τ (fig. 2.27 a)
- The ratio of lateral-gap to downstream-gap (G_y/G_x)

An additional design has been implemented to increase the separation distance between deviated and non-deviated particles thanks to different pillar orientations in the same DLD channel (fig. 2.27 (b) and (c)). For an upward-oriented pillar array, pillars located above the injection point are also upward-oriented, while pillars located below the injection point are downward-oriented. Pillars in front of the injection point do not have any orientation. This configuration enables to increase the deviation of large particles and, at the same time, small particles are deviated in the opposite direction, instead of following a horizontal zigzag trajectory. At the DLD channel exit, **both particle populations should be more separated compared to conventional DLD.**

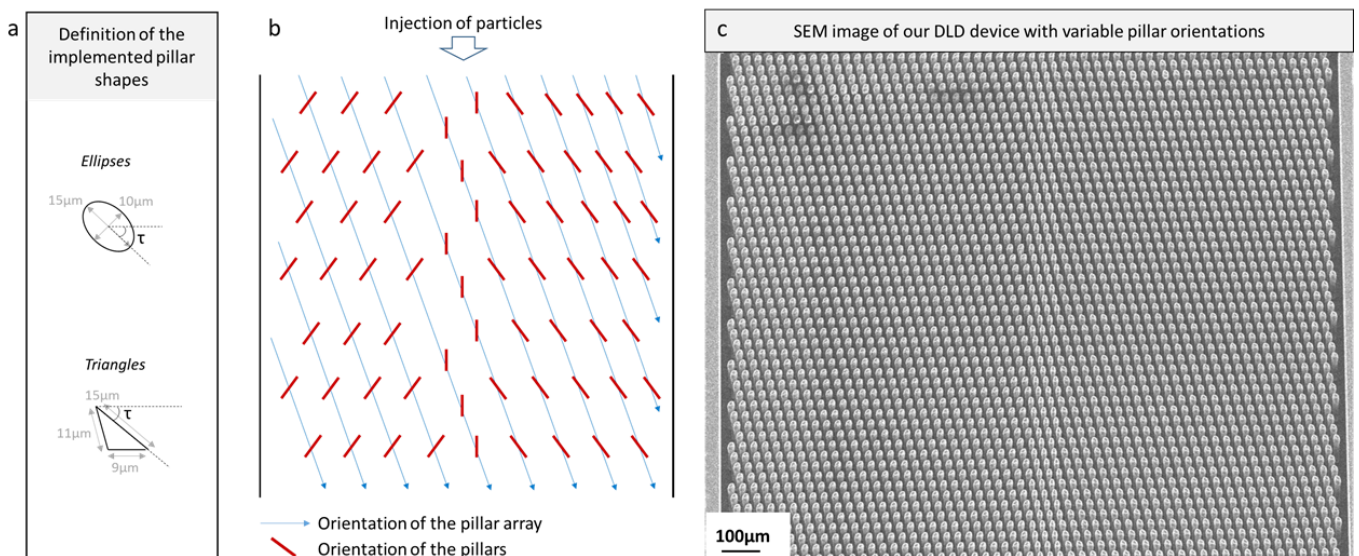


Figure 2.27: a) Geometrical parameters of the two implemented pillar shapes: ellipses and triangles. b) Schematic representation of our multi-orientation design: the blue arrows represent the orientation of the pillar array and the red lines correspond to the pillar orientation. c) SEM image of the DLD device with variable pillar orientations.

Table 2.1 defines the seven implemented designs. All the designs display three inlets (a central inlet to focus particles in the channel center and two lateral channels for the buffer solution) and one single outlet since the first objective is to observe the trajectory of particles without any flow disturbance that could be induced by several unbalanced output channels. Influence of multiple outlets is tested with design 7 (4 outlets). After experimental validation of the multi-separation effect with V3 designs, we will need to implement as many outlet channels as the number of separated particle subpopulations.

Table 2.1: Characteristics of version 3 DLD designs (anisotropic devices).

Design Number	1	2	3	4	5	6	7
Downstream Gap G_x (μm)	15	15	12	15	15	15	15
Lateral Gap G_y (μm)	15	15	15	15	15	15	15
Periodicity N	5	5	5	5	5	5	5
Pillar Orientation τ ($^\circ$)	-45	-60	-45	-45	+45	+45, 0, -45	-45
Pillar Shape	Ellipses	Ellipses	Ellipses	Triangles	Triangles	Ellipses	Ellipses
Number of Outlets	1	1	1	1	1	1	4

Examples of optical and SEM images are presented in fig. 2.28 for both ellipse and triangular pillars.

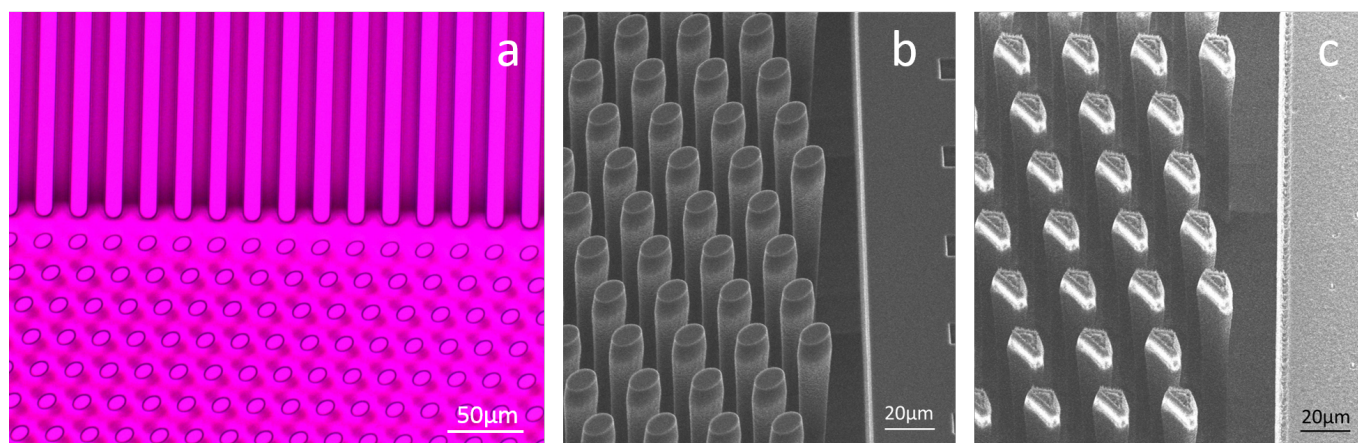


Figure 2.28: a) Optical image of version 3 design 2 (-60° oriented ellipses). b) SEM image of version 3 design 1 (-45° oriented ellipses). c) SEM image of version 3 design 5 ($+45^\circ$ oriented triangles).

DLD Concentration and Solvent Exchange

In addition to the separation effect, DLD can also be used to concentrate deviated particles. Indeed, the concentration of large particles is higher in the deviated outlets, compared to the initial injected sample. The concentration factor depends on the ratio between the exit channel width and the total width of the DLD channel. **For example, if the exit channel width with deviated particles is equal to one inter-pillar spacing (G), the concentration factor corresponds to the number of pillars in the total channel width.**

Thanks to mirror-symmetric channels, Feng et al. [354] recently demonstrated parallel concentration of deviated particles.

In addition, this mirror-symmetric geometry can be used for solvent exchange of deviated particles. By using two side inlets for sample injection and one center channel for the new solvent, large particles can be deviated through DLD towards the center channel to be transferred from the initial solvent to the new injected solvent. Solvent exchange can be required prior to some downstream analysis steps, such as mass spectrometry, which is performed with a volatile solvent that can be easily evaporated during the nebulization process. A geometry for solvent exchange has been proposed, with a specific inlet dedicated to the new buffer, connected to the center of the channel where pillars have been removed. As the hydraulic resistance is much lower in this area, velocity magnitudes are up to 10 times larger than the velocity magnitude between pillars (fig. 2.29 a). Another geometry has been proposed to perform concentration in addition to separation with a single inlet and a small collection outlet at the channel center, where all deviated particles are concentrated (fig. 2.29 b). In this case, the channel walls follow the pillar orientation in a herringbone shape, in order to keep a constant distance between the pillars and the side walls and avoid velocity variations in the DLD device.

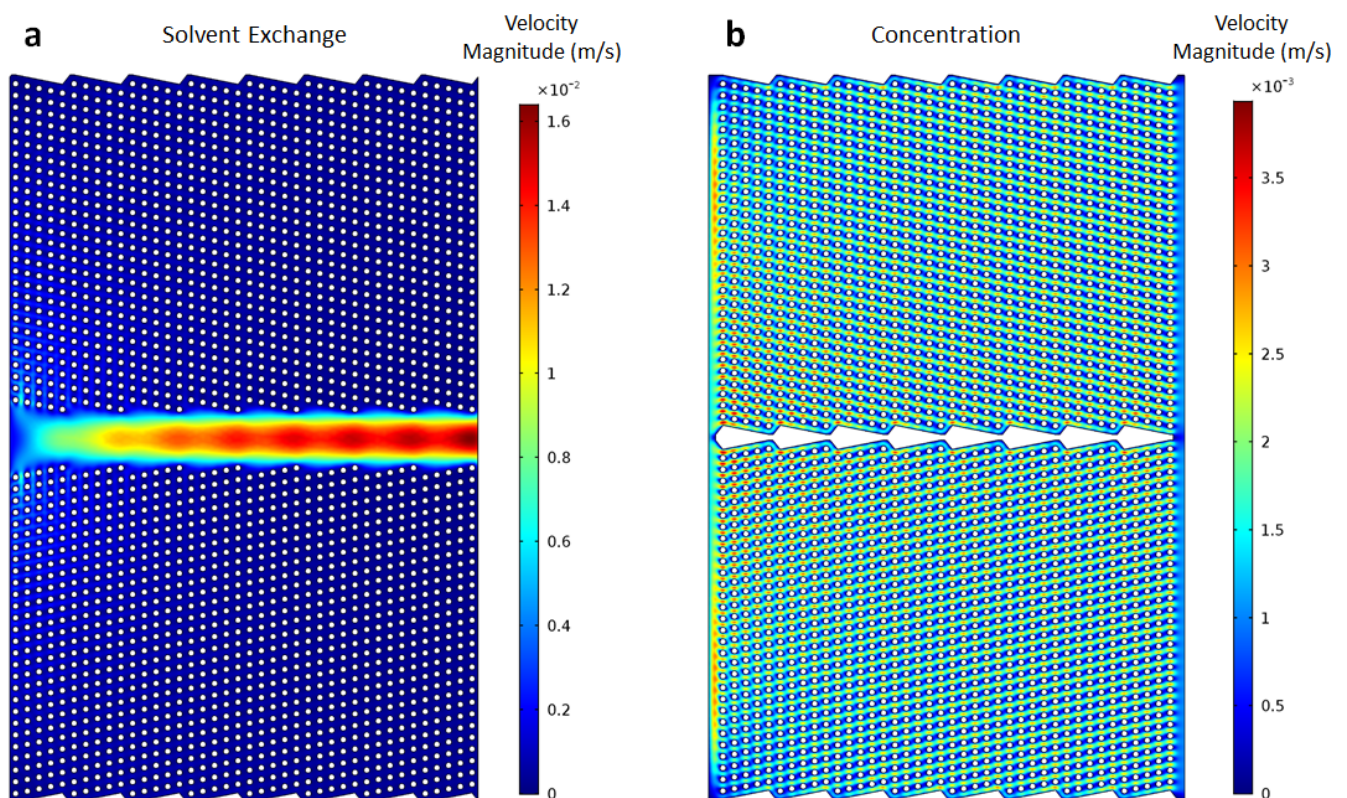


Figure 2.29: Numerical simulations of the velocity magnitude in two DLD devices for solvent exchange (a) and concentration of deviated particles (b)

The geometrical parameters of the four identified designs are given in table 2.2 and SEM images are presented in fig. 2.30.

Table 2.2: Characteristics of version 3 DLD designs (concentration and solvent exchange)

Design Number	1	2	3	4
Function	Concentration	Concentration	Solvent Exchange	Solvent Exchange
Pillar Shape	Circles	Circles	Circles	Circles
Pillar Diameter (μm)	12	12	12	12
Downstream Gap G_x (μm)	12	12	12	12
Lateral Gap G_y (μm)	12	12	12	12
Periodicity N	5	5	5	5
Number of gaps in the channel width	60	60	60	60
Number of gaps in the central outlet	2	6	3	1
Concentration Factor	30	10	20	60

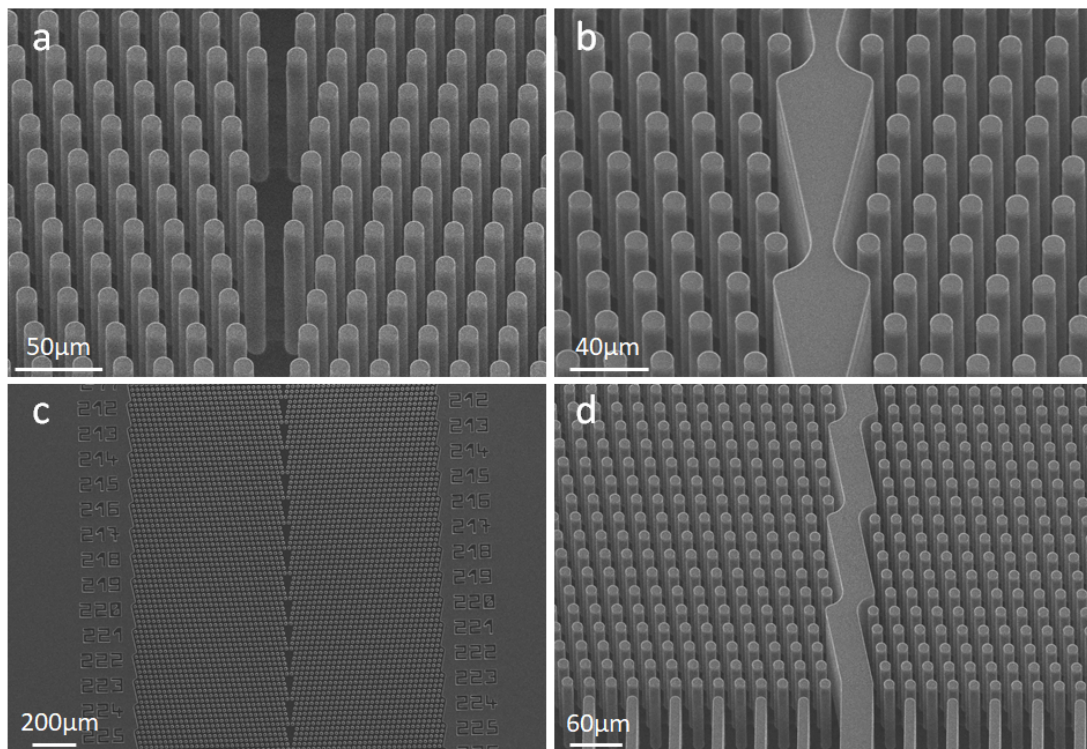


Figure 2.30: SEM images of version 3 design 4 (solvent exchange) (a,c), design 1 (concentrator) (b) and side walls (d).

The experimental testing of the three versions of DLD devices will be presented in the next Chapter.

2.5 Fabrication of DLD Devices

The fabrication process flow is based on silicon (Si) technologies to resolve DLD pillars with micrometric dimensions. The chips are fabricated in the cleanroom facility at CEA Leti on 200 mm Si wafers for versions 1 and 2 and 100 mm Si wafers for version 3. DLD chips of versions 2 and 3 have the same dimensions, while version 1 chips are 4 times shorter with the same width. Therefore, wafers contain 41 chips for version 1 (with 2 or 4 devices on each chip), 11 chips for version 2 (with 6 devices on each chip) and 3 chips for version 3 (with 6 devices on each chip) (fig. 2.31). The fabrication flow implemented for the first version of our DLD devices has been then improved for the versions 2 and 3.

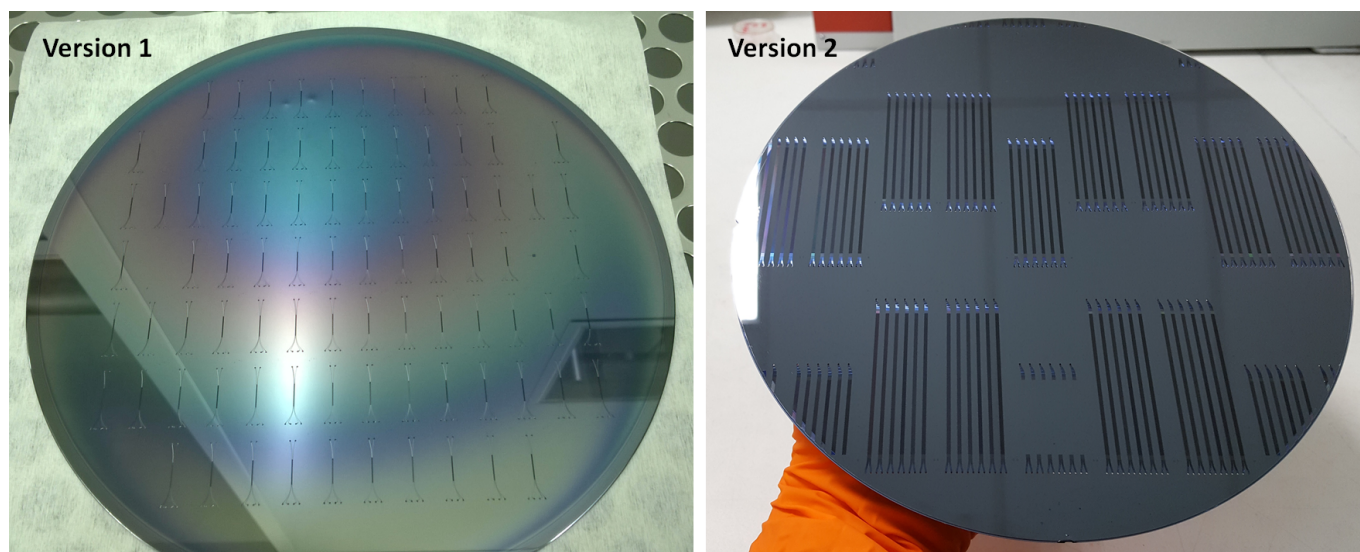


Figure 2.31: Examples of wafers for our first and second versions of DLD devices.

2.5.1 Fabrication Process Flow: Version 1

The fabrication flow for the version 1 of our DLD devices is composed of 59 steps for 25 wafers. The main steps are presented in fig. 2.32. The features of the fluidic channels and the inlet/outlet ports are defined by contact photolithography and Reactive Ion Etching (RIE) on a 3 μm -thick silicon dioxide hard mask (2 μm thermal SiO_2 followed by a deposition of 1 μm SiO_2). Following hard mask etching, fluidic ports are partially etched using deep UV photolithography and RIE. After stripping the resist, the microchannels are etched through the hard mask using RIE and the holes are etched until the bottom 2 μm -thick thermal silicon dioxide layer at the same time. After removing the oxide and cleaning the substrate, a second thermal oxide layer (100 nm thick) is grown prior to sealing the top 550 μm -thick borosilicate glass cover by anodic bonding. The oxide layer enables to smooth surface roughness and provide an hydrophilic surface (preferable to the fluidic injection of our samples). The wafers are then diced into 22 mm x 22 mm individual chips containing either 2 or 4 DLD devices.

Two issues were identified from this fabrication flow: residual silicon was not etched at the intersection

between the fluidic ports and the channels and some of the 1 μm -pillars toggled on each other (fig. 2.32 step 5). The main reason was the sequential etching of the holes and the channels on the same wafer side, especially because of the faster etching in larger areas (thus faster for the holes compared to the channels). Moreover, the design was changed around the holes to avoid bulges in the resist, as observed on fig. 2.32 (step 4). As the profile and stability of 1 μm -pillars was not satisfactory, it was not possible to get reliable results with these chips.

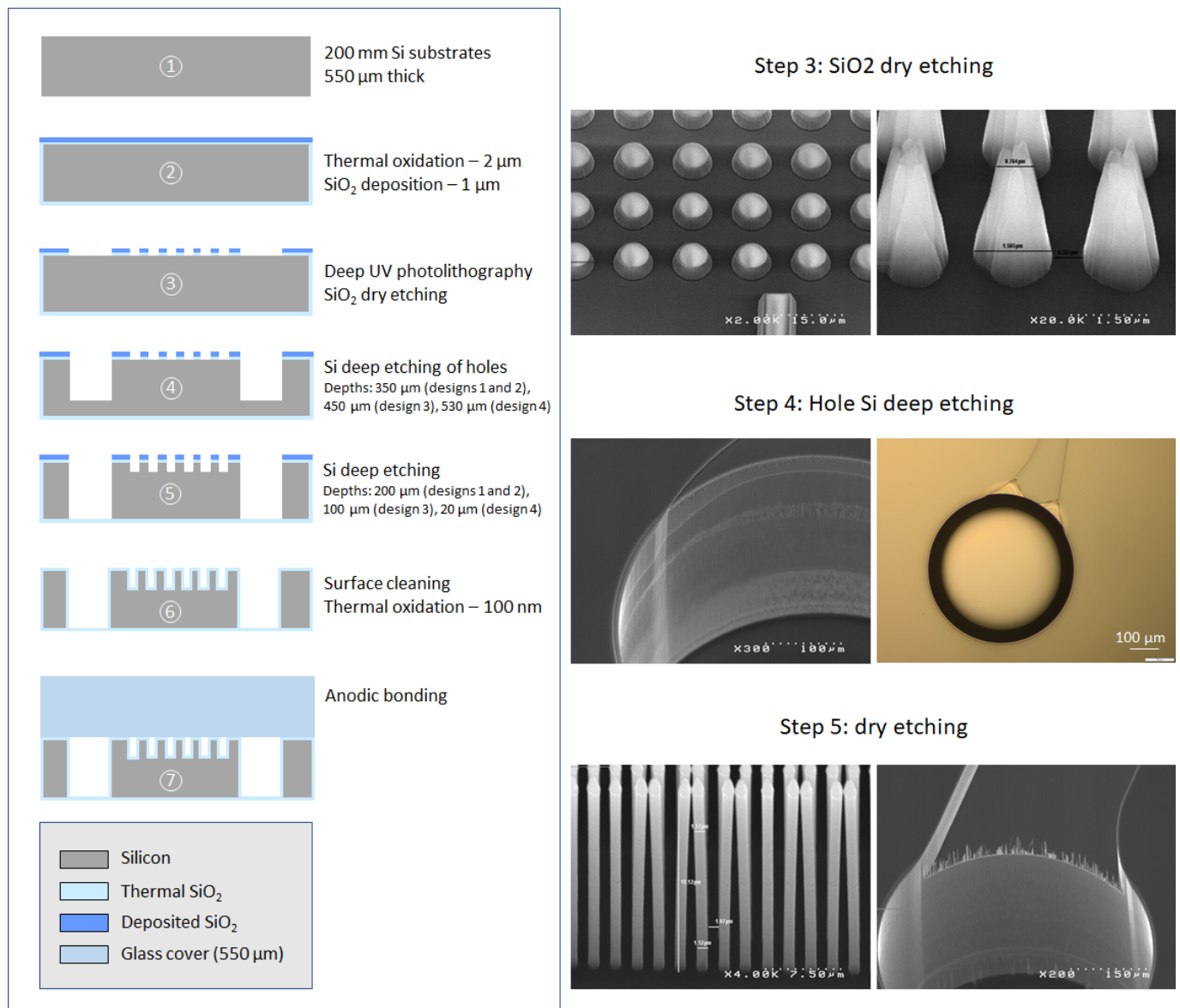


Figure 2.32: Main fabrication steps for the version 1 DLD devices with corresponding SEM and optical images for steps 3, 4 and 5.

2.5.2 Fabrication Process Flow: Improvements

A new fabrication flow has been implemented (39 steps) to avoid the issues encountered for the first version of DLD devices fig. 2.33.

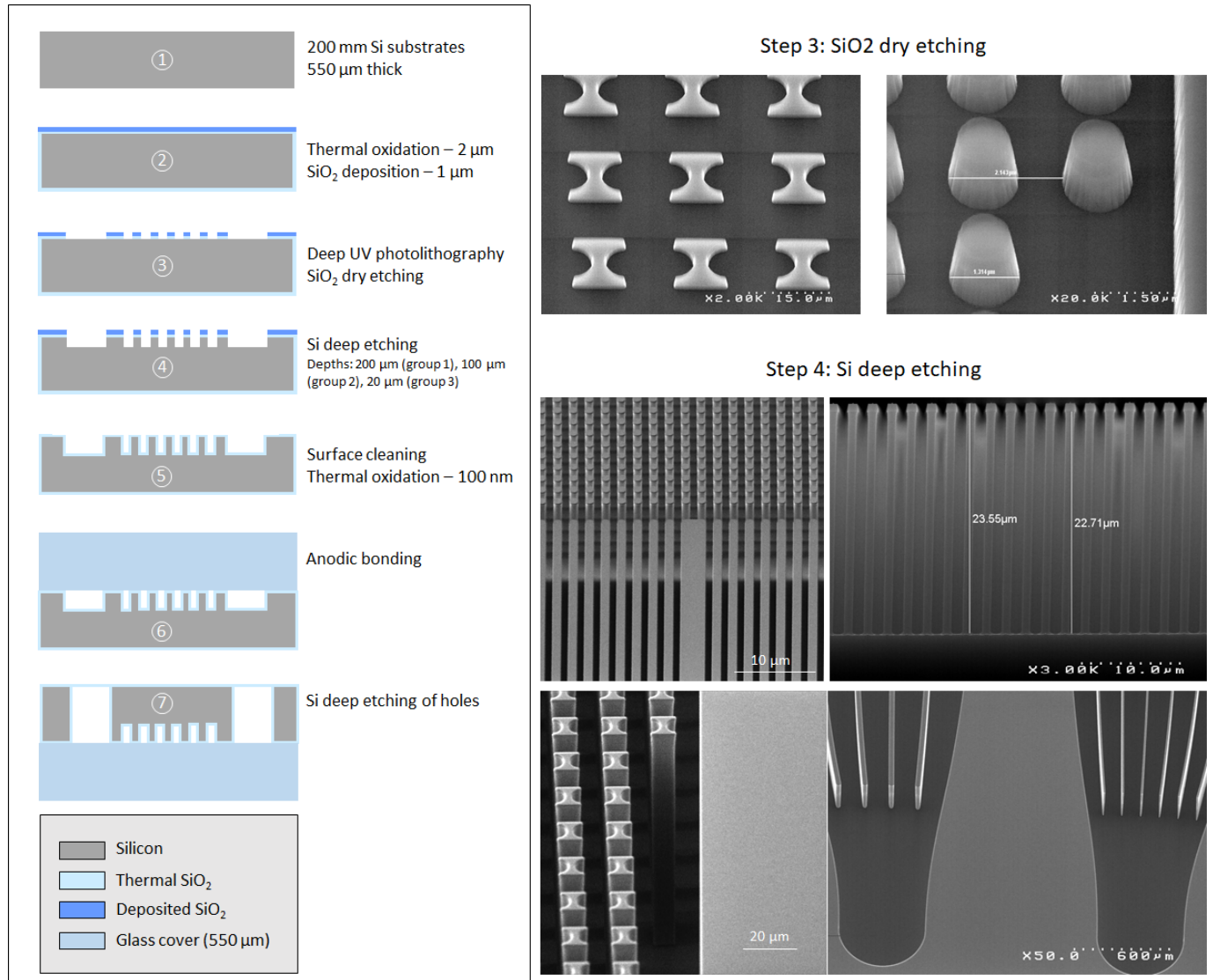


Figure 2.33: Main fabrication steps for the version 2 DLD devices with corresponding SEM images for steps 3 and 4.

As for version 1, contact photolithography and RIE are used to define the features of the fluidic channels and ports on a 3 μm -thick silicon dioxide hard mask (2 μm thermal SiO_2 followed by a deposition of 1 μm SiO_2). In this case, fluidic channels are first etched using deep UV photolithography and RIE, after hard mask etching. At the same time, fluidic ports are etched with the same depth as the channels (20 μm to

200 μm , according to the DLD group). After removing the oxide and cleaning the substrate, a 100 nm thick thermal oxide layer is grown prior to seal the top 550 μm -thick borosilicate glass cover by anodic bonding. Then, the holes are etched from the other side to open the fluidic ports until the glass cover. The wafers are then diced into 22 mm \times 60 mm individual chips containing 6 DLD devices. This new fabrication flow was fully satisfactory and enabled to avoid previous issues of residual silicon and fragile pillars.

2.6 Packaging

Effective packaging of microfluidic chips is required to simplify fluidic control and user manipulation. In our case the chips are packaged on a custom COC (Cyclic Olefin Copolymer) Fluidic Circuit Board (FCB) with female luer connectors. The FCB is composed of two COC cartridges: a bottom cartridge with the fluidic channels and a cover cartridge with the holes at the chip position and the luer connectors. Both cartridges are micromachined with an M07 Datron machine and thermally sealed. The cartridges have a standard credit card format and 600 μm -holes to connect to the 500 μm -holes in the silicon chips. The channel cross-section is 500 μm \times 500 μm . A plug and play solution has been developed in our laboratory by F. Boizot and N. Verplanck (pending patent DD16965) to connect the silicon chip to the plastic cartridge, by using magnets and silicone gaskets (fig. 2.34). A magnetic frame is connected to magnets located in the cartridge and ensures sealing between the chip and the cartridge holes thanks to two silicone gaskets located at the inlet and outlet ports. The use of magnets enables at the same time to align the chip on the cartridge and to apply a constant and homogeneous pressure on the gaskets. This packaging solution is very convenient, as it enables to connect any DLD chip to the same cartridge. This was also possible thanks to the standardization of the hole placement for all the different DLD designs.

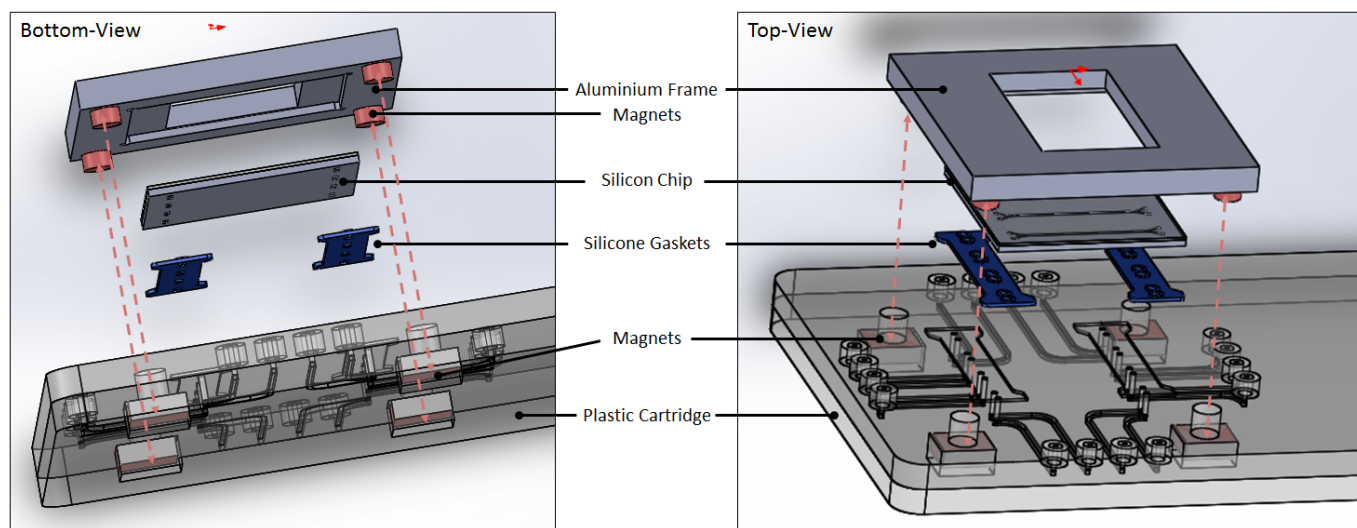


Figure 2.34: Exploded view of the assembly between the plastic cartridge, the silicon chip and the magnetic frame for fluidic connections and sealing between the chip and the cartridge.

For input pressures higher than 2 bars, fluidic leakage was observed at the luer connections and the silicone gaskets between the chip and the cartridge. Input pressures up to 6 bars were required to obtain acceptable flow rates in the version 2 group 1 DLD devices. In this case, a specific packaging solution with screws has been developed (fig. 2.36). A single aluminium frame enables, at the same time, to connect the tubings and the chip to the cartridge. Silicone gaskets are also used at the position of holes between the chip and the cartridge.

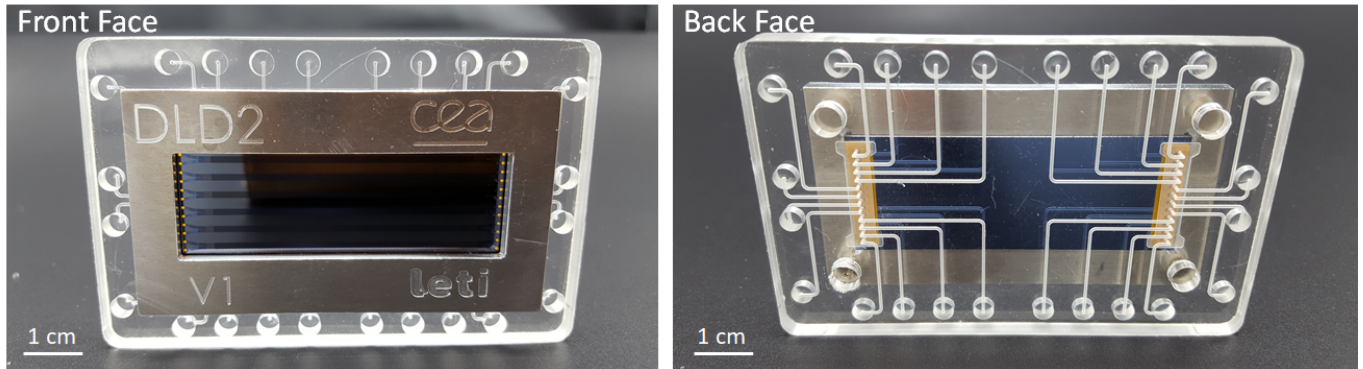


Figure 2.35: Pictures of our packaged chips (front and back sides).

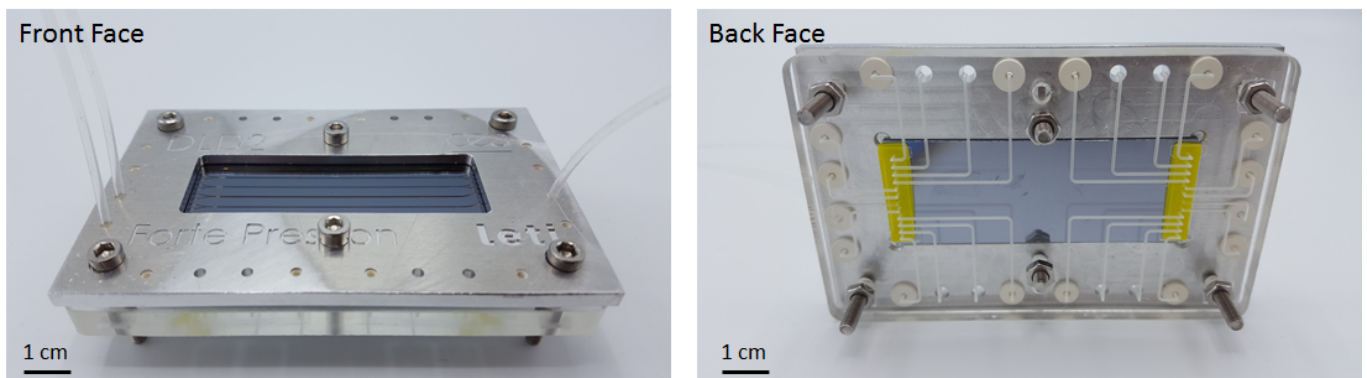


Figure 2.36: Pictures of our packaged chips for input pressures higher than 2 bars (front and back sides).

Chapter Summary: Development of DLD Devices

- Finite element models on COMSOL Multiphysics were used to identify optimized DLD designs for particle separation.
- The pillar shape was numerically shown to influence the critical diameter (D_c) in addition to the inter-pillar spacing and slant angle. A predictive model was proposed for the value of D_c according to the different pillar shapes and orientations. Triangular and hexagonal pillars were identified to decrease D_c for similar other geometrical parameters compared to circular pillars.
- Anisotropy in DLD arrays was quantified for elongated pillars, according to the orientation of the pillars and the array and the inter-pillar spacings. The anisotropy effect was shown to improve particle separation and enable multi-separation of tens of particle populations with similar sizes.
- The three versions of our DLD devices were presented with improvements, such as the channel dimension, pillar shapes and inlet sub-channels.
- The microfabrication flow was presented with improvements between the first and the second versions of our DLD devices.
- An innovative packaging solution with magnets was presented to plug silicon chips on plastic cartridges.

Résumé du Chapitre : Développement des dispositifs de DLD

- La modélisation numérique par éléments finis de la séparation de particules par DLD (COMSOL Multiphysics) a permis d'identifier les designs optimisés pour le tri de différents types de composants biologiques.
- La forme des piliers s'est révélée être un paramètre important dans la détermination du diamètre critique de séparation (D_c), en plus des paramètres généralement considérés, tels que la distance inter-piliers et l'angle d'orientation du réseau. Un modèle prédictif a été proposé afin d'intégrer les paramètres de forme et d'orientation des piliers dans la détermination du diamètre critique. En particulier, il a été montré que les piliers triangulaires et hexagonaux permettent de diminuer la valeur du diamètre critique, en comparaison avec les piliers circulaires (tout autres paramètres géométriques restant égaux par ailleurs).
- L'anisotropie des canaux de DLD a été quantifiée dans des réseaux de piliers allongés, en fonction de trois paramètres : l'orientation des piliers, l'orientation du réseau de piliers, et la distance inter-piliers. L'effet d'anisotropie s'est avéré particulièrement intéressant pour améliorer l'efficacité de séparation des particules, ainsi que pour permettre la multi-séparation de dizaines de populations de particules dans un seul et même dispositif de DLD.
- Trois versions de designs de DLD ont été implémentées, avec des améliorations progressives en termes de dimensions du canal, de formes de piliers, de géométries des accès fluidiques et de fonctions complémentaires au tri.
- Les technologies de microfabrication ont été présentées et optimisées entre la première et la deuxième versions de dispositifs de DLD.
- Une solution innovante de packaging, basée sur le maintien magnétique de la puce sur la cartouche fluidique, a été développée pour assurer l'étanchéité de nos dispositifs de façon rapide et robuste.

Validation of the DLD Separation with Beads

Introduction: Validation of DLD Separation with Beads

- In Chapter 2, DLD designs were selected from numerical studies and fabricated with silicon-based microtechnologies. A new packaging solution was proposed to enable a time-effective and user-friendly testing procedure.
- In this Chapter, the different designs of the first and the second versions of DLD devices are characterized with model microbeads.
- Several characteristics are evaluated and compared to the literature, such as the critical diameter (D_c) and recovery yield.
- The influence of the asymmetry of the inter-pillar spacings, as well as the pillar shape, is also evaluated.
- In addition to the classical geometrical parameters introduced in predictive models for D_c (that are the inter-pillar spacing G and slant angle θ), the number of pillars in the channel width (N_c) is also introduced here to fully anticipate the critical diameters obtained in our DLD devices.

3.1 Experimental Section

Monodisperse fluorescent polystyrene beads (ThermoFisher Scientific, Fluoro-Max Dyed Green Aqueous Fluorescent Particles) of different sizes are used to characterize the DLD devices. As recommended by the manufacturer, the beads are suspended in a 1 % surfactant solution (Tween 20, Sigma-Aldrich) in filtered DPBS (Life Technologies, 14190144) in order to prevent particle aggregation. Before injecting the bead solution, the chips are flushed with ethanol to remove any inter-pillar air bubbles. In order to decrease the adhesion of beads on the DLD pillars and walls, several surface treatments were tested on oxidized silicon samples (results in Appendix 4). Since no improvement was obtained with the tested surface treatments, the DLD chips were used without any chemical modification. So, the surface characteristics of the silicon oxidized pillars are: contact angle = $25^\circ \pm 5$, RMS rugosity < 1 nm, zeta potential = $-80 \text{ mV} \pm 10$. However, we should keep in mind that the high (1 %) surfactant concentration added to the beads may slightly modify these parameters.

The experimental setup is described in fig. 3.1. Imaging is performed by epifluorescence microscopy (Olympus, BX60) with a built-in 100 W mercury lamp (Osram, HBO 103W/2). A standard FITC (fluorescein isothiocyanate) filter cube (Olympus, U-MSWB2) is used to detect fluorescent beads. Imaging

is performed with a monochrome fluorescence CCD camera (Olympus, XM10) or with a digital CMOS camera (Hamamatsu, Flash 4.0 LT+). Sequences of images are overlaid and analyzed with ImageJ software to visualize the trajectory of particles flowing in the DLD channel. Fluids are actuated by a pressure-based flow controller (Fluigent, MFCS-EZ) with input pressures from 50 mbar to 6 bar according to the DLD design in order to obtain a maximum flow rate of about 100 $\mu\text{L}/\text{min}$ in the pillar array. The flow rate is adjusted to obtain a Stokes flow and avoid any flow stream mixing. In the Stokes regime, the flow rate does not influence the critical diameter [330].

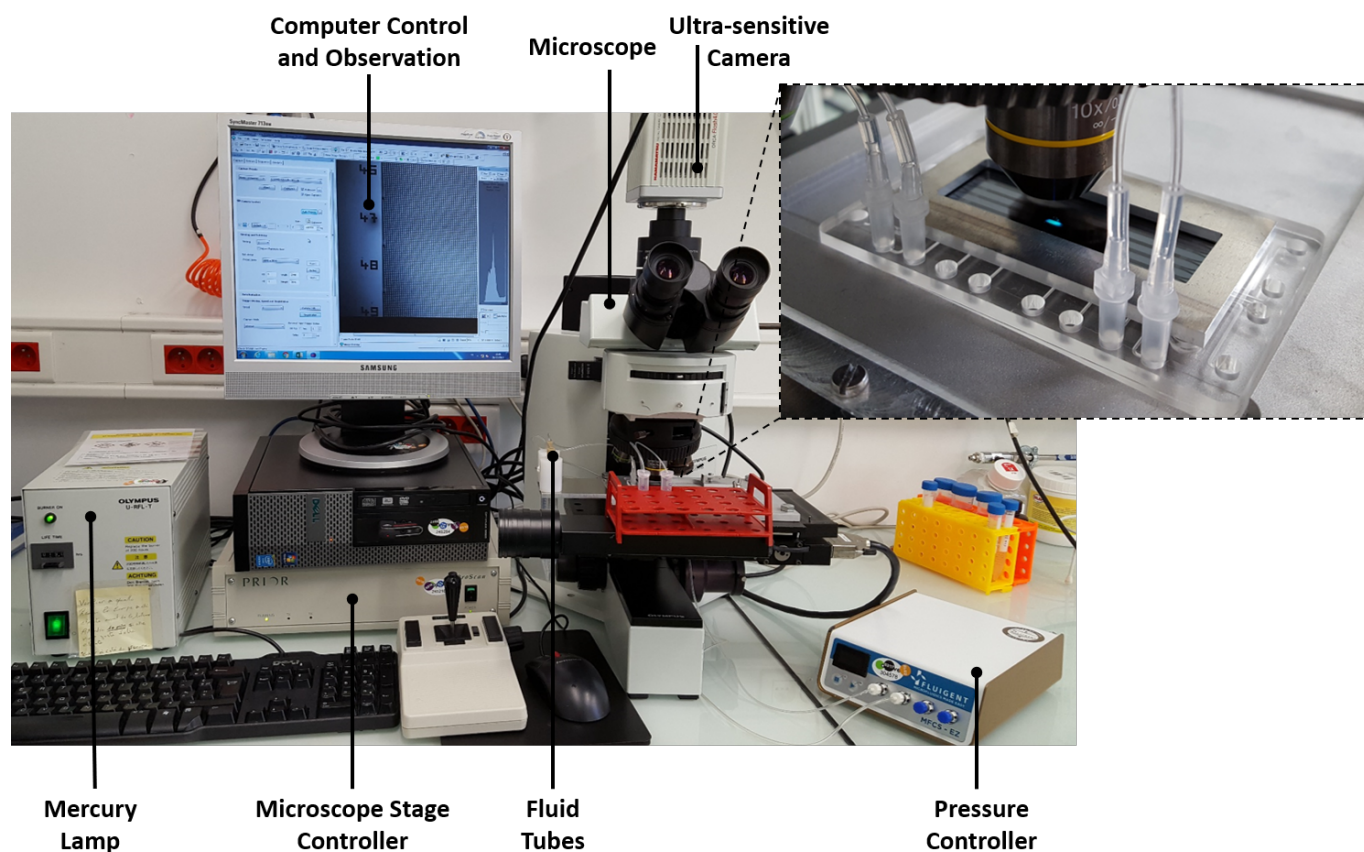


Figure 3.1: Experimental bench: global view and close-up view on the microfluidic cartridge located under the microscope.

3.2 Characterization of our DLD Devices

3.2.1 Determination of the Critical Diameters

An approximation of the experimental critical diameter was evaluated for each device by monitoring the trajectory of fluorescent polystyrene beads of different sizes. Typical zigzag and displacement trajectories observed experimentally are illustrated in fig. 3.2. The critical diameter is defined as the smallest bead

diameter for which the trajectory is a total displacement (particles deviated along the entire slanted array). The uncertainty on the critical diameter is determined by the size of available beads that could be injected in our DLD devices. The obtained results are given for each design of the first and the second versions in Appendix 5. Table 3.1 summarizes the obtained critical diameter (D_c) for each DLD device and fig. 3.3 (a) compares our experimental results to the D_c values predicted by Davis et al. [326].

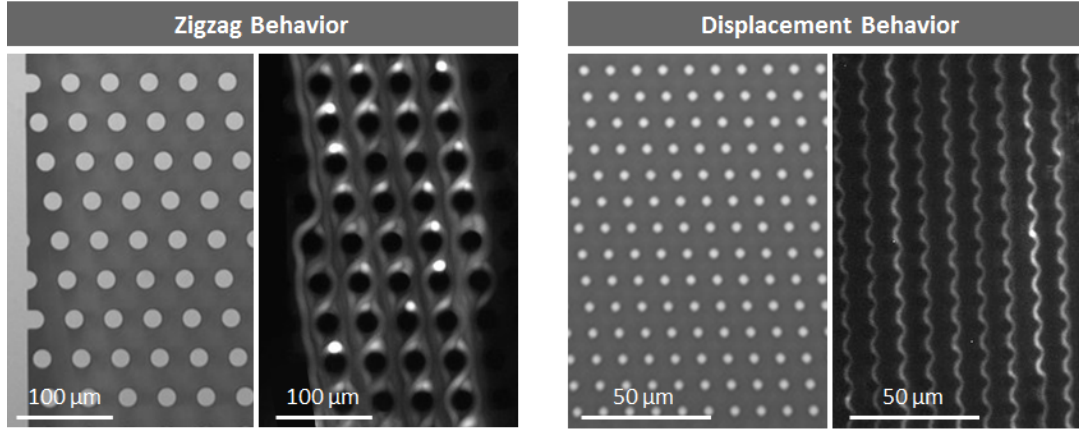


Figure 3.2: Observation of the zigzag (left) and displacement (right) trajectories of fluorescent beads and corresponding bright-field images.

Table 3.1: Experimental critical diameters (D_c) obtained for each DLD design from observations of the trajectory of fluorescent beads along the channel.

Device	Pillar Shape	D_p (μm)	G_y (μm)	G_x (μm)	N	Davis D_c (μm)	Exp. D_c (μm)
V1 Design 1	Circles	60	60	60	22	19	30
V1 Design 2 Section 1	Circles	20	20	20	5.7	12	15
V1 Design 2 Section 2	Circles	20	20	20	13.3	8	[10;15]
V1 Design 2 Section 3	Circles	20	20	20	50	4	[5;10]
V1 Design 3 Section 1	Circles	5.5	5.5	5.5	7.9	2.9	[3;5]
V1 Design 3 Section 2	Circles	5.5	5.5	5.5	18.3	1.9	3
V1 Design 3 Section 3	Circles	5.5	5.5	5.5	110	0.8	[1;2]
V2 Group 3 Design 4	Circles	30	30	30	15	11	15
V2 Group 3 Design 3	Circles	20	20	20	15	8	[5;10]
V2 Group 3 Design 2	Circles	15	15	15	15	6	[5;10]
V2 Group 3 Design 6	Circles	15	15	7.5	15	No Model	[5;10]
V2 Group 3 Design 1	Circles	11	11	11	15	4	[5;10]
V2 Group 3 Design 5	Circles	11	11	5.5	15	No Model	[5;10]
V2 Group 2 Design 2	Circles	9	9	9	30	2.5	[2;3]
V2 Group 2 Design 3	Circles	9	9	4.5	30	No Model	[2;3]
V2 Group 2 Design 1	Circles	5	5	5	40	1.2	NA*
V2 Group 1 Design 3	Circles	3	3	3	100	0.46	1
V2 Group 1 Design 2	Circles	2	2	2	100	0.31	[0.5;1]
V2 Group 1 Design 1	Circles	1	1	1	100	0.15	NA*

* The critical diameter of these devices could not be experimentally determined because of conditioning or flow rate issues.

From fig. 3.3 (a), the experimental evolution of the critical diameter with the array periodicity is in accordance with Davis' model, with a decrease of D_c/G as N increases. Experimental D_c values for version 1 devices are all higher than Davis' predicted values. As explained later in this Chapter, this shift is likely due to the limited channel width of these devices, which induces wall effects and intermediary modes of trajectory [392]. The same effect is observed in version 2 devices with the smallest channel width, such as Design 4 of Group 3 (30 μm -gaps) and Design 3 of Group 1 (3 μm -gaps).

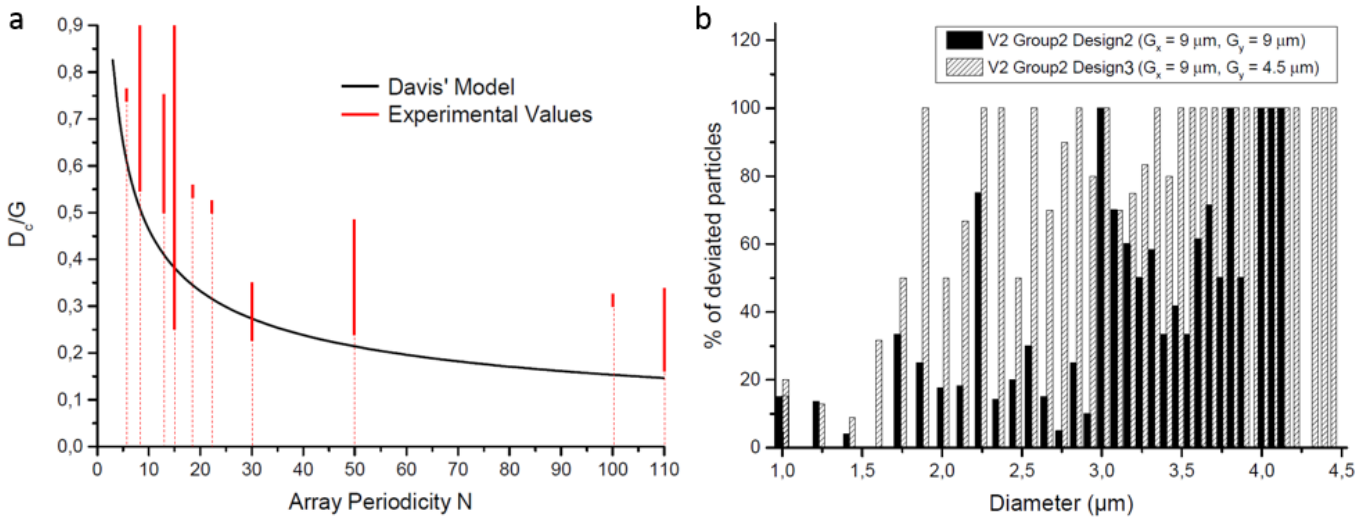


Figure 3.3: a) Comparison of our experimental values for D_c/G with Davis' model. The large uncertainty for the experimental results is due to the lack of intermediary bead sizes that could be tested. Therefore, extreme D_c/G values are given (particles in total zigzag or displacement modes), except when a transition mode could be observed with one bead size. b) Quantification of the percentage of output beads that are collected in the deviated outlet according to the bead size for symmetric and asymmetric inter-pillar spacings.

From the images of the bead trajectory (Appendix 5), no significant differences could be observed between devices with symmetric or asymmetric gaps (i.e. between Design 2 and Design 6 of Group 3 and between Design 1 and Design 5 of Group 3). However, the effect of asymmetric gaps appears on fig. 3.3 (b) that quantifies the ratio of deviated particles to the total number of output particles, according to the bead size. In this experiment, a mixture of beads with sizes from 1 μm to 4.5 μm (at the same concentration) is injected in Design 2 (symmetric gaps) and Design 3 (asymmetric gaps) of Group 2. **A decrease in the critical diameter is observed when the downstream gap is reduced.** Indeed, the first bead diameter for which 100 % of the particles are deviated is about 1.8 μm with Design 3 (reduced downstream gap), while it is about 3 μm with Design 2 (symmetric gaps). We will see in the next Chapter that the decrease of D_c with smaller downstream gaps is even more important with deformable and anisotropic biological particles.

3.2.2 Determination of the Recovery Yield

The recovery yield was determined with fluorescent optical counting and comparison between the number of beads in the injected initial sample and in the collected solutions at the DLD outlets. Figure 3.4 gives the obtained recovery yields according to the device geometry for the same bead mixture (a) and according to the bead size for a given device geometry (b). From these data, **the obtained recovery yields are all higher than 60 %**. As expected, for a given bead mixture, smaller recovery yields are obtained when inter-pillar spacings decrease (Designs 1 and 3 compared to Design 2 of Group 2 in fig. 3.4 a). In addition, triangular, hexagonal and I-shaped pillars seem to capture more beads than circular pillars (Designs 4, 5 and 6 of Group 2 compared to Design 2 Group2). Figure 3.4 (b) shows a correlation between the recovery yield and the ratio of the inter-pillar spacing to the bead diameter. Unexpectedly, the recovery yield seems to decrease for smaller particles, with a given inter-pillar gap. Therefore, it appears that **smaller beads likely adhere more easily to the pillars and/or to the cartridge channels, leading to a decrease in the number of collected particles.**

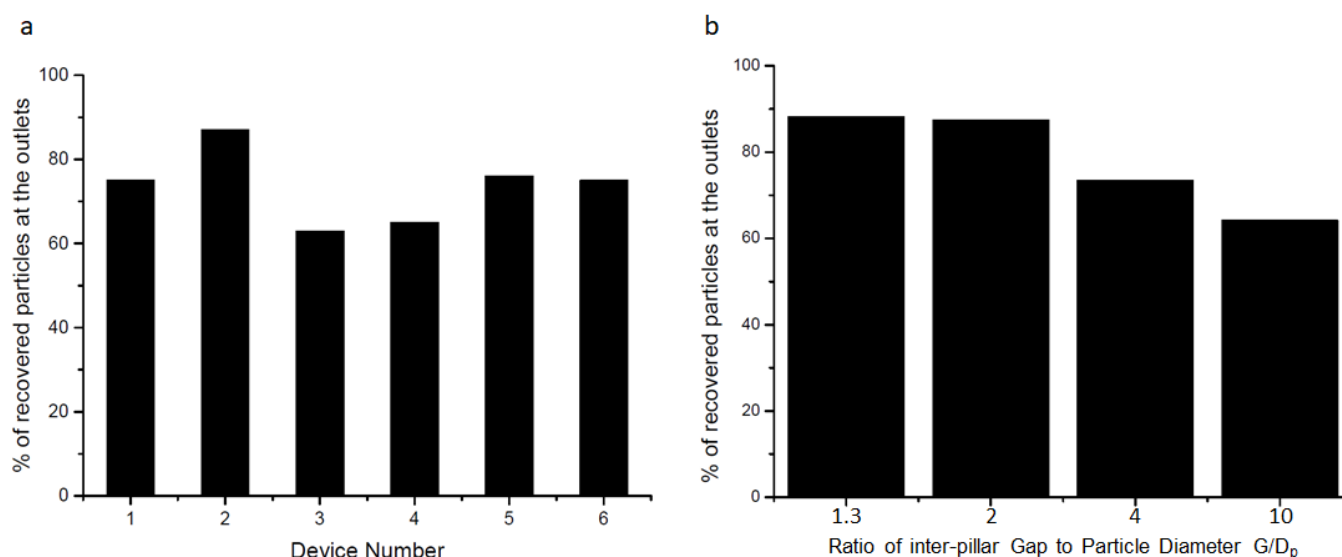


Figure 3.4: Quantification of the recovery yield for the DLD devices of group 2 and group 3 of version 2: (a) Percentage of collected particles in the 6 designs of group 2 by injecting a mixing of 1, 2 and 3 μm -beads (b) Percentage of collected particles in design 3 of group 3 by injecting successively 2, 5, 10 and 15 μm -beads.

3.2.3 Focus on “Nano-DLDs”

Nano-DLDs refer to the DLD devices with **submicronic critical diameters**. Three nano-DLD devices were experimentally available (Designs 1, 2 and 3 of Group 1, Version 2), with theoretical diameters ranging from 150 nm to 450 nm. These designs were initially implemented in the perspective of separating EVs. However, several limitations were encountered with the available nano-DLD devices, that made their characterization challenging, even for the first testing with model nanobeads. This section presents the

two main challenges to the characterization of our nano-DLD devices - limited flow rates and wall effects - before presenting the preliminary results that could still be obtained with some of the nano-DLD designs.

Limitation 1: Reduced Flow Rates

The first limitation to the testing of the nano-DLD devices is the **very limited flow rates** (in the range of 0.1 - 1 $\mu\text{l min}^{-1}$) that can be achieved at these dimensions. Achieving smaller critical diameters requires to decrease the inter-pillar spacings (G), which also strongly increases the hydraulic resistance of DLD arrays. Indeed, the critical diameter of DLD devices is linearly proportional to G, while the resistance is inversely proportional to the square of G, as suggested by the approximated formula for resistances of DLD channels (with length L, width W and height H), proposed by Davis [326] as a fit on simulations:

$$R = 4.6 \frac{\mu L}{W H G^2} \quad (3.1)$$

From this model, we propose a refined estimation of the hydraulic resistance in order to better anticipate the flow rate values when designing new DLD devices. A reliable model will enable to get an optimized set of nano-DLD parameters to obtain at the same time the smallest possible critical diameter and the largest flow rate.

New model for DLD hydraulic resistances:

Hydraulic resistances were evaluated with our COMSOL numerical simulations: a given flow velocity is applied at the entrance of the pillar array of interest, and the pressure loss across the entire array is measured. The ratio of the pressure loss to the flow rate gives the hydraulic resistance corresponding to the studied pillar array. A numerical evaluation of the resistance was performed on version 2 DLD designs (fig. 3.5). Groups 2 and 3 were tested to compare experimental values of the hydraulic resistance with the proposed model. This model will then be further used for nano-DLD design optimization. **Comparison between Davis' resistance model and numerical results gives poor correspondence, with errors above 60 %** (fig. 3.6). Therefore, a new model for the resistance was proposed in our laboratory by Léopold Virot, postdoctoral researcher at CEA Leti, by assuming a parabolic flow between the pillars and a high aspect ratio. In the approximated formula below, D_p is the pillar diameter, H is the channel height, W is the channel width, G_L is the lateral gap, G_D is the downstream gap, N_L is the number of pillars along the length of the array ($N_L = \frac{L}{G_D + D_p}$) and N_W is the number of pillars along the width of the array ($N_W = \frac{W}{G_L + D_p}$).

$$R = N_L \left(\frac{12 \mu D_p}{N_W G_L^3 H} \left(1 - 0.63 \frac{G_L}{H} \right)^{-1} + \frac{12 \mu G_D}{H^3 W} \left(1 - 0.63 \frac{H}{W} \right)^{-1} \right) \quad (3.2)$$

This new model is a better fit of our numerical results for the resistances of DLD arrays compared to Davis' model, with errors below 10 % for most evaluated cases (fig. 3.6).

Device	D_p (μm)	G_D (μm)	G_L (μm)	H (μm)	N	W (μm)	L (μm)
Group 1 Device 1	1	1	1	20	100	360	44000
Group 1 Device 1	1	1	1	30	100	360	44000
Group 1 Device 2	2	2	2	20	100	360	44000
Group 1 Device 2	2	2	2	30	100	360	44000
Group 1 Device 3	3	3	3	20	100	360	44000
Group 1 Device 3	3	3	3	30	100	360	44000
Group 2 Device 1	5	5	5	100	40	1100	44000
Group 2 Device 2	9	9	9	100	30	1100	44000
Group 2 Device 3	9	4.5	9	100	30	1100	44000
Group 3 Device 1	11	11	11	200	15	2500	44000
Group 3 Device 2	15	15	15	200	15	2500	44000
Group 3 Device 3	20	20	20	200	15	2500	44000
Group 3 Device 4	30	30	30	200	15	2500	44000
Group 3 Device 5	11	5.5	11	200	15	2500	44000
Group 3 Device 6	15	7.5	15	200	15	2500	44000

Experimentally tested devices

Figure 3.5: Parameters of the DLD arrays for which the resistance is numerically evaluated. A blue highlight gives the devices that were experimentally tested.

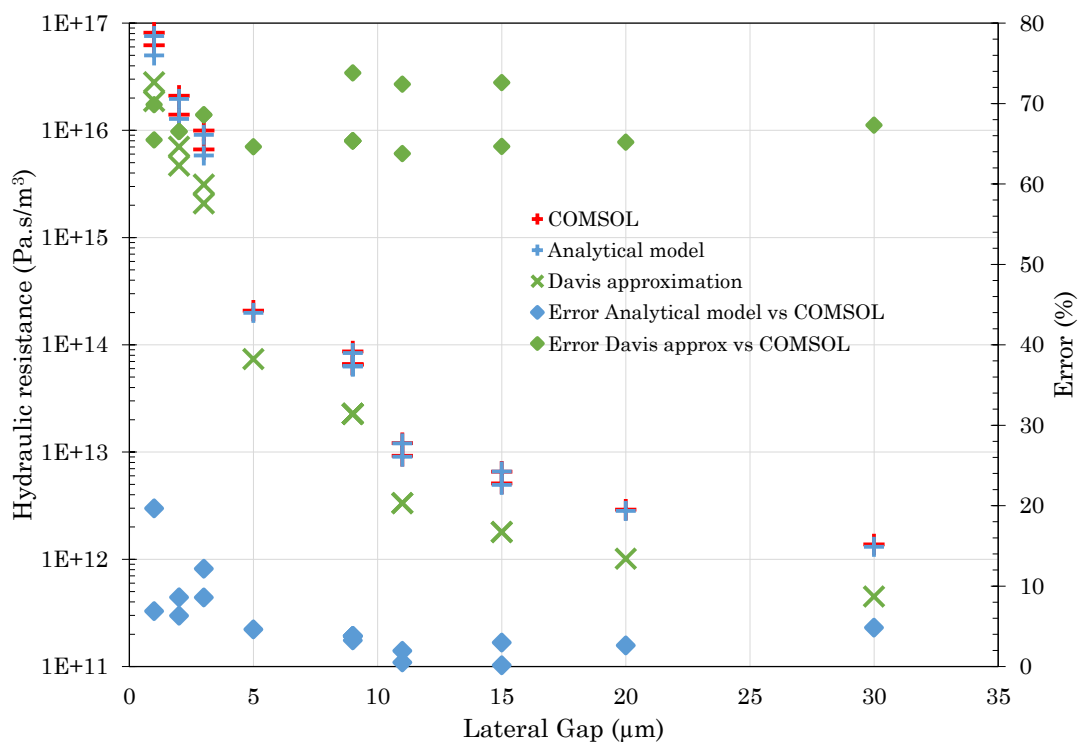


Figure 3.6: Comparison of Davis’ model and Léopold Viro’t’s model to COMSOL resistances and relative errors.

The resistance of some of our DLD devices (highlighted in blue in fig. 3.6 a) was experimentally determined and compared to Léopold Virót’s analytical model (fig. 3.7 a). The error between the model and the experimental data strongly depends on the design and ranges from about 4 % to 55 % (for each design, this error is determined for both extreme values of experimental resistance, which gives two error values for each experimental point). However, **for most devices, the error between model and experiment is of the same order of magnitude as the experimental variability (fig. 3.7 b), which suggests that this model is good enough to get a rough estimate of the resistance of DLD arrays.**

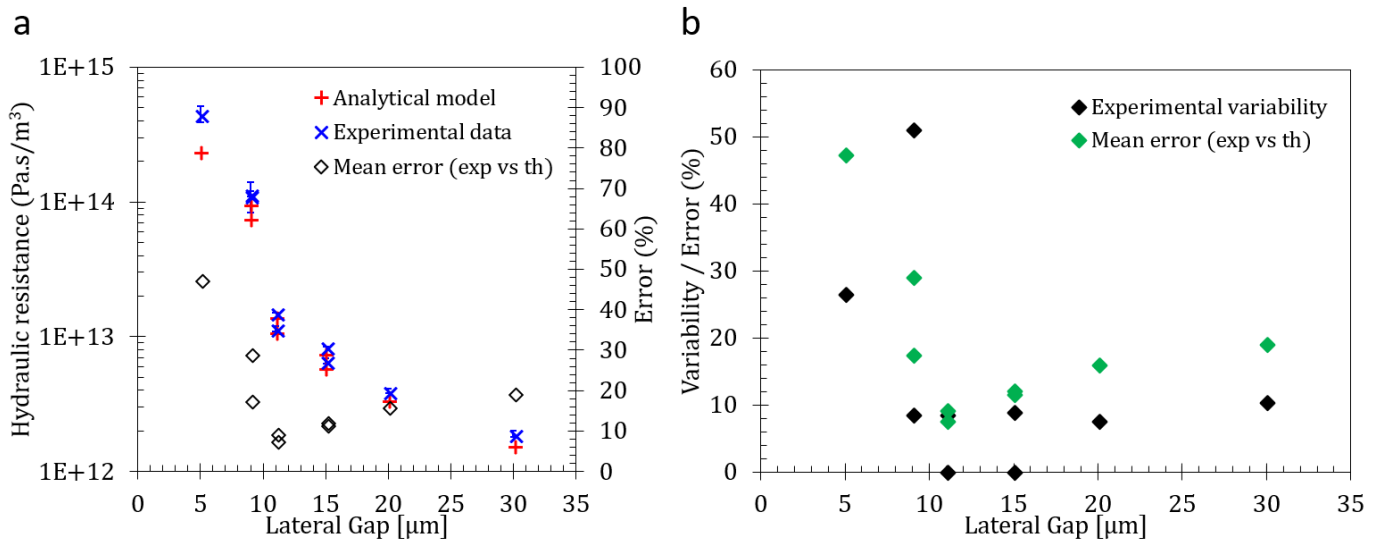


Figure 3.7: (a) Experimental and analytical (Virót’s model) values of resistance for the DLD arrays highlighted in blue in fig. 3.6 and representation of the error between each extreme experimental value and modeled values. (b) Comparison between experimental variability and experiment to model error for the resistance of the tested DLD arrays.

From Léopold Virót’s model it will be possible to optimize the DLD parameters in order to decrease the resistance for a given critical diameter. In particular, the formula for the resistance (eq. (3.2)) shows that the lateral gap is a critical parameter in the resistance value. This model shows good agreement with both experimental and numerical results. Typical values of flow rates obtained in nano-DLD devices are given in the next section.

Typical flow rate values in nano-DLD devices:

The values of flow rates for our nano-DLD devices obtained numerically and experimentally are given in table 3.2, for an input pressure of 6 bars (maximum pressure value that can be experimentally applied with our pressure controller):

Table 3.2: Numerical and experimental flow rates for a 6 bar input pressure (Group 1, Version 2).

Device	Numerical Flow Rate ($\mu\text{l min}^{-1}$)	Experimental Flow Rate ($\mu\text{l min}^{-1}$)
Design 1 (1 μm -pillars)	0.2	0.1
Design 2 (2 μm -pillars)	0.9	0.4
Design 3 (3 μm -pillars)	3.6	2.2

The lower flow rate values obtained experimentally compared to numerical predictions are probably due to the presence of air bubbles and clogged particles in the channels, that induce an increase in the hydraulic resistance of these channels. **The process of 100 μL of sample with these experimental flow rates takes about 17 hours** for design 1, 4 hours for design 2 and 45 min for design 3. Therefore, design improvements have to be implemented to increase the flow rate, especially for pillar gaps inferior to 2 μm . **The proposed model for DLD hydraulic resistances enables to identify the critical parameters of the pillar array (in particular the lateral gap and the channel height) to maximize the flow rate in nano-DLD devices.** Moreover, connecting the DLD channel in a bypass configuration would enable to accelerate the filling step of the nano-DLD channel. A large input channel could be filled with the sample very quickly before pressuring simultaneously both sides of the channel to force the sample to enter the pillar array.

Limitation 2: Trajectory Disturbance by the Channel Walls

With these devices, disturbance of the particle trajectory was induced by the channel walls. As shown by fig. 3.8, a wave particle trajectory is observed instead of the classical zigzag and displacement modes. This is due to the variation of the distance between the channel side walls and closest pillars along the DLD channel (shown in the close-up view of fig. 3.8). Therefore, at each new array period, a large gap (of about 3 G, where G is the inter-pillar spacing) appears on the channel side. This local enlargement induces the streamlines to be redirected towards the channel sides (where no pillars obstruct the fluidic pathway), which periodically attracts particles towards the walls (fig. 3.8).

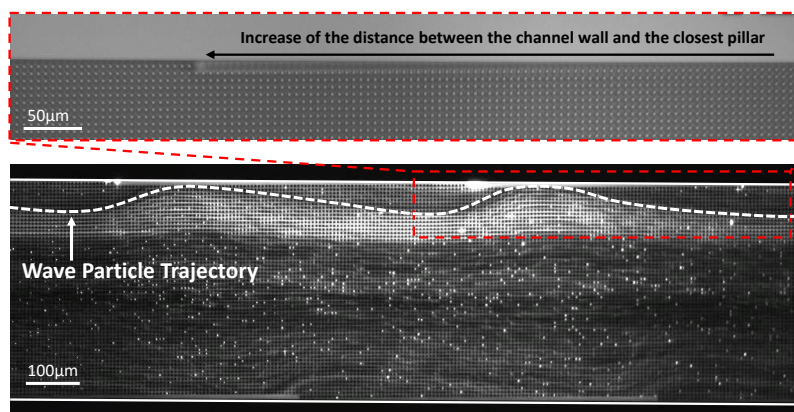


Figure 3.8: Trajectory of 2 μm fluorescent beads in an array of 3 μm -pillars (Design 3, Group1, Version2) and close-up view of the channel side in bright-field.

This wall effect is stronger in nano-DLD devices compared to the micro-DLD devices. Indeed, this wave-shape trajectory of deviated particles at high distance from the channel wall (more than 10 pillar columns) was not observed in the other tested DLD devices.

Wall effect in nano-DLD devices:

Disturbance of the particle trajectory is generated by the variations of the lateral velocity across the channel width due to irregular spacings between side pillars and channel walls. Figure 3.9 (a) shows the magnitude of the lateral velocity (orthogonal to the injection velocity) normalized to the total velocity magnitude. It is clearly observed that the lateral velocity is not constant across the entire pillar array. Larger velocity magnitudes are obtained at each array period, where the gap between side pillars and the channel wall changes abruptly. This may induce particles to move away from the channel wall, while they get closer to the walls where the lateral velocity has negative values, as observed in fig. 3.8. We clearly observe that velocity variations impact the entire channel width in the array of 3 μm -gaps (fig. 3.9 a), while it is limited to smaller pillar areas in the array of 9 μm -gaps (fig. 3.9 b). Therefore, with designs of larger inter-pillar spacings, disturbance of the particle trajectory is limited to a few pillar columns next to the channel walls, compared to the long-range influence with smaller dimensions.

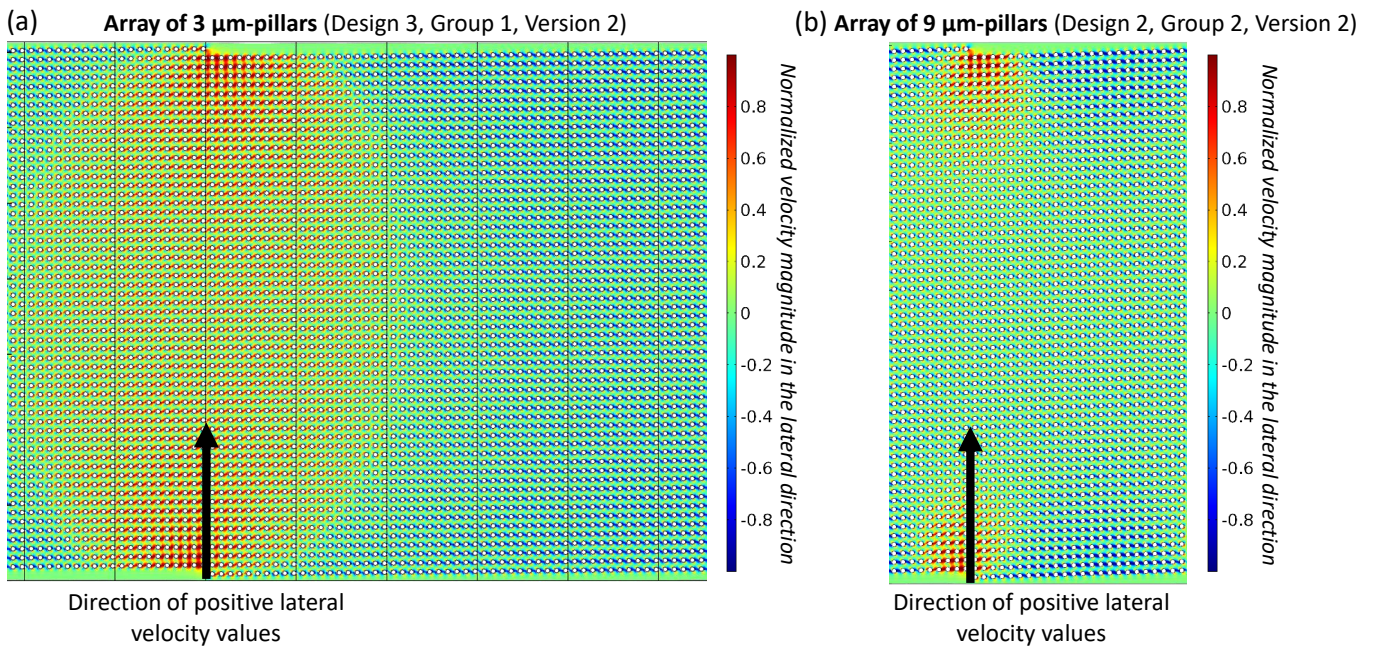


Figure 3.9: Mapping of the lateral velocity magnitude (normalized to the total velocity magnitude) in arrays of 3 μm (a) and 9 μm (b) gaps and pillar diameters.

Consequences on particle trajectories:

Because of this **wall effect**, large deviated particles cannot be completely focused on the top channel side, which **degrades the separation efficiency and induces an increase in the critical diameter compared to theoretical values** (as observed in table 3.1 for V2 Group 1 Designs 2 and 3). In order to avoid this behavior,

the next generation of DLD designs (version 3) will display **improved channel walls**, that follow the side evolution of the pillar array, with a **constant distance (G) between the extreme pillars and the walls**. This is achieved with undulatory channel walls, as shown in fig. 3.10. Improvements could still be made to obtain a completely uniform flow pattern in the entire DLD array, by moving the side walls of a specific amount at each pillar row, given by Inglis [393], that cancels the wall effect.

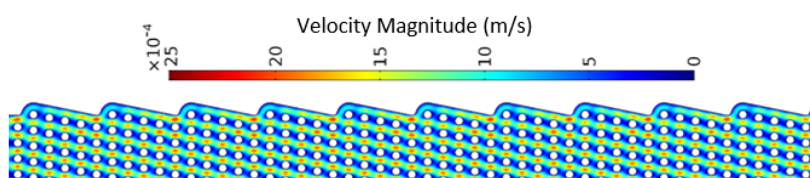


Figure 3.10: Numerical computation of the velocity magnitude in a DLD array with improved channel walls to avoid disturbance of the particle trajectory.

In addition to the channel walls, anisotropy also participates in modifying the value of the critical diameter compared to expected values from predictive models, as demonstrated in Chapter 2. In order to minimize anisotropy, another improvement that could be applied to current designs is the use of a rotated-square lattice instead of a row-shifted parallelogram lattice to build the pillar array, as suggested by Vernekar et al. [391].

Preliminary results for nano-DLD characterization:

Despite of the two main limitations introduced above (wall effect and flow rate), preliminary experiments were performed on our three available nano-DLD designs with model beads in order to quantify the performances and restraints of the current designs.

Design 3 (3 μm -pillars):

Fluorescent images of the particle trajectories in the array of 3 μm -pillars are given in Appendix 5. A summary table of the recovery yield and ratio of deviated particles is given in table 3.3 for several bead sizes. **This device enables to efficiently remove particles larger than 1 to 2 μm with recovery yields close to 100 % and a flow rate of about 2 $\mu\text{l min}^{-1}$.**

Table 3.3: Recovery yield and deviation efficiency of Design 3, Group 1, Version 2 (3 μm -pillars) for different bead sizes.

Bead Size	Recovery Yield	% of Deviated Beads
500 nm	73	49
1 μm	100	75
2 μm	93	98

Design 2 (2 μm -pillars):

Images of the trajectory of fluorescent beads in this device are given in Appendix 5. **Clogging issues** are

encountered at the inlet/outlet subchannels (fig. 3.11). This issue - that did not happen in the other devices with larger pillars - might be due to a lower velocity of particles in this channel of about 1 mm s^{-1} , arising from an increased hydraulic resistance of the DLD chip. Therefore, the flow rate might be not sufficient to drag the beads in the inlet subchannels and throughout the entire pillar array.

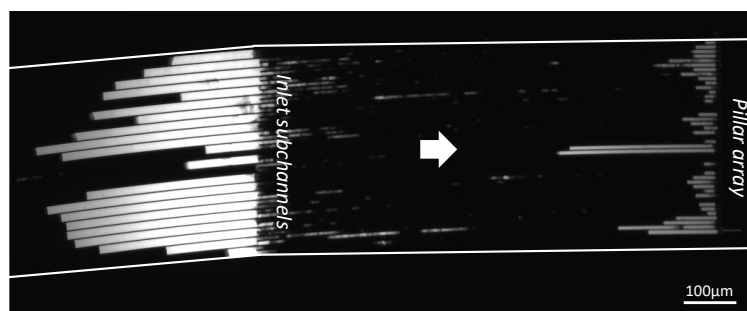


Figure 3.11: Clogging of fluorescent 500 nm-beads in the inlet subchannels of Design 2, Group 1, Version 2 ($2 \mu\text{m}$ -pillars).

Because of these clogging issues, 500 nm-beads could not be collected at the DLD outlets, which suggests that all the injected beads were blocked in the pillar array. However, $1 \mu\text{m}$ -beads were collected with a limited recovery yield of 30 %. This difference in the recovery yield might be due to velocity variations between the different bead populations according to their sizes. As represented in fig. 3.12, larger particles flow faster in the DLD array compared to smaller particles. Indeed, the zigzag trajectory length of non-deviated particles is longer than the deviated path, and it crosses areas of lower flow velocity (between the pillar rows). Therefore, because of the very low flow rate, 500 nm non-deviated beads must not have time to flow out of this DLD device during the duration of the experiment, while $1 \mu\text{m}$ deviated beads are partially collected.

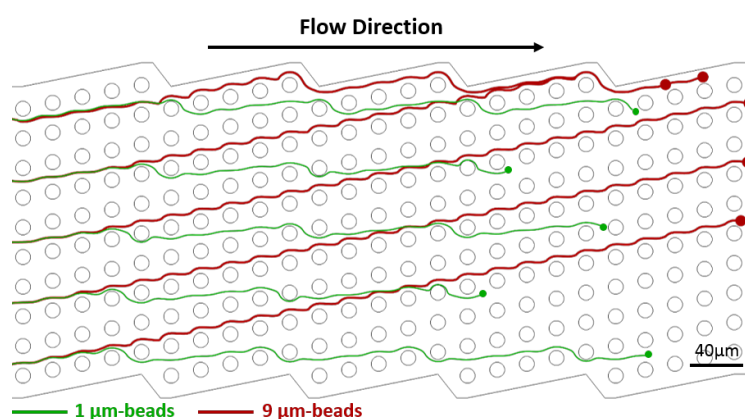


Figure 3.12: Numerical study of the trajectory of $1 \mu\text{m}$ (green) and $9 \mu\text{m}$ (red) particles in a DLD array with $D_p = G = 12 \mu\text{m}$ and $N = 5$. All particles are injected at the same time and same position. At the studied time point, large particles reach the channel outlet before smaller particles.

Design 1 (1 μm -pillars):

With this device, all the injected beads are stopped in the pillar array, because of their **extremely low velocity** (about 0.3 mm s^{-1}). Images in Appendix 5 show the stopped 500 nm-beads at the channel entrance, while no bead is observed further down in the channel.

In conclusion, only the design 3 (with 3 μm -pillars) is directly usable to remove most particles larger than 1 μm , even if the channel walls should be adapted to the shape of the pillar array to reach the predicted sub-micrometric critical diameter with this device. Design improvements are required to increase the flow rate of devices 1 and 2 in order to avoid particles from being stopped in the pillar array and reach larger recovery yields. **To overcome the nano-DLD limitations, an alternative solution to the design of a new DLD set is the capture of nanoparticles on larger microbeads before the separation [387]. This strategy enables to use pillar arrays with micrometer-sized features, which simplifies the fabrication process, increases the throughput and reduces diffusive effects.**

3.3 Influence of the Pillar Shape

From numerical studies presented in Chapter 2, the critical diameter was shown to be dependent on the pillar shape and orientation. In particular, a decrease in the critical diameter was observed with positive-slope triangles compared to circular pillars. This trend was confirmed experimentally with identical pillar arrays of circular or triangular pillars, with a shift of D_c from 5 - 10 μm with circles to 3 - 5 μm with triangles (fig. 3.13).

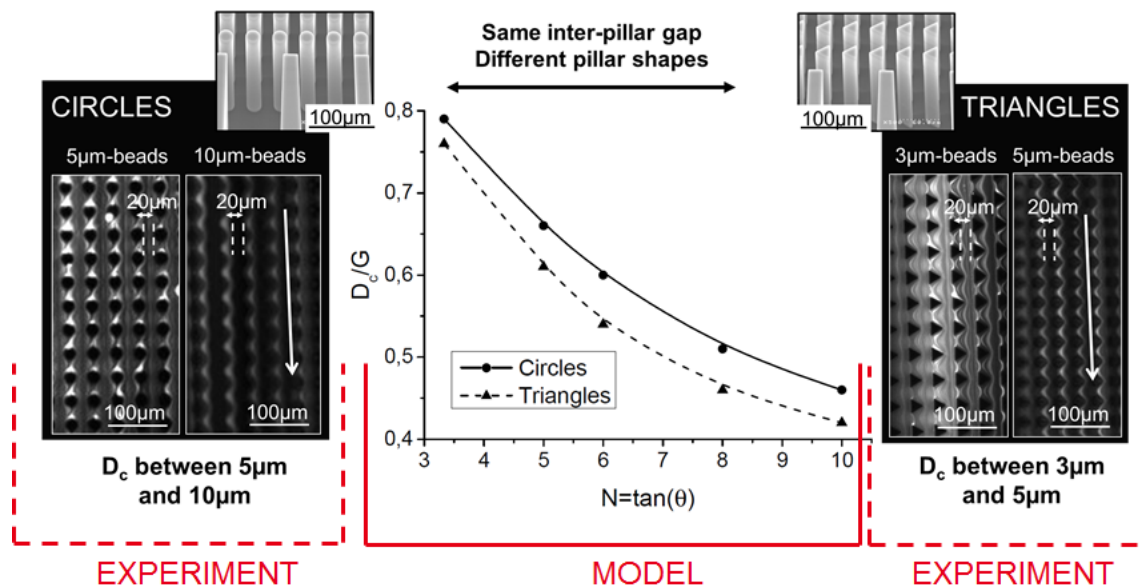


Figure 3.13: Numerical and experimental comparison of the critical diameter (D_c) obtained with circular or triangular pillars in the same arrays. A decrease in D_c is confirmed in both cases.

3.4 Influence of a New Parameter: the Channel Width

In addition to the classical zigzag and displacement modes, an **intermediary trajectory** was also observed in our DLD devices (version 1), with periodical zigzag and displacement areas along the pillar array. This intermediary behavior was amplified as the number of pillars along the channel width decreases. These experimental results were confirmed by numerical studies that showed that most particle sizes are subject to the intermediary mode.

Some previous studies have already shown the existence of two critical diameters and an additional "mixed" motion [327, 394]. However, in our case, it is demonstrated that there are actually as many critical diameters as the number of pillars in each periodic DLD lattice. A parametric model, supported by a Design Of Experiments (DOE), was developed to predict the values of these multiple critical diameters and the conditions required for the intermediary mode.

The intermediary mode was shown to appear when the number of pillars across the channel width (N_c) is not sufficient, which leads to wall effects. This situation is frequently encountered in DLD arrays. Indeed, reducing N_c enables to decrease the channel length. The miniaturization concern is important for DLD devices that are generally very long in order for the particles to be deviated enough. Our model enables to determine the smallest acceptable channel width to avoid intermediary modes of displacement. Indeed, **the intermediary mode degrades the sorting efficiency because particles of a given size are not directed in the same direction in the entire channel length.** Therefore, **this work shows how to reach a compromise between the miniaturization of the device and its efficiency** [392].

3.4.1 Multiple Critical Diameters in DLD Arrays

For a given pillar geometry, the value of the critical diameter has been shown to depend only on two geometrical parameters of the DLD array: the inter-pillar gap (G) and the periodicity (N) [324, 326]. Thus, as expected from previous theoretical models [324, 326], a given DLD design would result in a single value of D_c . In this section it is shown that a DLD design actually has several critical diameters, whose values depend on the position along the channel axis. Indeed, experiments supported by modeling highlight that **the trajectory of particles of a given size strongly depends on their axial position along the pillar array.**

An intermediary mode has been observed for some particle sizes, in which particles have a zigzag trajectory at specific locations in the DLD array, while they are displaced at other areas in the channel. The pattern of zigzag and displacement areas is observed periodically in the channel according to the N period, as illustrated on fig. 3.15 (b), with the trajectory of 13 μm fluorescent beads flowing from the left to the right side of the channel.

Only one period of pillars is shown in fig. 3.15 (b), as the particle behavior is periodic along the entire channel length. According to Inglis et al. [324], the critical diameter for this DLD geometry is about 15 μm . The same DLD channel is modeled with our finite element model and the streamlines are represented in red in fig. 3.15 (a). The exact same areas of zigzag or displacement modes are obtained in the numerical

(fig. 3.15 a) and experimental (fig. 3.15 b) results. It should be pointed out that the streamlines are represented in fig. 3.15 (a), while fig. 3.15 (b) shows the trajectory of the beads. Magnifications of the inter-pillar areas located inside the red dotted squares are represented in fig. 3.15 (c) and (d) showing different patterns of the streamlines in the numerical calculation. While the streamlines are clearly oriented downwards in the zigzag area (fig. 3.15 c), all the streamlines stay in the top side of the pillars in the displacement area (fig. 3.15 d).

The critical diameter was numerically determined from the position of the streamlines in the computed DLD channel. As represented in fig. 3.15 (e), the critical radius r_c at pillar 1 is the distance between the right edge of the pillar and the stall line that is stopped by pillar 2 (black bold line). The streamline orientation in fig. 3.15 (c) and fig. 3.15 (d) shows that larger critical diameters are obtained in the zigzag zones (fig. 3.15 c) while smaller critical diameters are obtained in the displacement zones (fig. 3.15 d). This suggests that the critical diameter in this device (Version 1, Design 1) is variable, even if the geometry of this pillar array is constant along the entire channel.

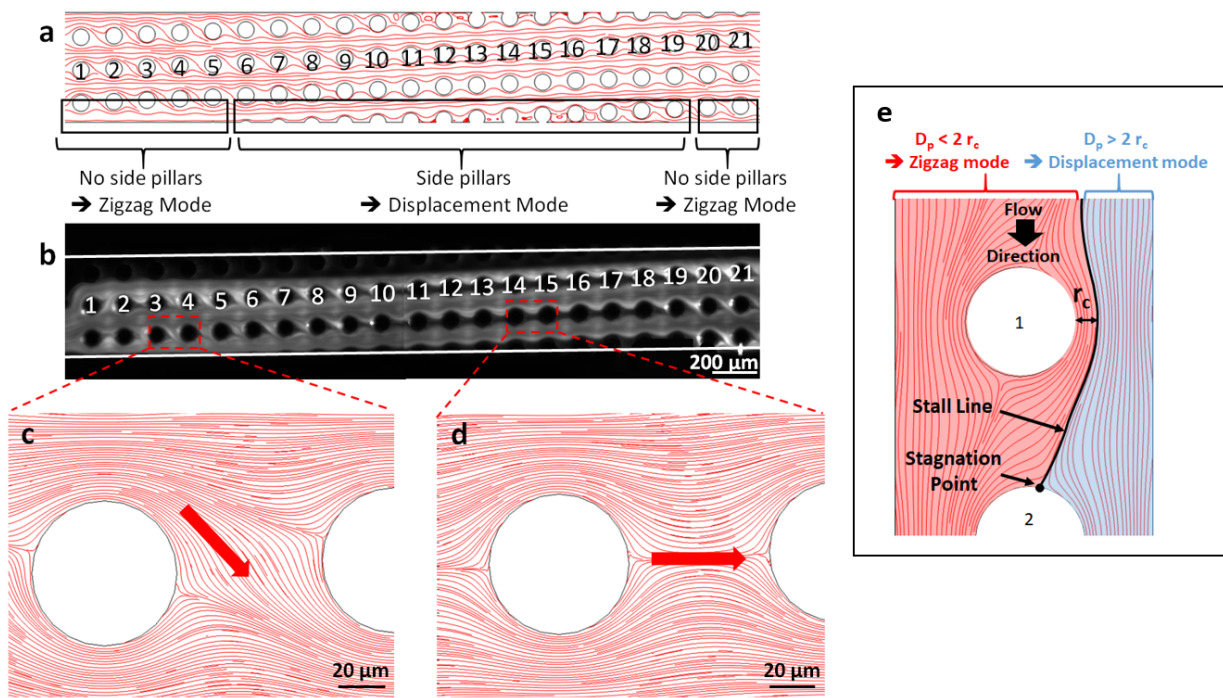


Figure 3.15: a) Modeling of Design 1, Version 1 ($G = 60 \mu\text{m}$, $N = 22$). b) Experimental image of $13 \mu\text{m}$ fluorescent beads flowing in the same device from the left to the right side of the channel. c) and d) Magnification of the calculated streamlines at the locations outlined by the red dotted squares in b. e) Representation of the numerical streamlines between two adjacent pillars. The stall line (black, bold) has zero velocity contact with pillar 2 (stagnation point). On the right-side of the stall line, the flow stream induces a displacement trajectory, while it induces a zigzag trajectory on the left-side of the pillar. The critical radius r_c is defined as the distance between the right edge of pillar 1 and the stall line.

An automated Matlab program was used to determine the position of the stall lines and compute the critical diameter at each pillar of the DLD array after determining the position of the stall lines. Briefly, in order to find the critical diameter at pillar 1 (fig. 3.15 e), our program first identifies the stall line at pillar 2 (fig. 3.15 e), from the coordinates of the computed streamlines. More precisely, we approximate the stall line as the closest streamline to the pillar 2 upper side, by computing each distance between the streamlines passing above pillar 2 and the top of pillar 2. Once the stall line at pillar 2 is identified, the program computes the distance between this same streamline and the top of pillar 1. This distance corresponds to the critical radius at pillar 1.

As the critical diameter is determined from the position of the stall line (fig. 3.15 e), increasing the number of streamlines improves the accuracy of the determination of D_c , which is illustrated with the studied device (Version 1, Design 1) (fig. 3.16 a). The optimal number of streamlines was validated before each D_c computation. Moreover, a mesh independence test was performed on the same geometry (fig. 3.16 b), for a given number of 1000 streamlines. Three mesh element sizes were considered: finer (element size between 0.2 μm and 11 μm), normal (element size between 0.8 μm and 18 μm) and coarser (element size between 1.6 μm and 35 μm). Similarly to the number of streamlines, the mesh size was optimized in the rest of the study.

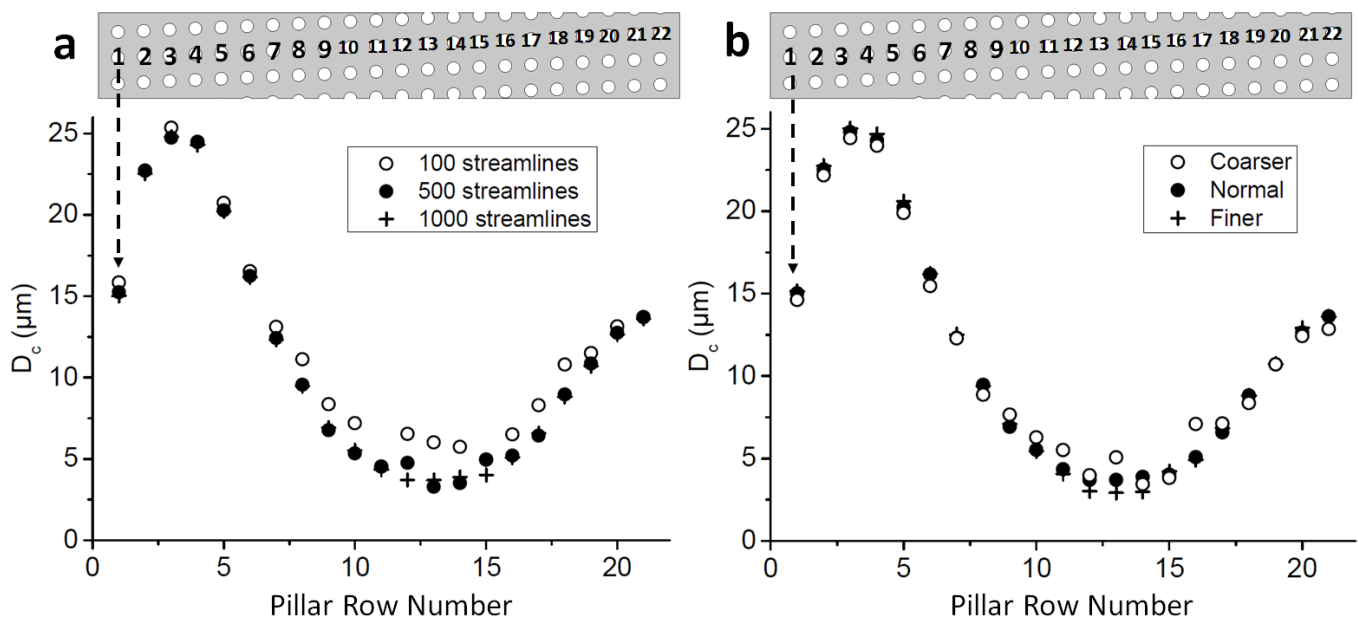


Figure 3.16: a) Variations in D_c determination accuracy in the studied device (Version 1, Design 1) for 100, 500 or 1000 streamlines in a constant stream width equal to 150 μm . The central column of pillars (second column) of the channel width is considered. b) Mesh independence test in the same device for three different mesh sizes: finer, normal and coarser. The central column of pillars (second column) of the channel width is also considered.

Figure 3.17 (d) represents the numerical critical diameter for each pillar row along the channel of the studied device (Version 1, Design 1). In the array period of 21 pillar rows, D_c varies from a few micrometers to more than 25 μm .

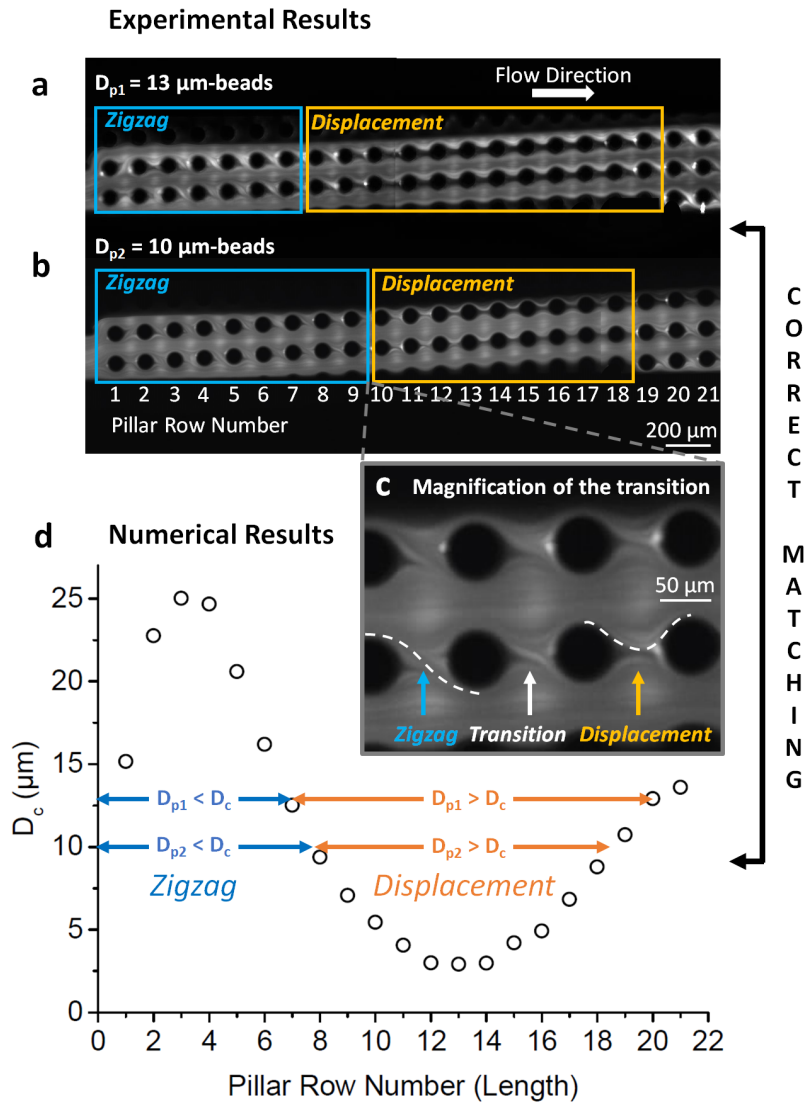


Figure 3.17: a) Experimental image of 13 μm polystyrene fluorescent beads flowing in the studied device (Version 1, Design 1) from the left to the right side of the channel. b) Experimental image of 10 μm polystyrene fluorescent beads flowing in the same device. c) Magnification of the transition area between the zigzag and the displacement domains in b). d) Numerically calculated evolution of D_c according to the pillar number along the DLD channel. The zigzag and displacement areas are represented in the two cases of 13 μm and 10 μm -beads. Good matching is found between experimental and numerical areas of zigzag and displacement modes for both particle sizes.

In this particular DLD geometry, D_c is not constant, which explains that the particle behavior varies while flowing along the DLD channel. The extent of the zigzag and displacement areas depends on the particle size. Particles have a zigzag mode at pillars where D_c is larger than the particle diameter, while they display a displacement behavior at pillars with smaller D_c . Figure 3.17 (d) shows that the ratio of zigzag areas to displacement areas increases when the particle size decreases. It is experimentally verified that 10 μm -beads display a larger zigzag area and a smaller displacement area than 13 μm -beads (fig. 3.17 a and b).

As our numerical model is in accordance with the experimental observations, we further study in the next section the variations of D_c along the DLD channel according to the main geometrical parameters: the inter-pillar gap (G), the array period (N) and the number of pillars in the channel width (N_c).

3.4.2 Influence of the Channel Width on the Intermediary Mode

From the periodic variation of D_c along the DLD channel, two extreme D_c values are defined: the minimum of D_c called D_{c1} and the maximum of D_c called D_{c2} (fig. 3.18). Only these two parameters will be considered in the rest of the study to characterize the DLD arrays of different geometries.

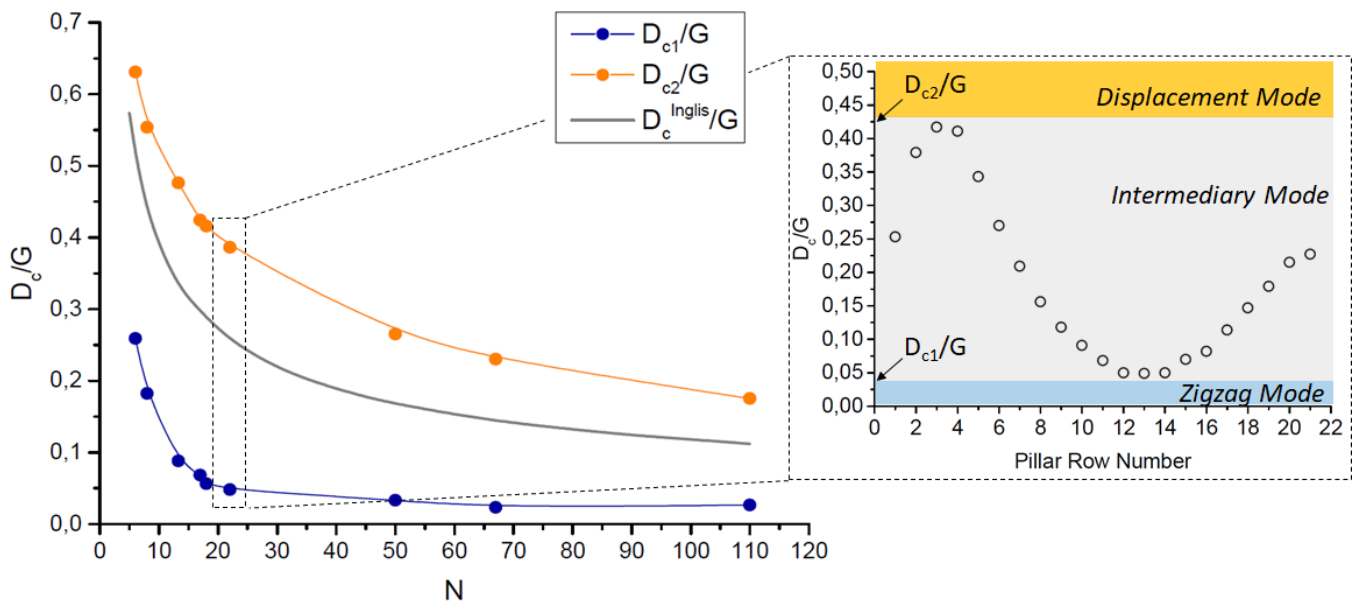


Figure 3.18: Influence of the array period N on both extreme critical diameters D_{c1} and D_{c2} with $N_c = 3$ and comparison with the critical diameter predicted by the Inglis' model (D_c^{Inglis}). The central column of pillars (second column) of the channel width is considered. The parameters D_{c1} and D_{c2} are presented in the figure at the right, showing the evolution of D_c/G along the pillar rows for $N = 22$.

Figure 3.18 shows the evolution of D_{c1} and D_{c2} with the array period N for a constant channel width $N_c = 3$. In order to take into account only the effect of the parameter N , without being influenced by the second geometrical parameter G , the ratio D_c/G is represented in fig. 3.18. This enables to generalize the evolution of D_c/G represented in fig. 3.18 to any DLD geometry, independently of the inter-pillar gap (G). The reference (D_c^{Inglis}) corresponds to the critical diameter given by the theoretical model of Inglis et al. [324].

When particles have a diameter smaller than D_{c1} , they are in the zigzag mode in the entire channel length, while particles larger than D_{c2} are always in the displacement mode. Between D_{c1} and D_{c2} , particles have an intermediary mode, as described in the previous section: they have a zigzag mode at some areas of the channel and they are displaced by the other pillars. When flowing in the intermediary mode, particles with diameters closer to D_{c1} display more zigzag areas while particles of dimension closer to D_{c2} are displaced by most pillars.

Figure 3.18 shows that the computed values of D_{c1} and D_{c2} follow the same evolution with N as the critical diameter predicted by the Inglis' model. However, for the considered channel width of 3 pillars, the area of intermediary mode is not negligible. Thus, **in case of narrow channels with a limited number of pillars in the channel width, it is not fully satisfactory to consider a unique critical diameter in the entire channel, as proposed by the Inglis' model.** By way of example, considering a channel width $N_c = 3$, the intermediary mode is experienced by at least 15 % of the particles (when we consider all the particles with diameters smaller than the inter-pillar gap G). If we compare to the Inglis' model, the displacement mode is observed for particle sizes up to 59 % larger than D_c^{Inglis} , and the zigzag mode is observed for particle sizes up to 84 % smaller than D_c^{Inglis} . According to the Inglis' theory, all the particles larger than D_c^{Inglis} should display a displacement mode while all the particles smaller than D_c^{Inglis} should be in a zigzag mode. Therefore, taking into account the intermediary mode is essential to have a good prediction of the particle sizes that are displaced or not by the DLD channel.

The intermediary mode decreases the efficiency of the particle sorting by DLD. Indeed, particles in the intermediary mode are not directed towards a specific location, contrary to particles in zigzag or displacement modes. Thus, it is hard to anticipate the presence of intermediate particles in each of the output channels. Therefore, **it is important to identify how the intermediary effect can be avoided when designing DLD devices.**

Figure 3.19 represents the influence of the channel width on D_{c1} and D_{c2} for two different numbers of pillar columns in the channel width ($N_c = 10$ or 100 pillar columns in the lateral direction). D_{c1} and D_{c2} are represented at each pillar column when $N_c = 10$ and every 10 columns when $N_c = 100$. In both cases, fig. 3.19 shows that D_{c1} and D_{c2} get closer to each other in the central part of the channel width. In addition, D_{c1} and D_{c2} get even closer when N_c increases. This means that increasing the number of pillars in the channel width results in a decrease of the intermediary mode area. Therefore, **the intermediary effect results from the boundary conditions of the channel walls: when the channel width decreases, particles are more sensitive to the conditions at the channel walls, and the intermediary mode appears.**

When the channel width is large enough, only the zigzag and the displacement modes take place in the central part of the DLD device while the intermediary mode is confined to the borders (fig. 3.19 b).

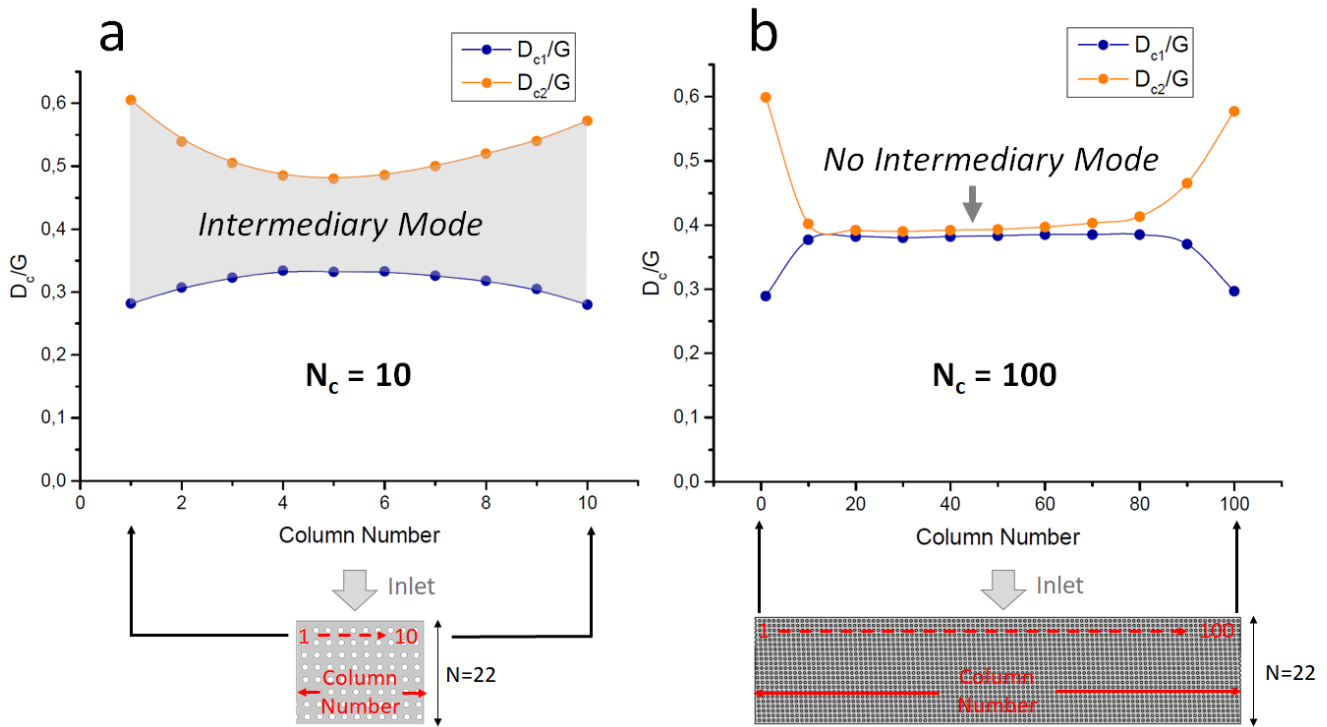


Figure 3.19: Evolution of D_{c1}/G and D_{c2}/G at different positions in the channel width ($N = 22$) for a width of 10 columns (a) or 100 columns (b). Values of D_c/G are given at each column for the 10 column width, while they are given every 10 columns for the 100 column width.

The effect of the channel walls can be clearly seen in fig. 3.15 (a). The zigzag mode is observed when the side pillars are separated from the channel wall, which enables the flow to zigzag in the pillar-to-wall spacing. The displacement mode is obtained when the side pillars are adjacent to the side walls, which forces the flow to follow the direction of the pillars.

In order not to degrade the sorting efficiency, the intermediary mode has to be avoided. Two approaches can be considered: first, as presented with “nano-DLDs” (fig. 3.10), the wall effect can be cancelled by improving channel boundaries. Then, even with straight channel walls, the intermediary mode can be minimized by choosing a number of pillars in the channel width (N_c) that is large enough. However, increasing N_c may cause miniaturization issues, especially for designs with large inter-pillar spacings. A DOE-based model is proposed to find the best compromise between efficiency and miniaturization by identifying the smallest N_c value that eliminates the intermediary mode. Our model investigates both the influence of the array period (N) and the number of pillars in the channel length (N_c) on the intermediary mode.

3.4.3 Prediction of the Critical Diameters with the Intermediary Mode Effect

In this section, a **quadratic model** is proposed to describe the evolution of D_{c1}/G and D_{c2}/G according to N and N_c . This model was based on a DOE that takes into account all the possible interactions between both variables N and N_c . The effect of the third geometrical parameter G is directly introduced in the expression of the responses $Y_1 = D_{c1}/G$ and $Y_2 = D_{c2}/G$. According to the quadratic model, their evolution can be written as:

$$Y_1 = a_0^1 + a_1^1 X_1 + a_2^1 X_2 + a_{11}^1 (X_1)^2 + a_{22}^1 (X_2)^2 + a_{12}^1 X_1 X_2 \quad (3.3)$$

$$Y_2 = a_0^2 + a_1^2 X_1 + a_2^2 X_2 + a_{11}^2 (X_1)^2 + a_{22}^2 (X_2)^2 + a_{12}^2 X_1 X_2 \quad (3.4)$$

where $X_1 = \frac{N - \bar{N}}{\Delta N / 2}$ (normalized array period) and $X_2 = \frac{N_c - \bar{N}_c}{\Delta N_c / 2}$ (normalized channel width), \bar{A} is the mean value of the variable A and $\Delta A = A_{max} - A_{min}$, with A_{max} and A_{min} respectively the maximum and minimum values of the variable A . The model is proposed for N and N_c values ranging from 3 (minimum required array period to obtain the DLD effect) to 100 (larger N values require larger computation resources and are not representative of experimental designs). Taking these limits into consideration, the following coded variables are obtained:

$$X_1 = \frac{N - 51.5}{49.5} \text{ and } X_2 = \frac{N_c - 51.5}{49.5} \quad (3.5)$$

In order to find the coefficients of the quadratic model, 9 experiments have to be performed with X_1 and X_2 taking 3 possible values: -1, 0, 1 (table 3.4). For each experiment, Y_1 and Y_2 are determined from the minimum and maximum values of D_c along the DLD channel at the central pillar column of the channel width. These experiments are performed numerically with our COMSOL model, for which the mesh size and the streamline density have been previously optimized.

Table 3.4: Values of both variables X_1 and X_2 for each of the 9 experiments of the experimental plan.

Experiment	1	2	3	4	5	6	7	8	9
X_1	-1	1	-1	1	0	-1	0	1	0
X_2	-1	-1	1	1	-1	0	0	0	1

The coefficients of the quadratic model are optimized from the 9 experiments presented in table 3.4. The following experimental laws are obtained to describe the evolution of both responses Y_1 and Y_2 :

$$Y_1 = 0.10 - 0.31 X_1 + 0.03 X_2 + 0.26 (X_1)^2 - 0.02 (X_2)^2 \quad (3.6)$$

$$Y_2 = 0.16 - 0.27 X_1 - 0.06 X_2 + 0.24 (X_1)^2 + 0.04 (X_2)^2 \quad (3.7)$$

This model shows that the values of Y_1 and Y_2 are mostly influenced by the array period N (X_1), but the effect of N_c (X_2) is not negligible. N_c has both a linear and a quadratic influence on Y_1 and Y_2 , but there is no coefficient of interactions between both variables N and N_c . From this model, the tendency obtained in fig. 3.19 is verified: D_{c1} and D_{c2} become closer to each other when N_c (X_2) increases, since Y_1 increases with N_c and Y_2 decreases with N_c .

Our model is compared to numerical values of D_{c1}/G and D_{c2}/G in fig. 3.20. A good correlation between numerical results and the proposed model is obtained. Figure 3.20 also clearly shows that the parameter N_c has to be taken into account in the model for D_{c1} and D_{c2} . So far, the proposed models do not consider the number of pillars in the channel width and they only give a single critical diameter for each DLD geometry. This appears to be insufficient for designs with reduced N_c . From fig. 3.20 we deduce that for a device with an array of $N = 22$, a minimum of 60 pillars in the channel width ($N_c = 60$) is required to avoid the intermediary mode. **The proposed model allows to determine the minimum required N_c value to be insensitive to the wall effect for any geometry with N between 3 and 100.**

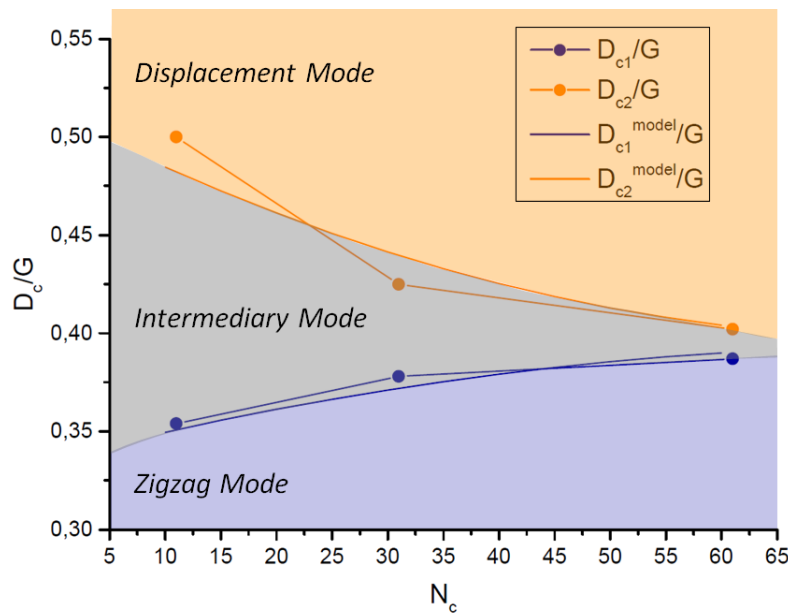


Figure 3.20: Evolution of D_{c1}/G and D_{c2}/G (numerical results and model) with the number of pillars in the channel width N_c . The values are taken in the center of the channel width and for an array period $N = 22$.

The correlation between the proposed model and experimental results is verified for devices with different N and N_c values (fig. 3.21). Experimental points are obtained from the observation of different-sized particles (Appendix 5, some examples are given in fig. 3.21). Figure 3.21 shows good agreement between the proposed model and experimental results. When the channel width is small ($N_c = 10$ pillars), the domain of particle sizes that are in the intermediary mode increases. This is experimentally observed for particle populations with sizes close to the spacing between D_{c1} and D_{c2} . Particles smaller than D_{c1} are in zigzag mode while most particles larger than D_{c2} are in displacement mode. This good correlation between our model and experimental data suggests that the proposed model can predict the trajectory of particles in all DLD geometries, including very narrow devices (small N_c) since it takes into account the boundary effects at the channel walls, in addition to the DLD separation effect.

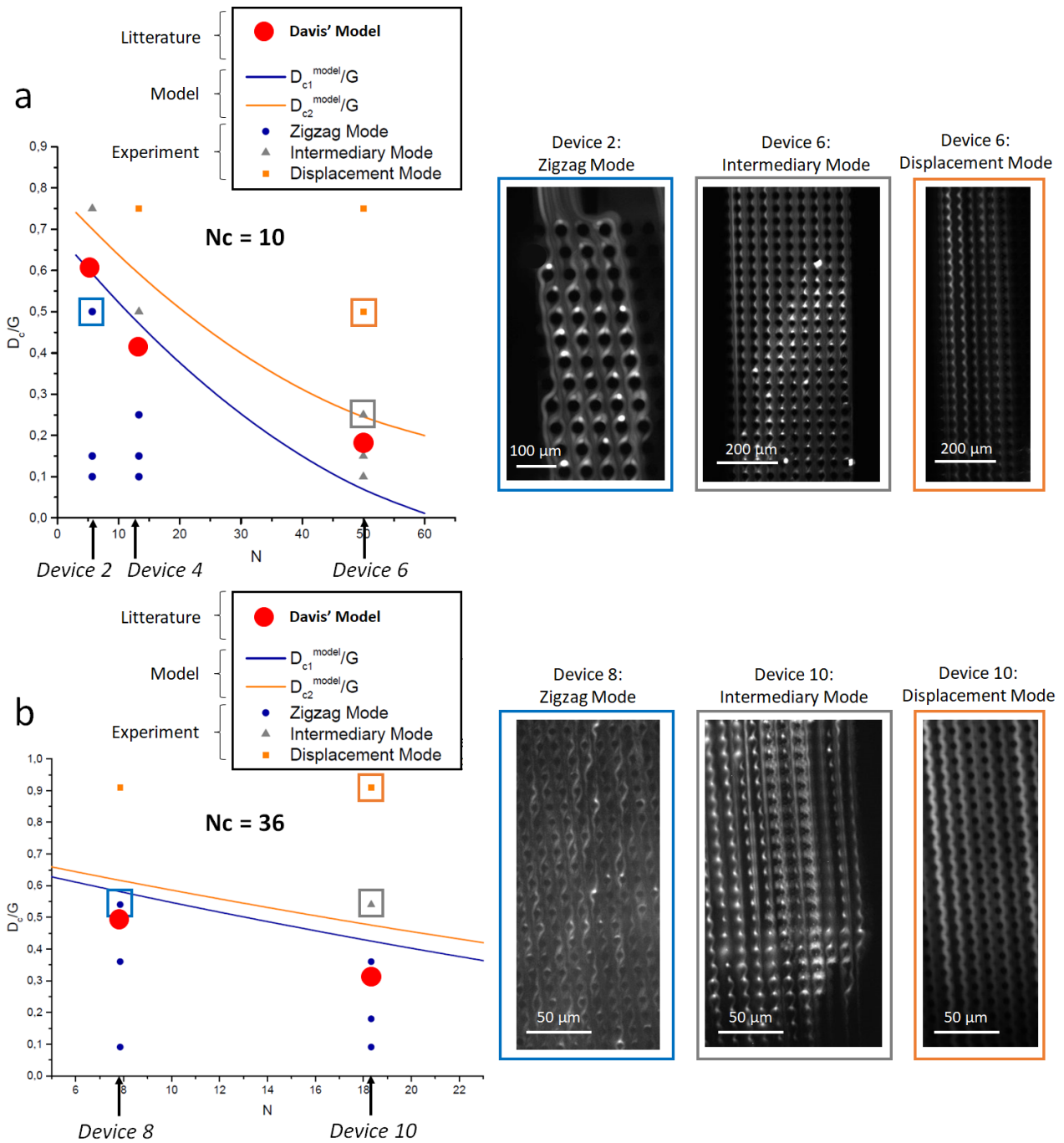


Figure 3.21: Experimental points showing the mode of trajectory (zigzag, intermediary or displacement) of particles of different sizes (ratio D/G , where D is the particle diameter and G is the inter-pillar spacing), according to the array period N , for a channel width of 10 (a) or 36 (b) pillar columns (N_c). The proposed model for D_{c1} and D_{c2} is also represented (solid curves). The squared markers are illustrated by the corresponding epifluorescence images of particles in zigzag, intermediary or displacement modes.

As a perspective, the intermediary mode of displacement could be exploited as well to design multi-separation DLD devices. Thanks to the multiple separation diameters in narrow DLD channels, several particle populations could be separated at the same time. Indeed, in the intermediary mode, each particle size has a different zigzag to displacement area ratio: larger particles display smaller zigzag areas and larger displacement areas. Therefore, **a gradient of particle sizes could be obtained in the output channel of narrow DLD devices, where the influence of the intermediary mode is maximized.**

3.5 New Separation Phenomena with Exploratory Designs

3.5.1 DLD Concentration

Preliminary experiments were performed to evaluate the concentration function of our DLD devices (version 3, $G = D_p = 12 \mu\text{m}$, $N = 5$) with $10 \mu\text{m}$ polystyrene fluorescent beads (larger than the critical diameter of about $8 \mu\text{m}$, given by Davis' model [326]). As observed in fig. 3.22, beads are effectively deviated towards the center of the channel, thanks to the mirror-oriented geometry. Therefore, this device design enables to concentrate particles larger than D_c at the center of the DLD channel, with a concentration factor equal to the ratio of the side channels width to the center channel width.

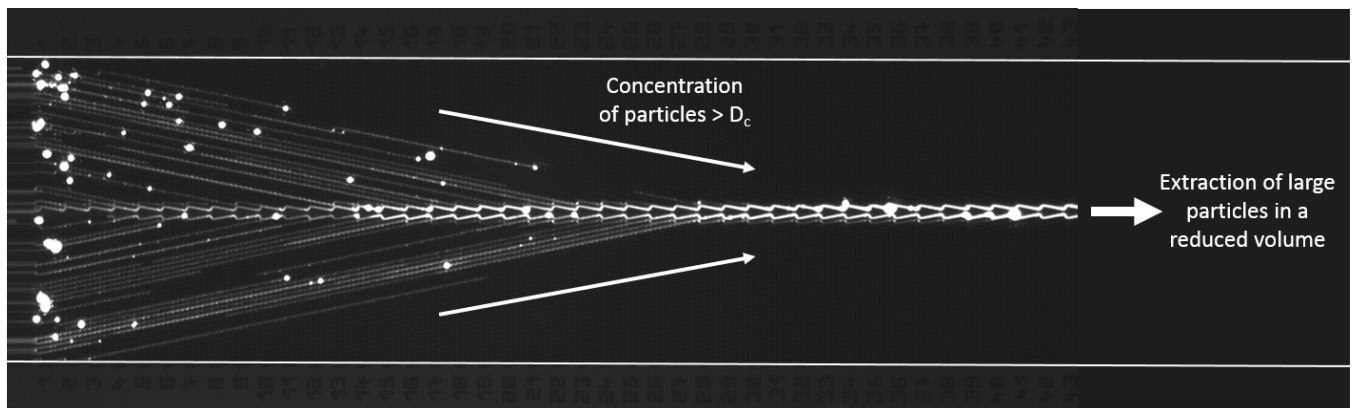


Figure 3.22: $10 \mu\text{m}$ fluorescent beads trajectory in a concentration DLD device (version 3, $G = D_p = 12 \mu\text{m}$, $N = 5$, $D_c = 8 \mu\text{m}$), experiment performed at CEA Leti by Nicolas Sarrut.

3.5.2 Multi-Separation with Elongated Pillars

The numerical study of anisotropy in DLD arrays - presented in the previous Chapter - was experimentally verified with devices that display elongated pillars (part of the version 3 devices). Two elongated pillar shapes (ellipses and triangles) were used to study the anisotropic behavior of particles. Here are presented the obtained trajectories in arrays of pillars with different positive and negative orientations.

Effect of Anisotropy on Particle Trajectories

The numerical predictions of particle trajectories in arrays of ellipsoidal pillars presented in the last Chapter were experimentally assessed with $15\ \mu\text{m}$ beads. Most beads display a displacement trajectory in the studied DLD device (fig. 3.23). However, some of them are subjected to a **reorientation** of their trajectory that follows the downward orientation of the pillars. This reorientation is clearly observed on fig. 3.23, with a particle trajectory that evolves from a displacement mode to a downward-oriented zigzag mode. According to our simulation work, particles that display a reorientation of their trajectory must have slightly smaller dimensions compared to displaced particles. For this experiment, only one particle population was injected in the pillar array ($15\ \mu\text{m}$ beads, Fluoro-Max, Thermo Scientific) with a size uniformity lower than 5 %. This means that the different observed trajectories are obtained with our DLD device for very close bead sizes between $14.5\ \mu\text{m}$ and $15.5\ \mu\text{m}$, which confirms that accurate separation of particles can be achieved with arrays of oriented ellipsoidal pillars.

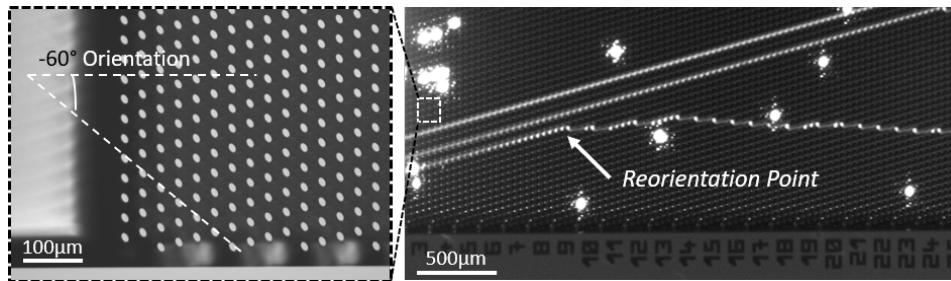


Figure 3.23: Fluorescent streaks of $15\ \mu\text{m}$ -beads in an array of downward-oriented ellipsoidal pillars with $G = 15\ \mu\text{m}$, $N = 5$, $\tau = -60^\circ$ showing the reorientation of displaced particles, and magnified bright-field image of the pillar array.

As a result, two trajectory directions were observed with $15\ \mu\text{m}$ beads (fig. 3.24): the displacement direction that follows the orientation of the pillar array (with an array period $N = 5$) and the **downward-oriented zigzag direction** that displays an angle of about -4.5° compared to the horizontal direction of injection, for the studied array of -45° -oriented ellipsoidal pillars.

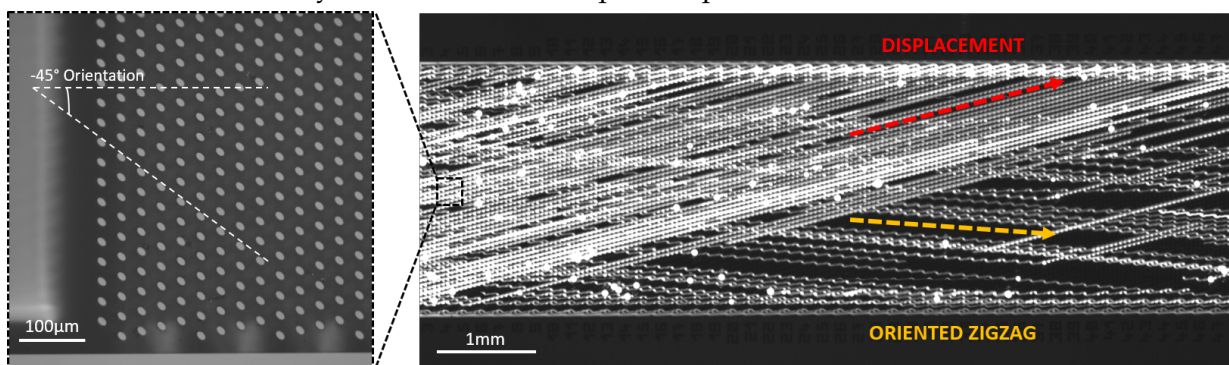


Figure 3.24: Fluorescent streaks of $15\ \mu\text{m}$ -beads in an array of downward-oriented ellipsoidal pillars with $G = 15\ \mu\text{m}$, $N = 5$, $\tau = -45^\circ$ showing both particle trajectories, and magnified bright-field image of the pillar array.

The same angle of -4.5° was obtained for downward-oriented $15\ \mu\text{m}$ beads in an array of ellipsoidal pillars with a -60° direction instead of -45° . This suggests that increasing the pillar orientation above 45° does not allow further increase of the anisotropy effect. In addition to the displacement and downward-oriented zigzag modes, a third zigzag trajectory was actually observed, without any deviation from the horizontal injection direction (fig. 3.25). The particles that follow this “classical” zigzag trajectory display a lower fluorescence intensity compared to the particles in the two other modes, which suggests that the horizontal zigzag mode is followed by the smallest beads (ending up with lower intensity signals).

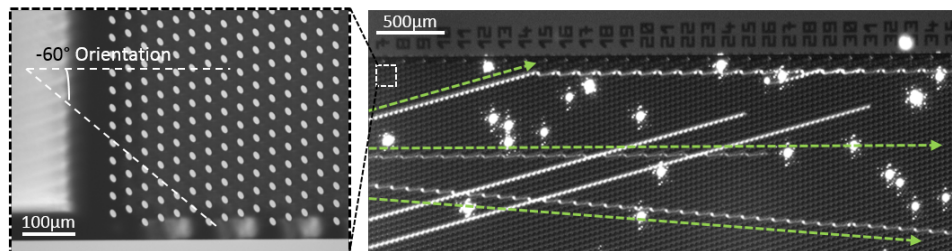


Figure 3.25: Fluorescent streaks of $15\ \mu\text{m}$ -beads in an array of downward-oriented ellipsoidal pillars with $G = 15\ \mu\text{m}$, $N = 5$, $\tau = -60^\circ$ showing the three particle trajectories.

Positive or Negative Anisotropy

The direction of the streamlines in different anisotropic DLD devices was observed with non-deviated $3\ \mu\text{m}$ beads (fig. 3.26). At the channel entrance, streamlines follow the direction of the pillars, while they recover a horizontal direction further into the channel. This result is in accordance with observations made by Vernekar et al. [391] with arrays of circular pillars in a row-shifted parallelogram layout. Indeed, the effect of anisotropy on the streamlines is effective only at the array edges, where the bending of the streamlines in the array can be compensated in the inlet and outlet free channel areas.

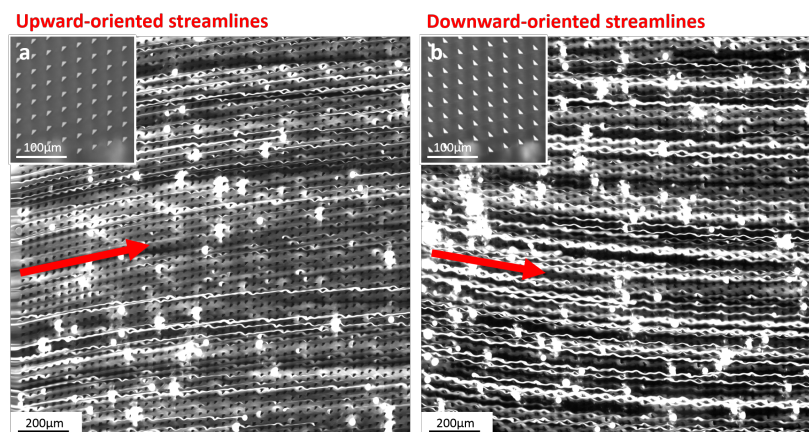


Figure 3.26: Fluorescent streaks of $3\ \mu\text{m}$ -beads in an array of upward-oriented (a) and downward-oriented (b) triangular pillars with $G = 15\ \mu\text{m}$, $N = 5$, $\tau = 45^\circ$ or -45° .

Therefore, in order to maximize the effect of anisotropy, a possible design improvement would be to decrease the channel length and introduce gap sections between each section of pillar arrays.

Chapter Summary: Validation of DLD Separation with Beads

- In this Chapter the capacity of the implemented DLD devices to separate model beads was demonstrated, with a characterization of the main DLD separation parameters: the critical diameter, the recovery yield and the deviation efficiency.
- The numerical results presented in Chapter 2 for different pillar shapes were experimentally verified: smaller critical diameters were obtained with triangular and hexagonal pillars compared to circular pillars. However, no significant differences could be observed experimentally between triangles, hexagons and I shapes.
- Decreasing the downstream inter-pillar spacing also led to a decrease of the critical diameter compared to symmetric lateral and downstream gaps.
- Recovery yields higher than 60 % were obtained with polystyrene beads in the DLD devices with micrometric dimensions (groups 2 and 3 of version 2). The recovery yield decreases with smaller particles for a given device geometry.
- Among the three available “nano-DLD” devices (group 1 of version 2), only the design with 3 μm -pillars was usable to achieve separation of particles around 1 μm with recovery yields close to 100 %. Design improvements are required to avoid disturbance of the particle trajectory at the channel walls and improve flow rates in nano-DLD devices.
- Higher critical diameters (D_c) were obtained with some of our DLD designs compared to the critical diameters predicted by the Davis’ model. This shift was observed in DLD devices that display a limited number of pillars in the channel width. It was demonstrated that wall effects are responsible for variations of D_c along the DLD channel, inducing an intermediary mode of trajectory in addition to the classical zigzag and displacement modes.
- A new predictive model was proposed to take into account the number of pillars in the channel width (N_c) in addition to the inter-pillar spacing (G) and array period (N) in the estimation of D_c .
- Some of the exploratory designs presented in Chapter 2 were experimentally tested for two different functions: the concentration of deviated particles and the multi-separation of particles with anisotropic devices. Both functions were demonstrated with preliminary results and further studies will enable to better quantify the associated efficiency.

Résumé du Chapitre : Validation de nos Dispositifs sur Billes Modèles

- Ce chapitre a permis de démontrer la capacité de nos dispositifs de DLD à séparer en taille différentes populations de billes modèles. Les principaux paramètres de la séparation par DLD ont été déterminés pour chacun des dispositifs : le diamètre critique, le taux de collecte et l'efficacité du tri.
- Les résultats numériques présentés au Chapitre 2 ont été vérifiés expérimentalement pour différentes formes de piliers. En effet, nos validations expérimentales ont confirmé la diminution du diamètre critique par les piliers triangulaires et hexagonaux, en comparaison avec les piliers circulaires. Cependant, les différences observées numériquement entre piliers triangulaires, hexagonaux et en forme de I ne sont pas apparues comme expérimentalement significatives.
- La réduction de la distance inter-piliers longitudinale a permis de diminuer efficacement la valeur du diamètre critique, tout autres paramètres géométriques restant égaux par ailleurs.
- Des taux de collecte supérieurs à 60 % ont été obtenus pour tous les dispositifs de DLD aux dimensions micrométriques (groupes 2 et 3 de la version 2), avec un rendement plus faible pour les plus petites particules dans un dispositif donné.
- Parmi les trois dispositifs de "nano-DLD" disponibles (groupe 1 de la version 2), seul le dispositif présentant des piliers de $3\ \mu\text{m}$ a pu être implémenté, avec un diamètre de séparation autour de $1\ \mu\text{m}$, et un rendement proche de 100 %. Des améliorations du design seront nécessaires pour éviter la perturbation de la trajectoire des particules proches des parois du canal et augmenter le débit dans les dispositifs de nano-DLD.
- Plusieurs de nos dispositifs de DLD ont conduit à des diamètres critiques (D_c) supérieurs à ceux donnés par le modèle prédictif de Davis. Cet écart a été observé lorsque le canal de DLD présente un faible nombre de piliers. Ce chapitre a démontré que des effets de bord génèrent une variation du diamètre critique sur la longueur du canal, donnant lieu à un mode de trajectoire intermédiaire, différent des modes de zigzag et de déplacement généralement observés.
- Un nouveau modèle prédictif a été proposé afin de prendre en compte cet effet de bord dans la détermination du diamètre critique, en tenant compte du nombre de piliers sur la largeur du canal (N_c), ainsi que des paramètres classiques de distance inter-piliers (G) et de périodicité du réseau (N).
- Certains designs exploratoires présentés au Chapitre 2 ont été testés expérimentalement, avec la validation de deux fonctions complémentaires à la séparation par DLD : la concentration des particules déviées et la multi-séparation dans des dispositifs anisotropes. Des analyses complémentaires seront nécessaires pour quantifier plus précisément l'efficacité de ces effets.

DLD Purification of Biological Samples

Introduction: DLD Purification of Biological Samples

- In Chapter 3, the performances of the implemented DLD devices were characterized in the perspective of the biological applications presented in this Chapter.
- Two main applications are presented in this Chapter: the isolation of *E. coli* bacteria from blood samples in the perspective of Sepsis diagnosis and the isolation of extracellular vesicles (EVs) from cell culture media. The first application enables to identify limitations and optimize operational conditions with large objects (bacteria and blood cells) before focusing on our application of interest that is the isolation of EVs.
- The first DLD application is demonstrated with the purification of 10x-diluted human blood samples, through the depletion of blood cells (with a quantification of red blood cells deviation), while *E. coli* bacteria follow a zigzag trajectory.
- For the second biological application, a standard ultracentrifugation protocol is first implemented and the obtained EVs are characterized through cryo-Transmission Electron Microscopy (TEM) and Nanoparticle Tracking Analysis (NTA). This reference protocol allows to identify the limitations of current isolation techniques and the improvements that could be provided by DLD. Then, DLD is implemented to replace the first purification steps from THP-1 cell culture media, with similar depletion performances compared to centrifugation.
- In complement to DLD, two other standard protocols (size-exclusion chromatography and magnetic isolation with functionalized beads) are also implemented to obtain higher EV sample purity. In particular, the magnetic isolation protocol is integrated in a complete microfluidic device, downstream to DLD, in order to minimize sample manipulation and optimize integration to further analysis techniques.

4.1 Isolation of Bacteria in Blood Samples

The particles we aim at isolating in this thesis with our DLD technology are extracellular vesicles (EVs). However, the handling and analysis of these biological objects are particularly challenging because of the nanometric dimensions of EVs. Therefore, as a first proof-of-principle study on real biological samples we address the isolation of bacteria from human blood. This work enables us to separate different particle size ranges (from a few μm to a few tens of μm) and optimize our device operation without the issues

of submicronic particle visualisation. Moreover, the isolation of bacteria from blood samples was part of an ongoing project in our laboratory (called [BactiDIAG](#)), funded by BPI France under the FUI framework (FUI-AAP18).

The general objective of this project is to use LPS-based antigens for rapid Sepsis diagnosis. Sepsis is a very frequent pathology, that represents about 2 % of hospitalization cases in industrialized countries. Sepsis is defined as a systemic inflammatory response syndrome due to an infection. In 80 % of sepsis cases, this infection is bacterial. The detection of pathogens enables to differentiate between systemic inflammatory syndrome associated to an infection (sepsis) or without infection (SIRS). This discrimination is essential for an increase of the life expectancy of patients, a better control of resistance to antibiotics and a decrease of costs. Currently, only 50 % of the infections inferior to 1 CFU/mL are detected through classical blood culture [395]. The clinical challenge is to develop a rapid, unitary and easy to handle test to detect bacterial infections in order to stratify patients as fast as possible.

To that purpose, the DLD technology appears as a promising method to extract spiked *E. coli* bacteria by purifying blood samples.

4.1.1 Validation of Blood Purification

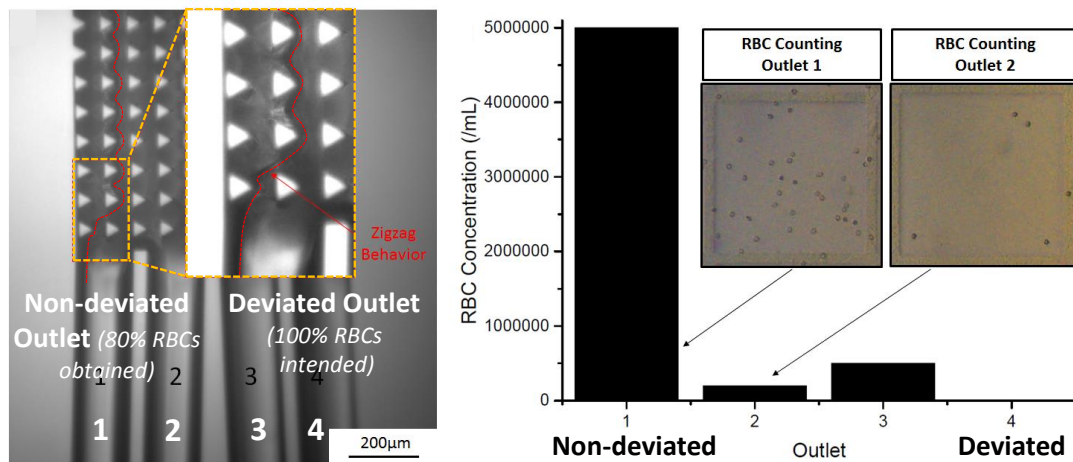
DLD is used to remove Red Blood Cells (RBCs) - that are the most abundant cells in blood, accounting for about 40 to 45 % of its volume - as a primary step for blood purification. Thus, the objective is to deviate the largest possible fraction of RBCs, that display a biconcave disc shape, with a diameter of about 8 μm and a thickness of about 2.5 μm at the sides (wider than the middle of the disk). Blood samples are collected from EFS ("Etablissement Français du Sang") after testing for HIV-1, HIV-2, Hepatitis C and Hepatitis B. Our experiments are performed from 6 mL blood samples collected in standard Vacutainer tubes with ethylenediamine tetraacetic acid (EDTA) anticoagulant. The studied blood samples are taken two days before lab testing.

With the first version of DLD devices

Different strategies have been first implemented to achieve RBC deviation with version 1 devices. This version of DLD devices does not enable to perform efficient removal of RBCs without clogging problems, but it helps to identify the design improvements that have been implemented in the second version of DLD devices. The first trials that were performed with the aim of deviating RBCs are summarized in [fig. 4.1](#), together with their related conclusions.

In order to reduce clogging issues, **injected blood samples were diluted 10 times in DPBS (1x)** (Gibco life technologies, 14190-144). The tested devices display 2 inlets and 4 outlets. The diluted blood sample is injected in the 100 μm -wide sample inlet, while DPBS solution is injected in the 300 μm -wide buffer inlet. The number of output RBCs is determined at each of the four DLD outlets by optical counting with bright-field microscopy imaging on cell counting chamber slides (Kitvia Cell Fast-Read, Fisher Scientific, H01BVS100).

1) 20 μm -pillars (triangles): $D_c \sim [5;10] \mu\text{m}$



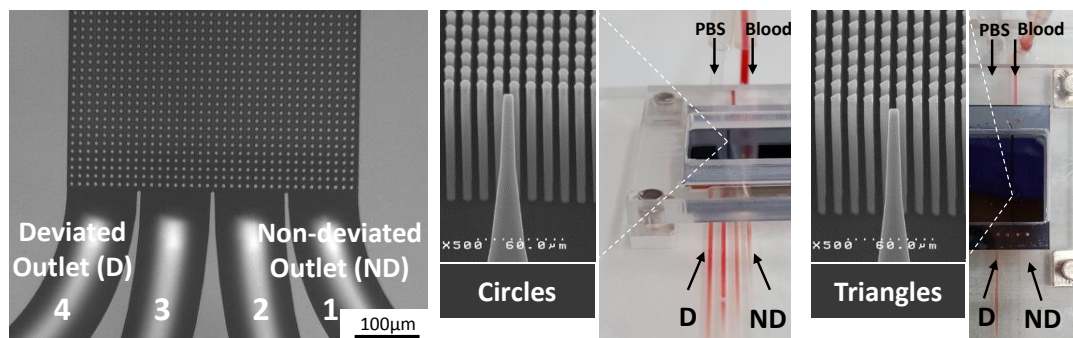
→ Very weak deviation of RBCs (more than 80 % of RBCs in the non-deviated outlet)

2) RBC treatment with glutaraldehyde (GTA) to increase stiffness (and effective size)

See Appendix 5 for protocols and results

→ Improvements but only 30 % of RBCs are deviated

3) 5.5 μm -pillars (circles and triangles): $D_c \sim [1;2] \mu\text{m}$



→ Visually observed RBC deviation (even improved with triangular pillars compared to circular pillars)

→ But, strong clogging (injection of only 100 μL of 10x-diluted blood before complete channel obstruction), makes it impossible to collect sample for RBC counting

Figure 4.1: Summary of the three tested strategies to deviate RBCs from 10x-diluted blood samples with version 1 DLD devices: 1) Use of 20 μm triangular pillars with 4 outlets numbered from 1 (non-deviated) to 4 (completely deviated). 2) Use of the same DLD design with glutaraldehyde (GTA)-treated RBCs to try to increase their effective size through cell membrane stiffening. Detailed results are presented in Appendix 6. 3) Use of smaller pillar dimensions (5.5 μm instead of 20 μm). RBC quantification at the outlets was not possible because of clogging problems after 100 μL of injected sample.

With the second version of DLD devices

The efficiency of blood purification through DLD was further improved with the second version of devices. Listed below are the improvements of V2 devices compared to V1:

- The pillar channel is wider to avoid the wall effects described in the previous chapter and to get away from the impact of clogged inter-pillar spacings.
- The pillar channel is longer to increase the separation efficiency of the DLD device.
- Inlet subchannels enable to focus particles in inter-pillar spacings and avoid clogging.
- Outlet subchannels enable to balance output pressures and avoid final re-direction of particles towards the less resistive outlet.
- Intermediate pillar dimensions are tested, between 5.5 μm - that completely deviates RBCs - and 20 μm - that do not deviate RBCs, in order to get the best compromise between deviation efficiency and throughput.
- More pillar shapes and asymmetric inter-pillar spacings are tested to further improve the deviation of blood particles.

Results with version 1 devices have shown that designs with critical diameters around 2 μm are required to efficiently deviate RBCs. This is why designs 2 to 6 of Group 2 were selected for these new trials with version 2 DLD devices (with pillar dimensions of 9 μm , both symmetric and asymmetric gaps and four different pillar shapes). These five devices were tested with **10x-diluted blood samples** with a constant flow rate of about 50 $\mu\text{L min}^{-1}$ in order to identify the most efficient device to deviate RBCs. Deviated (D) and non-deviated (ND) samples were collected from both DLD outlets and centrifuged for visual inspection of the pellet of blood particles, and RBCs were counted with cell counting chambers. Figure 4.2 shows that **I-shaped pillars with symmetric gaps and circular pillars with asymmetric gaps enable to significantly increase the deviation of RBCs compared to the three other pillar designs, with less than 5 % of RBCs collected in the non-deviated outlet.**

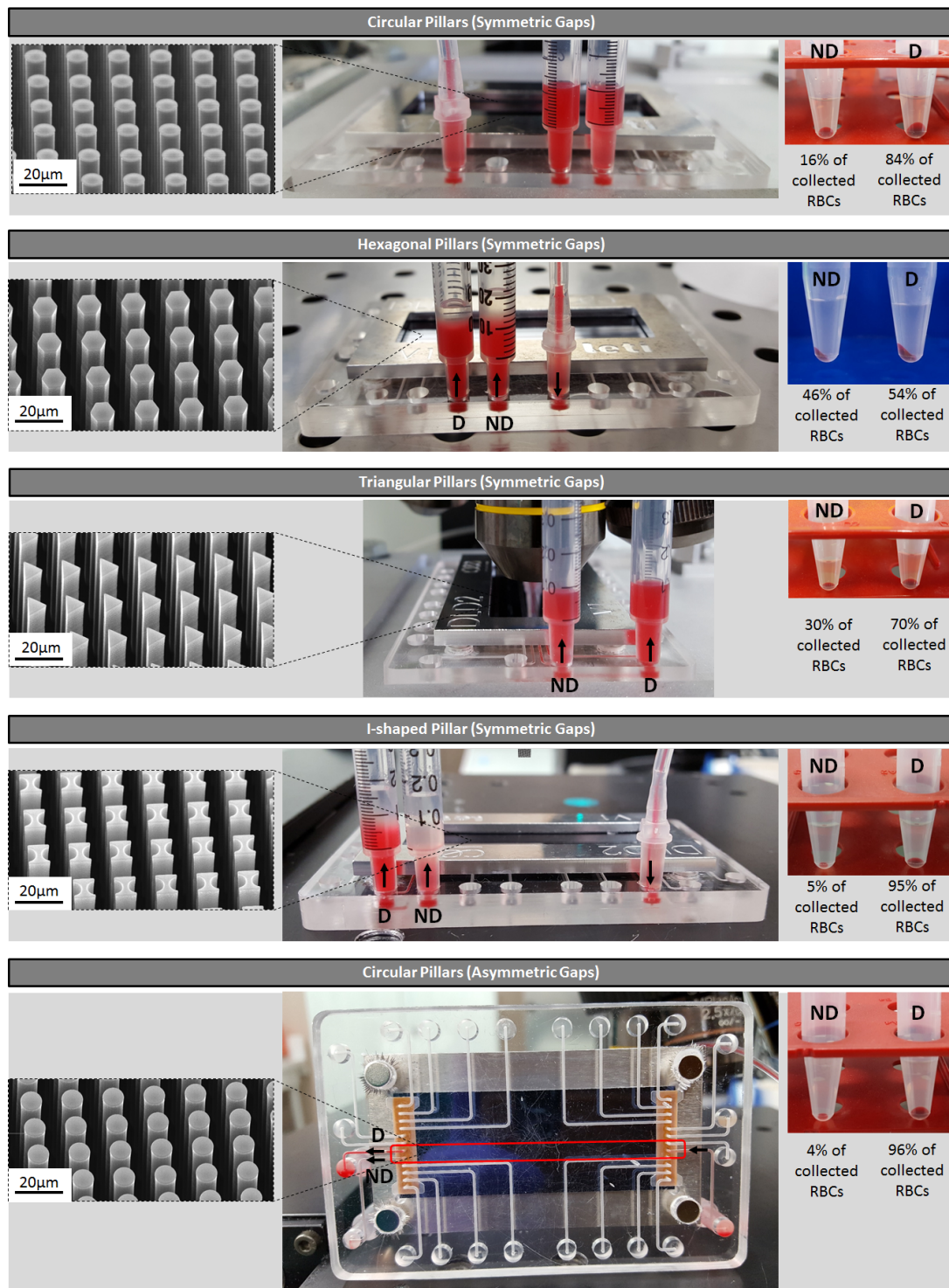


Figure 4.2: Comparison of circular (symmetric gaps), hexagonal (symmetric gaps), triangular (symmetric gaps), I-shaped (symmetric gaps) and circular (asymmetric gaps) pillars to deviate RBCs from 10x-diluted blood sample at $50 \mu\text{L min}^{-1}$ with a single-inlet configuration, and corresponding pictures of the non-deviated (ND) and deviated (D) samples after centrifugation.

Strong improvement of the deviation of RBCs was further obtained by decreasing the injection flow rate. Indeed, higher flow rates induce more squeezing of RBCs and smaller effective sizes, that are less deviated by the DLD array. Figure 4.3 shows that injection of a **10x-diluted blood sample at $7 \mu\text{L min}^{-1}$ instead of $50 \mu\text{L min}^{-1}$ enables to increase the deviation of RBCs to up to 99.3 %** with the promising design of circular pillars with asymmetric inter-pillar spacings. However, this induces a decrease in throughput of about 7 times. Further optimization should be performed in order to identify intermediate flow rates that enable sufficient deviation efficiency while maintaining acceptable throughput.

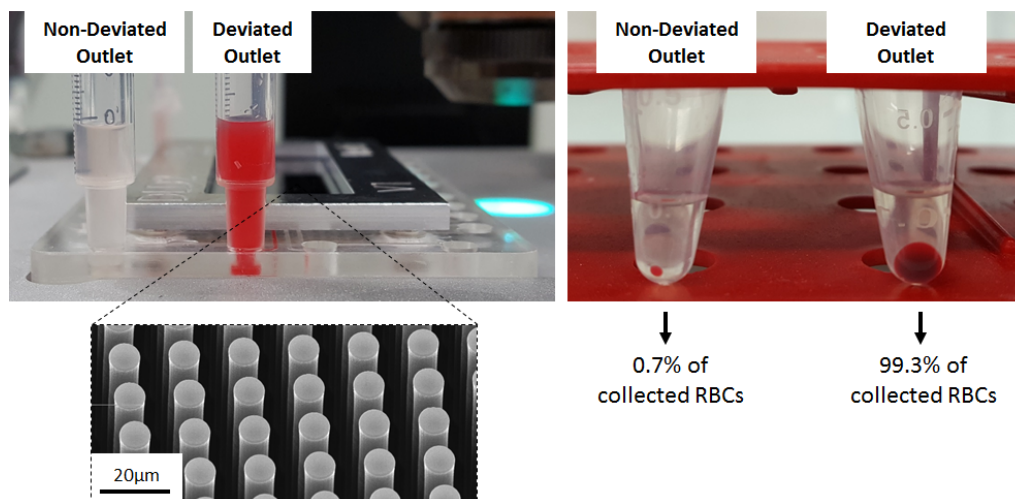


Figure 4.3: Tested device (with $9 \mu\text{m}$ -pillars and asymmetric gaps) with collected samples from both DLD outlets for an injection at $7 \mu\text{L min}^{-1}$, and picture of both output solutions after centrifugation.

4.1.2 Validation of Bacteria Recovery

From the last section, two DLD designs were identified to efficiently deviate blood particles: design 3, group 2, version 2 ($9 \mu\text{m}$ circular pillars with asymmetric gaps) and design 6, group 2, version 2 ($9 \mu\text{m}$ I-shaped pillars with symmetric gaps). The next step is to assess if bacteria are deviated or not by these devices and to evaluate resulting recovery yields. The presented preliminary results will focus on *E. coli* bacteria, as a first validation step.

A 1-inlet DLD configuration will be used for these experiments in order to simplify the fluidic control at the DLD entrance (since no balancing is required between several input solutions). **With this configuration, non-deviated particles are collected in both outlets at the same concentration**, as represented in fig. 4.4. Therefore, the 1-inlet configuration enables to deplete up to 100 % of deviated particles but with a recovery yield for non-deviated particles limited to 50 %. The 2-inlets configuration is preferred when 100 % of non-deviated particles have to be collected, but it requires precise balancing of both input flow rates. In our 1-inlet configuration, we expect bacteria to follow a zigzag trajectory given the value of the critical diameter of this device (between 2 and $3 \mu\text{m}$) and the dimensions of *E. coli* bacteria (with a diameter of about $1 \mu\text{m}$ and a length of $2 \mu\text{m}$).

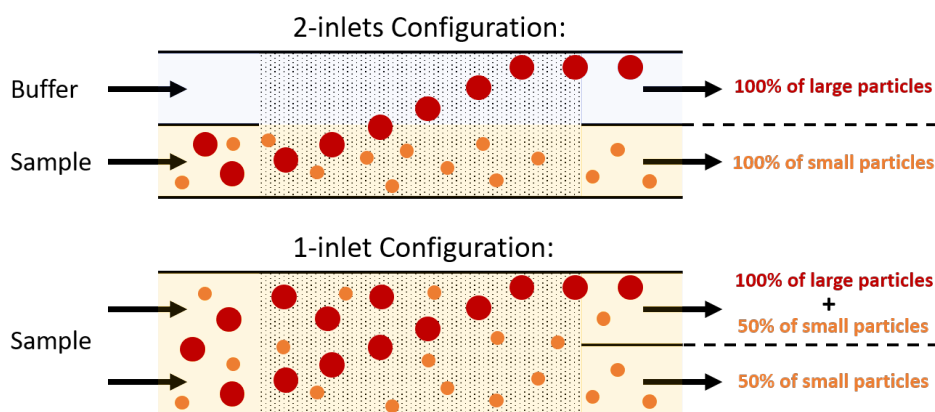


Figure 4.4: Schematic representation of the 2-inlets and 1-inlet configurations for DLD devices and respective recovery yield for ideal deviated and non-deviated behaviors. “Small” particles are smaller than the critical diameter while “large” particles are larger than the critical diameter.

Both devices that showed promising results on blood were tested with a sample of *E. coli* bacteria diluted in DPBS (1x) (Gibco life technologies, 14190-144) at 5.10^4 bacteria/mL. 800 μL of sample was injected in the single inlet at a flow rate of about $50 \mu\text{L min}^{-1}$. The output concentration of bacteria was then quantified in the non-deviated and deviated outlets after microbial growth on Petri dishes (fig. 4.5). The recovery yield is about 1.6 times higher with circular pillars compared to I-shaped pillars, which may be due to the concave profile of I shapes, that capture more bacteria (fig. 4.5 a). Therefore, **circular pillars seem more appropriate to limit loss of bacteria in the DLD device**, although even these pillars only recover 13 % of the injected bacteria at the outlets.

However, high counting variability (up to 47 %) was obtained from microbial culture on Petri dishes, due to variations in the spreading, accessibility of bacteria to nutrients, homogeneity in the deposited droplet of bacteria sample, etc... In addition, it is challenging to count bacteria optically with cell counting chambers because of the small dimension of these particles. Therefore, fluorescent bacteria were then used to avoid culture on Petri dishes and simplify optical microscopy counting. We tested a clone of *E. coli* that contains a multicopy vector encoding the green fluorescent protein GFP. In order to avoid elimination of this vector by bacteria, another gene responsible for resistance to ampicillin antibiotics (β lactamase) was also integrated in this vector. GFP-*E. coli* were cultured in TSA (Tryptic Soy Agar, Sigma, 22091) media containing $100 \mu\text{g mL}^{-1}$ of ampicillin. From this culture, GFP-*E. coli* were grown for one day before the experiment in a new TSA media without ampicillin in order to avoid shape inhomogeneity induced by antibiotics, that could disturb the behavior of bacteria in DLD arrays. The fluorescent bacteria were injected at $7 \mu\text{L min}^{-1}$ in the device of interest (design 3, group 2, version 2, with 9 μm circular pillars and asymmetric gaps). **Zigzag trajectories** were visualized in the pillar array (fig. 4.6), which supports our previous results with the same amount of bacteria counted in the non-deviated and in the deviated outlets from culture Petri dishes (fig. 4.5).

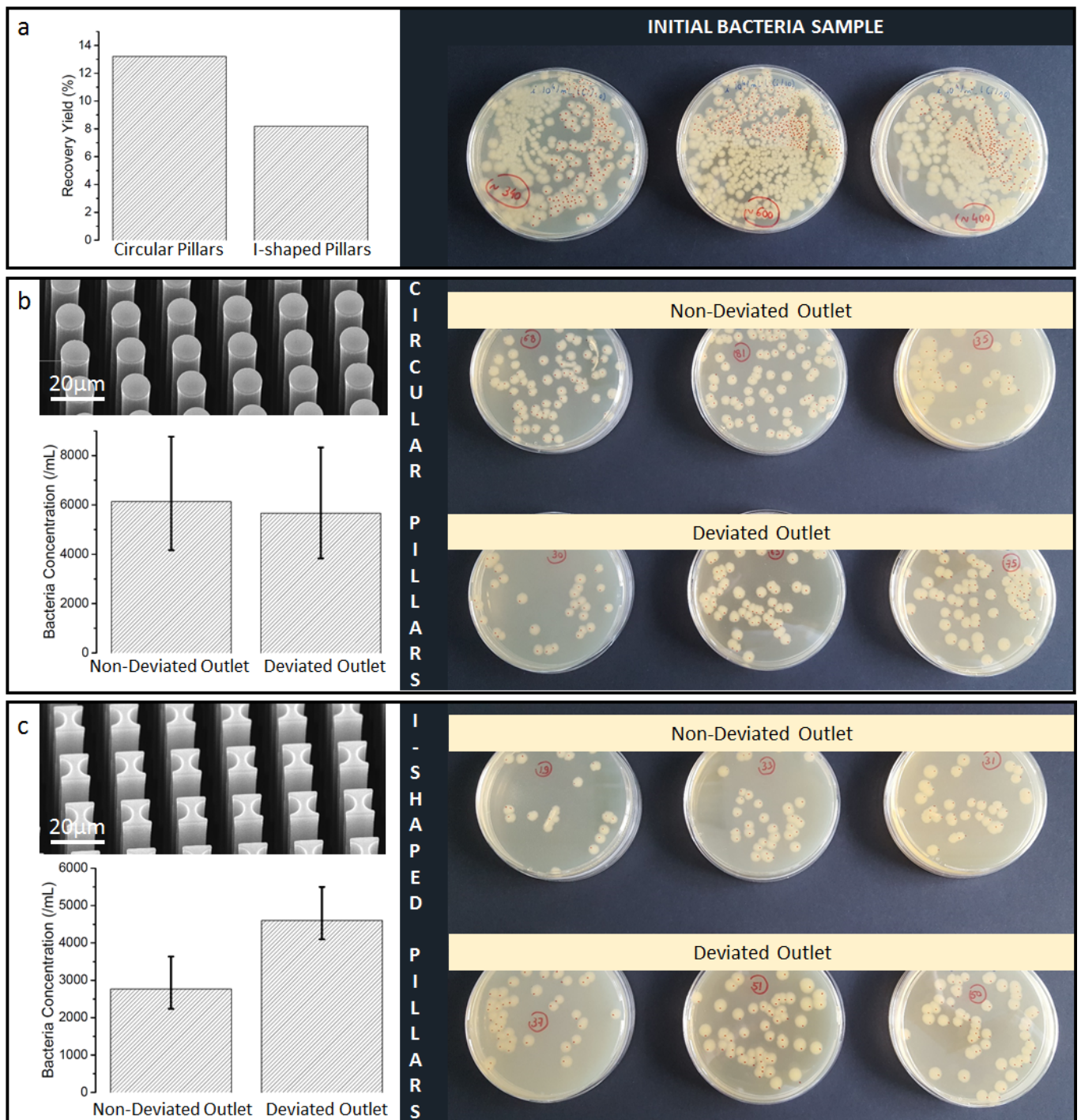


Figure 4.5: Petri dishes (triplicate) of the initial bacteria sample (diluted 10x) at 5.10^4 bacteria/mL and recovery yield for both tested devices: design 3, group 2, V2 (9 μ m circular pillars with asymmetric gaps) and design 6, group 2, V2 (9 μ m I-shaped pillars with symmetric gaps) (a). Petri dishes (triplicate) of the non-deviated and deviated output samples (diluted 10x) for design 3 (b) and design 6 (c) and corresponding bacteria concentrations.

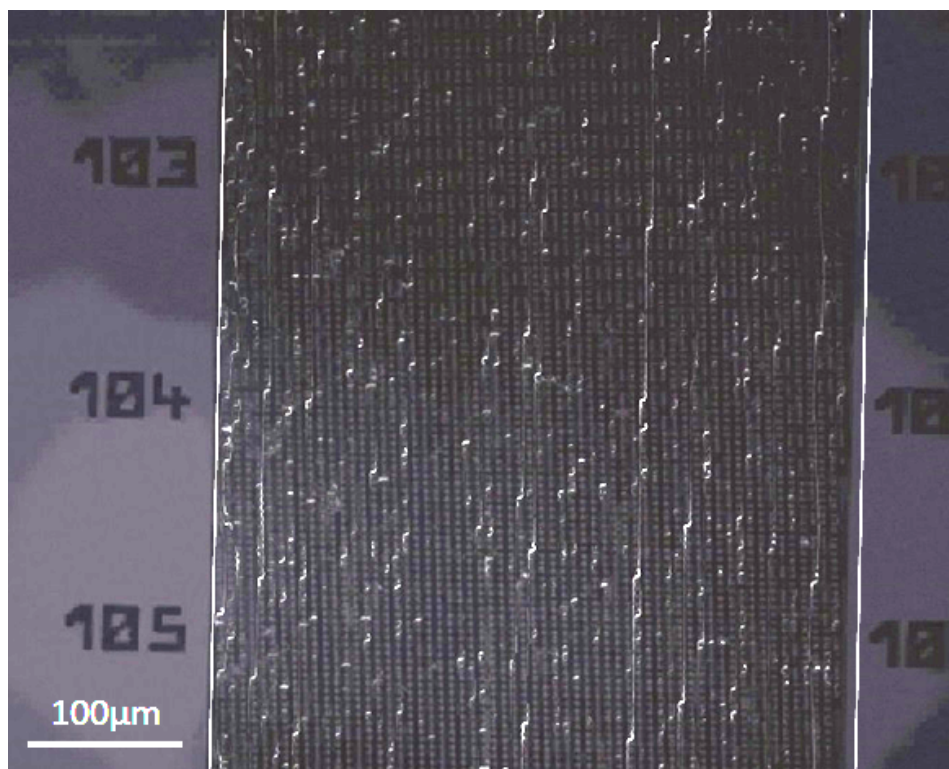


Figure 4.6: Fluorescence microscopy image of the zigzag trajectory of GFP-E. coli bacteria injected at $7 \mu\text{L min}^{-1}$ in an array of $9 \mu\text{m}$ circular pillars with asymmetric gaps (design 3, group2, V2).

Finally, the **extraction of bacteria from blood** was verified with the optimized conditions that were previously identified: $9 \mu\text{m}$ -circular pillars with asymmetric gaps (design 3, group 2, version 2) and injection at $7 \mu\text{L min}^{-1}$. GFP-E. coli bacteria were added to a sample of 10x-diluted blood at a concentration of about $2.4 \cdot 10^6$ bacteria/mL. The initial solution and output deviated and non-deviated solutions were then characterized through optical microscopy to count RBCs and fluorescent bacteria in each sample. The obtained results are presented in fig. 4.7 and table 4.1.

Table 4.1: Quantification of RBCs and GFP-E. coli bacteria in the initial solution, non-deviated and deviated outlets. The recovery yield corresponds to the percentage of RBCs and bacteria that are collected in the outlets compared to the injected solution.

	Non-Deviated	Deviated	Recovery Yield
Bacteria	56 %	44 %	100 %
RBCs	0.2 %	99.8 %	100 %

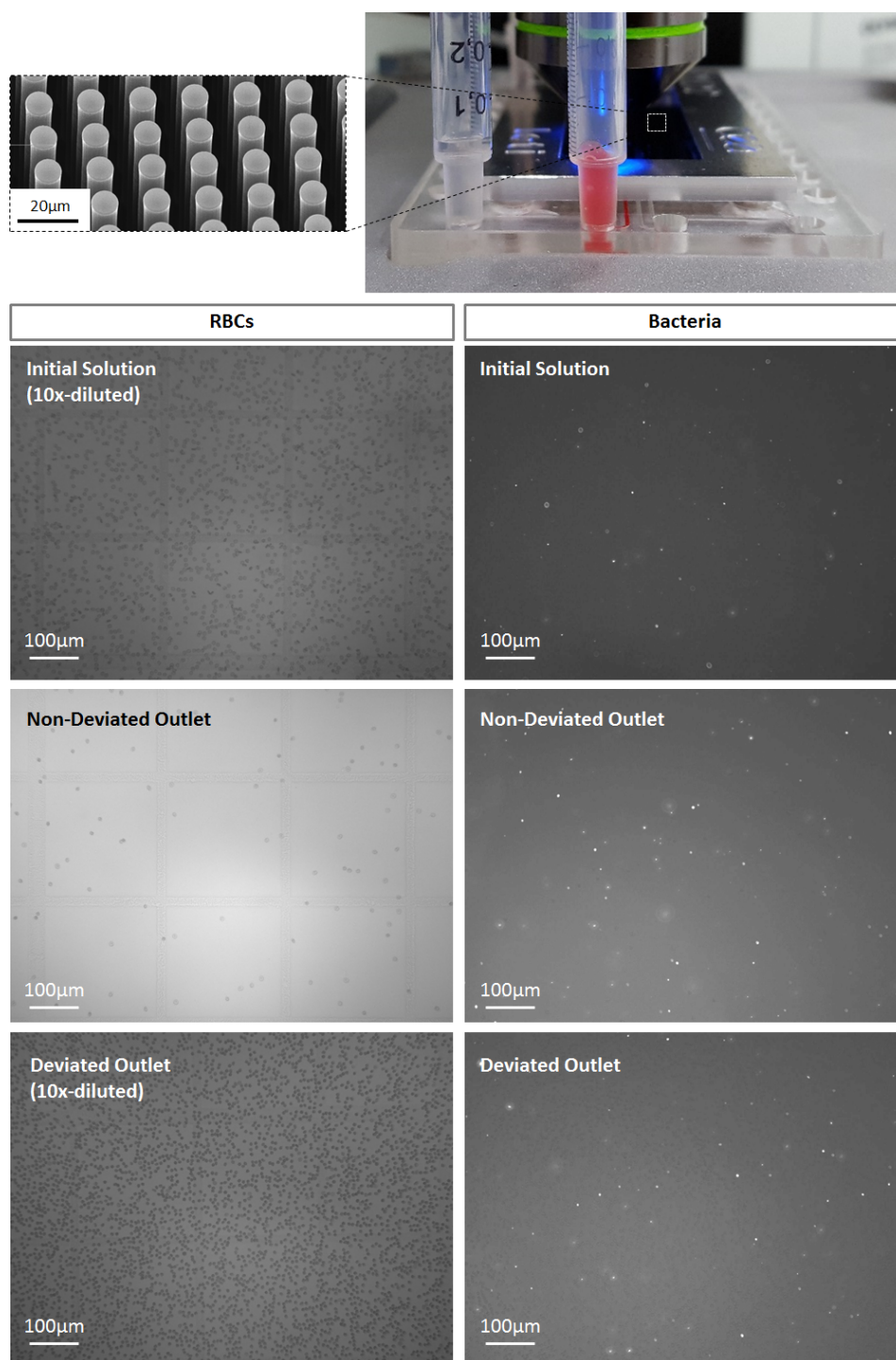


Figure 4.7: Picture of the tested single-inlet device (design 3, group 2, V2) and corresponding SEM image of the pillars. GFP-E. coli bacteria in 10x-diluted blood are injected at $7 \mu\text{L min}^{-1}$. Microscopy (fluorescence) pictures of RBCs and bacteria on cell counting chamber slides in the initial injected sample, non-deviated outlet and deviated outlet.

These results are very encouraging, since **99.8 % of the injected RBCs are removed from the initial sample through deviation by the pillars, with no loss of particles in the pillar array**. The 100 % recovery yield for bacteria is in contradiction with the results presented in fig. 4.5, that showed a recovery yield of about 13 %. Possible reasons could be the impact of the counting technique (culture in Petri dishes vs direct microscopy counting), the impact of the bacteria type (*E. coli* vs GFP-modified *E. coli*) and the impact of the surrounding media (PBS vs 10x-diluted blood). As explained earlier, only 56 % of the injected bacteria are collected in the purified non-deviated outlet since a single-inlet device is used (thus theoretically half of the non-deviated particles flow through each of the two DLD outlets). With a two-inlet device, 100 % of the bacteria could be collected in the purified non-deviated outlet, but this configuration slightly increases the fluidic control complexity at the DLD inlets to balance both input flow rates. In the next chapter, we will see that using a 1-inlet configuration is also an advantage when cascading several DLD devices for multi-step separations of complex samples. Another improvement could be an increase in the flow rate thanks to modifications of the DLD design (for example by increasing the channel depth and/or decreasing the channel length) or with a parallelized configuration of DLD channels.

4.2 Extraction of Extracellular Vesicles from Cell Culture Media

The extraction of bacteria from blood have enabled us to implement our DLD devices with biological material and identify the best operating conditions, before moving to the samples of interest that are extracellular vesicles (EVs). In order to extract and purify EVs from biological samples (such as biofluids or cell culture media), several techniques are commonly used with complementary performances (fig. 4.8). First, centrifugation and filtration steps enable to remove most cells and cell debris. Then, ultracentrifugation enables to concentrate EVs in the pellet of small particles. Size Exclusion Chromatography (SEC) performs EV purification from other protein contaminants. This can also be achieved by centrifugal filtration, that concentrates EVs on top of a filter at low centrifugation velocities, while smaller contaminants are eluted through the filter pores. Finally, immunocapture on functionalized beads enables to target specific EVs and concentrate them (for example thanks to magnetic nanobeads). In this section will be first presented the purification performances obtained with the three main standard techniques: ultracentrifugation, SEC and magnetic immunocapture. Then, an automated microfluidic device will be proposed to perform the complete sample preparation of EVs from cell culture media thanks to the integration of a DLD purification step (that replaces the first centrifugation for cell and cell debris removal) and a magnetic immunocapture (to extract and concentrate specific EVs).

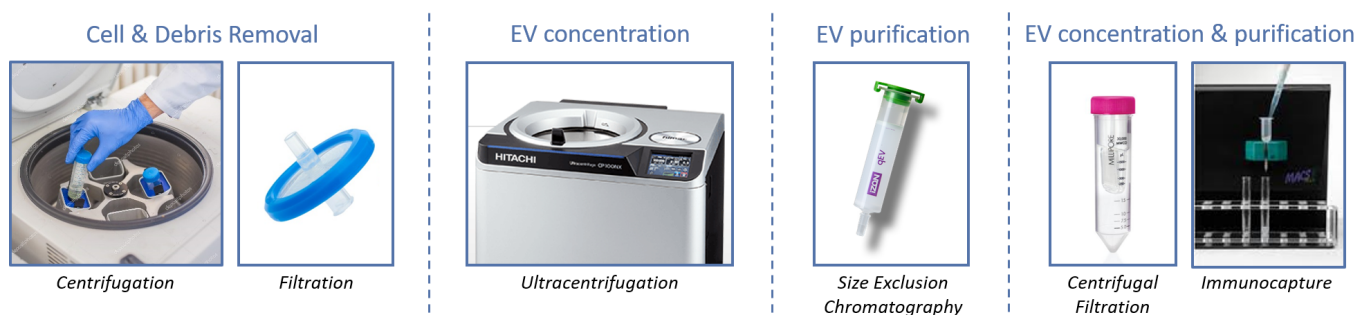


Figure 4.8: Overview of the main standard purification techniques for EV extraction and concentration

4.2.1 Standard Ultracentrifugation and Limitations

As stated by the ISEV, the most common sample preparation technique to isolate exosomes is ultracentrifugation [213], with **two main steps**: a first step in the 10,000-20,000 g range to remove large vesicles, and a second step at higher speed (typically 100,000 g) to pellet and concentrate exosomes. Therefore, this standard protocol was first performed as a reference sample preparation technique. EVs were extracted from cell culture media of a THP-1 human monocytic cell line, that was identified as a convenient cell line to start with, owing to its availability, fast growth, high EV secretion (especially after stimulation with calcium ionophore [10, 25]) and characteristics (non-adherent cells with homogeneous size).

Ultracentrifugation Protocol

THP-1 cells are cultured in RPMI-1640 Medium (ThermoFisher Scientific, 61870) containing 10 % FBS (fetal bovine serum). THP-1 cells are then seeded at 500,000 cells/mL after centrifugation at 300 g for 10 min (Eppendorf centrifuge, 5810R) and incubated for 20 min at 37 °C in DMEM Medium (Gibco Life Technologies, 31966-021), with 10 $\mu\text{mol L}^{-1}$ Calcium Ionophore A23187 (Sigma-Aldrich, C7522), in order to stimulate the exosome secretion by the THP-1 cells. Cells are then removed by centrifugation at 300 g for 10 min. The supernatant is centrifuged twice at 1,500 g for 15 min to remove dead cells and cell debris. Large vesicles are then removed by a first ultracentrifugation step at 20,000 g for 60 min at 4 °C with a Beckman Coulter Optima L-90K centrifuge and a swing rotor SW-32Ti. The supernatant is then centrifuged at 100,000 g for 60 min at 4 °C and the pellet is collected in DPBS (Gibco Life Technologies, 14190-144). Appendix 7 gives the protocol of THP-1 cell differentiation for experiments with macrophages.

cryo-TEM Observations

Cryo-transmission electron microscopy (TEM) was used to verify that EVs were effectively isolated by our standard ultracentrifugation protocol. Vitrification of our sample enables to avoid damaging of the sample structure by rapid cooling of the vesicles in liquid ethane and consequent crystallization of water molecules. Cryo-TEM observations were performed on fresh samples within 2 hours after EV extraction through centrifugation with an FEI Tecnai Osiris TEM microscope. The protocol for cryo-fixation of EV samples on carbon grids is presented in Appendix 8.

First, **EVs from THP-1 cells stimulated with Calcium Ionophore** (according to the protocol given in the last section) were observed by cryo-TEM. In particular, we compared the size and morphology of the vesicles contained in the pellet or in the supernatant after a 60 min ultracentrifugation step at 20,000 g (the last one being collected thanks to an additional 100,000 g centrifugation step for 60 minutes, as recommended in the literature [213]). Figure 4.9 shows images of EVs from the pellet of the **20,000 g step**. Round-shaped vesicles are clearly identified between carbon meshes, with a dark contour and a grainy interior aspect. High heterogeneity is observed, with typical **vesicle sizes from about 100 nm to more than 800 nm** (fig. 4.9 a,b). It must be noticed that this apparent diameter is certainly biased by the lateral confinement of the vesicles due to the sample width on the grid that is typically lower than 100 nm. Therefore, EVs larger than 100 nm are squeezed and may display larger apparent diameters. In addition, the ice thickness is lower at the center of the carbon nests compared to the sides, which explains that most EVs are observed near the carbon pattern. Very large vacuoles are also identified, that do not have a round structure contrary to the other vesicles (identified by the white arrows in fig. 4.9 c,d). These massive vesicles were identified by Issman et al. [219] as artifacts induced by sample freezing. However, in our case, these structures are observed in fresh samples and could be due either to the ultracentrifugation process or to the vitrification step. Moreover, a large number of EVs display a multi-membrane structure, as shown in fig. 4.9 (e) and (f). When a second centrifugation step at **100,000 g** is applied to the supernatant of the 20,000 g centrifugation step, high heterogeneity is still observed in the obtained EV population, with **typical sizes between 50 nm and 700 nm** (fig. 4.10 a,b). However, in this case, the large deformed bodies (observed in fig. 4.9 (c) and (d)) are not detected anymore. This suggests that **this isolation protocol enables to remove very large contaminants of about 1 μm , but it is not sufficient to collect only the exosome fraction (with diameters smaller than 100 nm).**

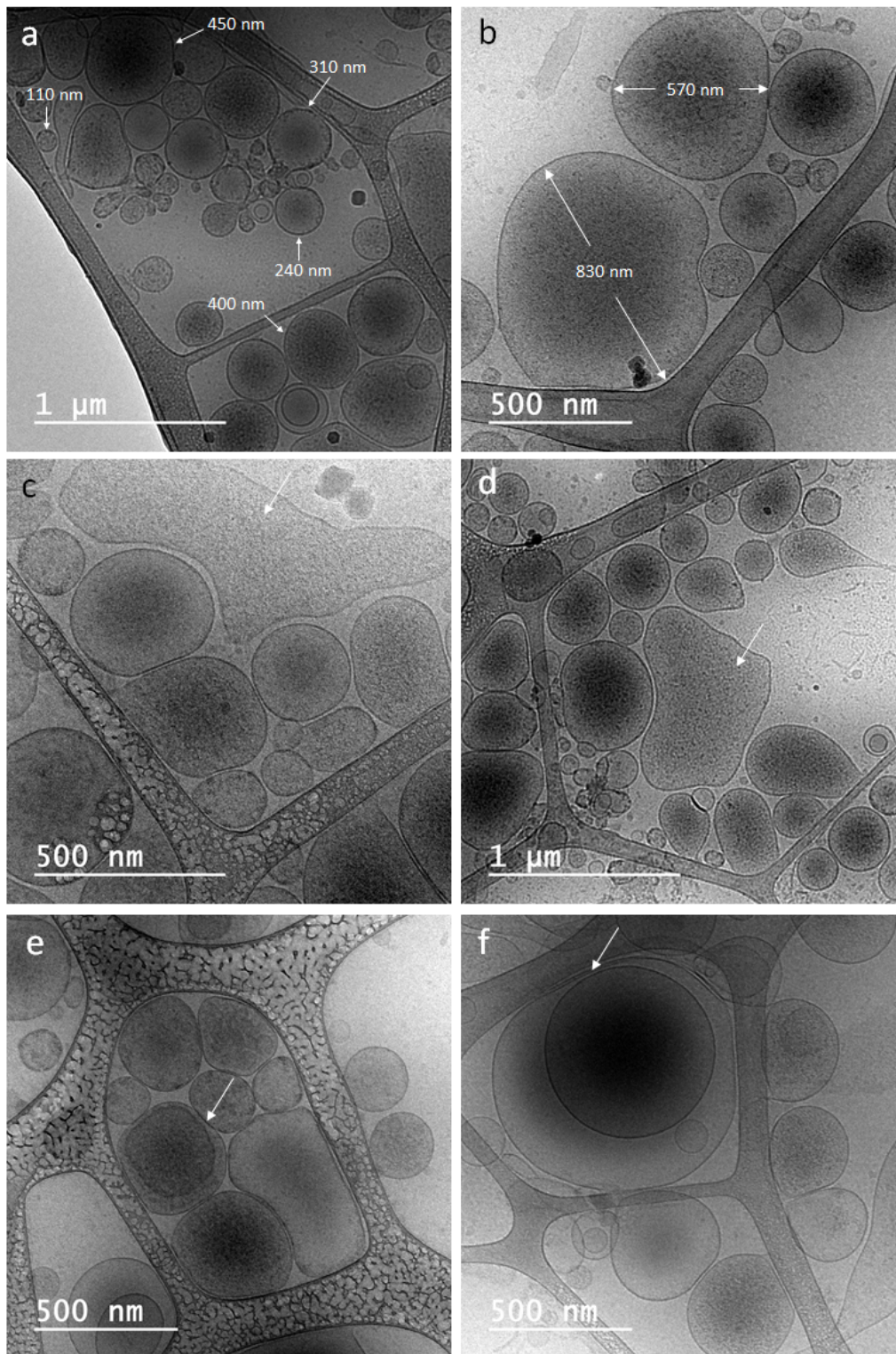


Figure 4.9: Cryo-TEM images of THP-1 EVs after 60 minutes of centrifugation at 20,000 g. White arrows show large vacuoles in figures (c) and (d) and deformation areas of multi-layered vesicles in figures (e) and (f).

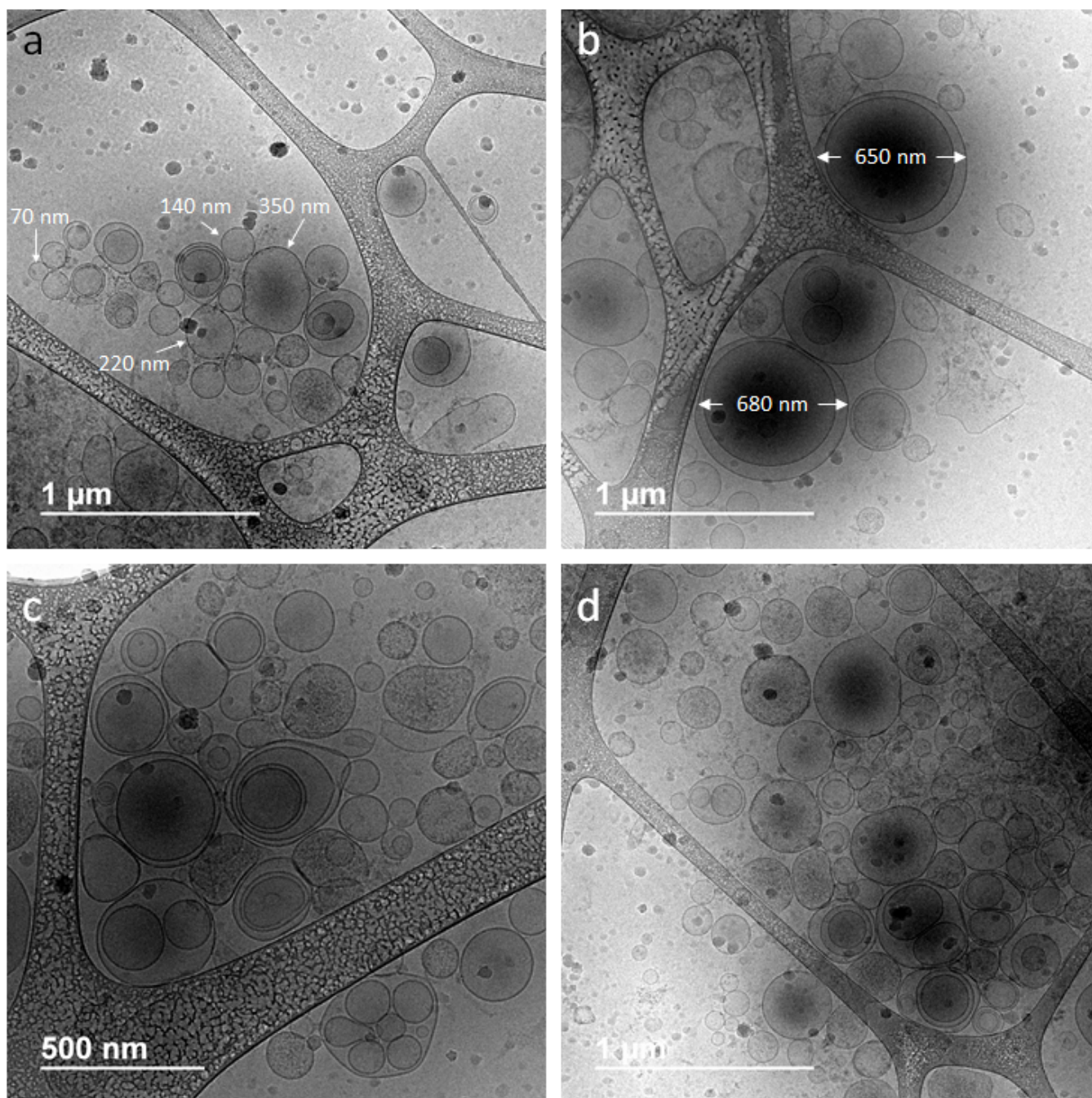


Figure 4.10: Cryo-TEM images of THP-1 EVs: the supernatant obtained after 60 minutes at 20,000 g is then centrifuged at 100,000 g for 60 minutes.

As already mentioned with the single 20,000 g centrifugation step, a large fraction of EVs have a multi-layered structure (fig. 4.10) after the 100,000 g centrifugation step, with some of them displaying up to 6 different EVs enclosed in another larger vesicle (fig. 4.10 c). Additional images of multi-layered vesicles are given in fig. 4.11, with a very large number of nested membranes. The images framed in blue correspond to spherulites prepared from hydrated lipids that are manually sheared with a plastic paddle [396]. Vesicles obtained through shearing have a similar structure to EVs isolated by ultracentrifugation, which suggests that **the multi-layered structure might be induced by high shearing forces applied to the vesicles during ultracentrifugation**. It is worth mentioning that this effect is observed not only after the last centrifugation step at 100,000 g, but already with the first step at 20,000 g, that was applied for the images presented in fig. 4.11.

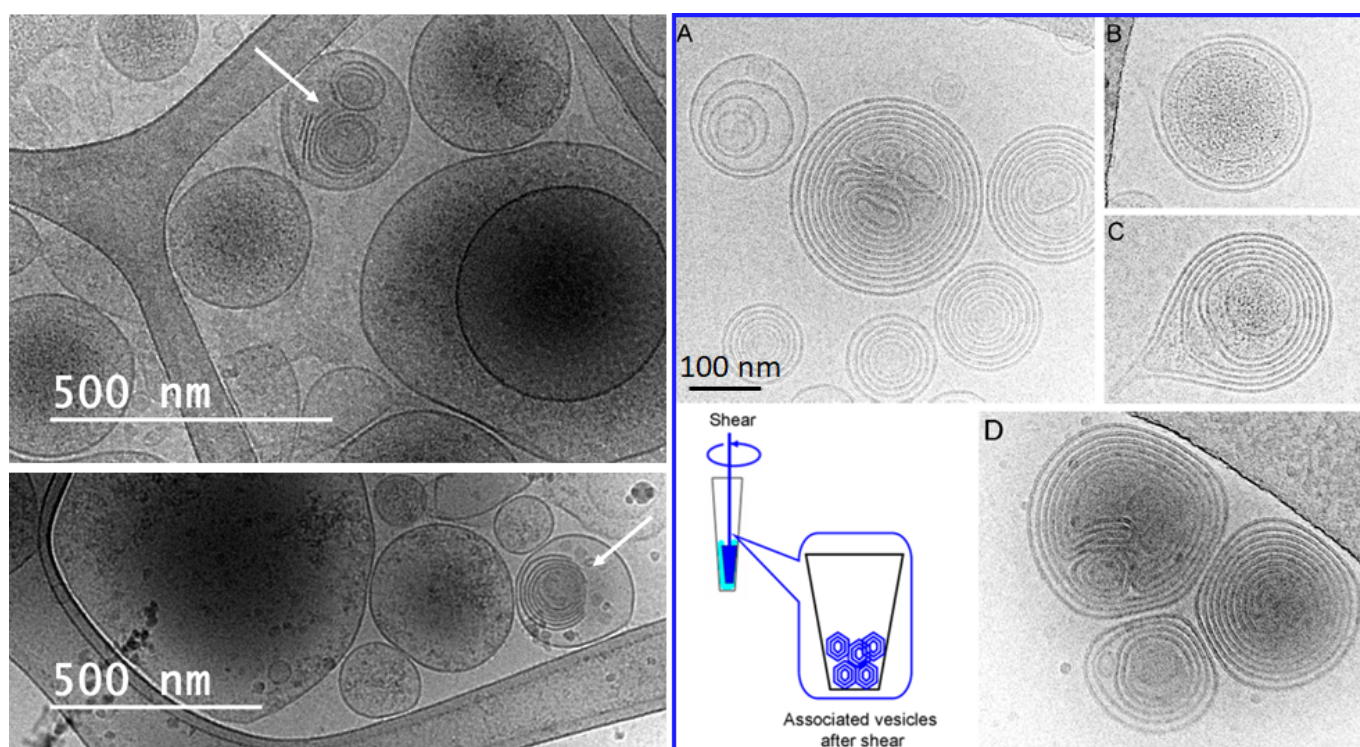


Figure 4.11: Left images: multi-layered THP-1 EVs (pointed by the white arrows) after centrifugation at 20,000 g for 60 minutes. Images framed in blue: spherulites obtained through shearing of hydrated lipids [396].

In addition to the multi-layered structure, other types of damages are also observed in the EV population isolated by a 20,000 g centrifugation step (fig. 4.12): some of the obtained EVs display **broken membranes**, which leads to the release of the intravesicular content into their surrounding environment. Two hypotheses can explain the observed membrane disruption: it can be induced either by the ultracentrifugation step or by the vitrification process. **If ultracentrifugation is responsible for these damages, as well as the multi-layered structure, an alternative isolation technique is highly required to obtain EVs with physiological structures, that are clinically relevant.**

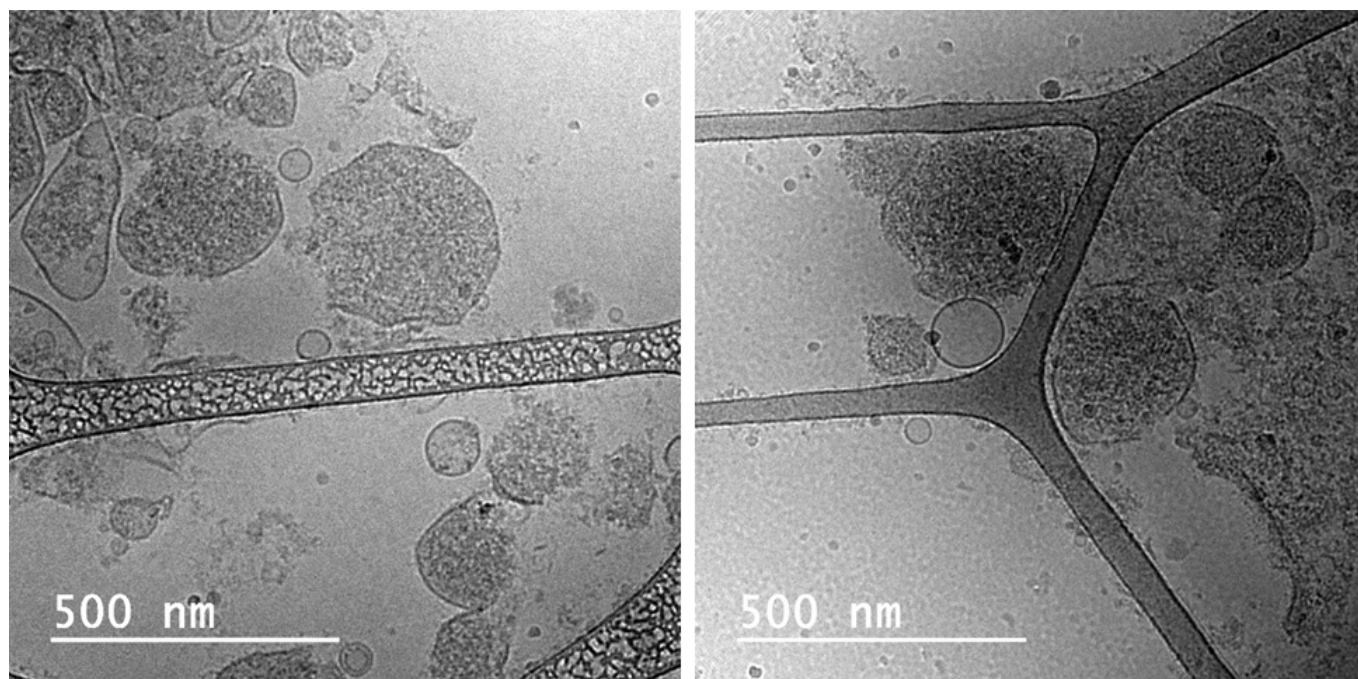


Figure 4.12: Cryo-TEM images of broken THP-1 EVs after 60 minutes of centrifugation at 20,000 g.

In the perspective of future studies on differentiated THP-1, a comparative study was performed to observe EVs from **M0 (unpolarized)**, **M1 (pro-inflammatory)** and **M2 (anti-inflammatory) macrophages** with cryo-TEM (fig. 4.13). Interestingly, structural differences are observed between pro- and anti-inflammatory macrophages, while M0 macrophages are structurally closer to M2 macrophages. Indeed, in the EV samples from M0 and M2 macrophages, most vesicles display a particular structure, that was not observed in EVs from undifferentiated THP-1 cells. In this case, a relatively homogeneous population of particles (with diameters below 200 nm) displays a circular shape composed of one or several smaller vesicles surrounded by a thick grainy layer. **To the best of our knowledge, this vesicle structure was not described elsewhere, and further studies would be required to understand the composition and origin of these particles.** In the EV population from M1 macrophages, the number of vesicles of this type is much lower, and most EVs display the “classical” shape, with high heterogeneity and without the thick grainy layer, as previously observed in EVs from undifferentiated THP-1. **These observations suggest that structural differences exist between EVs from different types of macrophages, which should be taken into account for the development of an appropriate sample preparation device, with target EV sizes and shapes.**

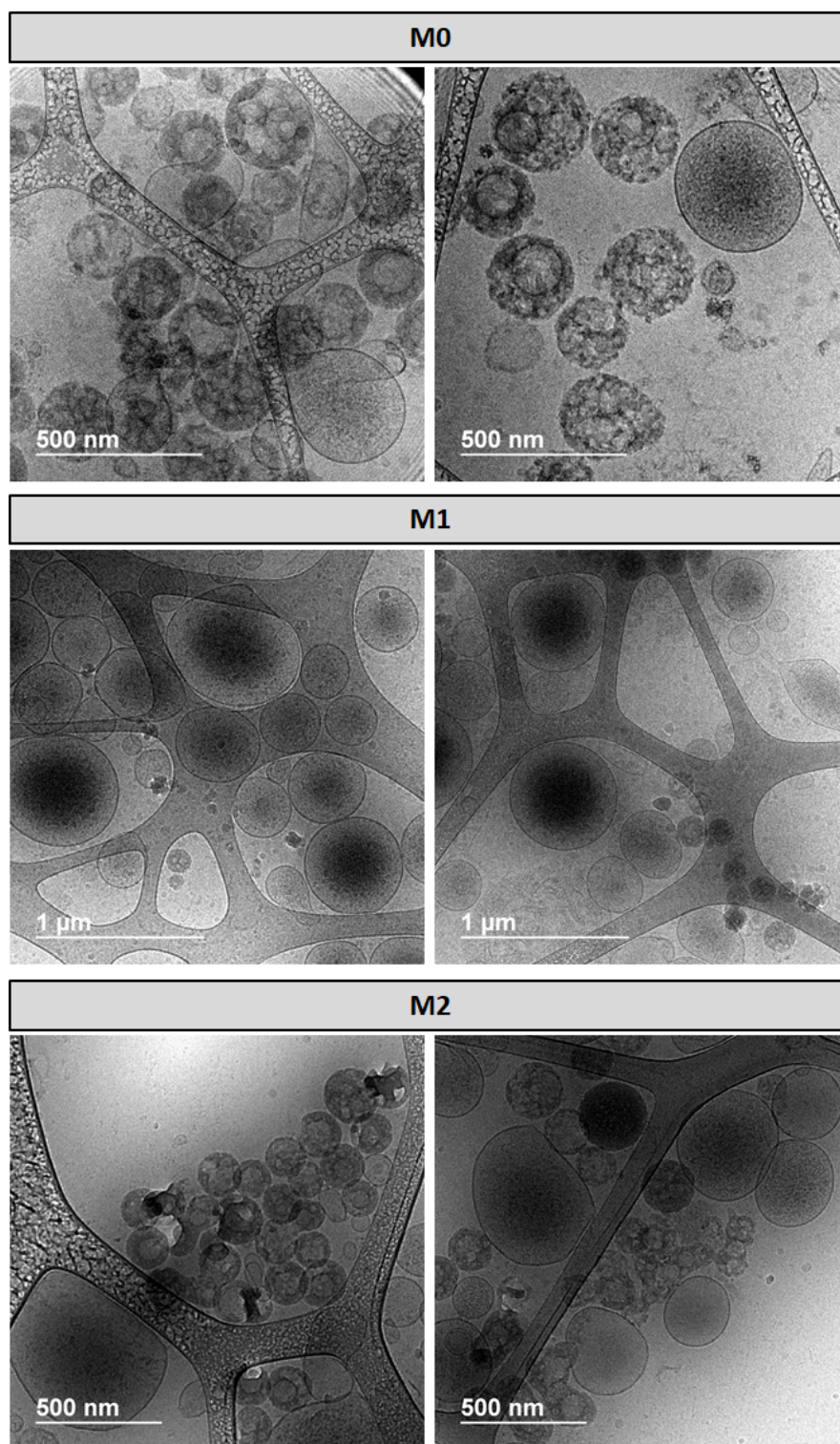


Figure 4.13: Cryo-TEM images of EVs from M0 (unpolarized), M1 (pro-inflammatory) and M2 (anti-inflammatory) macrophages after 60 minutes of centrifugation at 20,000 g.

NTA Characterization

As recommended by the ISEV [212, 213], another technique was used in addition to microscopy observations to fully characterize our samples of EVs. From preliminary tests with three standard characterization techniques (Dynamic Light Scattering DLS, Resistive Pulse Sensing RPS and Nanoparticle Tracking Analysis NTA), we have selected NTA as the most appropriate method for several reasons:

- Compared to DLS and RPS, NTA is the most suitable technique for heterogeneous samples, since it analyzes single nanoparticles flowing in the path of a beam scatter light in order to combine information on light scattering and Brownian motion. Unlike NTA, DLS collects the scattered light signal from the entire particle population at the same time. Therefore, when measuring heterogeneous samples with DLS, histograms are shifted towards larger sizes, that scatter more light. Experimentally, the invalidity of this technique for EV analysis was confirmed since the obtained histograms from different runs with the same sample did not coincide with each other. With RPS, clogging issues were encountered since the measurement is based on the flow of the sample through a pore of optimized size. Small pore size was required to detect the smallest particles, but this was responsible for clogging issues because of our highly heterogeneous EV samples.
- Particle concentrations that are required for NTA measurements are compatible with our sample concentrations and volumes, whereas it is too diluted for DLS measurements, even with micro-cuvettes (70 μ L, Sigma-Aldrich, BR759200).
- NTA provides information on both size and concentration of particles, while DLS does not measure the concentration.

A Nanosight NS300 instrument (Malvern) was used with the Nanosight NTA 3.1 software, located in the laboratory of Pr. Remy Sadoul at GIN (Grenoble Institut des Neurosciences). All measurements were performed under the same camera settings (Slider Shutter: 890, Slider Gain: 146, FPS: 25).

First, typical analysis results obtained with NTA are presented below in order to highlight some limitations that have to be taken into account for the characterization of our samples.

The detection threshold corresponds to the number of pixels that are required to consider a signal as a particle. Therefore, smaller particles can be detected by using a smaller detection threshold, but the detection threshold needs to be set above the noise value. This analysis setting is essential, as it can introduce significant bias in the resulting histograms, as demonstrated by fig. 4.14. In this case, the same videos (thus the same sample of THP-1 EVs) are processed with different values of detection threshold, from 2 to 30. As shown on fig. 4.14, the resulting histograms display significant differences according to the chosen detection threshold in terms of peak position and distribution. In particular, peaks are shifted towards smaller particle dimensions when decreasing the threshold. Thus, in our measurements, it is essential to keep the same detection threshold in order to reliably to compare different samples. **It must be noticed that this high measurement variability according to the chosen detection threshold is one of the main drawbacks of this technique: the entire population cannot be characterized with a single analysis since different size ranges are detected according to the analysis settings.**

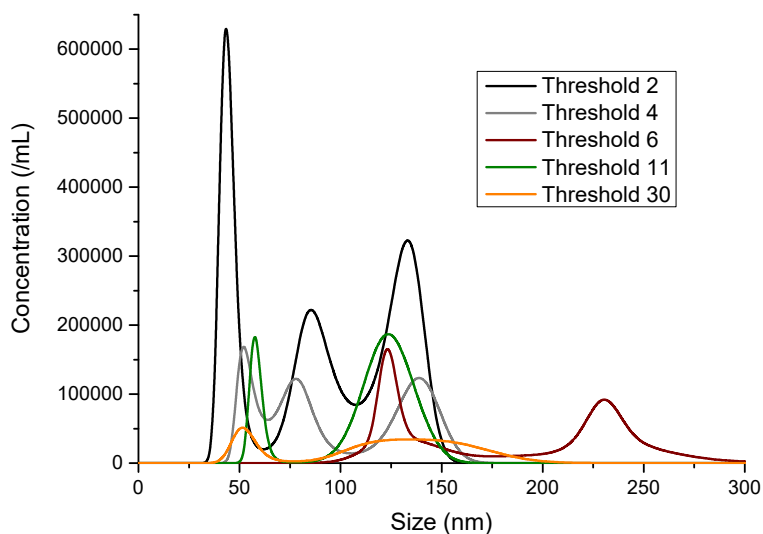


Figure 4.14: NTA histograms of the same EV sample with different detection threshold values.

Another important parameter is the camera level, which basically determines the sensitivity of the camera. When both large and small particles are mixed together, the camera sensitivity needs to be decreased to avoid any signal saturation, and the smallest particles cannot be detected anymore. This is illustrated with the same sample of THP-1 EVs at different concentrations (fig. 4.15). At initial concentration, a camera level of 9 is required to detect most EVs without saturation, and only the vesicles larger than 100 nm are detected (fig. 4.15 a). A 600 times dilution is required to get rid of large EVs and detect vesicles smaller than 100 nm (fig. 4.15 b). Thus, small vesicles are up to $5 \cdot 10^5$ times more concentrated than larger vesicles. However, they are not visible at high concentrations because of the intense signal originating from large vesicles. Therefore, **analysis of the sample at several concentrations is required to get a complete characterization of the entire EV population.**

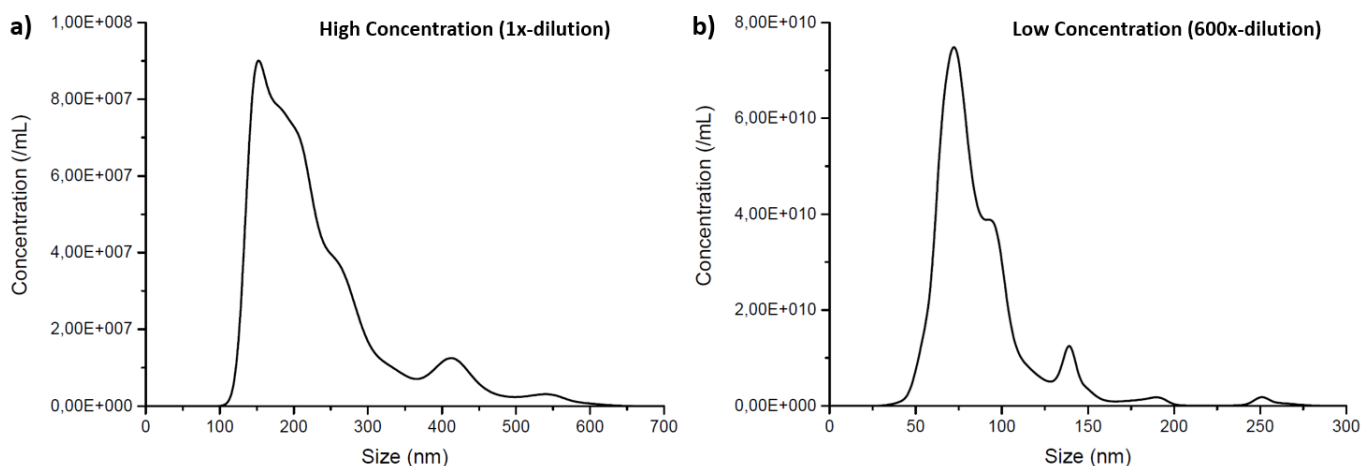


Figure 4.15: NTA histogram of a sample of THP-1 EVs at initial concentration with a camera level of 9 (a) and diluted 600 times with a camera level of 16 (b).

Taking these considerations into account, our ultracentrifugation protocol to isolate EVs from THP-1 cells (stimulated with Calcium Ionophore) was first evaluated through NTA. The standard isolation protocol with two successive centrifugation steps (at 20,000 g and 100,000g), as mentioned earlier in this Chapter, was implemented for NTA characterization of EVs at each step: in the pellet after the first 20,000 g centrifugation step (called “20 000 g” in fig. 4.16 a) and in the supernatant of this first step, that corresponds to the pellet of the second 100,000 g centrifugation step (called “20 000 g + 100 000 g” in fig. 4.16 b). The obtained EV samples were studied at the same high concentration, that does not allow to detect vesicles smaller than 100 nm. When considering this population of large EVs, **no differences in size and concentration could be detected between EVs in the pellet (20 000 g) or in the supernatant (20 000 g + 100 000 g) of the first centrifugation step** (fig. 4.16 a), which confirms cryo-TEM observations. This suggests that the first 20,000 g centrifugation step enables to remove only half of the large EVs that are initially contained in the THP-1 cell culture media. In addition, no vesicle is larger than 500 nm, even in the pellet of the first ultracentrifugation step. This supports our hypothesis with cryo-TEM observations that large EVs are laterally squeezed on the EM grid because of the limited depth of the vitrified sample. EV squeezing naturally generates a diameter increase in the TEM observation plane, where EVs are free to expand. This is certainly the reason why EVs larger than 500 nm could be observed by cryo-TEM, while they are not present in NTA histograms.

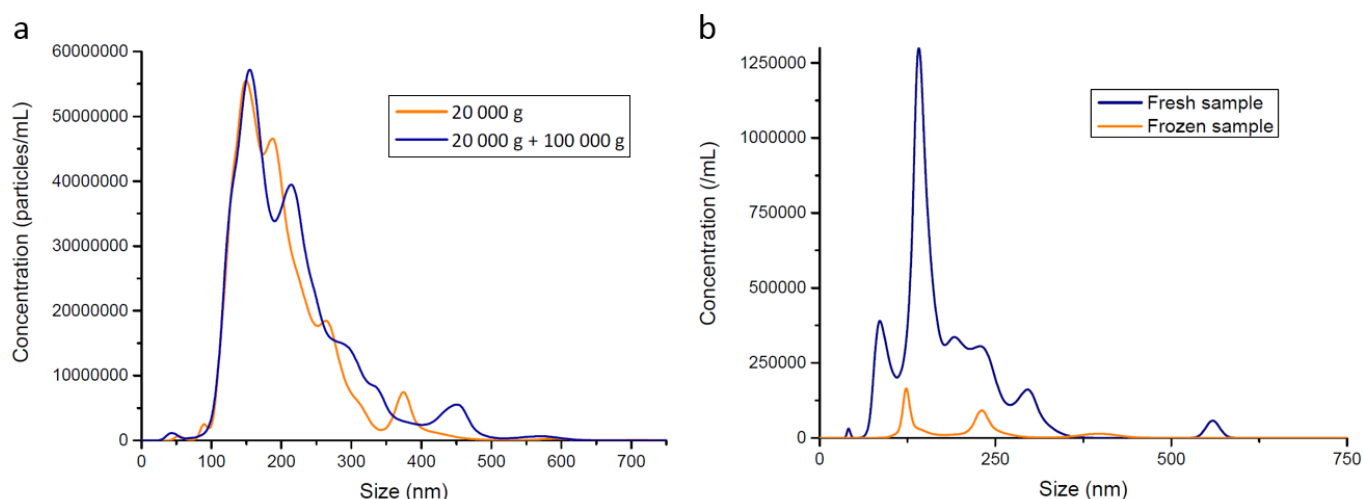


Figure 4.16: a) NTA histograms of a sample of THP-1 EVs in the pellet (20 000 g) or in the supernatant (20 000 g + 100 000 g) of a 20,000 g ultracentrifugation step. In the last case, another 100,000 g ultracentrifugation step is applied to pellet EVs contained in the supernatant of the first step. Detection Threshold = 6, Camera Level = 11. b) NTA histograms of a sample of THP-1 EVs isolated by ultracentrifugation at 100,000 g for 120 minutes, right after isolation (Fresh sample) or after freezing at -80°C for 60 days (Frozen sample). Detection Threshold = 6, Cam. Level = 8.

For reference, both conditions lead to a total EV concentration of about 6.10^9 vesicles/mL when the pellet of 10 mL of THP-1 cell culture media is collected in 1 mL of PBS.

Our isolation protocol was adapted from these observations. In order to collect the entire EV population without loss, a **single ultracentrifugation step at 100,000 g for 120 minutes** was applied to the cell culture media supernatant after the classical centrifugation steps at 300 g for 10 minutes and 1,500 g for 15 minutes (two times). This new protocol was used to extract the EV samples studied in the remainder of this section.

With this new centrifugation protocol, the influence of the storing conditions and stimulation with Calcium Ionophore on the concentration and size distribution of the isolated EVs was studied by NTA. Figure 4.16 (b) shows the NTA histograms of the same sample of THP-1 EVs right after isolation (Fresh sample) or after 60 days of freezing at -80°C (Frozen sample). **Much less vesicles are contained in the frozen sample compared to the fresh sample, with a total number of EVs of $2.6 \cdot 10^7$ in the fresh sample and $2.3 \cdot 10^6$ in the frozen sample**, after centrifugation at 100,000 g for 120 minutes of 30 mL of cell culture media. As a result, the histogram of the frozen sample only reflects the most abundant vesicle sizes around 100 nm. In addition, it can be assumed that larger EVs are more likely to break during freezing than smaller EVs since they display a lower Laplace pressure. **This study highlights that measured concentrations can be biased by the storage method, with about 10 times less EVs after a 60 day-freezing for example.**

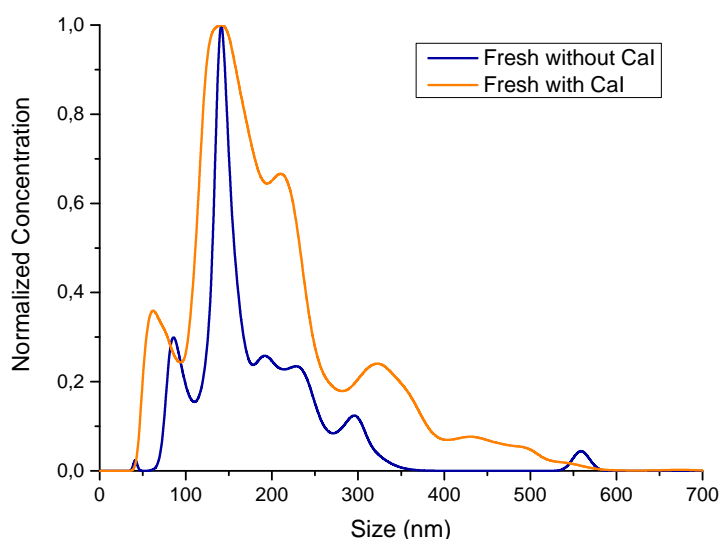


Figure 4.17: NTA histograms of a sample of THP-1 EVs isolated by ultracentrifugation at 100,000 g for 120 minutes, from stimulated (Fresh with CaI) or non-stimulated (Fresh without CaI) THP-1 cells. Detection Threshold = 6, Camera Level = 11.

Stimulation with Calcium Ionophore (CaI) was also shown to influence the concentration and size distribution of the isolated EVs. Figure 4.17 shows the normalized histograms of fresh EVs isolated from THP-1 cells with CaI stimulation, as described above in this chapter part (Fresh with CaI), or without CaI stimulation (Fresh without CaI). In both cases, EVs are isolated by a single ultracentrifugation step at 100,000 g for 120 minutes. **100 times higher EV concentration is obtained after CaI stimulation**

compared to non-stimulated cells, with a total number of EVs of about $2.6 \cdot 10^7$ without stimulation and $1.9 \cdot 10^9$ with stimulation from 30 mL of cell culture media. In terms of size distribution, it seems that CaI stimulation induces an enlargement of the histogram. The presence of larger vesicles may be due to cell damaging induced by CaI stimulation, which leads to large apoptotic bodies. This confirms that cells of interest should not be stimulated if we want to get EV properties reflective of physiological populations, for example for diagnosis purposes.

In conclusion, both cryo-TEM observations and NTA characterizations show that the standard ultracentrifugation protocol to isolate EVs leads to a wide distribution of vesicle sizes, typically between 50 nm and 500 nm. Indeed, the first ultracentrifugation step at 20,000 g is not sufficient to remove all the microvesicles and pellet only the exosomes through the second step at 100,000 g. Moreover, this isolation technique seems to damage EVs, with broken membranes and multi-layered structures. This might not be an issue for proteomic analyses that are performed after EV lysis. However, for structural and physical characterizations of EVs, a more gentle isolation technique is required to preserve physiological properties of EV populations.

4.2.2 Alternative Standard Isolation Protocols

As presented in Chapter 1, two main standard isolation techniques are available to replace ultracentrifugation or to further purify the obtained EVs: chromatography (size-based separation) and magnetic isolation (affinity-based separation). These two alternative standard protocols were implemented and protein quantification was performed and compared to ultracentrifugation (at Prof. Scott Manalis' laboratory as part of a MISTI funded exchange program).

Size-exclusion Chromatography (SEC)

SEC columns are commercially available from Izon (qEV exosome isolation kit) to increase purity of EV samples by separating EVs from soluble proteins [397, 398].

As for the ultracentrifugation protocol, THP-1 cells were cultured in RPMI 1640 (ThermoFisher Scientific, 61870) containing 10 % FBS (fetal bovine serum). THP-1 cells were then seeded at 500,000 cells/mL after centrifugation at 300 g for 10 min (eppendorf centrifuge, 5810R) and incubated for 20 min at 37 °C in 30 mL of DMEM media (gibco life technologies, 31966-021), with $30 \mu\text{mol L}^{-1}$ Calcium Ionophore A23187 (Cayman Chemical). Cells were then removed by centrifugation at 600 g for 10 min. The supernatant was filtered at $0.8 \mu\text{m}$ (Whatman Puradisc syringe filter, FP 30/0.8). A new centrifugation at 1,500 g for 15 min enabled to remove remaining cell debris. The sample was concentrated from 30 mL to 500 μL with a centrifugal filter (Amicon Ultra-15, 100K) spinned at 4,000 g. 1 mL of DPBS was added to the sample in order to collect all the EVs concentrated on the filter. The final sample volume of 1.5 mL was then injected in the qEV column for further purification of the isolated EVs.

The pink color of the DMEM media could be visually followed while flowing into the qEV column (fig. 4.18). As the column has a dead volume of 3 mL, the first 3 mL of solution flowing out from the

column are removed immediately after sample injection. Then EVs are collected in the next 1.5 mL, and the following sample is discarded as it contains smaller contaminants held up by the column. The EV sample is then concentrated from 1.5 mL to 100 μ L with a small-volume centrifugal filter (Amicon Ultra-2, 100K).

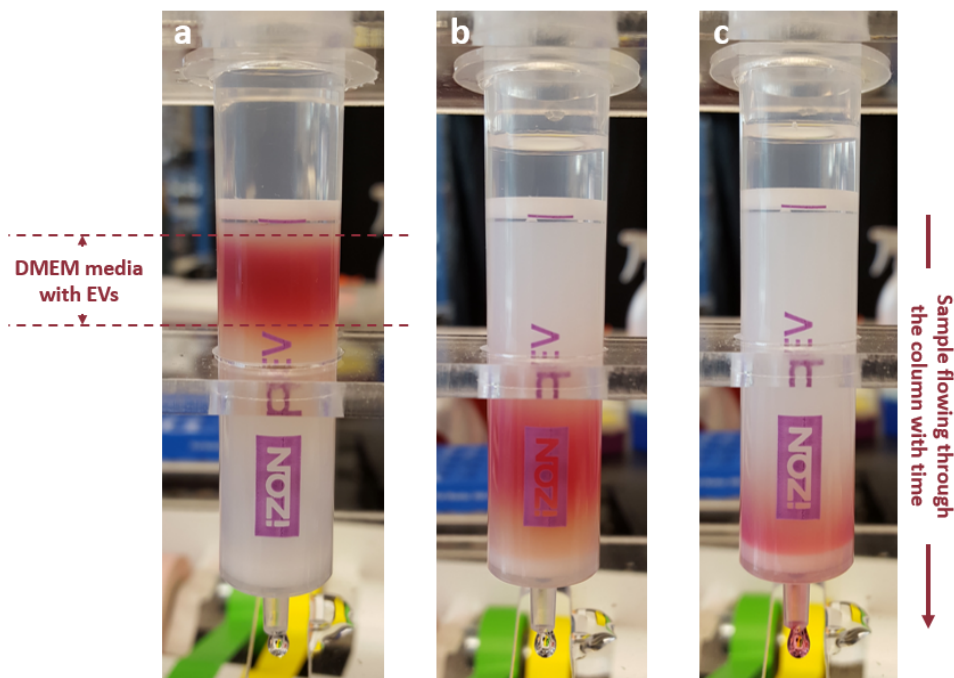


Figure 4.18: Pictures of the qEV column (Izon) during purification of the EV sample. Different time points are shown (from (a) to (c)) while the sample flows into the column (from top to bottom).

Compared to ultracentrifugation, this isolation protocol is more time-effective, since only a few minutes are required to let the sample flow through the column and collect the purified EVs. However, in order to make the column reusable, the washing protocol advised by Izon takes at least one hour, since a large volume of sodium hydroxide and surfactant solution has to be injected in the column. Moreover, reusing columns raises the issue of potential contaminants in the purified sample from previous experiments with the same column. When using only fresh columns, this protocol is quite expensive, since each column costs about \$60.

Magnetic Isolation

Magnetic isolation enables to specifically isolate EVs presenting target surface antigens, which is not possible with the other tested ultracentrifugation and SEC protocols. Here we are interested in isolating a large quantity of EVs from THP-1 cells in order to collect enough vesicles for downstream analysis steps. CD63 is known to be a common transmembrane extracellular protein [399]. Therefore, the exosome isolation kit CD63 (human) from Miltenyi Biotec was used as a third standard isolation protocol.

Similarly to the two other isolation protocols, THP-1 cells were cultured in RPMI with 10 % FBS. THP-1

cells were then seeded at 500,000 cells/mL after centrifugation at 300 g for 10 min and incubated for 20 min at 37 °C in 30 mL of DMEM media with 30 $\mu\text{mol L}^{-1}$ Calcium Ionophore A23187. Cells were then removed by centrifugation at 600 g for 10 min. The supernatant was filtered at 0.8 μm and a new centrifugation at 1,500 g for 15 min enabled to remove remaining cell debris. The sample was concentrated from 30 mL to 500 μL with a centrifugal filter and 1 mL of DPBS was added to collect all the EVs concentrated on the filter. 50 μL of magnetic beads was then added to the total 1.5 mL sample volume. The sample was incubated with the beads at room temperature for 60 minutes. A column was placed in the magnetic field of a MACS (Magnetic-Activated Cell Sorting) holder. The column was conditioned with 100 μL of Equilibration Buffer and 3 x 100 μL of Isolation Buffer. New buffer was added only when the column reservoir was empty. The EV sample with the beads was applied onto the column (fig. 4.19 a). Once all the sample volume had run through the column, 4 x 200 μL of Isolation Buffer was applied onto the column. Then, the column was removed from the magnetic holder and placed onto a 1.5 mL tube. 100 μL of Isolation Buffer was added to the the column and immediately flushed out by firmly pushing the plunger into the column. This protocol enables to collect only the EVs that are attached to magnetic beads in a final volume of 100 μL .

4.2.3 Comparison of the three Isolation Protocols

The three standard isolation protocols (UC, SEC and magnetic labeling) are compared by **protein quantification with the Bradford assay**. As presented in Chapter 1, the Bradford assay is a colorimetric-based technique to quantify the total amount of proteins after EV lysis. The color shift of a Coomassie Reagent is detected with a spectrophotometer after incubation with the sample. As the dye binds unspecifically to all the proteins of the sample, proteins from EVs cannot be distinguished from protein contaminants. Therefore, the Bradford assay is an interesting technique to compare the purity of isolated EVs with our three different protocols.

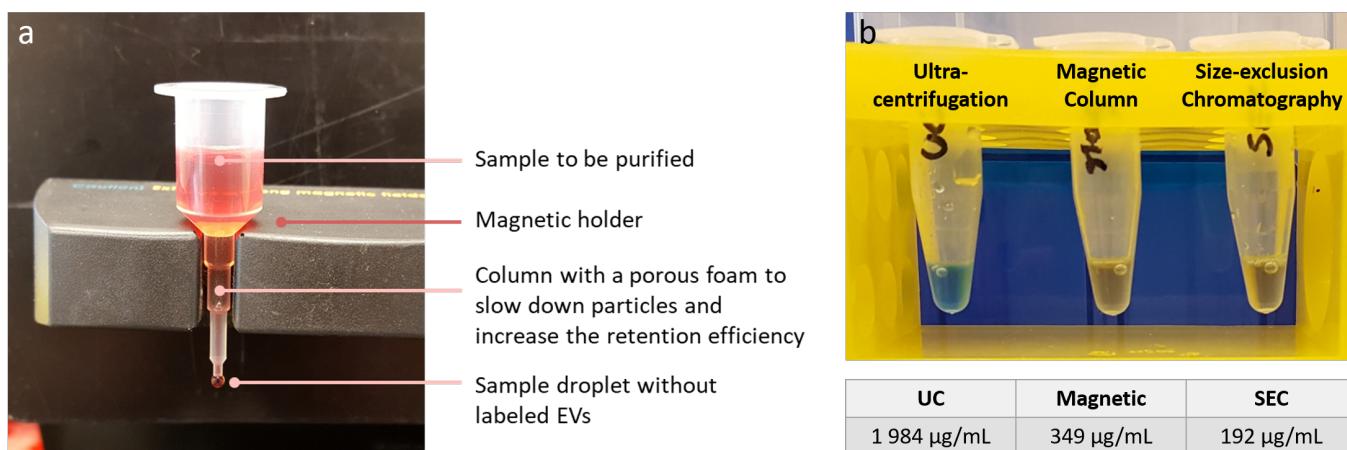


Figure 4.19: a) Magnetic isolation column (Miltenyi Biotec) after injecting the EV sample to be purified. b) Picture of the three samples of isolated EVs incubated with the Coomassie dye after purification through ultracentrifugation (UC), magnetic separation or size-exclusion chromatography (SEC). The protein concentration obtained with the Bradford assay is given for each condition.

In order to be able to compare the amount of proteins with the three purification techniques, the same initial number of THP-1 cells was used with the same stimulation condition (incubation of 30 mL of THP-1 cells at 500,000 cells/mL in DMEM media with 30 $\mu\text{mol L}^{-1}$ of Calcium Ionophore for 20 min at 37 °C). The final purified EV samples are collected in a total volume of 100 μL for the three protocols. EVs are then lysed to extract proteins through multiple temperature cycles of freezing in dry ice and thawing at 37°C. A calibration curve is first generated from absorbance measurements (NanoDrop Spectrophotometer ND-1000) of BSA (Bovine Serum Albumin) samples of known concentrations (Protein Assay Standard II, Bio-Rad) incubated with a given volume of Coomassie dye (Protein Assay Dye Reagent, Bio-Rad). It is important to select a range of BSA concentrations that corresponds to the order of magnitude of our sample protein concentrations to be identified.

First, all our three samples are diluted 50 times in the same amount of dye reagent. Differences in the protein concentration are clearly visible between the three conditions (fig. 4.19 b). Ultracentrifugation (UC) leads to an intense blue color, suggesting a much higher protein concentration compared to the two other isolation protocols, for which the protein concentration does not lead to a visible color change of the Coomassie dye. In order to quantify the absorbance value of our samples, a 250X-dilution in the dye reagent was required for the UC sample, while a 5X-dilution allowed to detect proteins in the magnetic and SEC samples. The obtained protein concentrations are given for each isolation protocol in the table of fig. 4.19 (b).

The protein concentration with the ultracentrifugation protocol is 6 times higher compared to the magnetic protocol and 10 times higher compared to the SEC protocol, which is in agreement with previous studies showing that ultracentrifugation leads to higher protein contamination rates [400]. This result was expected since ultracentrifugation does not enable to selectively extract EVs from other contaminants of similar densities, while the two other protocols either target a specific surface antigen or separate EVs from smaller contaminants. Theoretically, higher EV concentrations (and so protein concentrations) should be obtained with the SEC protocol since it isolates the entire EV population, while the magnetic protocol targets the subpopulation expressing CD63.

Two hypotheses could explain that more proteins are detected with the magnetic protocol compared to SEC:

- In addition to THP-1 EVs, contaminants may also present surface CD63 antigens (such as cell debris) and participate in the total amount of proteins after magnetic isolation. These contaminants are not collected in the same fractions as EVs if they display smaller dimensions.
- With the SEC protocol, small EVs may be delayed in the column (similarly to protein contaminants), which does not enable to collect them in the first fractions. With the magnetic isolation, all EVs presenting CD63 surface antigen are collected, irrespective of their size.

In conclusion, SEC and magnetic isolation enable to improve the purity of the isolated EVs compared to ultracentrifugation, regarding the protein content of the extracted samples. Magnetic isolation has the advantage of targeting a specific subpopulation of EVs that present surface biomarkers of interest.

However, the main issue of the standard isolation protocol is that it requires sample manipulation at each step. Thanks to a combination of DLD and magnetic capture, here we show that the entire isolation protocol can be integrated in portable and automated microfluidic cartridges.

4.2.4 Microfluidic Extraction of Extracellular Vesicles including DLD

The selected strategy to isolate EVs from cell culture media with a two-step integrated microfluidic protocol was based on conclusions from previous experiments:

- DLD has several advantages over other sample preparation techniques for EV purification: it preserves the integrity of the vesicles, it is fast for pillars at the micro-scale and it provides a portable and automated device with minimized sample manipulation steps. Previous results with both model beads and biological samples showed that DLD efficiently depletes large contaminants (typically above 2 μm), however, the currently available nano-DLD devices are challenging to use for the separation of submicronic particles. Therefore, with the implemented designs, DLD seems to be well appropriate for the first purification steps to remove cell contaminants, but another complementary technique is required to extract EVs from the DLD-purified media.
- Among the standard isolation techniques, the most promising one seems to be magnetic capture on beads since it enables to extract a specific EV subpopulation (presenting specific protein biomarkers) with an easy integration on chip.

Therefore, here we propose to combine DLD with a magnetic isolation on functionalized beads with minimized sample manipulation.

Integrated Microfluidics to replace Standard Protocols

The standard magnetic isolation protocol implemented in the last section is summarized in fig. 4.20. After stimulating THP-1 cells with calcium ionophore, the cell culture media is subjected to a low-speed centrifugation step to remove the cells. Then, the supernatant is filtered and centrifuged at higher speed to remove cell debris and contaminants with densities larger than those of EVs. Instead of using ultracentrifugation, EVs are concentrated thanks to a centrifugal filter, before incubation with beads and magnetic separation on a MACS column. Each step of this protocol requires sample manipulation, which is time-consuming and increases the contamination risks.

Current Protocol (sample manipulation at each step)



Figure 4.20: Successive steps of the standard magnetic isolation protocol implemented in the last section.

The volume histogram of particles was studied in the sample throughout the different purification steps, thanks to a Coulter Particle Analyzer (Multisizer 4e Coulter Counter model, Beckman Coulter). Determination of the particle volume is based on the Coulter principle from measurements of the resistance change when particles flow between two electrodes. In the initial sample (fig. 4.21 (1)), a large peak is obtained for volumes between about $500 \mu\text{m}^3$ and $10^4 \mu\text{m}^3$ (which corresponds to diameters between $5 \mu\text{m}$ and $13 \mu\text{m}$). This peak is characteristic of THP-1 cells, while the smaller detected volumes correspond to cell debris and smaller contaminants. The first centrifugation step at 600g clearly enables to remove all the THP-1 cells and about half of the smaller contaminants (fig. 4.21 (2)). The filtration step efficiently eliminates most cell debris (fig. 4.21 (3)), while the second centrifugation step at 1500g does not provide significant further purification (fig. 4.21 (4)). Indeed, the volume histogram obtained after this additional purification step is similar to that obtained after a simple filtration. Therefore, **the centrifugation step at 1500g seems not to be required for the purification of our samples when filtration is used upstream.**

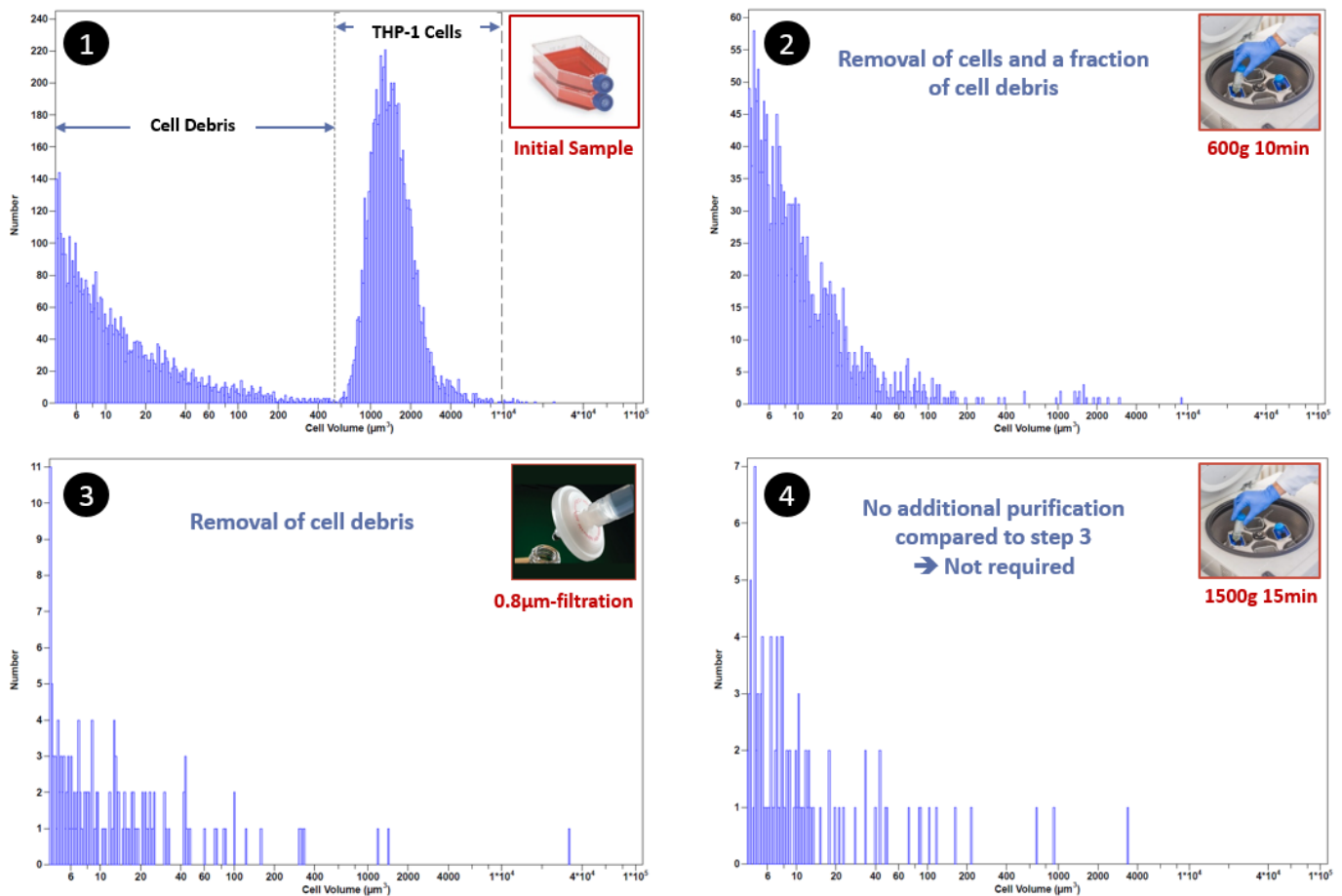


Figure 4.21: Coulter particle analysis of the initial sample of cell culture media (1), after centrifugation at 600g for 10min (2), filtration at $0.8 \mu\text{m}$ (3) and centrifugation at 1500g for 15min (4).

Each step of the standard isolation protocol was adapted to microfluidics in order to propose a completely integrated sample preparation platform with minimized sample manipulation (fig. 4.22):

- The standard protocol uses an initial sample volume of 30 mL at 500,000 cells/mL. In our microfluidic platform, it is challenging to store and handle volumes larger than about 2 mL without sample manipulation. Therefore, we will first validate our isolation protocol with a reduced initial sample volume of 2 mL. The main possible issue when reducing the initial sample volume is to have not high enough concentration of EVs to perform downstream analysis. If this problem is encountered, we will consider increasing the concentration of THP-1 cells in the initial 2 mL volume (higher than the current 500,000 cells/mL concentration).

Conversion into an integrated microfluidic protocol (no sample manipulation)

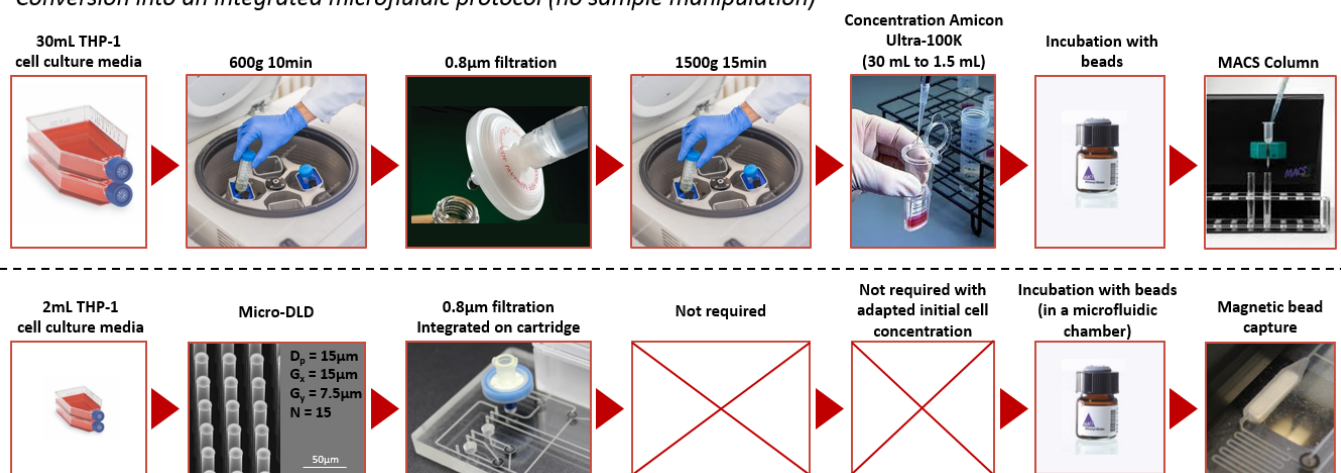


Figure 4.22: Illustration of the different purification steps of our microfluidic protocol, corresponding to each step of the standard magnetic-based protocol.

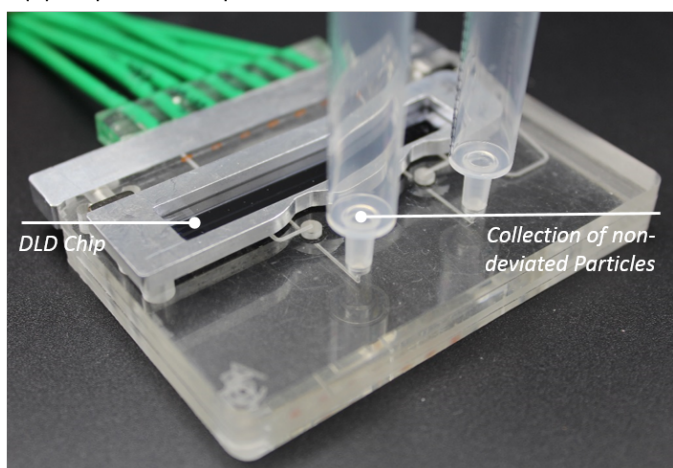
- DLD replaces the first centrifugation step to remove THP-1 cells from the initial sample of cell culture media. The DLD design selected for this application is chosen with asymmetric gaps since this feature has previously shown to improve the deviation efficiency. Considering the heterogeneous diameters of THP-1 cells from about $5\mu\text{m}$ to $13\mu\text{m}$, the Design 6 of Group 3 Version 2 seems well appropriate ($D_p = 15\mu\text{m}$, $G_y = 15\mu\text{m}$, $G_x = 7.5\mu\text{m}$, $N = 15$, $D_c \in [5;10]\mu\text{m}$). Indeed, THP-1 cells tend to be squeezed between pillars under the flow, which confers them a smaller effective dimension. Moreover, as we are interested in collecting small particles while removing the largest possible fraction of cells, it is not an issue in our case to experience cell clogging in the pillar array, as long as this clogging does not disturb the sample flow. For these two reasons, it is preferred to use an inter-pillar spacing that is close to the cell diameter.
- The filtration step is conserved in our microfluidic protocol to remove any cell debris and other small contaminants. The filter is simply plugged onto the cartridge so that it can be easily replaced at each new experiment.
- As demonstrated from volume histograms in fig. 4.21, the second centrifugation step is not required to further purify the sample after filtration. Therefore, this step will not be implemented in our microfluidic protocol. In a future version of this device, the filtration step could be replaced by a

second integrated DLD step of 0.8 μm critical diameter. One of the integration techniques presented in the next Chapter could be implemented for that purpose.

- The concentration step is used in the standard protocol to decrease the sample volume from 30 mL down to 1.5 mL, before incubation with magnetic beads. In our microfluidic protocol, this step is not required since the initial volume is already sufficiently low. However, we will have to make sure that the initial EV concentration is large enough to detect them after the magnetic purification.
- The incubation with beads is performed in an incubation chamber plugged onto the cartridge. A removable cover on the chamber enables to manually add the beads and mix them with purified EVs through pipetting. This step will be first carried out manually in order to ensure effectiveness of the mixing, but future improvements could enable to automatically inject the beads in the chamber and mix them with EVs (for example by actuating a flexible membrane, as those presented in the next Chapter).
- After incubation, beads are captured in another microfluidic chamber in contact with a magnet. Bead collection is performed thanks to automated cycles of sample injection at a controlled flow rate in the capture chamber. Beads are then released by removing the magnet and injecting a small volume of new buffer towards a small collection chamber that can be pipetted for further analysis steps.

Two cartridges are used to implement the overall sample preparation. A first cartridge (fig. 4.23 a) integrates the DLD purification and collects the output sample in a syringe that is directly plugged onto the cartridge. Then, a single user manipulation step enables to connect the syringe to a new cartridge (fig. 4.23 b) that integrates all the next steps. The sample is automatically pumped through the filter towards the incubation chamber, in which the magnetic beads are added and manually mixed with the sample. After incubation, the sample is transferred to the collection chamber where the position of the magnet is controlled to maximize the collection yield. Extracted beads can then be collected in the collection chamber with a pipet for further treatment or characterization of the sample.

(a) Step 1: DLD Separation



(b) Step 2: Magnetic Capture

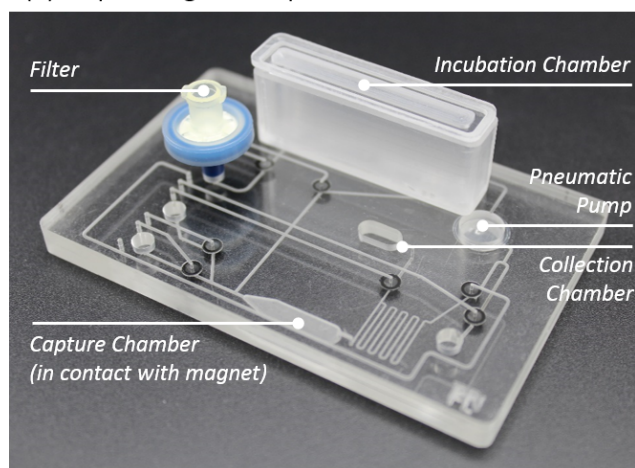


Figure 4.23: Cartridges for the DLD purification (a) and magnetic capture (b).

The position of the magnet, as well as the fluidic and pneumatic actuation in the magnetic capture cartridge (step 2) are automatically regulated thanks to an automated instrument (fig. 4.24) without any sample manipulation. This instrument was developed by Remco Den Dulk and Camille Echampard as part of another project dealing with RNA extraction from lysed blood samples.

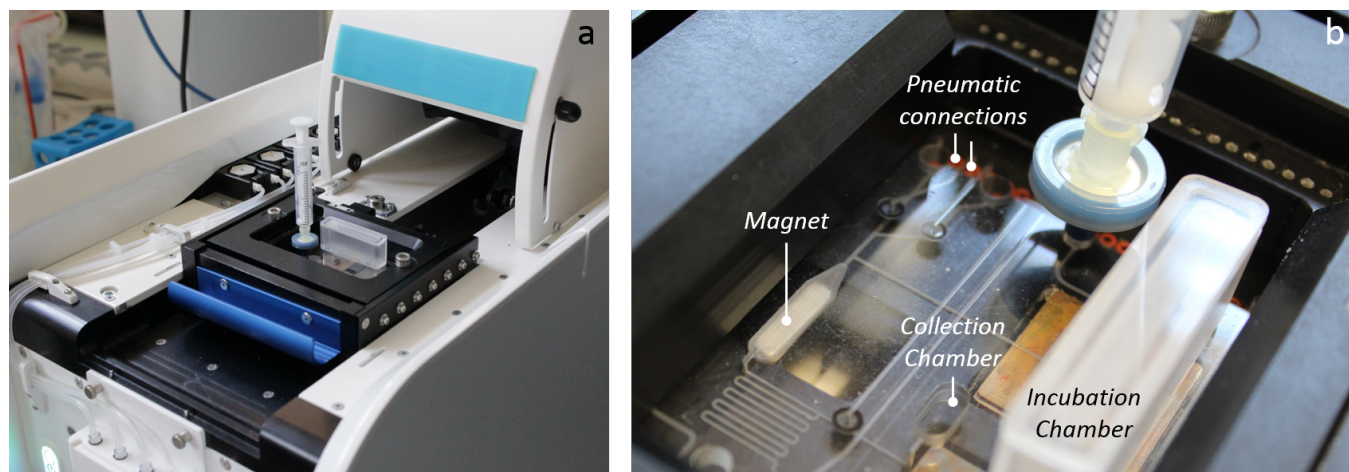


Figure 4.24: (a) Picture of the instrument that automatically actuates the position of the magnet and the fluidic and pneumatic inlets of the magnetic isolation cartridge. (b) Close-up view of the magnetic isolation cartridge in the instrument.

Optimization of the first Purification Step: DLD removal of Large Contaminants

First, the DLD purification step was optimized in order to obtain the same cell depletion efficiency compared to the centrifugation step of the standard protocol. Two main conditions were analyzed to maximize the deviation of THP-1 cells: **the injection flow rate and the chip surface conditioning**. For each condition, the number of cells and cell debris was determined with a Coulter Counter in the initial sample and in both deviated and non-deviated DLD outlets. From these measurements were determined the cell recovery yield (total number of cells in both DLD outlets compared to the initial number of injected cells), the percentage of deviated cells (number of cells in the deviated DLD outlet compared to the total number of cells in both outlets) and the percentage of non-deviated cell debris (number of particles in the non-deviated DLD outlet compared to the total number of cell debris in both outlets) (fig. 4.25).

The range of tested flow rates was chosen to ensure both a stable control of the input pressure and an efficient fluidic sealing. The conditioning conditions were inspired from previous reported work [401], using Kolliphor or Pluronic nonionic copolymer-based buffers to decrease nonspecific attachment of CTCs to DLD surfaces.

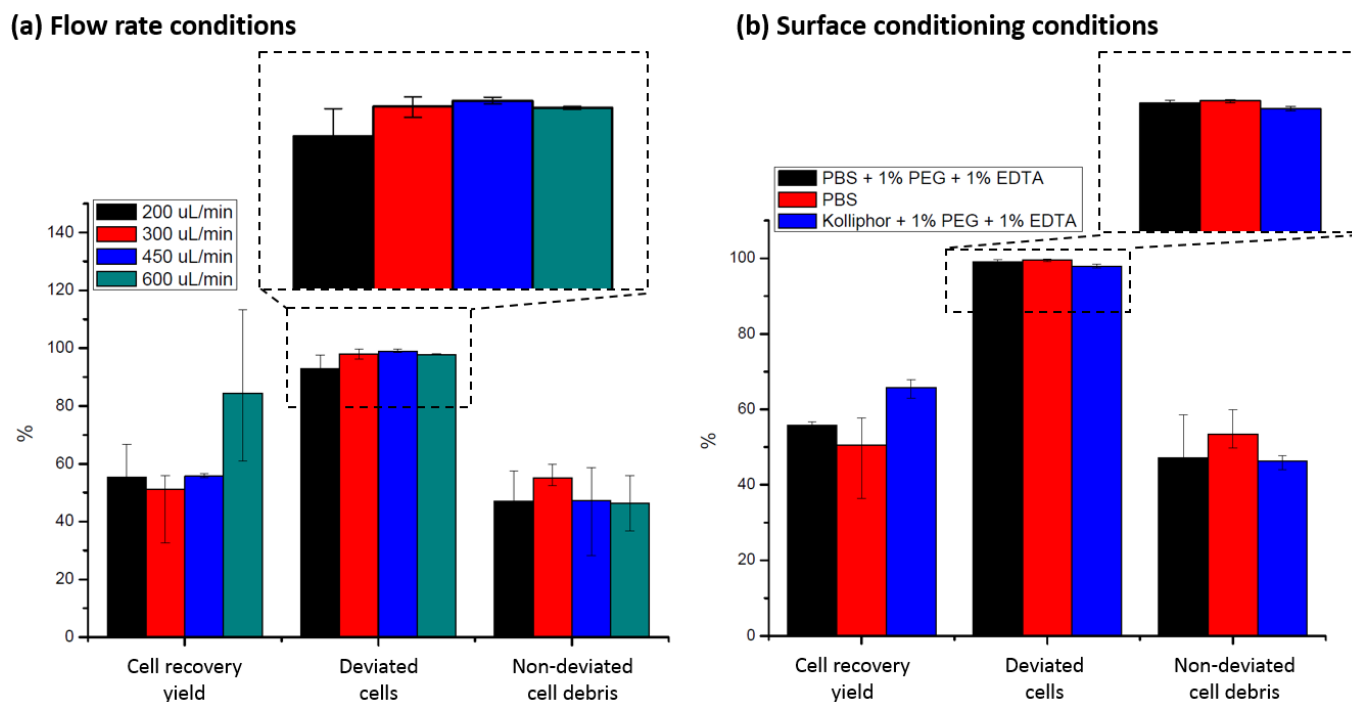


Figure 4.25: Quantification of the cell recovery yield, the percentage of deviated cells and the percentage of non-deviated cell debris for different flow rate conditions (at a given conditioning condition: PBS + 1% PEG + 1% EDTA) (a) and for different surface conditioning conditions (at a given flow rate condition of 450 $\mu\text{L}/\text{min}$) (b).

From the results presented in fig. 4.25, the best DLD performances are obtained for a flow rate of 450 $\mu\text{L}/\text{min}$ and a PBS conditioning:

- *Flow rate conditions:* Similar performances are obtained with the four tested flow rate conditions, with a ratio of deviated cells larger than 95 %. This is in accordance with the DLD property of flow rate independency. In this section, experiments will be performed at a flow rate of 450 $\mu\text{L}/\text{min}$ in order to maximize both the deviation efficiency and the cell recovery yield. Indeed, lower flow rates tend to increase cell aggregation between pillars. Higher flow rates slightly degrade the ratio of deviated cells through higher cell squeezing that decrease cell effective sizes.
- *Surface conditioning conditions:* Surface conditioning with Kolliphore (+ 1% PEG + 1% EDTA) effectively decreases cell interactions with DLD surfaces and increases the total cell recovery yield, but also slightly reduces the ratio of deviated cells. A simple conditioning with PBS seems to be the most appropriate condition in our case to maximize the deviation efficiency of cells, as well as the collection rate of small particles.

These optimized conditions are implemented to obtain the volume histograms presented in fig. 4.26 for the initial sample of cell media and for both the deviated and the non-deviated samples at the DLD outlets. The characteristic peak corresponding to THP-1 cells in the initial sample is also found in the sample at the deviated DLD outlet, with a significant loss of particles (especially for cells of larger dimensions). This result is in accordance with the previously reported cell recovery yield of about 50 - 60 % under these operating conditions (fig. 4.25). In our case, we are interested in collecting the non-deviated sample that contains EVs. It is verified in fig. 4.26 that this sample displays a negligible number of residual THP-1 cells and mostly contains particles smaller than 3 μm .

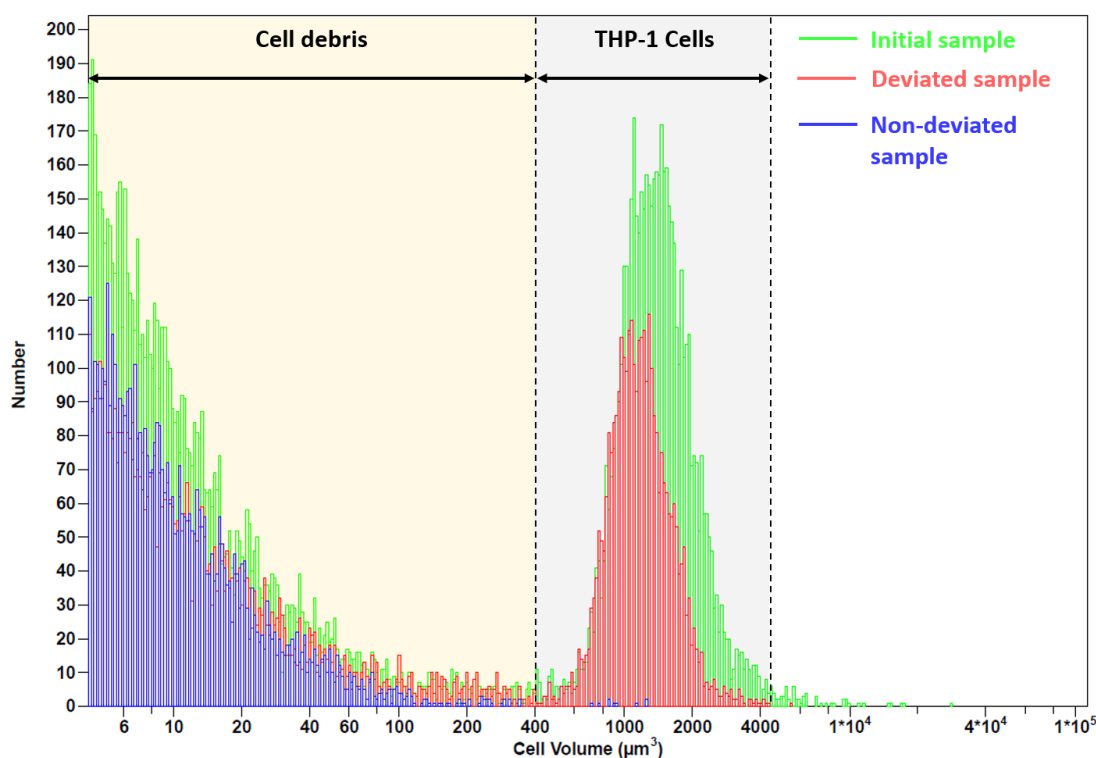


Figure 4.26: Volume histograms of the initial sample of cell culture media at 500 000 cells/mL (in green), particles collected in the deviated DLD outlet (in red) and particles collected in the non-deviated DLD outlet (in blue).

The last validation step to replace centrifugation with DLD is to compare samples obtained after centrifugation and after DLD purification. From the volume histograms of the initial sample, the non-deviated DLD outlet and the supernatant of a 600g/10min centrifugation, similar performances are obtained for both purification techniques, with a complete removal of the THP-1 cells (fig. 4.27). Quantification of the collected “small particles” (below 400 μm^3) and discarded “large particles” (above 400 μm^3) shows that DLD actually allows to collect a larger amount of small particles, with similar depletion yield of large particles compared to centrifugation. Therefore, **DLD can be used to replace the first centrifugation step of the standard protocol with similar purification performances.**

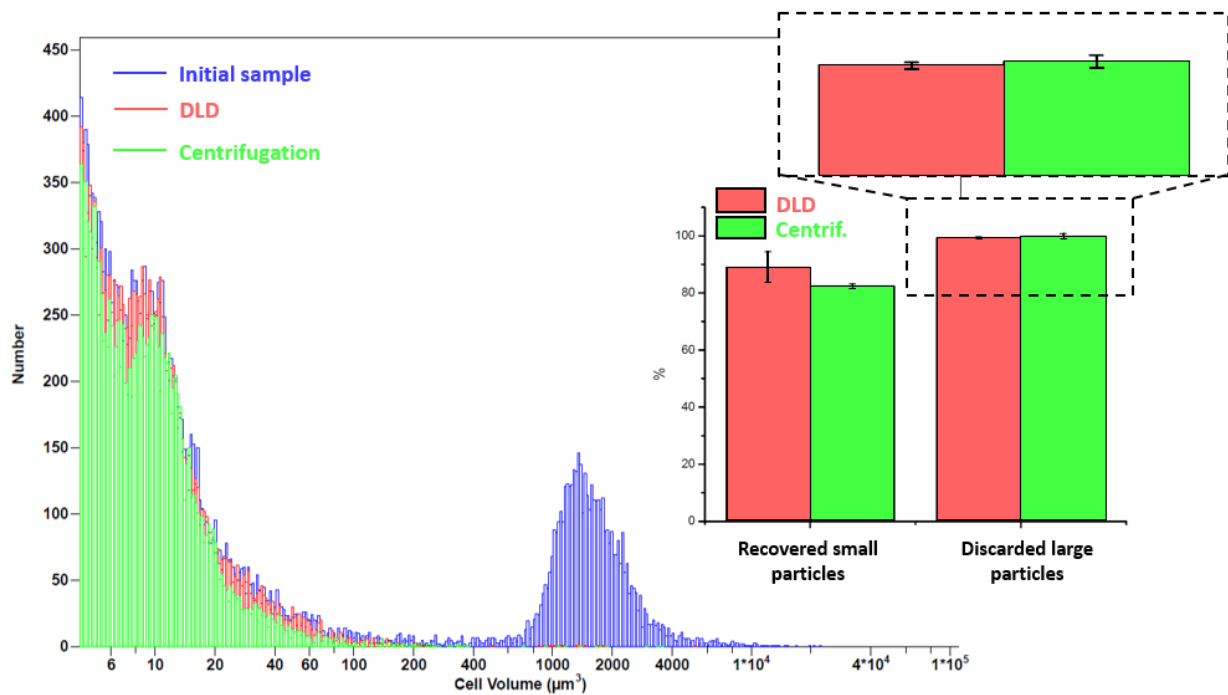


Figure 4.27: Volume histograms of the initial sample of cell culture media at 500 000 cells/mL (in blue), particles collected in the non-deviated DLD outlet (in red) and particles collected in the supernatant of a 600g/10min centrifugation cycle (in green). From these histograms is quantified the ratio of collected small particles (below 400 μm^3) and discarded large particles (above 400 μm^3), compared to the number of respectively small and large particles in the initial sample.

Optimization of the second Purification Step: Magnetic Extraction and Concentration of target EVs

The previous section enabled to find the optimized DLD conditions (DLD design, flow rate and surface treatment) in order to obtain similar purification performances compared to the first centrifugation step of the standard EV extraction protocol. After removal of cell and cell debris with DLD and on-chip filtration, a second microfluidic cartridge enables to perform the specific extraction of CD63+ EVs with the same kit from Miltenyi Biotec as presented in the last section of standard isolation protocols.

Microfluidic Steps of the Magnetic Extraction Cartridge

The successive automated steps of our microfluidic protocol for EV magnetic extraction are given in fig. 4.28:

- 1) After DLD purification and on-chip filtration, the sample is injected in the incubation chamber and anti-CD63 functionalized nanobeads (Exosome Isolation Kit CD63, human, Miltenyi Biotec, 130-110-918) are added to target CD63+ EVs through a 1 hour incubation at room temperature.
- 2) The vacuum pump is activated to suck the sample (with magnetic-targeted EVs) towards the extraction chamber that contains the magnet.

- 3) Beads (with targeted EVs) are captured on the magnet and the non-captured sample is discarded from the vacuum pump to the waste syringe.
- 4) Magnetic beads are released by removing the magnet from the extraction chamber, and a collection solution (in our case DPBS) is injected through a new inlet to collect the purified EVs in the collection chamber.

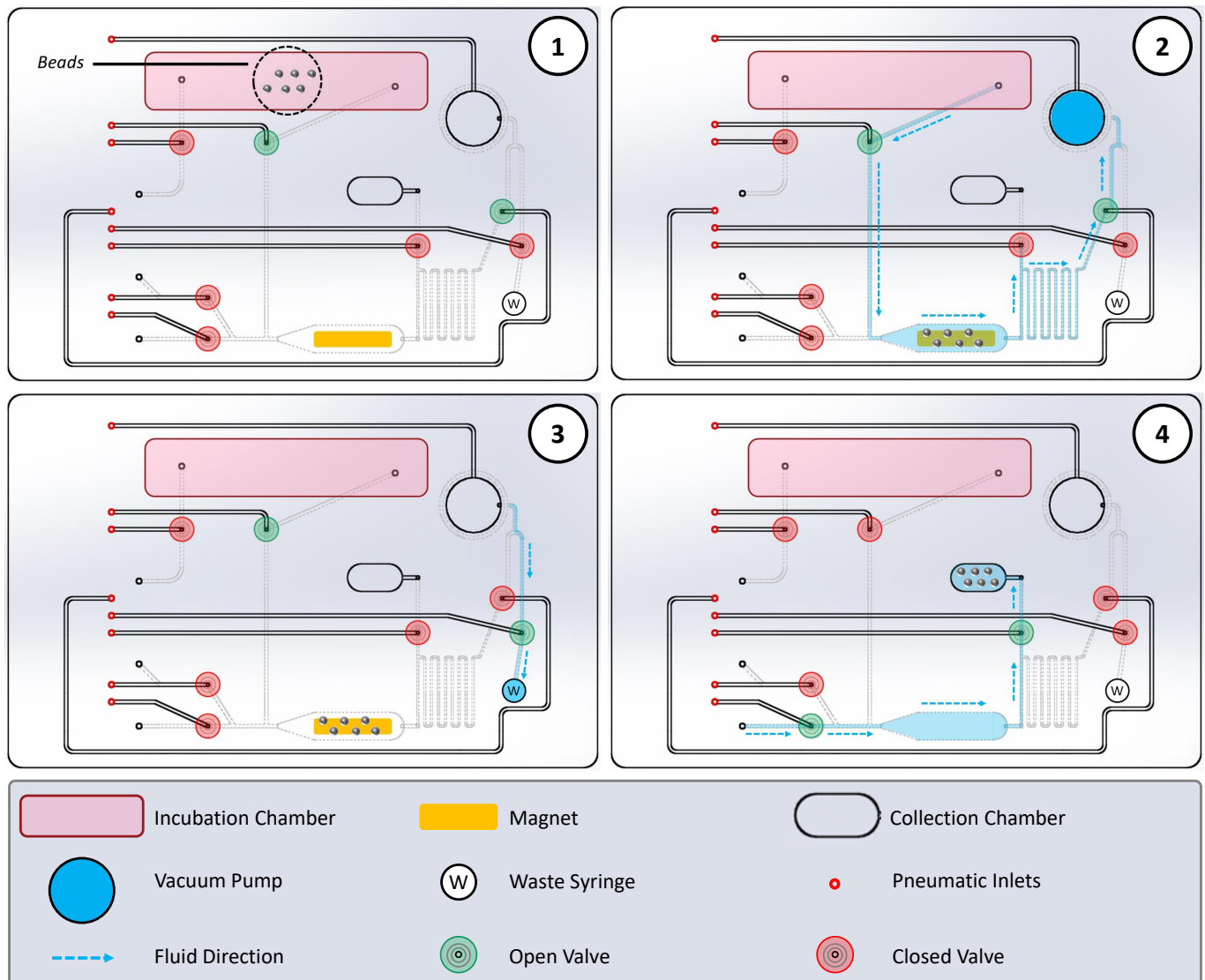


Figure 4.28: Schematic representation of the 4 microfluidic steps for automated EV magnetic capture on chip.

The use of a vacuum pump enables to reduce the risk of sample leakage, compared to pressure injection. Each pumping cycle enables to inject 200 μL of sample (determined by the volume of the vacuum pump).

Therefore, several cycles (steps 2 and 3 above) were performed to process the entire sample volume of 2 mL. All these steps were automated to control the actuation of valves, the injection time and the motion of the magnet.

The capture efficiency is mainly determined by the **affinity between functionalized beads and target EVs**, which is given by the chosen extraction kit from Miltenyi Biotec. However, our platform needs to be optimized in order to **capture the highest number of beads (and so the highest number of target EVs)**, and obtain the highest concentration ratio. This optimization was performed by NTA characterization of the collected beads after our magnetic protocol, compared to the initial concentration of beads in the incubation chamber.

Optimization of the Bead Concentration Ratio

Beads were injected in the incubation chamber at the working concentration required to capture CD63+ EVs, ie at $3.5 \cdot 10^9$ beads/mL (as recommended by the manufacturer). This initial solution was characterized by NTA (black dotted curve on fig. 4.29). A main peak was obtained around 65 - 80 nm, which is in accordance with the manufacturer information on the bead diameter.

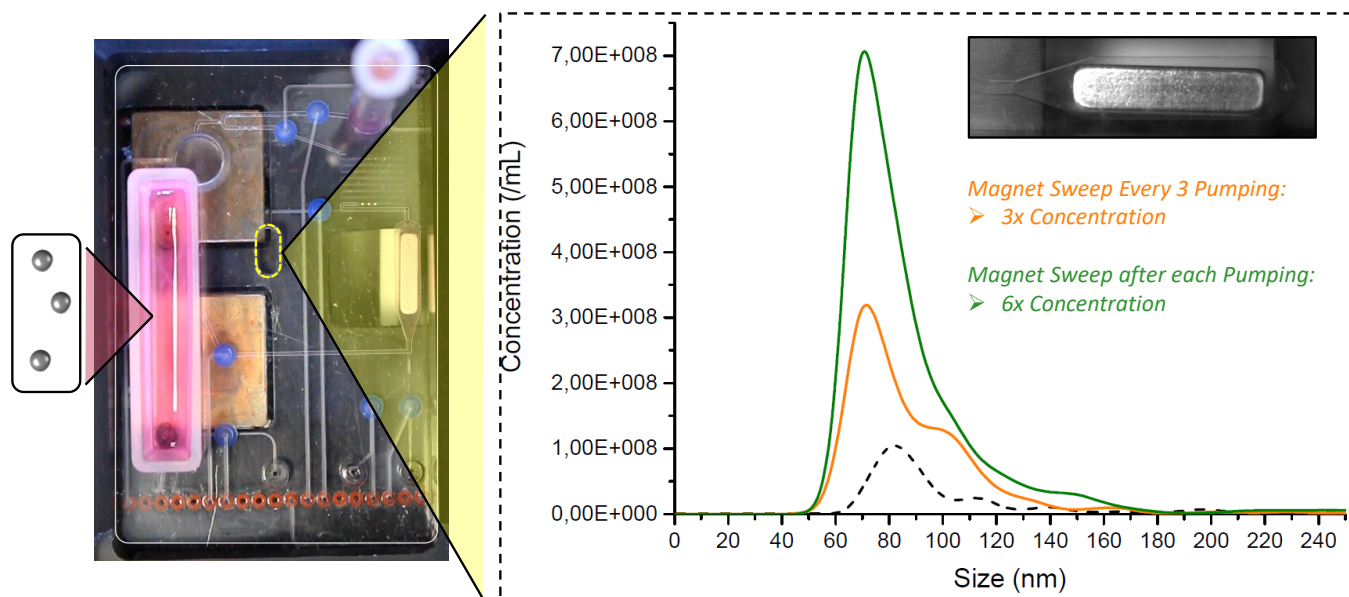


Figure 4.29: NTA characterization of the bead sample: before the magnetic extraction in the incubation chamber (black dashed line) and after the magnetic extraction with two different magnet sweep parameters (orange and green curves).

Two protocols were tested in order to maximize the concentration of collected beads after on-chip capture on the magnet: in the first protocol (in orange), a magnet sweep was performed in the capture chamber **every three pumping cycles**, while in the second protocol (in green), a magnet sweep was performed **after each pumping cycle**. All other parameters were identical in both protocols. The up-and-down magnet

sweep enables to capture beads from the entire capture chamber, including those that flow near the chamber walls. The NTA analysis of the collected sample after both protocols gives a 3x concentration factor with the first protocol, while **the second protocol enables to improve it up to 6x concentration factor**. Thus, a magnet sweep was performed after each pumping cycle in the next experiments. Further improvements could be performed to further increase the concentration factor (and reach the 30x concentration ratio obtained with the commercially-available magnetic column from Miltenyi Biotec), such as optimized flow rates, magnet parameters and pumping volumes.

The protocol proposed here was applied to the extraction of CD63+ EVs with our microfluidic cartridge. NTA analysis was used to characterize the purified sample and compare it to both bead and EV references.

Characterization of the EV magnetic extraction on-chip

In this section, beads were incubated with the sample obtained after DLD purification and on-chip filtration and the purified sample was characterized by NTA after magnetic extraction on-chip. The obtained histogram (black curve on fig. 4.30) was compared to which obtained after on-chip capture of beads alone (bead control, dashed black line) and after collection of the EV sample without beads (EV control, orange line). In this last case, no capture occurs since EVs are not magnetically labelled, and we simply collect the same unpurified EV sample as injected in the incubation chamber.

Several observations arise from this NTA analysis:

- In both the sample graph and the bead control, a main peak is observed around 65 nm, which corresponds to free functionalized nanobeads. This means that **in the sample of interest, some beads are not attached to EVs**, either because beads are in excess compared to the EV concentration, or because the affinity between beads and EVs is not high enough.
- Differences are observed between the sample graph and the bead control for sizes larger than 100 nm. When looking at the close-up view of this graph area, we can see that the sample graph actually displays three main peaks for sizes between 100 and 350 nm. Two of these peaks have a **similar distribution to which of the EV control, with a 65 nm shifting towards larger sizes in the sample graph compared to the EV control**. This suggests that these two peaks might correspond to EVs captured on beads, since the 65 nm shifting corresponds to the bead diameter.
- The third peak in the sample graph around 130 nm is aligned with the main peak of the EV control, which suggests that this peak might correspond to free EVs in the sample that have not been captured by beads. This also suggests that beads might not be in excess compared to the EV concentration and both free beads and free EVs are still collected in the sample after incubation, which implies that **the affinity technology between beads and EVs can be further improved**.

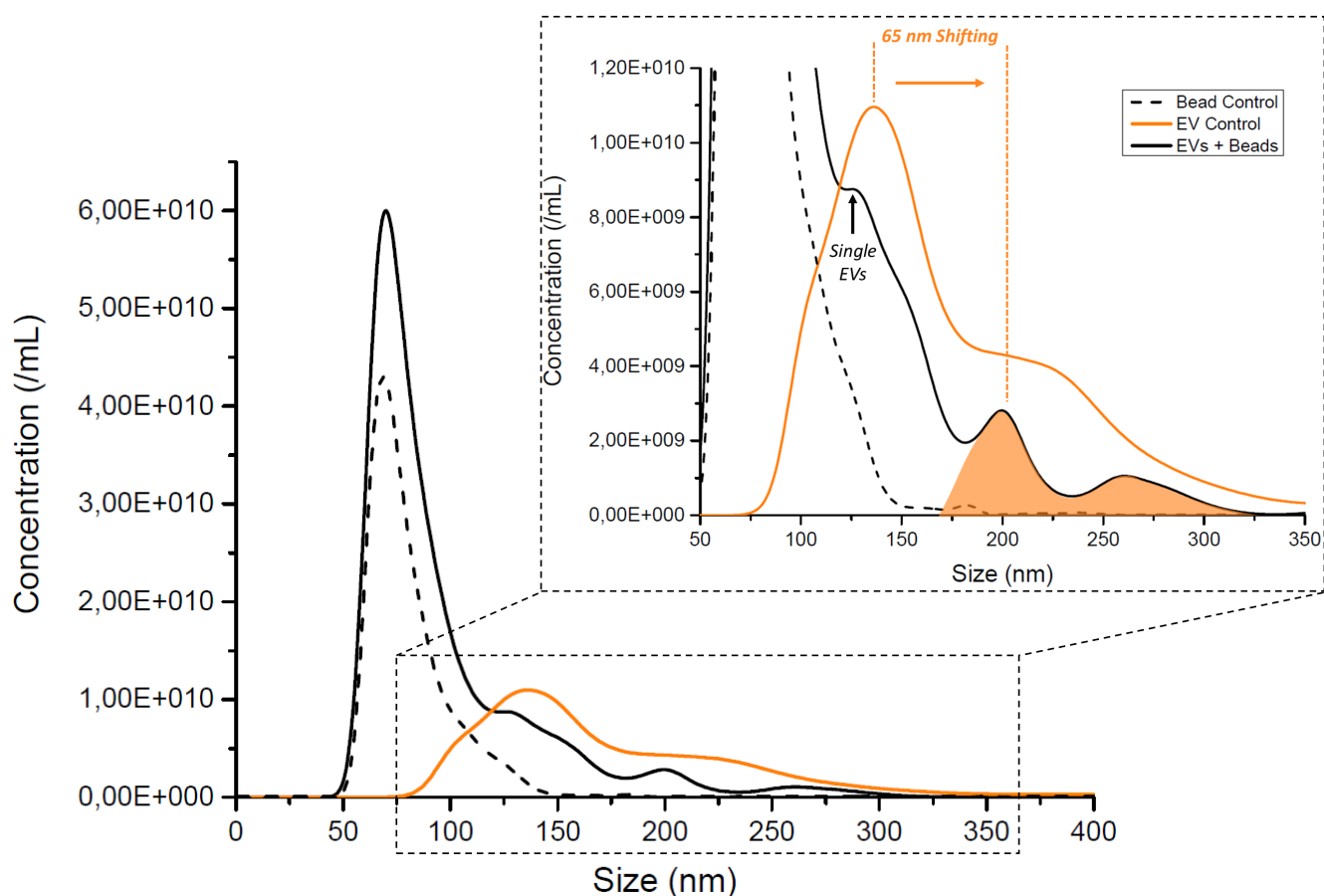


Figure 4.30: NTA characterization of the purified EV sample (black curve) and comparison to the bead reference (dotted black) and the EV reference (orange). Close-up view of the dashed area from 50 to 350 nm.

Overall, these preliminary data are very encouraging to demonstrate that captured EVs can be extracted and concentrated by our automated microfluidic device, even if further improvements will be required regarding the bead-EV affinity and the cartridge concentration factor. In addition to the automatization of the purification protocol, another advantage of the presented microfluidic platform is the ability to directly connect the sample preparation step to the characterization step without any external sample manipulation. For example, EV analysis with Suspended Nanochannel Resonators (SNRs) (presented in Chapter 1 among emerging EV characterization techniques [239]) could benefit from an integrated microfluidic EV extraction technology to provide an automated device for EV biophysical characterization including both sample preparation and analysis. Compared to other available characterization techniques, SNRs have the capacity to be directly connected to sample preparation (unlike TEM) and do not introduce any measurement bias (unlike NTA).

Chapter Summary: DLD Purification of Biological Samples

- Following the characterization of our DLD devices presented in the last Chapter with model beads, two main biological applications were demonstrated here: first, the extraction of *E. coli* bacteria from blood samples (that allowed the optimization of the purification conditions), before going to our application of interest with the extraction of extracellular vesicles (EVs) from cell culture media.
- Plasma isolation was performed from 10x-diluted blood samples, with a removal rate of red blood cells as high as 99.8 % and a particle recovery yield of 100 %. This enabled the extraction of *E. coli* bacteria in a purified blood sample depleted from blood cells, as required for sepsis diagnosis. Further improvements can still be made to increase the throughput (for example with parallelization of DLD devices) and reduce biofouling through adapted surface treatments.
- From the standard multi-step EV isolation protocol, DLD was demonstrated to efficiently substitute the first centrifugation step to remove cells and large cell debris from cell culture media with similar performances. Then, ultracentrifugation was compared to size-exclusion chromatography and magnetic isolation for the extraction of EVs. Magnetic isolation was shown to give higher extraction purity regarding the protein content of extracted EV samples, as well as higher integration and miniaturization potential. Moreover, magnetic isolation enables to specifically purify target EV subpopulations.
- A completely integrated and automated microfluidic platform was proposed to extract CD63+ EVs from THP-1 cell culture media, thanks to these successive purification steps: DLD removal of large contaminants, on-chip filtration, on-chip incubation with functionalized nanobeads and on-chip magnetic capture. The collected EVs on beads were analyzed by NTA and a 6x concentration of target EVs was demonstrated by our system, compared to the concentration of EVs in the initial sample.
- Compared to standard EV purification protocols, our microfluidic platform enables to minimize sample manipulation, preserve the EV integrity and connect EV preparation to characterization. As a perspective, this platform could be connected to suspended nanochannel resonators (SNRs), that appear as very promising sensors to extract the biophysical signatures of single EVs.

Résumé du Chapitre : Purification par DLD d'Echantillons Biologiques

- La caractérisation de nos dispositifs présentée dans le Chapitre 3 a permis d'adresser ici deux principales applications biologiques : tout d'abord l'extraction de bactéries *E. coli* à partir d'échantillons de sang humain, afin d'optimiser les conditions opératoires de la purification par DLD, avant de passer à l'application visée d'extraction d'EVs à partir de milieu de culture cellulaire.
- Nos dispositifs nous ont permis d'accomplir une extraction de plasma à partir de sang dilué 10x, avec l'élimination à 99.8% des érythrocytes, et un taux de collecte de 100%. Grâce à ces résultats, l'extraction de bactéries *E. coli* dans le sang a pu être réalisée dans la perspective du diagnostic du sepsis. Des améliorations futures sont encore à envisager afin d'augmenter le débit de purification (par exemple par la parallélisation de plusieurs purifications par DLD simultanées) et de réduire l'affinité biologique sur les piliers par un traitement de surface adapté.
- La purification des EVs a ensuite été adressée dans l'optique de remplacer les étapes successives du protocole standard de purification des EVs par un protocole microfluidique tout intégré. La technique de DLD s'est positionnée comme une alternative efficace à la première étape de centrifugation du protocole standard. En effet, des performances similaires ont été obtenues par DLD et par centrifugation pour l'élimination des cellules et des débris de cellules à partir de milieu de culture. Pour l'étape suivante d'extraction des EVs, trois techniques standards ont été testées : l'ultracentrifugation, la chromatographie par exclusion de taille et la capture magnétique. L'isolement magnétique a conduit à une meilleure pureté d'extraction au regard du contenu protéique des échantillons d'EVs extraits. De plus, la capture magnétique offre un plus grand potentiel d'intégration et de miniaturisation, en comparaison avec les deux autres méthodes considérées, et permet de cibler spécifiquement une sous-population d'EVs.
- Une plateforme microfluidique intégrée et automatisée a été développée pour extraire une sous-population d'EVs CD63+ à partir de milieu de culture de cellules THP-1. Cette plateforme intègre plusieurs étapes de purification successives : l'élimination des plus larges contaminants par DLD, une filtration sur puce, une étape d'incubation de l'échantillon purifié avec les nanobilles magnétiques fonctionnalisées, et une capture magnétique sur puce. La caractérisation par NTA des EVs capturées par notre dispositif a mis en évidence la concentration d'un facteur 6 des EVs ciblées par rapport à leur concentration initiale dans le milieu de culture.
- Notre plateforme microfluidique d'isolement des EVs apporte de nombreuses améliorations au protocole standard : une manipulation d'échantillon automatisée et intégrée, la préservation de l'intégrité des EVs, et la connection directe de l'étape de préparation d'échantillon à l'étape de caractérisation. Un exemple intéressant de développements futurs est l'intégration de notre dispositif à l'analyse des EVs par les capteurs SNR (Suspended Nanochannel Resonators), pour permettre la caractérisation biophysique de chaque vésicule individuelle.

Multi-DLD Platforms for Complex Samples

Introduction: Multi-DLD Platforms for Complex Samples

- In the last Chapter, purification of biological samples was performed with single DLD devices. This enables the separation of particles around a single critical diameter. However, for complex samples containing more than two groups of particles to separate, several cascaded DLD devices are required.
- Connecting one outlet of a first DLD stage to the inlet of a second DLD stage involves an imbalance of hydraulic resistances at the output of the first DLD module, which degrades the sorting efficiency.
- Two strategies are presented in this Chapter to balance hydraulic resistances when connecting two DLD purification stages and optimize the efficiency of the multi-separation process.
- The first strategy involves droplet generation at T-junctions connected to the DLD outlets. This droplet-based platform enables at the same time to encapsulate the sorted particles and apply controlled pressures at the DLD outlets thanks to an immiscible oil solution. A predictive model is presented to determine the optimized input pressure parameters to apply in order to balance the entire droplet-based platform.
- A second strategy is proposed when digital microfluidics is undesirable. In this other platform, the DLD purification stages are performed successively thanks to collection chambers located between the first and the second DLD modules. These transient chambers enable to collect the samples purified by the first DLD module and to inject the non-deviated particles in the second DLD module after completion of the first purification. In order to avoid sample manipulation by the user, the chambers are integrated in the microfluidic cartridge and automatically actuated. This strategy is implemented for the problematic of bacteria purification from blood samples presented in the last Chapter.

5.1 Connection of DLD Modules: Presentation of the Problem

Most biological samples contain a wide range of particle sizes (from the nanometer scale to the micrometer scale). Therefore, clogging issues make it inadequate to use a unique DLD system to remove all the large contaminants of the sample. For example, isolating exosomes from whole blood requires the successive

removal of particles from several tens of micrometers down to a few hundreds of nanometers.

In order to progressively purify complex biological samples through DLD, the most common strategy is to **cascade different separation modules into a single chip** [346, 365, 361, 402, 403, 356, 404]. This strategy presents some limitations due to the fabrication process. For example, the DLD process of a heterogeneous sample containing particles with size scales in the micrometer and nanometer ranges - the typical content of a biofluid sample - would require inter-pillar spacings ranging from a few tens of micrometers [346] down to the submicron scale [322]. However, etching such range of dimensions on a single silicon wafer is limited by a maximum pillar depth to gap ratio of approximately 20 (with our fabrication technology) unless several complex intermediary lithography and etching steps are incorporated into the fabrication protocol. Another limitation of this approach is related to the system integration. Indeed, when a single multi-stage DLD chip is developed, this does not enable to target different applications with the same device. In this Chapter, we propose **modular approaches** by assembling several individual DLD building blocks separately (fabricated on separate wafers each with optimized etching conditions). The most efficient DLD modules and flow rates can then be identified separately before cascading the different devices onto a single microfluidic cartridge to allow for sequential flow. This approach allows for a higher sample throughput as the flow rate in the entire device is no longer limited by the most resistive DLD section represented by the smallest inter-pillar spacing.

The principal challenge when connecting a DLD module to downstream microfluidic steps is to keep a constant flow velocity across the different DLD outlets in order not to disturb the trajectory of particles. Indeed, DLD separation is based on the streamline distribution around the pillars. It is thus critical to ensure **hydraulic resistance balance** at the DLD outlets. If different resistances apply on the DLD outlets, all the streamlines and all the particles will follow the path presenting the lowest resistance. Connecting a following step to a DLD module involves hydraulic resistance imbalance at the DLD outlets: an additional resistance is applied on the outlet connected to the second module (and containing the particles of interest) while the other outlets called “waste” are not connected to the same module.

This effect is illustrated in fig. 5.1 (a) with two cascaded DLD modules. A first DLD module called “DLD1” separates particles around a critical diameter D_{c1} . DLD1 has two inlets – particle solution from the right inlet and buffer solution from the left inlet – and two outlets – non-deviated particles in the right outlet and deviated particles in the left outlet. Non-deviated particles from DLD1 (with diameters smaller than D_{c1}) are injected into DLD2, for which the critical diameter D_{c2} is smaller than D_{c1} . Figure 5.1 (a) shows the streaks of injected 10 μm -beads at the DLD1 outlet. These streaks are initially focused on the right side of the pillar channel because the DLD1 critical diameter is superior to 10 μm . Imbalance of the hydraulic resistances is generated at DLD1 outlets since the right outlet is connected to DLD2 (that displays high hydraulic resistance), while the left outlet is not connected to a DLD module (thus it displays a lower hydraulic resistance). Therefore, all the streaks are deviated from the top right side to the bottom left side of the DLD channel, in order to flow towards the T-junction. The beads should follow their trajectory towards the right outlet, but they are finally deviated towards the T-junction since this outlet presents a lower hydraulic resistance. **A solution is required in this case to balance backpressures at the DLD1 outlets and avoid unwanted reorientation of the particles.**

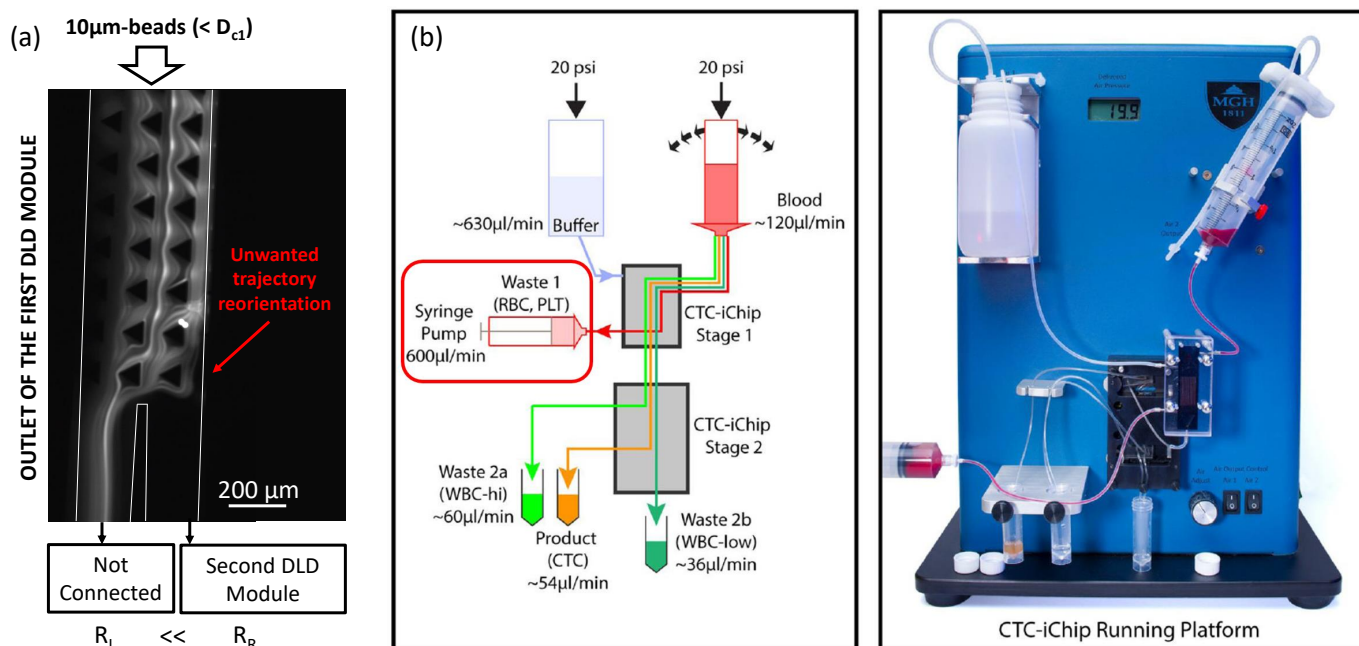


Figure 5.1: a) Illustration of the problem of hydraulic resistance imbalance when connecting two DLD modules. The outlet of a first DLD stage is imaged while injecting $10\ \mu\text{m}$ -beads (smaller than D_{c1} , not deviated by the first DLD stage). The right outlet of DLD1 is connected to the inlet of a second DLD stage, while the left outlet of DLD1 is not connected. Therefore, the left DLD1 outlet displays lower hydraulic resistance (R_L) than the right DLD2 outlet (R_R). b) Running setup from Karabacak et al. [401]. Schematic (left) and picture (right) of their CTC-iChip device. A first DLD stage enables to remove small blood cell contaminants. This stage 1 is connected to a second stage for further purification of CTCs. A syringe pump (framed in red) is connected to the waste outlet of stage 1 to balance the output flow rates.

To our knowledge, the first existing strategy to date to connect DLD steps in an integrated platform was presented by Karabacak et al. [401]. They proposed a CTC-iChip with two cascaded devices to isolate CTCs from whole blood (fig. 5.1 b): a first DLD step is connected to a second device downstream that contains both inertial focusing and magnetophoresis. Only the DLD outlet that contains large deviated cells is connected to the downstream step, which induces higher hydraulic resistance on this outlet compared to the non-deviated outlet that contains waste blood contaminants. A syringe pump was connected to this waste channel in order to apply a controlled output flow rate and compensate for the resistance imbalance. This solution is appropriate when only one of the two particle subpopulations has to be collected. Otherwise, connecting a syringe pump does not allow to collect particles flowing through this outlet, which is problematic when further purification or analysis is required. Indeed, in the CTC-iChip [401], particles flowing through the waste channel are lost in an external waste syringe. **The objective of our platform is to collect particles from all DLD outlets in flow so that all the sorted particles can be analyzed in flow on the same cartridge, without external sample manipulation.**

5.2 Solution n°1: Droplet-based Platform

A droplet-based solution with T-junctions intersecting the DLD outlets is presented to balance output DLD backpressures in a completely modular and reconfigurable sample preparation device. Our platform is composed of silicon-based DLD chips connected to a plastic-based cartridge with T-junction channels supplied by an additional oil solution to generate water-in-oil droplets. Three configurations using this droplet-based technology are proposed, with a particular example of two cascaded DLD modules. In this configuration, a general predictive model has been developed in order to anticipate the optimized input pressure parameters maximizing the separation efficiency at each step.

5.2.1 Experimental Section

Fabrication of the silicon-based devices

Version 1 devices were used for this section on our droplet-based platform, with the 2 inlets / 2 outlets configuration. The fabrication process flow of these silicon-based devices was presented in Chapter 2. Briefly, the chips are fabricated on 200 mm silicon wafers and they are cut into 22 x 22 mm individual square pieces, each containing 4 DLD devices. The fluidic channels and the inlet/outlet ports are defined by contact photolithography and Reactive Ion Etching (RIE) on a 3 μm -thick silicon dioxide (SiO_2) hard mask (2 μm thermal SiO_2 followed by a deposition of 1 μm SiO_2). Following hard mask etching, fluidic ports are partially etched using deep UV photolithography and RIE. After stripping off the resist, the microchannels are etched through the hard mask using RIE and the holes are etched until the bottom 2 μm -thick thermal SiO_2 layer at the same time. After removing the oxide and cleaning the substrate, a second thermal oxide layer (100 nm-thick) is grown and a top 500 μm -thick borosilicate glass cover is sealed by anodic bonding.

Fabrication of the microfluidic cartridge

The chips were packaged on a custom COC (cyclic olefin copolymer) Fluidic Circuit Board (FCB) with plug and play tubing connectors. Fluidic sealing between the silicon chip and the plastic cartridge was achieved by a magnetic frame holding silicone-based gaskets. The cartridge channels were micromachined and then thermally sealed with a COC cover. T-junction geometries were part of the cartridge channels, with 500 μm x 500 μm cross-sections. In order to soften COC roughnesses on the walls of the microfluidic channels after milling, a solution of 1/3 toluene – 2/3 acetone was injected in the channels before rinsing with acetone, ethanol and water. In addition to the aqueous solution coming from the DLD chip, a corn oil solution (Sigma-Aldrich, C8267) was injected in the cartridge at the T-junctions to generate water-in-oil droplets. The association of the silicon DLD chip and the plastic cartridge containing T-junction areas is called the platform.

Experimental test bench

As already described in Chapter 3, imaging was performed by epifluorescence microscopy (Olympus, BX60) with a built-in 100 W mercury lamp (Osram, HBO 103W/2). A standard FITC (fluorescein isothiocyanate) filter cube (Olympus, U-MSWB2) was used to detect fluorescent beads. Imaging was performed with a monochrome fluorescence CCD camera (Olympus, XM10). Sequences of images were superimposed and analyzed with ImageJ software to visualize the trajectory of particles flowing in the DLD channel. Fluids were actuated by a pressure-based flow controller (Fluigent, MFCS-EZ) with input pressures from 50 mbar to 1 bar according to the DLD design in order to obtain a flow rate of about $100 \mu\text{L min}^{-1}$ in the pillar array. The flow rate was chosen to obtain a Stokes flow and avoid flow stream mixing. In the Stokes regime, the flow rate does not influence the DLD separation of particles.

Protocol

10 μm and 5 μm -monodisperse fluorescent polystyrene beads (ThermoFisher Scientific, Fluoro-Max Dyed Green Aqueous Fluorescent Particles) were used to characterize the DLD devices. As recommended by the manufacturer, the beads were suspended in a 1 % surfactant solution (Tween 20, Sigma-Aldrich) in filtered DPBS 1x (gibco life technologies, 14190144) in order to prevent particle aggregation. The solution injected in the “buffer” inlet of DLD modules was also a 1 % surfactant solution in filtered DPBS 1x. The oil solution injected at the T-junction was corn oil (Sigma-Aldrich, C8267).

5.2.2 Droplet T-Junctions as Pressure Controllers at DLD Outlets

In the presented platform, droplet formation at T-junctions is proposed as a new solution to control hydraulic pressures. Indeed, **generating droplets at a T-junction enables to apply a specific pressure on the dispersed phase thanks to an additional continuous phase.** In our DLD setup, two output hydraulic resistances have to be controlled and balanced at both DLD outlets (fig. 5.2): the left outlet that contains large deviated particles, and the right outlet that contains smaller, non-deviated particles. These two outlets are generally connected to different downstream microfluidic stages. For example, the left output channel could be connected to an integrated sensor in order to analyze the deviated particles, while the right output channel could be connected to another DLD module for further purification of the sample with a smaller critical diameter. Therefore, the two outlets are usually connected to microfluidic steps with different hydraulic resistances, called R_1 and R_2 . In this case, a solution is required to balance both output pressures in order to optimize the sorting efficiency of the DLD stage. Our droplet-based approach can also be applied to DLD modules with more than two outlets, by connecting a T-junction to each of the DLD output channel.

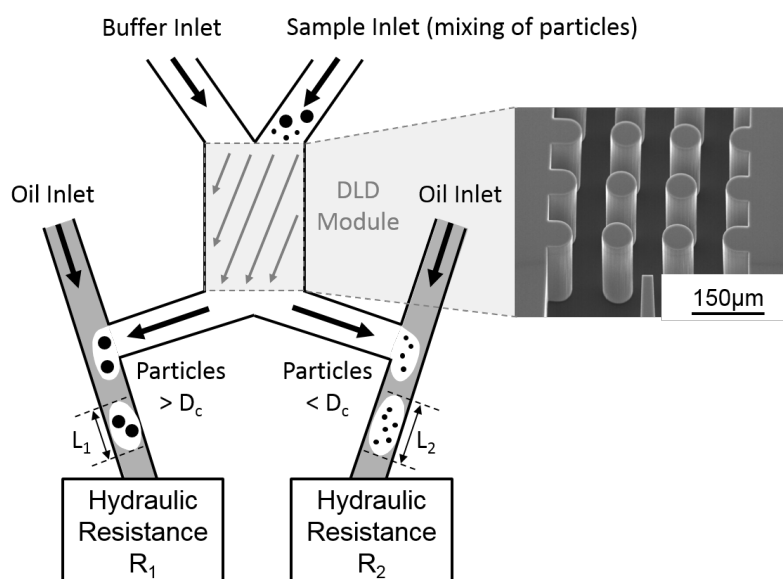


Figure 5.2: Schematic of the droplet-based pressure control principle. A mixing of particles of different sizes is injected in the right inlet of a DLD module. Particles larger than the critical diameter (D_c) are deviated towards the left outlet, while smaller particles flow in the right outlet. Each DLD outlet is connected to a T-junction with an oil inlet, for generation of droplets of lengths L_1 and L_2 . Additional microfluidic modules are connected to the T-junction, with hydraulic resistances called respectively R_1 and R_2 .

Thanks to an additional immiscible phase – called “oil inlet” in fig. 5.2 – the aqueous phase leaving from DLD outlets is encapsulated in T-junctions. By changing the input oil pressure at the T-junction, the end pressure applied on the DLD aqueous phase is locally controlled [405]. This solution has several advantages when compared to the direct pressure control at the DLD outlets (such as connecting a syringe pump to the outlet [401]). First, it enables to keep all the sorted particles in flow inside the cartridge. This is particularly useful when downstream DLD or analytical sensor modules are also integrated in the same microfluidic system. Moreover, encapsulating particles can be very advantageous for various down-stream particle analysis techniques [406, 407, 408, 409, 410, 411]. Finally, the oil sections between each analyzed droplet can also be exploited as calibration references, for example when the analysis module measures particle density [412]. Indeed, the baseline of the density sensor can be regularly calibrated in this case, thanks to the oil phase of known density.

In case the injection of an oily continuous phase in the downstream analysis module is problematic, it can be considered to use an aqueous solution instead of the oil solution to form water-in-water droplets [413]. Therefore, pressure control through droplet generation can be adaptable to different applications and analysis techniques.

Yan et al. [414] have numerically shown that the pressure at the junction point – at the interface between the dispersed and the continuous phases – fluctuates periodically during the whole generation cycle.

For given input pressures, capillary number, contact angle and channel geometry, the local pressure at the junction point fluctuates at the same rate as the droplet formation process. It was shown that the evolution of the junction point pressure is dependent on the droplet generation regime [414]. In particular, the amplitude of the pressure fluctuations during the cycle decreases in the order: dripping regime, squeezing regime, jetting regime and parallel flow regime. In our case, it is important to minimize pressure fluctuations on the DLD aqueous phase, in order to simplify pressure balancing at both sides. On the other hand, jetting and parallel flow regimes do not allow to apply sufficiently high pressures to balance the important hydraulic resistance of DLD modules. From these two considerations, a squeezing regime was chosen for our droplet-based pressure control platform. In this regime, the break-up process is determined by the pressure drop across the droplets, which form in a plug-like shape [415].

In the next sections, it will be demonstrated that the droplet generation at T-junctions can be modeled as an additional hydraulic resistance that is applied on the DLD output solution. The droplet-associated resistance is considered as a constant average value. This approximation is valid because the period of the droplet generation cycle – in the order of 10 milliseconds in the squeezing regime [414] – is highly inferior to the processing time of DLD – in the order of several minutes at a flow rate of $100 \mu\text{L min}^{-1}$.

5.2.3 Possible Droplet Platforms

Two platforms were first implemented with one single DLD module presenting two output channels. This DLD module has $20 \mu\text{m}$ triangular pillars (D_p), $20 \mu\text{m}$ inter-pillar spacing (G) and an array periodicity (N) of 50, with a corresponding critical diameter (D_c) of $3.5 \mu\text{m}$. Each platform makes use of the droplet-based pressure control system with T-junction geometries in the cartridge. In both platforms, two T-junctions are used so that each output DLD channel can be connected to an oil inlet. These platforms enable to balance both backpressures when the DLD outlets are connected to two different microfluidic modules (for example two different analysis systems, adapted to each particle size coming from the DLD outlets).

In platform 1 (fig. 5.3 a), **T-junctions are independent**, which means that two oil inlets are required to supply each droplet generation area. When oil pressures are not applied, the system has an intrinsic resistance imbalance at the outlets since the DLD output channels do not have the same width. Therefore, application of oil pressures is required to balance output resistances and direct the bead streaks towards the correct outlet. The equilibrium is reached for the generation of droplets of different sizes at both DLD outlets. It was verified that the fluorescence intensity of the beads was focused inside the droplets at the T-junctions. Indeed, no fluorescence was detected in the oil solution, which suggests no bead escape from the water phase to the oil phase.

In platform 2 (fig. 5.3 b), the **T-junctions are dependent** since the same oil inlet supplies both droplet generation areas. A longer serpentine channel is connected to the left DLD outlet, when compared to the right side, in order to mimic the connection of different hydraulic resistances to DLD outlets. Thanks to the common oil inlet, both DLD backpressures are balanced at the same time, which is confirmed by the bead streak profile inside the DLD channel.

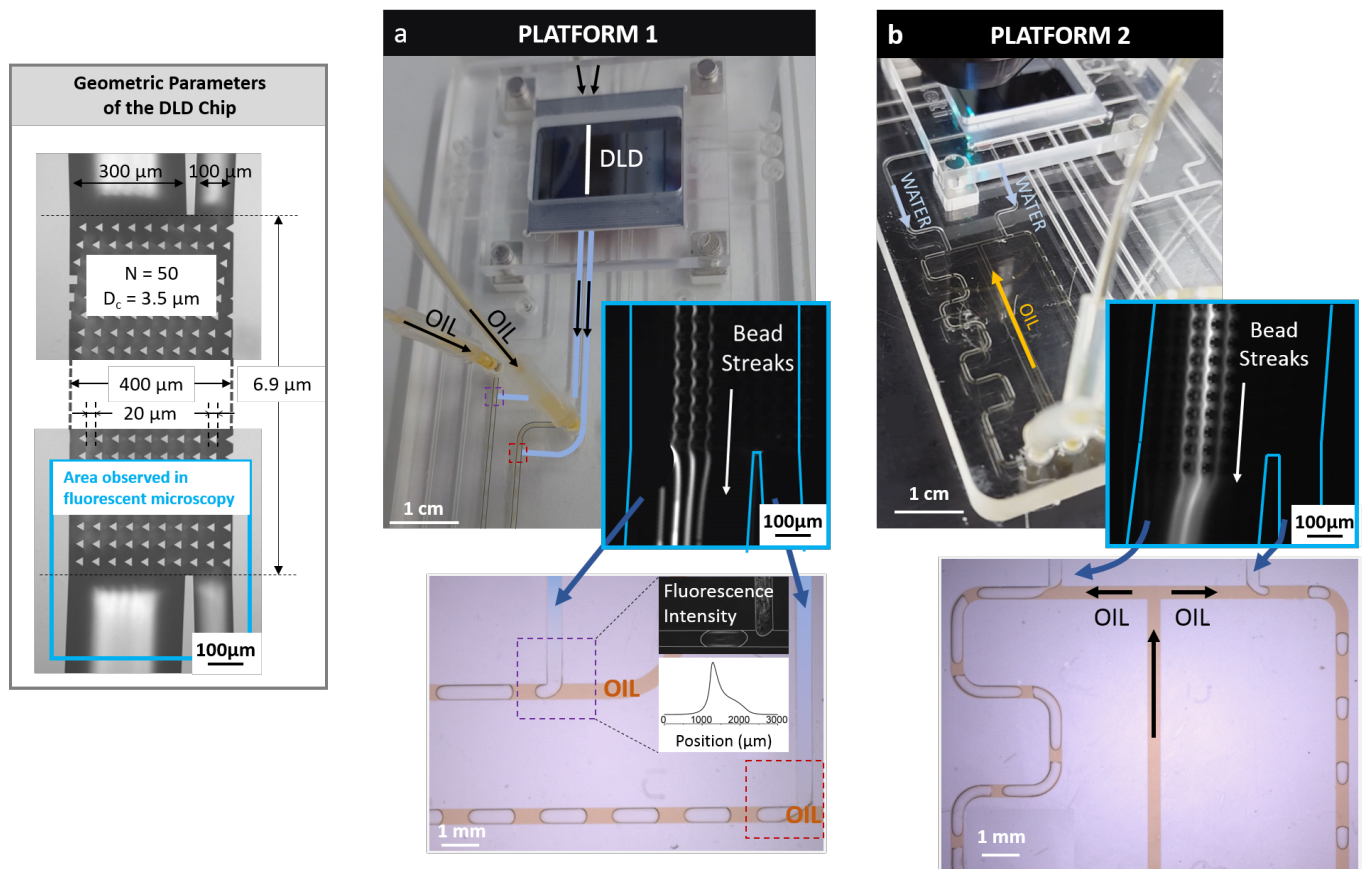


Figure 5.3: Platform 1 (a) and Platform 2 (b) with the DLD silicon chip connected to a plastic cartridge and two independent T-junctions supplied by two oil inlets (a) or two T-junctions supplied by the same oil inlet (b). Fluorescent images of the streaks for 10 μm-beads at the DLD outlet and bright-field images of the T-junctions connected to the DLD outlets are also given for both platforms.

Platform 2 is easier to control than platform 1 since only one oil inlet has to be controlled instead of two. However, it can be useful to control both oil inlets independently, especially when the connected microfluidic modules feature strongly different hydraulic resistances at the DLD outlets.

A third platform is proposed to **cascade DLD modules** (fig. 5.4). A first DLD module called “DLD1” separates particles around a critical diameter D_{c1} . DLD1 has two inlets – particle solution from the right inlet and buffer solution from the left inlet – and two outlets – non-deviated particles in the right outlet and deviated particles in the left outlet. Non-deviated particles from DLD1 (with diameters smaller than D_{c1}) are injected into DLD2, for which the critical diameter D_{c2} is smaller than D_{c1} . The other DLD1 outlet is connected to a T-junction that enables to balance the important hydraulic resistance presented by DLD2. In our experimental example, DLD1 has 60 μm triangular pillars (D_p), 60 μm inter-pillar spacing (G) and an array periodicity (N) of 22, with a predicted critical diameter (D_c) equal to 15 μm. DLD2 has the following parameters: $D_p = 20 \mu\text{m}$, $G = 20 \mu\text{m}$, $N = 50$ and $D_c = 3.5 \mu\text{m}$.

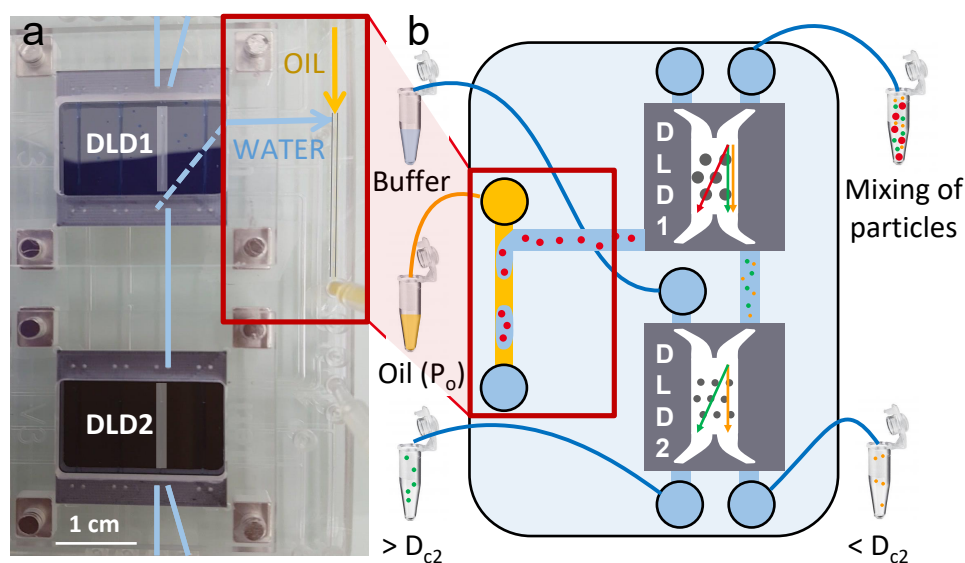


Figure 5.4: a) Photograph of platform 3, showing the connection of two DLD silicon chips (DLD1 and DLD2). One outlet of DLD1 is connected to the inlet of DLD2, while the other DLD1 outlet is connected to a T-junction in the cartridge. b) Schematic representation of platform 3. DLD1 deviates the largest red particles ($> D_{c1}$), while DLD2 separates the green ($> D_{c2}$) and the yellow ($< D_{c2}$) particles. The red particles are encapsulated in a T-junction, supplied by an oil inlet at an input pressure P_o .

Figure 5.5 illustrates how the input oil pressure at the T-junction (P_o) influences the particle flow inside the DLD1 module, when DLD1 is connected to a DLD2 module. Figure 5.5 (b) represents 10 μm -bead streaks at the DLD1 outlet. The right output channel is connected to DLD2, while the left output channel is connected to a T-junction. In the three presented conditions, the streaks are rather focused on the right side of the pillar channel because the 10 μm -beads are not deviated by the DLD1 module ($D_{c1} = 15 \mu\text{m}$, larger than the bead size).

When no pressure is applied on the oil solution at the T-junction (condition $n^{\circ}1$, $P_o = 0 \text{ mbar}$), all the streaks are deviated from the top right side to the bottom left side of the DLD channel, in order to flow towards the T-junction: in this case, DLD1 backpressures are not balanced. The beads should follow their trajectory towards the right outlet, but they are finally deviated towards the T-junction since this outlet presents a lower hydraulic resistance. When the oil pressure is increased (condition $n^{\circ}2$, $P_o = 30 \text{ mbar}$), droplets start to be generated at the T-junction (fig. 5.5 b) and some particles start to follow the correct trajectory towards DLD2. By further increasing the oil pressure (condition $n^{\circ}3$, $P_o = 60 \text{ mbar}$), the droplet length decreases (fig. 5.5 c), which means that the flow rate at the left DLD outlet decreases. At this P_o value, both hydraulic resistances are balanced at the DLD1 outlets, as shown by the bead streaks on fig. 5.5 (b).

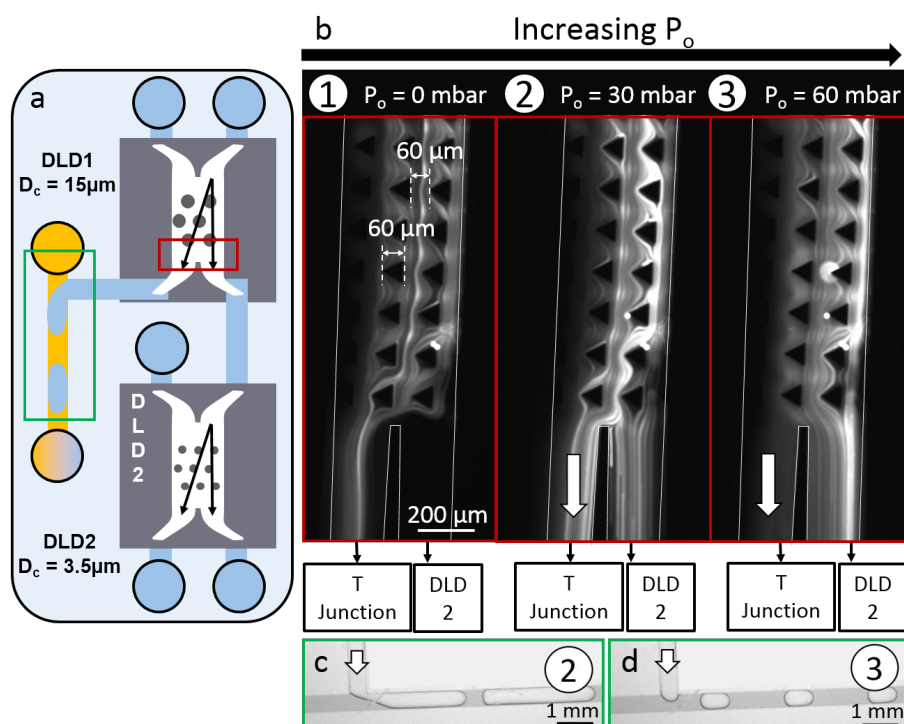


Figure 5.5: a) Schematic representation of the cascaded configuration: the area located in the red frame corresponds to the images in b) and the area located in the green frame corresponds to the images in c) and d). b) 10 μm -bead streaks at the DLD1 outlet for three values of the oil pressure at the T-junction (P_o). The left outlet of DLD1 is connected to a T-junction, while the right outlet is connected to a DLD2 module. c) Droplet generation at the T-junction connected to the DLD1 left outlet in condition $n^{\circ}2$ ($P_o = 30 \text{ mbar}$). d) Droplet generation at the T-junction connected to the DLD1 left outlet in condition $n^{\circ}3$ ($P_o = 60 \text{ mbar}$).

These results illustrate the importance of choosing the correct oil pressure at the T-junction to efficiently handle the particle flow in the DLD modules. This specific oil pressure has to be adapted to the other input parameters of the platform, like the input pressures at the DLD modules and the hydraulic resistances of the chips and the cartridge. In order to anticipate the optimum pressures to apply to maximize the separation efficiency of the DLD platform, a predictive model has been established. This model takes into account all the input parameters of the platform and aims at determining what are the right pressure conditions to apply in any configuration, regardless of the DLD1 and DLD2 dimensions.

5.2.4

Predictive Model to Apply Optimized Input Pressures

In order to build a predictive model of the entire droplet-based system, all the fluidic elements of platform 3 have been modeled by hydraulic resistances (fig. 5.6 a).

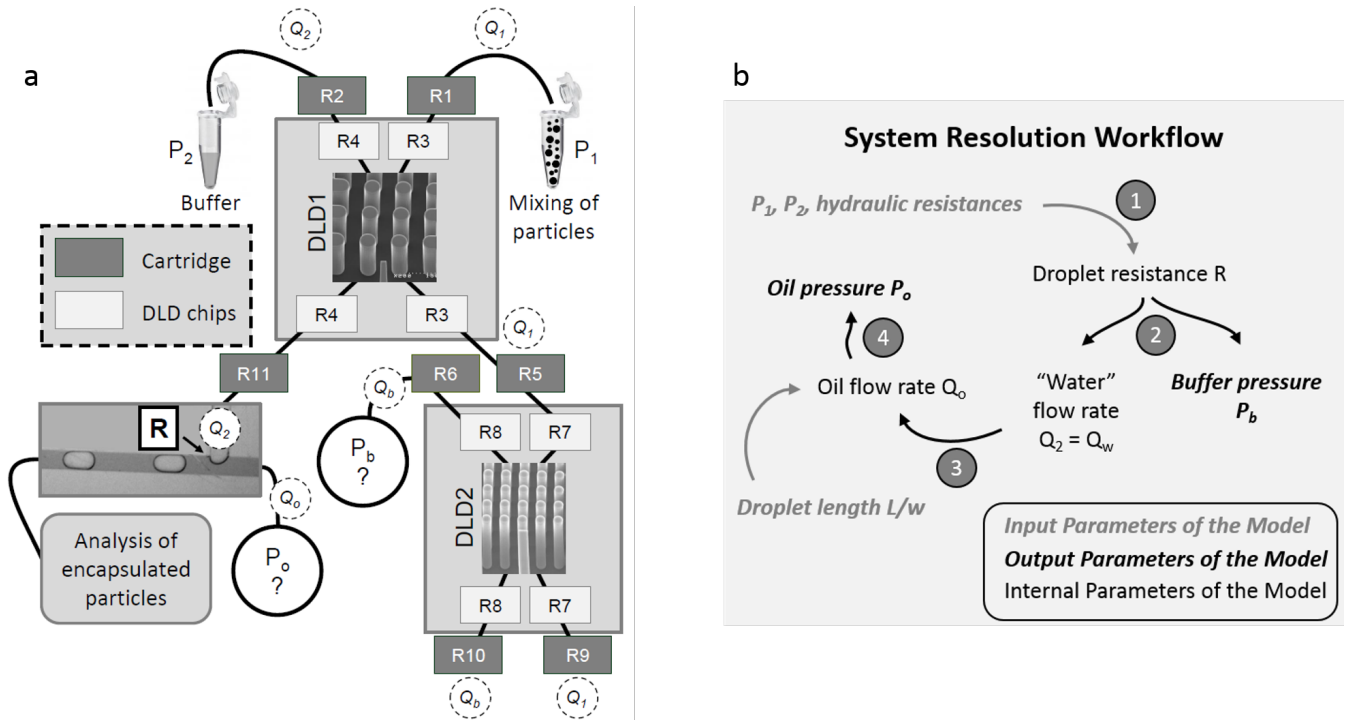


Figure 5.6: a) Modeling of platform 3: R1 to R11 represent the hydraulic resistances of the microchannels in the cartridge and in the DLD chips. P_1 and P_2 are the input pressures at the DLD1 entrance. P_b is the buffer pressure at the DLD2 entrance. P_o is the input oil pressure at the T-junction. Q_1 , Q_2 , Q_b and Q_o are the flow rates in the DLD channels and in the T-junction. b) Schematic of the successive resolution steps

The input parameters of the model are the hydraulic resistances R1 to R11 and the pressures at the DLD1 entrance P_1 and P_2 . The objective of the model is to give two optimum output parameters: the buffer pressure at the DLD2 entrance (P_b) and the oil pressure at the T-junction (P_o). Optimization of these output parameters is based on two conditions expressed in the DLD1 and DLD2 channels:

- *Condition 1:* The average velocity amplitude is constant in the entire DLD1 channel width (local variations are observed because of the parabolic flow profile between pillars [324], but the global velocity amplitude is the same from both DLD1 inlets):

$$Q_1 = v^{DLD1} S_1^{DLD1} \quad (5.1)$$

$$Q_2 = v^{DLD1} S_2^{DLD1} \quad (5.2)$$

where Q_1 and Q_2 are the input flow rates at the DLD1 sample and buffer inlets respectively, v^{DLD1} is the flow velocity in the DLD1 channel, and S_1^{DLD1} and S_2^{DLD1} are the channel cross-sections at the DLD1 sample and buffer inlets respectively.

- *Condition 2*: The same condition has to be applied at the DLD2 module:

$$Q_1 = v^{DLD2} S_1^{DLD2} \quad (5.3)$$

$$Q_b = v^{DLD2} S_2^{DLD2} \quad (5.4)$$

where Q_1 and Q_b are the input flow rates at the DLD2 sample and buffer inlets respectively, v^{DLD2} is the flow velocity in the DLD2 channel, and S_1^{DLD2} and S_2^{DLD2} are the channel cross-sections at the DLD2 sample and buffer inlets respectively.

From the Hagen-Poiseuille law for a steady-state flow and an incompressible fluid, three additional relationships between the input pressures and the flow rates can be written:

$$P_1 = (R_1 + R_3)Q_1 + R_{DLD1}(Q_1 + Q_2) + (R_3 + R_5 + R_7)Q_1 + R_{DLD2}(Q_1 + Q_b) + (R_7 + R_9)Q_1 \quad (5.5)$$

$$P_2 = (R_2 + R_4)Q_2 + R_{DLD1}(Q_1 + Q_2) + (R_4 + R_{11} + R)Q_2 \quad (5.6)$$

$$P_b = (R_6 + R_8)Q_b + R_{DLD2}(Q_1 + Q_b) + (R_8 + R_{10})Q_b \quad (5.7)$$

The key approach here is to consider droplet generation at the T-junction as contributing as an additional constant hydraulic resistance R that is applied on the DLD1 left outlet.

By using the two conditions and eqs. (5.5) to (5.7), the unknown input pressures (P_b and P_o) can be determined with the system resolution workflow described on fig. 5.6 (b).

- *Step 1*: The droplet resistance R at the T-junction is determined by solving the following equation, obtained from the two conditions and eqs. (5.5) to (5.7) presented above:

$$P_1 \left(1 - \frac{1}{1 + \gamma(R)/\beta\eta} \right) + P_2 \left(\frac{\gamma(R)}{X\zeta(R) + R_{DLD1}} + \frac{\alpha(R)}{1 + \gamma(R)/\eta\beta} - \alpha(R) \right) = 0 \quad (5.8)$$

where:

$$X = s_2^{DLD1}/s_1^{DLD1} \quad (5.9)$$

$$x = s_2^{DLD2}/s_1^{DLD2} \quad (5.10)$$

$$\alpha(R) = \frac{R_{DLD1}}{R_2 + 2R_4 + R_{11} + R_{DLD1} + R} \quad (5.11)$$

$$\gamma(R) = R_1 + 2R_3 + R_5 + 2R_7 + R_9 + R_{DLD1} + R_{DLD2} - \frac{R_{DLD1}^2}{R_2 + 2R_4 + R_{11} + R_{DLD1} + R} - \frac{R_{DLD2}^2}{R_6 + 2R_8 + R_{10} + R_{DLD2}} \quad (5.12)$$

$$\zeta(R) = R_2 + 2R_4 + R_{11} + R_{DLD1} + R \quad (5.13)$$

$$\beta = \frac{R_{DLD2}}{R_6 + 2R_8 + R_{10} + R_{DLD2}} \quad (5.14)$$

$$\eta = x(R_6 + 2R_8 + R_{10} + R_{DLD2}) + R_{DLD2} \quad (5.15)$$

- *Step 2:* After determining the droplet resistance R , the buffer pressure P_b and the water flow rate at the T-junction Q_2 can be determined as follows:

$$P_b = \frac{P_1 - \alpha(R)P_2}{\beta + \gamma(R)/\eta} \quad (5.16)$$

$$Q_2 = \frac{P_2}{R_{DLD1}/X + \xi(R)} \quad (5.17)$$

- *Step 3:* The oil flow rate Q_o is then determined from the water flow rate Q_2 (denoted Q_w in the following sections). The relationship between Q_o and Q_w was first determined from a simplified T-junction geometry that has the same geometry as the T-junction of platform 3, but without DLD modules. The oil flow rate Q_o was experimentally determined (by measuring the weight loss of the oil tube during injection) to obtain the fitting data in the simplified geometry.

A linear relationship was found between the droplet length ratio l_w and the flow rate ratio $\frac{Q_w/Q_o}{Q_w+Q_o}$ (fig. 5.7 a), with the slope $1.3 \cdot 10^{-9} \pm 0.2 \cdot 10^{-9} (m^3/s)$ and the intercept 0.9 ± 0.1 . This linear trend is in agreement with the model of Zhang et al. [416]. Our model was obtained with the same oil and water solutions as for DLD experiments in order to get the correct fitting pre-factor. However, Garstecki et al. [415] showed that this factor is independent of the viscosity and interfacial tension of the fluids for low capillary numbers, which is the case in the squeezing regime that is used in our platform.

The relationship found in the simplified geometry was verified in the entire platform of fig. 5.4, by measuring the corresponding droplet length when changing the water and oil flow rates at the T-junction. Therefore, when using this platform, the oil flow rate to apply is determined from the calculated water flow rate (Q_2 from step 2 of the resolution workflow in fig. 5.6 b) and from the chosen droplet length.

Thus, an additional advantage of this platform is the ability to tune the droplet size that can be adapted to the requirements of the connected downstream module.

- *Step 4:* If the system is controlled with input pressures instead of flow rates, an additional relationship is required to find the oil pressure P_o from the oil flow rate Q_o . This relation was first determined with the simplified T-junction geometry, by measuring the obtained flow rate Q_o when applying different pressure values P_o . The obtained linear fitting parameter ($3.7 \cdot 10^{11} \pm 0.6 \cdot 10^{11} \text{ mbar.s/m}^3$) was then verified with the complete DLD platform (fig. 5.7 b).

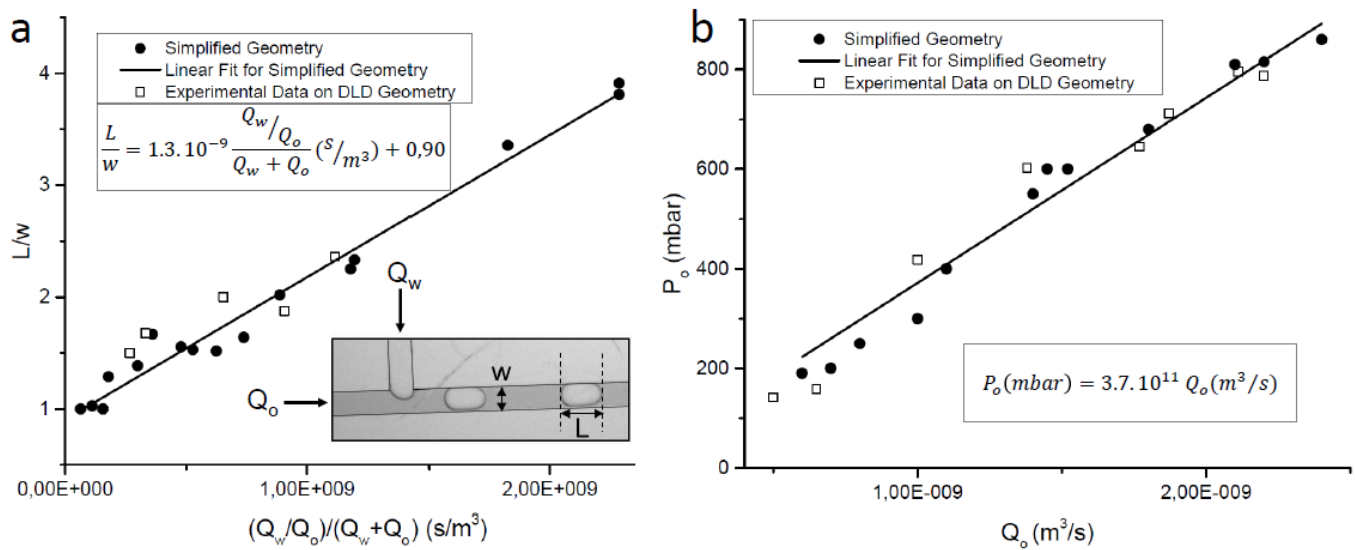


Figure 5.7: a) Experimental relation between the length ratio of the droplets (L/w , where w is the channel width) and the flow rate ratio (where Q_w and Q_o are the water and oil flow rates respectively). A linear fit is proposed from data obtained with a simplified T-junction geometry without DLD modules. This relation is then verified with the complete DLD cascaded platform, including the same T-junction geometry. b) Experimental relation between the oil input pressure P_o and the oil flow rate Q_o at the T-junction. The linear fit is again obtained from the simplified T-junction geometry and verified with the complete platform.

The proposed model was used to determine the optimum input parameters of the complete DLD platform in several configurations. In the first configuration (configuration 1 in fig. 5.8), the DLD1 module features a pillar array of $60 \mu\text{m}$ circular pillars with $60 \mu\text{m}$ inter-pillar spacings and array periodicity of 22 (Design 1 of Version 1 with critical diameter of $20 \mu\text{m}$) and the DLD2 module has $20 \mu\text{m}$ circular pillars with $20 \mu\text{m}$ inter-pillar spacings and array periodicity of 6 (Design 2 of Version 1 with critical diameter of $15 \mu\text{m}$). The second configuration (configuration 2 in fig. 5.8) has the same DLD1 module but a different DLD2 module with $5.5 \mu\text{m}$ circular pillars, $5.5 \mu\text{m}$ inter-pillar spacings and an array periodicity of 8 (Design 3 of Version 1 with critical diameter of $4 \mu\text{m}$).

After choosing the input pressures at the DLD1 entrance (P_1 and P_2), our model resolution workflow (fig. 5.6 b) was implemented to determine the other input parameters of the platform: the buffer pressure at the DLD2 entrance (P_b) and the oil pressure at the T-junction (P_o), for a chosen droplet size (L/w). The obtained values for P_b and P_o are given in fig. 5.8 for both configurations. Then these pressure values were applied on the platform in each configuration to verify the agreement between our predictive model and experimental droplet size and particle trajectory (fig. 5.8).

$10 \mu\text{m}$ -fluorescent beads were injected in the platform in configuration 1, while $5 \mu\text{m}$ -beads were used in configuration 2. Therefore, according to the critical diameter of each module, beads are expected to follow a zigzag trajectory in both DLD modules for configuration 1, and they are expected to be displaced only by

the second DLD module in configuration 2. So, in both configurations, when the system is well balanced, beads should flow out of the DLD1 module from the same side as at the entrance. This was verified when the predicted input pressures were applied on the platform (fig. 5.8): beads have a zigzag trajectory along the DLD1 module and flow out from DLD1 through the correct outlet on the DLD1 right side, before entering into the DLD2 module. In the DLD2 stage, it is verified that the particle trajectory is in accordance with predictions (zigzag mode in configuration 1 and displacement mode in configuration 2), which means that the DLD2 input buffer pressure is well adapted to the bead flow rate at the DLD2 entrance. Thus, the proposed model efficiently anticipates the required input pressures to optimize the flow distribution in both DLD modules of the cascaded platform.

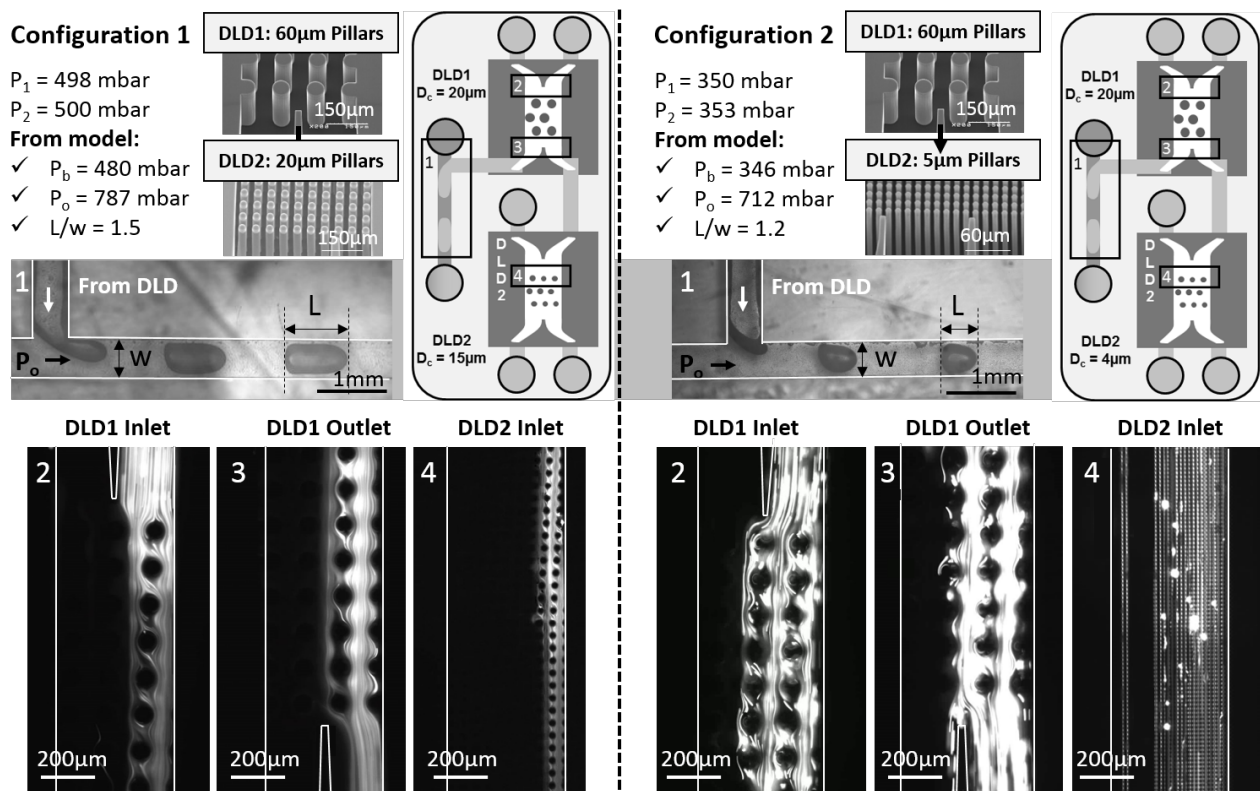


Figure 5.8: Validation of the model on the complete DLD platform in two configurations. Configuration 1 has a DLD1 module with 60 μm pillars ($D_{c1} = 20 \mu\text{m}$) and a DLD2 module with 20 μm pillars ($D_{c2} = 15 \mu\text{m}$), while configuration 2 has the same DLD1 module ($D_{c1} = 20 \mu\text{m}$) but a DLD2 module of 5 μm pillars ($D_{c2} = 4 \mu\text{m}$). 10 μm -beads are injected in configuration 1, while 5 μm -beads are injected in configuration 2. Input pressures P_1 and P_2 at the DLD1 entrance are chosen; then the buffer pressure P_b and oil pressure P_o are calculated from the proposed model, by choosing a given droplet size ratio L/w . In both cases, the validity of the model is verified by measuring the droplet length at the T-junction (area n^o1) and the particle distribution at the DLD1 inlet (area n^o2) and outlet (area n^o3) and at the DLD2 inlet (area n^o4). Areas 1 to 4 are located on the schematic representations of the cascaded platform for both configurations.

The stability of droplet generation was verified in both configurations with the predicted pressure conditions, as droplets were formed in the squeezing regime. However, large flow rate ratio Q_w/Q_o should be avoided to maintain the droplet breakup process at the channel intersection and avoid droplet generation instabilities and parallel flows [417].

In conclusion, droplet generation in T-junctions was proposed as a solution to balance backpressures of DLD modules. Pressure balancing at DLD outlets is essential to ensure high separation efficiency. While usual balancing methods require either a specific chip design or a waste syringe pump, here we propose a completely modular and reconfigurable platform to cascade DLD modules together or to other analysis steps. **By connecting T-junctions to DLD outlets, droplet generation ensures at the same time pressure balancing and encapsulation of the sorted particles.**

In order to anticipate the optimum pressures to apply on the different modules of the platform, a general model was proposed for a configuration of two cascaded DLD steps. Thanks to this model, the separation efficiency of the cascaded platform was optimized with any DLD modules. This capacity enables a modular approach, where the same platform and its predictive model can be used for a wide range of applications, with different DLD dimensions.

Moreover, pressure balancing through droplet generation can be generalized to any multi-step microfluidic devices. Indeed, droplet formation enables to connect two – or more, providing the connection to corresponding T-junctions – successive microfluidic steps without interference between each other. This is particularly useful when the first step needs a constant output pressure at all the different outlets, and the second step requires particle encapsulation.

5.3

Solution n°2: Transient Flexible Chambers

A second strategy is presented here to cascade several DLD devices without the need for an immiscible solution. Moreover, **this new approach simplifies the fluidic control since each DLD step is performed both successively and independently.** Indeed, DLD devices are temporarily isolated during each purification step by **valves and collection chambers**, that are integrated in a common platform and **automatically actuated** without any requirement for intermediary sample manipulation. The implemented chambers are flexible and collapsible thanks to a hyperelastic material. The advantage of this new type of chamber is to avoid air injection in the microfluidic channels in order to minimize bubble formation that is critical for DLD separation. Thanks to the high elasticity of the membrane, we achieve the storage of sample volumes of up to 1 mL in our cartridge between the different DLD stages. These chambers have a dual function for both collection and injection steps in order to transfer the sample from one DLD stage to the subsequent module.

In particular, this cascaded separation solution was applied to our objective of *E. coli* bacteria isolation from blood samples, as described in the previous Chapter. In addition to bacteria and blood cells, PC3 human prostate cancer cells were added to the sample, in order to demonstrate the ability to sort particles over a wider range of sizes. Thanks to the cascaded platform, we were able to separate three main particle dimensions (*E. coli* bacteria, Red Blood Cells (RBCs) and prostate cancer cells) across **10X different particle length scales**, in the perspective of sepsis diagnostics.

5.3.1 Experimental Section

Devices

Two DLD designs were selected for this application: a first DLD module (DLD1) - intended to remove PC3 cells - with lateral gap (G_L) = 20 μm , downstream gap (G_D) = 20 μm , array periodicity (N) = 15, channel depth (H) = 200 μm , channel length (L) = 44 mm, channel width (W) = 2.5 mm (Version 2, Group 3, Design 3); and a second DLD module (DLD2) - that was identified in the previous chapter to efficiently remove RBCs - with G_L = 9 μm , G_D = 4.5 μm , N = 30, H = 100 μm , L = 44 mm, W = 1.1 mm (Version 2, Group 2, Design 3).

The chips are packaged on a custom COC cartridge with plug and play tubing connectors. As described earlier, the fluidic sealing between the silicon chip and the plastic cartridge is achieved by a magnetic frame holding silicone-based gaskets. Pneumatic and fluidic channels are micromachined in the cartridge and the different COC sheets of each cartridge are thermally sealed. The valves are made of an EPDM (Ethylene Propylene Diene Monomere, Diacom, EC6508) patch (3.4 mm diameter) that is thermally sealed between two cylindrical apertures. The stretchable membranes for the chambers are prepared by spin coating an Ecoflex 00-50 (Smooth-On, Inc.) rubber to get a final thickness of about 300 μm . This material has been characterized elsewhere [418]. Ecoflex patches are thermally sealed between COC sheets and are free to deform during sample filling through 10.5 mm wide cylindrical openings in the cartridge. Each chamber can contain up to 1 mL of sample. In order to apply controlled pressures on these chambers, removable reservoirs are plugged on top of the cartridge during the injection step.

Experimental Setup

Two cartridges are connected together with plug and play tubing connectors. The first cartridge holds the first DLD chip and the collection chambers with the valves isolating the two DLD stages. The second cartridge holds the second DLD chip. Valves can be closed by applying a constant pressure of 2 bars through pneumatic channels integrated in the cartridge. Four different pressure values are controlled independently with a pressure-based flow controller (Fluigent, MFCS-EZ): P_1 = 100 mbar at the entrance of the first DLD device (resulting in a flow rate of about 200 $\mu\text{L}/\text{min}$), P_2 = 500 mbar on the chamber collecting the non-deviated sample (resulting in a flow rate of about 30 $\mu\text{L}/\text{min}$ in the second DLD device), P_3 = 200 mbar on the chamber collecting the deviated sample, and P_4 = 2 bar for valve closing. Valves and chambers are controlled through pneumatic channels integrated in the first cartridge (fig. 5.9)). The closing of each independent valve is automatically controlled by a data acquisition system (USB-1208FS, Measurement Computing). The flow rates in both DLD modules are chosen to obtain a Stokes flow and avoid flow stream mixing, while optimizing the particle separation efficiency (obtained for minimized cell deformation and clogging issues).

Again, imaging is performed by epifluorescence microscopy (Olympus, BX60) with a built-in 100 W mercury lamp (Osram, HBO 103W/2). A standard FITC (Fluorescein IsoThioCyanate) filter cube (Olympus, U-MSWB2) is used to detect fluorescent beads. Imaging is performed with a digital CMOS camera (Hamamatsu, Flash 4.0 LT+). Sequences of images are superimposed and analyzed with ImageJ software to visualize the trajectory of particles flowing in the DLD channel.

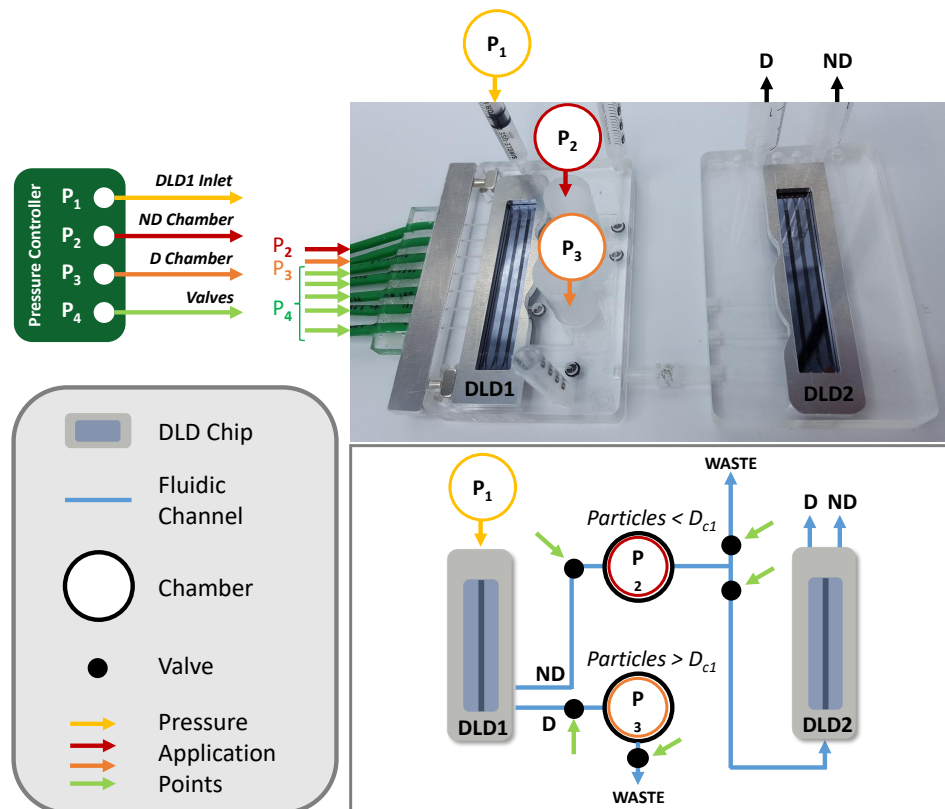


Figure 5.9: Picture of the cascaded platform and corresponding schematic representation of the fluidic and pneumatic elements. The pressure application points are given for the DLD1 inlet ($P_1 = 100$ mbar), non-deviated DLD1 output chamber ($P_2 = 500$ mbar), deviated DLD1 output chamber ($P_3 = 200$ mbar) and valves ($P_4 = 2$ bar).

Sample Solutions

Fluorescent polystyrene beads (ThermoFisher Scientific, Fluoro-Max Dyed Green Aqueous Fluorescent Particles) of different sizes ($1 \mu\text{m}$, $5 \mu\text{m}$ and $10 \mu\text{m}$) are used to characterize the DLD devices, by modeling the three characteristic sizes of our biological samples (PC3 cells that display sizes from 13 to $18 \mu\text{m}$, RBCs with diameters from 6 to $8 \mu\text{m}$ and thicknesses from 1 to $2.5 \mu\text{m}$ and *E. coli* bacteria with a width of $0.5 \mu\text{m}$ and a length of $2 \mu\text{m}$). As recommended by the manufacturer, the beads are suspended at 10^6 /mL in a 1 % surfactant solution (Tween 20, Sigma-Aldrich) in filtered DPBS 1x (gibco life technologies, 14190144) in order to prevent particle aggregation.

PC3 cells (ATCC, CRL-1435) are transfected with pEGFP-C1 plasmids. GFP-PC3 cells (~ 80 % confluent) are harvest in trypsin (0.05 % Trypsin-EDTA, Gibco, 25300-054) and resuspended in fresh medium (RPMI 1640-Gibco, 10 % Fetal Bovine Serum, 1 % Penicillin-Streptomycin, 0.5 % Geneticin).

Blood samples are collected from healthy donors (Etablissement Français du Sang (EFS), Grenoble, FRANCE) in EDTA BD Vacutainer tubes and diluted in a ratio of 1:10 in DPBS 1x. Informed consent was

given by blood donors, according to the ethical and legal standards of EFS. Blood usage was regulated by the Health Department of Research Ministry, according to the French directive DC-2008-334. Blood tubes were delivered 3 days after withdrawal and were used for experiments at room temperature the same day as delivery. After 10x dilution in DPBS 1x, we verify that the hematocrit is between 4 and 5 % for all blood experiments.

The *Escherichia coli* GFP (ATCC, 25922GFP) strain is grown in ampicillin-treated Luria Bertani (LB) agar plates at 37 °C in 5 % CO₂ and incubated overnight in LB agar plates without ampicillin to avoid filamentous forms of *E. coli* bacteria that would induce variabilities in bacterial dimensions. Therefore, in our experiments, bacteria display the same dimensions as wild *E. coli* strains grown in LB agar plates²⁸.

PC3 cells are resuspended at 5 × 10⁶ cells/mL in 2mL of 10x-diluted blood, after centrifugation at 300 × g for 5 minutes. Bacteria are then scraped from the plates and resuspended in the 10x-diluted blood sample containing GFP-PC3 cells to a final concentration of 1.0 × 10⁶ - 1.0 × 10⁷ bacteria/mL.

The concentration of particles in initial samples and output solutions after experiments is quantified by optical counting of at least 400 particles per condition with Kitvia Cell Fast-Read plates (fisherscientific, H01BVS100). For each condition, a sample of at least 500 μL is collected without any problematic clogging.

5.3.2 Two-Stage Separation Principle

We present a two-stage purification platform with two successive DLD modules, called respectively "DLD1" and "DLD2" (fig. 5.10 a). The sample is first injected in DLD1 to separate particles around the critical diameter $D_{c1} = 8 \mu\text{m}$, according to Davis' model [326]. Each DLD1 outlet is connected to a chamber. The inlet of DLD2 is connected to the chamber that contains non-deviated particles from DLD1. DLD2 separates particles around a critical diameter $D_{c2} = 2 \mu\text{m}$, according to our experiments with different bead sizes (Appendix 4).

The chambers are made of a hyperelastic membrane that is initially pressed against one of the cartridge sheets and then progressively swells to get filled with the sample flowing out from DLD1 (fig. 5.10 b). When the membrane reaches its maximal deformation amount - which corresponds to a chamber filling of about 1 mL - air pressure is applied on top of the membrane to press it down and inject the sample towards a downstream fluidic channel. Similar membranes were implemented by Parent et al. [419] to control liquid volumes of up to 100 μL. Here we have adapted this technology to achieve a storage volume of up to 1 mL in our flexible chambers, using openings in the cartridge that allow free deformation of the membrane (fig. 5.10 b). Therefore, in our case, the maximum filling volume is only limited by the deformation before rupture of the membrane. In order to apply high pressures on the membrane, a removable reservoir is plugged on the chamber opening, resulting in a closed controlled environment around the chamber (shown in fig. 5.10 b and schematically represented for the third step in fig. 5.10 b). The advantage of these stretchable membranes compared to rigid chambers is that they address the issues of air bubble injection during filling in the second DLD stage. Indeed, no air is introduced in the chamber when pressure is applied on the membrane, since the pneumatic channel controlling injection is located on the opposite side of the membrane compared to the fluidic channels (fig. 5.10 b).

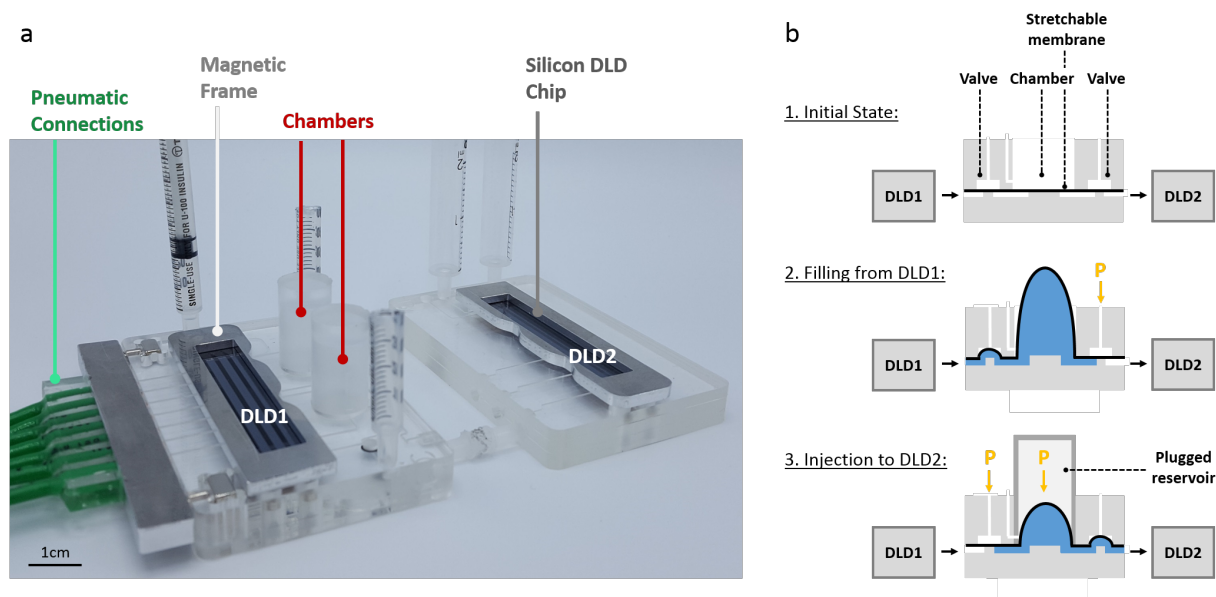


Figure 5.10: a) Experimental setup with both cascaded DLD modules, called DLD1 and DLD2. b) Schematic of the three successive actuation steps of the stretchable membranes. Step 1: the valves are not actuated and the chamber is empty, the stretchable membrane is flat and undeformed. Step 2: The downstream valve is closed by applying pressure on the membrane, while the upstream valve from DLD1 is open to enable the filling of the chamber through the swelling of the stretchable membrane. Step 3: The upstream valve is closed to avoid backflow towards DLD1 and the downstream valve connected to DLD2 is open. Controlled pressure is applied on the chamber, thanks to a plugged reservoir, to inject the sample towards DLD2.

The two-stage purification protocol is composed of successive automatically controlled steps. First, the sample is injected in DLD1 and the chambers are filled with the non-deviated and deviated samples. Both chambers fill up simultaneously with the same amount of sample since our DLD modules have been designed to allow the sample to flow out from both outlets at the same flow rate. Valves are placed upstream and downstream of both chambers to achieve purification steps successively. First, the downstream valves (between the chambers and DLD2) are closed, while the upstream valves (between DLD1 and the chambers) are open to store the samples from DLD1 in the chambers and perform DLD1 purification without any disturbance from DLD2 (Step 1 in fig. 5.11). When both chambers are filled with about 1 mL of sample, injection at the DLD1 entrance is stopped and the upstream valves between DLD1 and the chambers are closed. The deviated sample can be collected for further analysis simply by opening the valve placed downstream of the deviated chamber (Step 2 in fig. 5.11). The non-deviated sample is then injected in DLD2 by closing the upstream valve connected to DLD1 and opening the downstream valve connected to DLD2 (Step 3 in fig. 5.11). An alternative downstream valve enables to collect or remove the non-deviated sample without passing through DLD2. Sample injection in DLD2 requires to apply pressure on the membrane owing to the high hydraulic resistance presented downstream. This is why a solid reservoir is plugged on the cartridge above the membrane and connects it to a pneumatic channel

from the cartridge. We verify the filling of both DLD2 outlets (to output syringes) while applying pressure on the non-deviated chamber in the plugged reservoir. At the end of the protocol, particles smaller than D_{c2} are extracted from particles larger than both D_{c1} and D_{c2} .

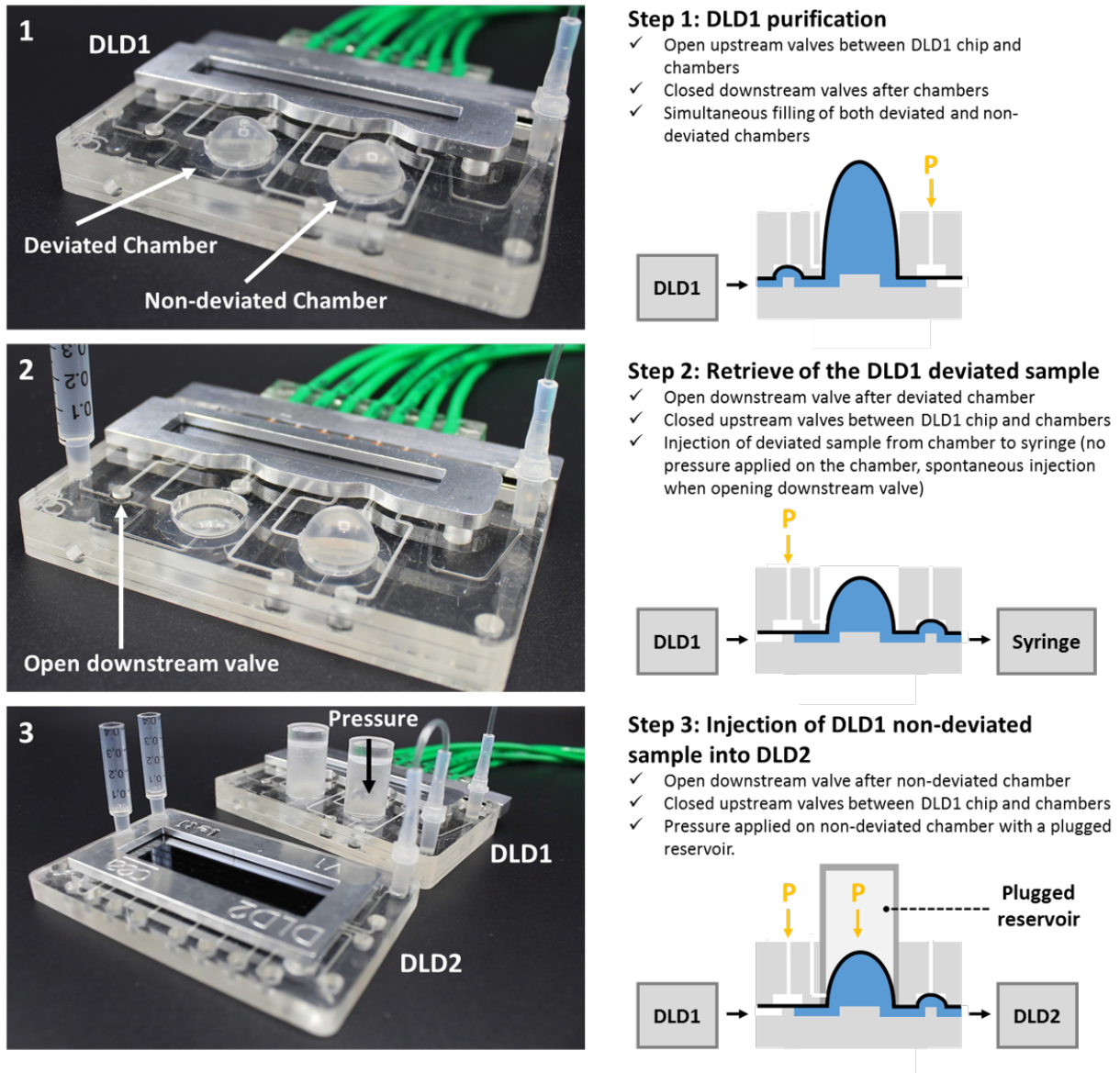


Figure 5.11: Pictures of the platform and corresponding schematics for the different actuation steps.

The DLD1 module integrates the chip, both output chambers, the valves and their pneumatic actuation channels and connectors (fig. 5.12). Fluidic sealing of the chip on the cartridge is performed by a plug-and-play magnetic holder and silicone gaskets. The cartridge consists of four different levels: a first level (1 on fig. 5.12) that contains both chamber openings and pneumatic channels to actuate the valves and chambers

located in the second level (2 on fig. 5.12). The valve and chamber membranes are sealed between levels 2 and 3 of fig. 5.12 and are connected to the fluidic channels of the bottom layer (represented in the enlarged box of fig. 5.12). These fluidic channels connect the DLD1 outlets to the chambers and to the valves placed upstream and downstream of each chamber. Pressure is controlled through the pneumatic channels thanks to a lateral connector, that is maintained against the layer n°1 with magnets.

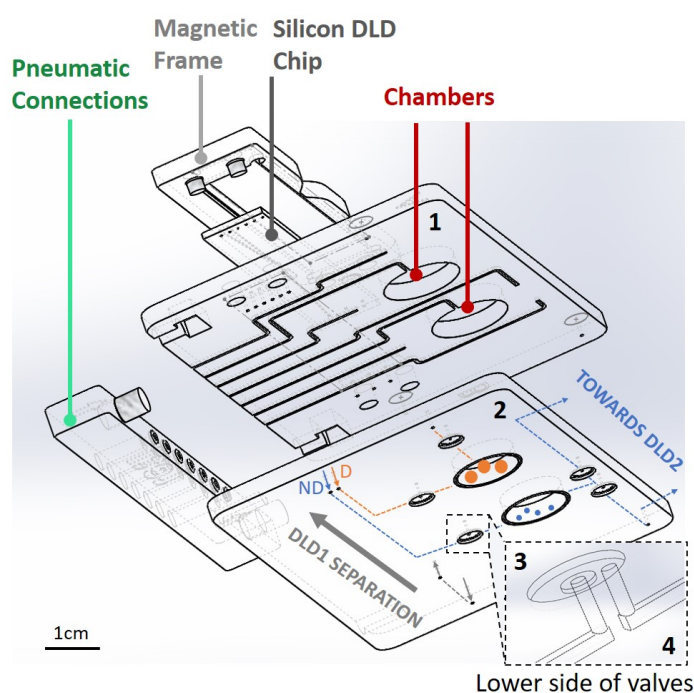


Figure 5.12: Exploded view of the first module (DLD1) with pneumatic connections to actuate the valves, magnetic holding of the silicon DLD chip and the four layers of the plastic cartridge: pneumatic channels and chamber openings (layer 1), upper side of the valves and chamber openings (layer 2), lower side of the valves (layer 3 in the enlarged box), fluidic channels (layer 4 in the enlarged box).

Thus, **integrated valves and collection chambers between both DLD modules enable automatic control of successive DLD purification steps without any intermediary sample manipulation.** Sequential operation of the DLD steps is demonstrated for the first time using our integrated flexible chambers, while previous work used either a single chip or external flow rate balancing with syringe pumps or droplets.

5.3.3 Validation of the Two-Stage Fractionation with Beads

First, we validated the developed integrated platform for cascaded separation with model microbeads. A mixture of $10\ \mu\text{m}$, $5\ \mu\text{m}$ and $1\ \mu\text{m}$ -beads is used as a model sample for two successive separations around the respective critical diameters $D_{c1} = 8\ \mu\text{m}$ and $D_{c2} = 2\ \mu\text{m}$. The sample is injected through the DLD1 inlet (fig. 5.13) and flows through the DLD1 chip. Non-deviated (ND) beads are collected in the left chamber of fig. 5.13, while deviated (D) beads are simultaneously collected in the other chamber. We observe that the deviated chamber displays a light green shade compared to the non-deviated chamber (fig. 5.13), which is attributed to the presence of larger beads, with higher fluorescence intensity. Then, non-deviated beads are injected in the DLD2 module and this second purification step enables to collect two bead populations in the DLD2 outlets called ND (2) and D (2) on fig. 5.13. In order to simplify the fluidic control at the channel entrance, our DLD devices feature only one inlet. Thus, the injected particles span the full width of the channel at the entrance of the device. Therefore, in the case of particles smaller than the cutoff diameter D_c , at least 50 % of the injected beads should actually flow out through the deviated outlet, since they display a non-deviated trajectory. Conversely, all particles larger than D_c should be deviated. We experimentally validated this capacity, and observed that the entire population of large particles - including those initially injected in the non-deviated side - are retrieved at the deviated outlet.

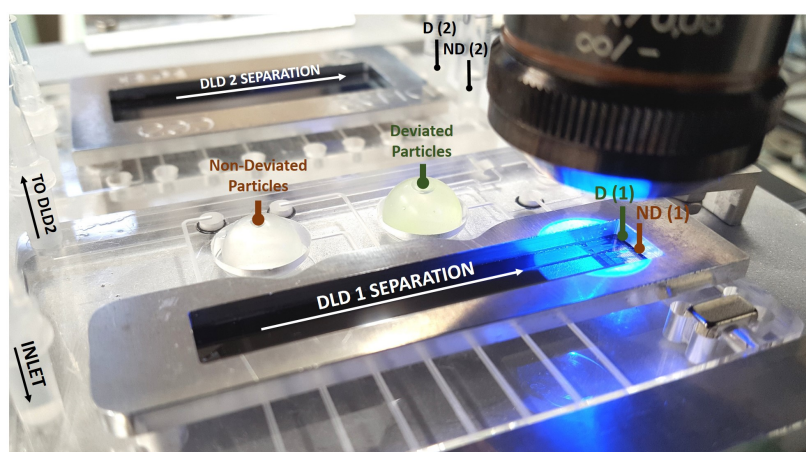


Figure 5.13: Cascaded DLD devices during testing with model microbeads. A mixing of $10\ \mu\text{m}$, $5\ \mu\text{m}$ and $1\ \mu\text{m}$ -beads is injected through the inlet of the DLD1 module and the flexible chambers are filled respectively with the non-deviated particles (flowing out through the DLD outlet called ND) and with the deviated particles (flowing out through the DLD outlet called D). The non-deviated particles are then injected in the DLD2 module for further separation.

During DLD sorting, we monitor the trajectory of the fluorescent particles in both modules (fig. 5.14). The results obtained with the cascaded platform are compared to the separation efficiency of each independent module. Images at the outlet of DLD1 clearly show intense fluorescent streaks on the right side, that correspond to deviated $10\ \mu\text{m}$ -beads, while $5\ \mu\text{m}$ -beads flow out through the entire channel width since they are not deviated from the single inlet.

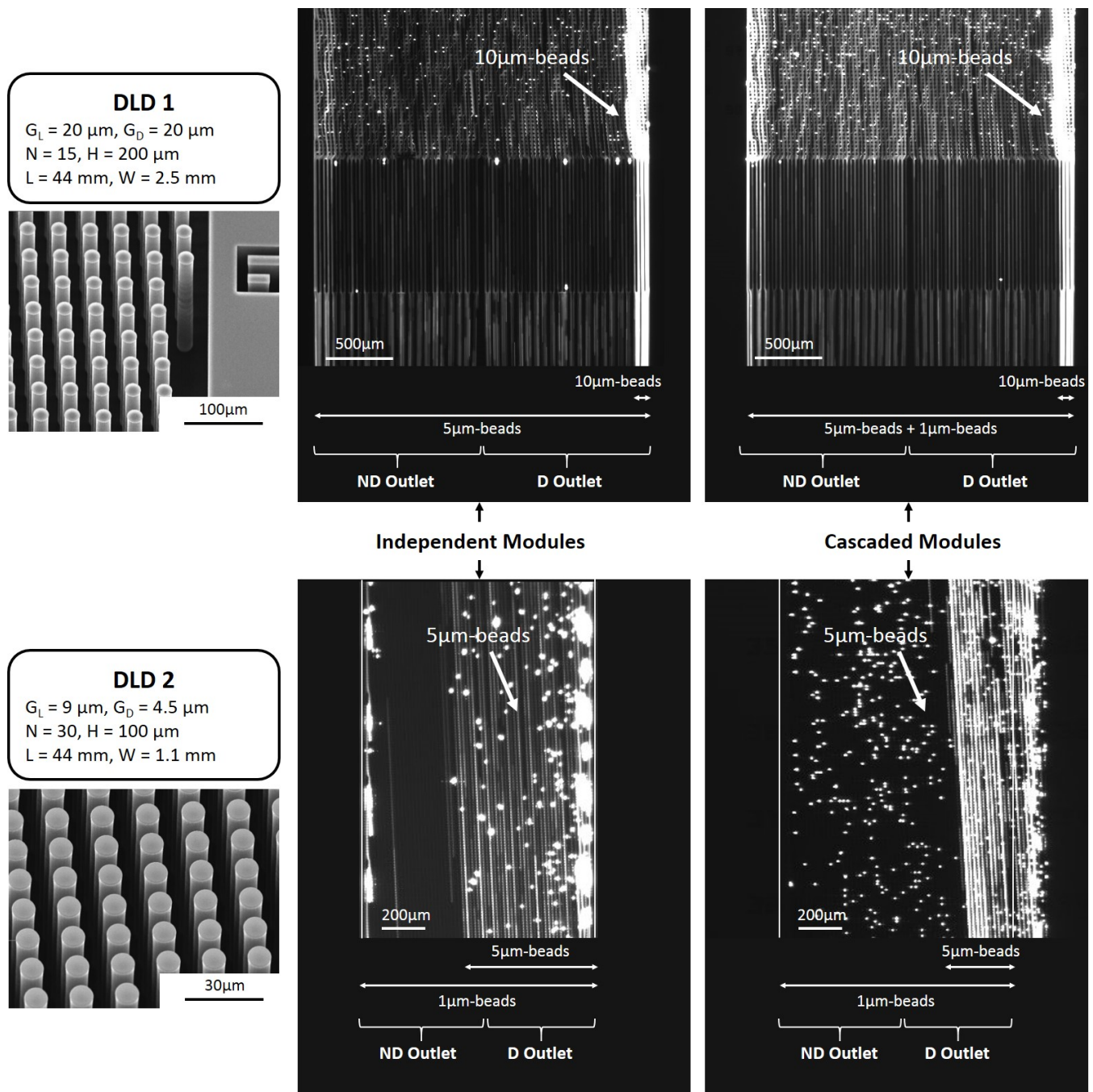


Figure 5.14: Fluorescent images of the trajectory of microbeads in the DLD1 and DLD2 modules in both the independent (left images) and cascaded (right images) configurations. The outlet position of the non-deviated (ND) and deviated (D) outlets is given for each observed channel. White deviated streaks correspond to $10 \mu\text{m}$ -beads in DLD1 and $5 \mu\text{m}$ -beads in DLD2.

No significant difference can be noticed in the deviation efficiency between the independent and the cascaded configurations, which is confirmed after quantification of the beads in both DLD1 outlets (fig. 5.15). Indeed, 88 % of the collected 10 μm -beads are detected in the deviated outlet in the independent configuration, while the cascaded configuration leads to the deviation of 100 % of the collected 10 μm -beads. In the channel of DLD2 (fig. 5.14), white deviated streaks corresponding to the trajectory of 5 μm -beads are observed. Intense fluorescent streaks near the channel walls can be seen when beads are captured on both sides, which is particularly important in DLD2 since the downstream gap is smaller than the 5 μm bead diameter. We verify that more than 98 % of the collected 5 μm -beads are deviated by Module 2 in both the independent and the cascaded configurations (the zigzag path is not possible in this case for 5 μm -beads given the 4.5 μm downstream gap), while 1 μm -beads are also partly deviated by Module 2, with 62 to 65 % of them counted in the deviated outlet (fig. 5.15). It should be pointed out that the percentages given for DLD2 in the cascaded configuration are relative to the number of 5 μm and 1 μm -beads that are collected in the non-deviated outlet of DLD1 (about 50 % of the beads initially injected in DLD1 because of the one-inlet / two-outlets configuration).

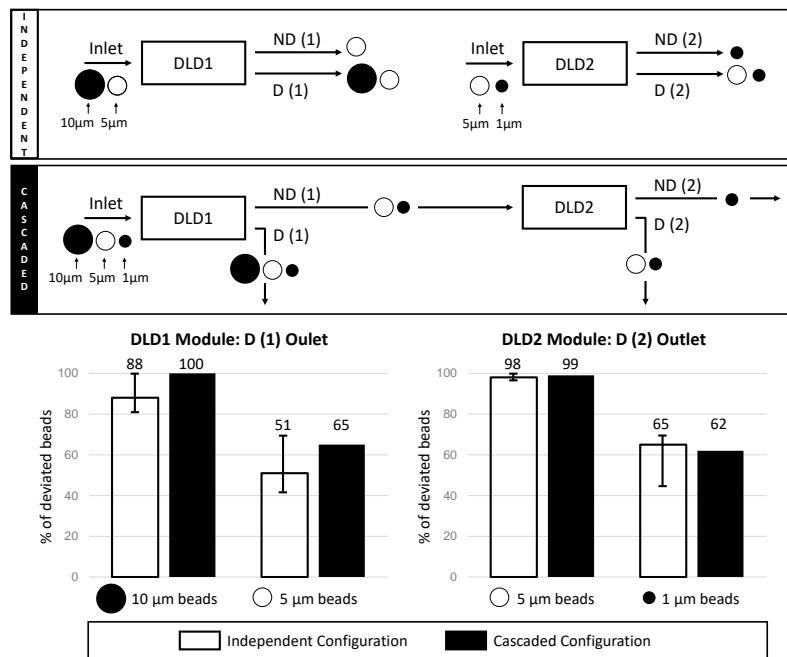


Figure 5.15: Schematic representation of the compared independent and cascaded configurations to separate 10 μm , 5 μm and 1 μm -beads. The deviated outlets (D (1) for DLD1 and D (2) for DLD2) are analyzed in both cases to quantify the ratio of deviated beads among the total output particles for each bead size.

We also verify that the recovery yield (defined as the percentage of injected particles that are collected at the DLD outlets) is not degraded in the cascaded configuration, which confirms that the beads are efficiently injected out of the flexible chambers. The obtained recovery yield at the DLD1 stage was 100 % in both the independent and the cascaded configurations for the 10 μm and 5 μm beads. The DLD2

module displays recovery yields of 68 % and 80 % for 5 μm beads, and 65 % and 70 % for 1 μm beads, respectively in the independent and the cascaded configurations. Thus, **our cascaded platform displays similar performances as independent modules to successively separate particles around two different critical diameters.**

5.3.4 Application to the isolation of Bacteria from Blood Samples

We implemented the same cascaded platform to **fractionate a complex biological sample, containing three main particle dimensions: PC3 human prostate cancer cells, blood cells and E. coli bacteria.** A two-step purification is required in this case to isolate bacteria and remove both PC3 cells and blood contaminants (mainly RBCs). PC3 cells were GFP-transfected to enable to follow their trajectory in DLD modules. The number of particles in each sample was determined on counting plates, in fluorescence microscopy for PC3 cells and GFP-modified bacteria, and in bright-field microscopy for RBCs.

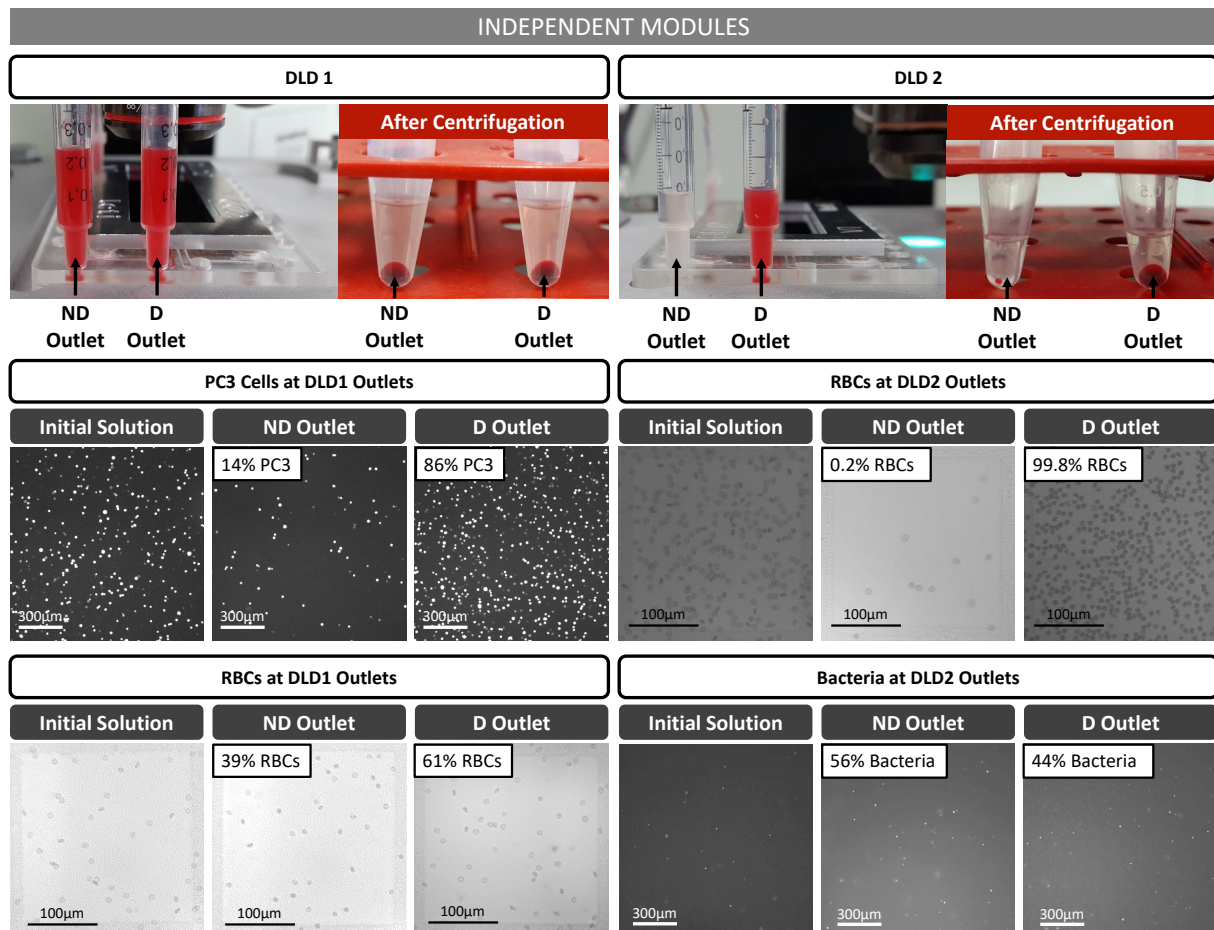


Figure 5.16: Independent modules: DLD outlets of DLD1 and DLD2 before and after centrifugation. Quantification of GFP-PC3 cells, RBCs and GFP-E. coli bacteria in the initial sample solution and in both outlets of DLD1 and DLD2.

We first validated both DLD1 and DLD2 modules independently (fig. 5.16): DLD1 deviates 61 % of the collected RBCs and removes 86 % of PC3 cells, while DLD2 removes 99.8 % of RBCs. As expected from the critical diameter of DLD2 ($D_{c2} = 2 \mu\text{m}$), bacteria are not deviated (suggesting that they are oriented along their smallest dimension while flowing along DLD pillars) and can be found at similar concentrations in both DLD outlets since the sample is initially injected through a single inlet. Since white blood cells (WBCs) were not labeled, their trajectory and distribution could not be visualized, but most of them are expected to be deviated by DLD1 ($D_{c1} = 8 \mu\text{m}$), since their dimensions range from 7 to 20 μm . Moreover, given the low concentration of WBCs relative to PC3 cells in our 10x-diluted blood samples, the obtained results should not be influenced by the behavior of WBCs.

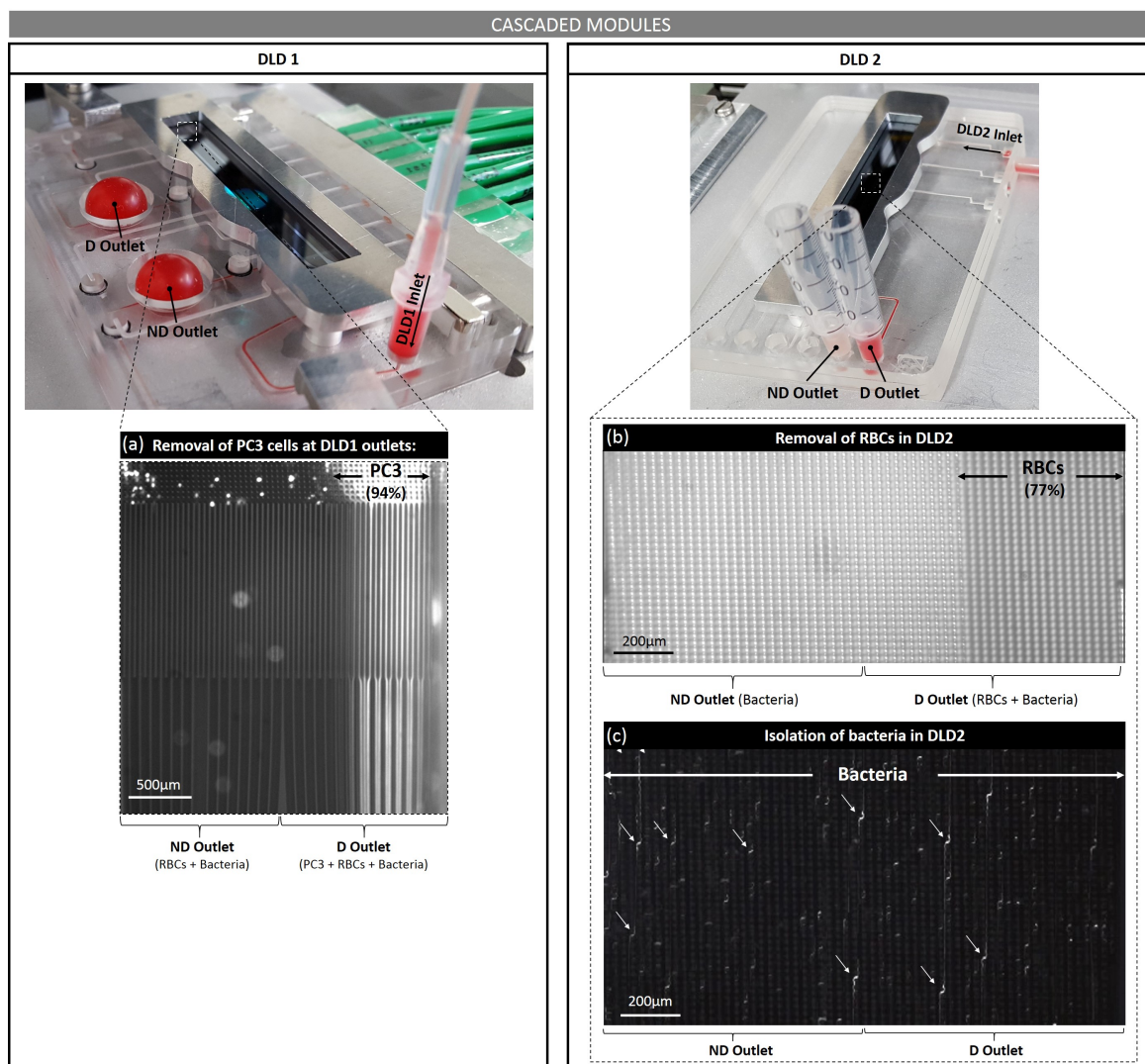


Figure 5.17: Cascaded modules: Images of both modules with the corresponding trajectory of deviated PC3 cells at DLD1 outlets (a), deviated RBCs in DLD2 (b) and non-deviated bacteria in DLD2 (c). Periodic zigzag displacements of bacteria are pointed by white arrows.

Both modules were then connected together in the cascaded platform. Figure 5.17 shows the chambers at the outlet of Module 1 respectively filled with the non-deviated (ND) and deviated (D) particles. PC3 cells are clearly focused on the deviated side of DLD1 from fluorescent imaging of the outlet (fig. 5.17 a).

Similarly to the independent configuration, Module 1 enables depletion of 94 % of the collected PC3 cells, while 68 % of RBCs are removed by the first DLD stage (fig. 5.18). Images of DLD2 show the focus of RBCs on the right deviated side of the channel and the zigzag trajectory of GFP-modified *E. coli* bacteria (fig. 5.17 b and c). We verify that 77 % of RBCs flowing out of DLD2 are collected in the deviated outlet, while 46 % of output bacteria are not deviated by DLD2 (fig. 5.18).

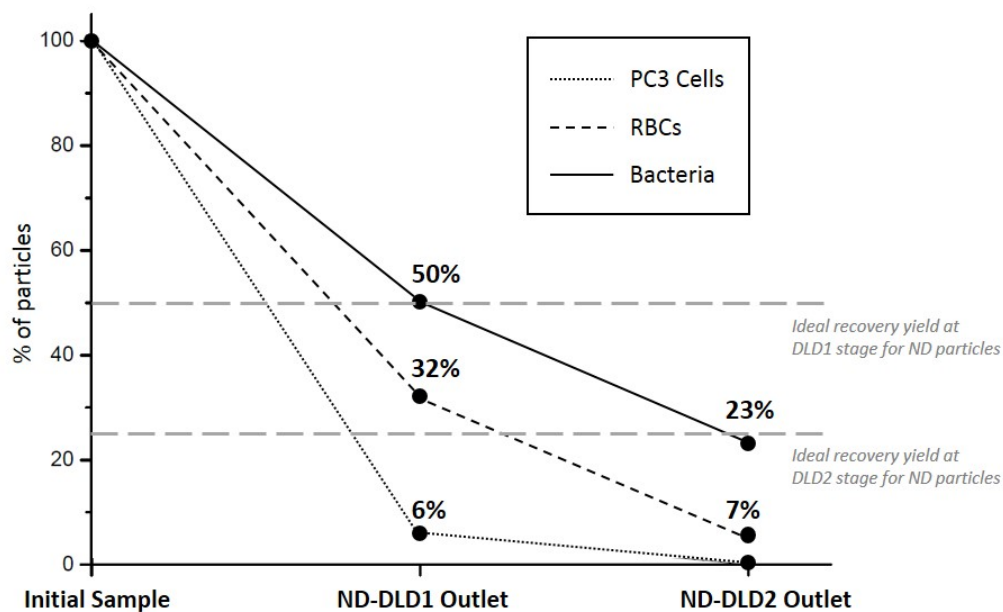


Figure 5.18: Cascaded modules: Quantification of residual non-deviated PC3 cells and RBCs, as well as collected non-deviated *E. coli* bacteria, at each DLD purification stage. 94 % of PC3 cells and 68 % of RBCs are removed by DLD1, while 77 % of RBCs are eliminated by DLD2. In the final non-deviated channel of DLD2, that contains our sample of interest, 23 % of bacteria are depleted from 100 % of the initial PC3 cells and 93 % of RBCs.

Therefore, after both purification steps through the cascaded platform, the non-deviated outlet of Module 2 contains more than 20 % of the initially injected *E. coli* bacteria with less than 8 % of the initial number of RBCs and 0 % of PC3 cells. The recovery yield of bacteria after both DLD purification steps closely approaches the ideal 25 % recovery yield (fig. 5.18), owing to our one-inlet / two-outlets configuration at each step. This final recovery yield could still be improved by using DLD devices with two inlets instead of the single entrance configuration used in this paper. DLD devices with two inlets would enable to reach 100 % recovery of the non-deviated particles although it requires balancing control of both injected solutions (sample and buffer) at the channel inlets.

Chapter Summary: Multi-DLD Platforms for Complex Samples

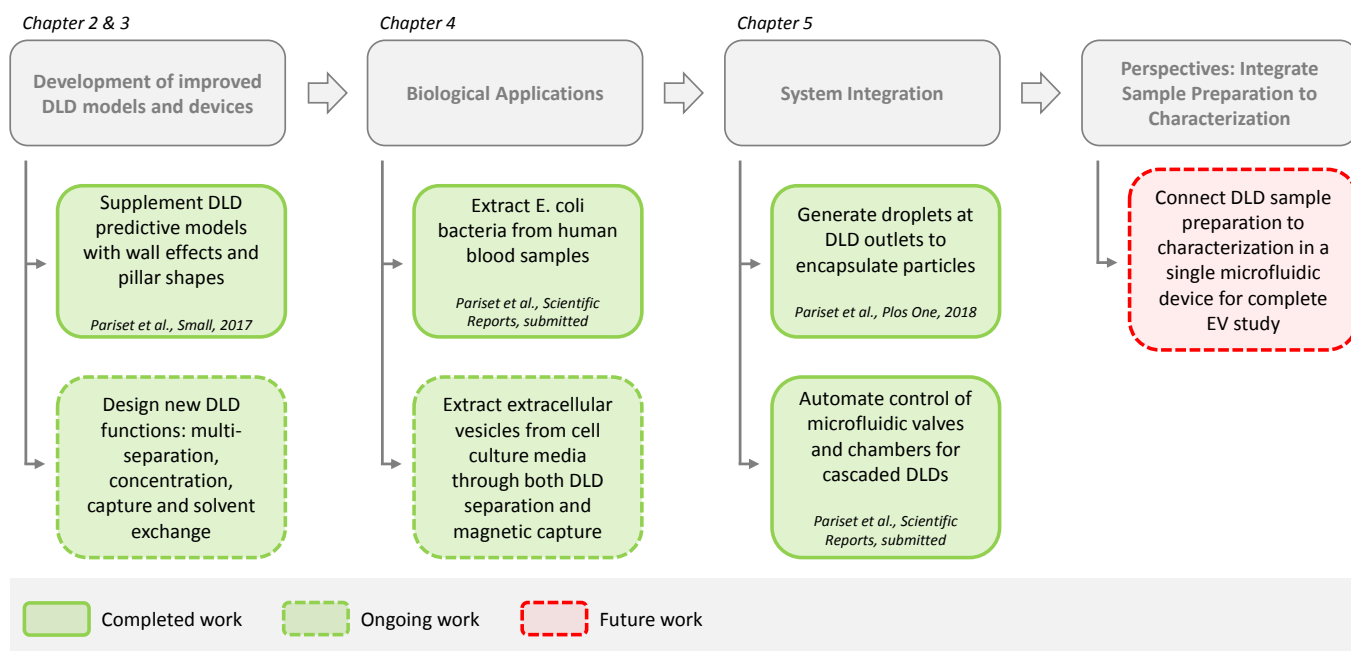
- Purification of complex samples that contain a wide range of particle sizes requires several successive DLD steps. Two strategies were presented to cascade DLD modules without degrading the separation efficiency of each purification step.
- The first approach consists in connecting DLD outlets to droplet generation T-junctions in order to apply controlled pressures on the output DLD samples thanks to an immiscible oil solution. At the same time, sorted particles are encapsulated, which can be advantageous for some downstream applications that require digital microfluidics. A general predictive model was proposed in order to identify the optimal pressure conditions to apply at the different inlet channels to ensure efficient particle sorting.
- Another approach was proposed when the use of an oil solution is undesirable. Moreover, this second solution enables to integrate the entire fluidic and pneumatic control inside the cartridge and avoid any intermediate sample manipulation. This was achieved thanks to intermediate collection chambers that enable to perform the different DLD purification steps both successively and independently. This platform was implemented for the extraction of *E. coli* bacteria from a blood sample, in which larger prostate cancer cells were added in order to demonstrate separation over 10X different length scales.

Résumé du Chapitre : DLDs en Cascade pour Purifications Complexes

- La purification d'échantillons complexes contenant une large gamme de tailles de particules nécessite la mise en cascade de plusieurs étapes de DLD successives. Deux stratégies ont été présentées dans ce chapitre pour mettre en série plusieurs modules de DLD sans dégrader l'efficacité de séparation de chaque étape de purification.
- La première approche consiste à placer en sortie de chaque étape de DLD un module de génération de gouttes par jonction en T, afin d'appliquer une pression contrôlée sur les échantillons purifiés par DLD grâce à une solution d'huile non miscible. Dans le même temps, cette technique permet d'encapsuler les particules triées, ce qui peut être avantageux pour certaines applications placées en aval de la purification par DLD et basées sur la microfluidique digitale. Un modèle prédictif généralisé a été développé afin d'identifier les conditions de pression optimales à appliquer au niveau des différentes entrées fluidiques pour assurer un tri des particules efficace au niveau des modules de DLD.
- La seconde approche proposée fournit une alternative lorsque l'utilisation d'une solution organique est indésirable. Cette approche permet d'intégrer à la fois le contrôle pneumatique et fluidique au sein d'une même plateforme et d'éviter toute manipulation externe de l'échantillon. Pour cela, des chambres flexibles ont été développées et placées entre les modules de DLD afin de réaliser chaque étape de tri successivement et indépendamment. Cette plateforme a été validée par une application biologique introduite dans le Chapitre 4, à savoir l'extraction de bactéries *E. coli* à partir d'échantillons de sang humain contenant des cellules cancéreuses, pour un tri successif d'une large gamme de dimensions de particules.

Conclusion

The main achievements of this thesis and future perspectives are summarized below:



Several DLD designs were numerically modeled and experimentally implemented in this thesis to improve DLD separation performances and provide advanced DLD functions, such as multi-separation, concentration, capture and solvent exchange. Improved models were proposed, taking into account the influence of the pillar shape and the side channel walls, in order to better anticipate particle behavior in DLD arrays.

Testing of the DLD devices with model microbeads was leveraged to identify the required design improvements in order to avoid particle clogging, increase separation capacity and reduce side wall effects. From this preliminary characterization were identified appropriate DLD devices for different biological applications. First, the isolation of E. coli bacteria from human blood samples was used as a first proof of principle with large objects (bacteria and blood cells) in order to optimize operational conditions, before addressing the extraction of extracellular vesicles (EVs). For this target application, DLD was identified to be highly performant in the separation of micrometer-sized components, whereas nano-DLD devices had major limitation - such as very limited flow rates - that made them hardly usable for the separation of nano-objects. This is why a multi-step microfluidic protocol was proposed for EV extraction from cell culture media, with a DLD step to remove large cellular contaminants and a magnetic capture step to extract EV subpopulations on functionalized nanobeads.

In addition to optimizing the separation capacity of each individual DLD device, this thesis also considered the problem of system integration. As each DLD device can only separate two particle populations around a single critical diameter, several cascaded DLD steps are required when purifying

complex samples over a wide range of particle sizes. However, performance loss was observed with serial DLD configurations, because of pressure unbalance at DLD outlets. Thus, two complementary approaches were proposed to keep the same separation efficiency with cascaded DLD steps compared to single DLD devices. In the first approach, droplet generation was integrated in DLD cartridges to ensure at the same time sample encapsulation and pressure control. The second approach implemented microfluidic valves and chambers to perform each DLD step both independently and automatically.

The next objective is to go further in integration to build an all-in-one microfluidic device including both sample preparation and characterization. For this purpose, emergent technologies, such as suspended nanochannel resonators, could provide new clinical answers through correlations between EV physical signature and biological functions. Biomarker discovery and early diagnostics would certainly benefit from the emergence of such new EV biophysical fingerprinting methods, especially if they integrate automated sample preparation, with high purity, high speed and low sample volume.

Pour conclure, les travaux présentés dans ce manuscrit ont permis de traiter l'amélioration des performances de la séparation par DLD et d'apporter de nouvelles fonctions complémentaires (telles que la multi-séparation, la concentration, la capture et le changement de solvant), en s'appuyant sur des simulations numériques et validations expérimentales. De nouveaux modèles prédictifs ont été proposés afin de mieux anticiper le comportement des particules séparées par DLD, en tenant compte de la géométrie des piliers et des effets de bord au niveau des parois du canal.

Grâce à la validation de nos dispositifs de DLD avec des microbilles modèles, de nombreuses améliorations du design ont pu être proposées de façon incrémentale, telles que la diminution du colmatage des particules entre les piliers, l'augmentation de l'efficacité de séparation, et la réduction des effets de bord. Ces résultats préliminaires ont aussi permis d'identifier les composants adaptés aux différentes applications biologiques adressées dans ce manuscrit. Une première preuve de principe a pu être démontrée par l'isolement de bactéries *E. coli* à partir d'échantillons de sang humain. Ce cas d'étude simplifié (avec de plus larges composants) nous a permis d'optimiser les conditions d'opération de nos dispositifs, avant de passer à l'application d'intérêt, à savoir l'extraction d'EVs à partir de milieu de culture cellulaire. Les limitations rencontrées avec nos composants de "nano-DLD" (telles que de très faibles débits) ont conduit au développement d'un dispositif microfluidique couplé, préférable à l'utilisation de modules de DLD pour l'ensemble des étapes de purification des EVs. En effet, notre dispositif intègre une étape de séparation par DLD pour éliminer les plus larges contaminants cellulaires, mais aussi une étape de capture magnétique sur puce, afin d'extraire une sous-population ciblée d'EV.

Au-delà de l'optimisation indépendante de chaque module de DLD, cette thèse a aussi permis de développer de nouvelles techniques d'intégration de plusieurs dispositifs connectés au sein d'un même système. En effet, chaque étape de DLD ne peut séparer que deux populations de particules autour d'un seul diamètre critique. Ainsi, la purification d'échantillons plus complexes nécessite la mise en cascade de plusieurs dispositifs de DLD afin de séparer une large gamme de tailles de particules. Cependant, la mise en série de plusieurs modules de DLD entraîne une dégradation des performances de la séparation, en raison du déséquilibre des pressions au niveau des canaux de sortie de chaque module. Afin de conserver les performances de chaque module placé en série, deux approches complémentaires ont été proposées ici. La première approche consiste à connecter chaque sortie de DLD à une zone de génération de gouttes, ce qui permet d'assurer à la fois le contrôle en pression au niveau des sorties de DLD par une solution non miscible, et l'encapsulation des particules triées. La seconde approche repose sur l'intégration de valves et de chambres microfluidiques pour permettre la collecte et l'injection successives de l'échantillon entre chaque étape de DLD.

Ces technologies d'intégration des modules de DLD pourront être étendues à la connexion directe de l'étape de préparation d'échantillon à l'étape de caractérisation. Pour cela, certaines technologies d'analyse, telles que les SNRs (Suspended Nanochannel Resonators), développés par le laboratoire du Professeur Manalis (MIT), pourront permettre d'extraire à la fois les signatures biologique et physique des EVs pour un diagnostic clinique plus complet. L'intégration de cette analyse à une extraction des vésicules automatisée, plus efficace et plus rapide pourra permettre un réel bon en avant vers l'utilisation des EVs comme biomarqueurs précoces en biopsie liquide.

Bibliography

- [1] Maria Yáñez-Mó, et al. Biological properties of extracellular vesicles and their physiological functions. *Journal of Extracellular Vesicles*, 4(0), May 2015. 23, 29
- [2] Wang Yiran, et al. Global scientific trends on exosome research during 2007–2016: A bibliometric analysis. *Oncotarget*, 5(0), April 2017. 23, 24
- [3] Erwin Chargaff et al. The Biological Significance of the Thromboplastic Protein of Blood. *Journal of Biological Chemistry*, 166(1):189–197, January 1946. 24
- [4] Peter Wolf. The Nature and Significance of Platelet Products in Human Plasma. *British Journal of Haematology*, 13(3):269–288, May 1967. 24
- [5] Bin-Tao Pan et al. Fate of the transferrin receptor during maturation of sheep reticulocytes in vitro: Selective externalization of the receptor. *Cell*, 33(3):967–978, July 1983. 24
- [6] B lymphocytes secrete antigen-presenting vesicles. *The Journal of Experimental Medicine*, 183(3): 1161–1172, March 1996. 24
- [7] Clotilde Théry, et al. Exosomes: Composition, biogenesis and function. *Nature Reviews Immunology*, 2 (8):569, August 2002. 24, 27
- [8] Basant Kumar Thakur, et al. Double-stranded DNA in exosomes: A novel biomarker in cancer detection. *Cell Research*, 24(6):766–769, June 2014. 24
- [9] J. Ratajczak, et al. Embryonic stem cell-derived microvesicles reprogram hematopoietic progenitors: Evidence for horizontal transfer of mRNA and protein delivery. *Leukemia*, 20(5):847–856, February 2006. 24, 29, 35
- [10] Hadi Valadi, et al. Exosome-mediated transfer of mRNAs and microRNAs is a novel mechanism of genetic exchange between cells. *Nature Cell Biology*, 9(6):654–659, June 2007. 24, 26, 35, 148
- [11] Johan Skog, et al. Glioblastoma microvesicles transport RNA and proteins that promote tumour growth and provide diagnostic biomarkers. *Nature Cell Biology*, 10(12):1470–1476, December 2008. 24, 32
- [12] Charles P. Lai, et al. Visualization and tracking of tumour extracellular vesicle delivery and RNA translation using multiplexed reporters. *Nature Communications*, 6:7029, May 2015. 24
- [13] Michele Guescini, et al. Astrocytes and Glioblastoma cells release exosomes carrying mtDNA. *Journal of Neural Transmission*, 117(1):1, January 2010. 24
- [14] Leonora Balaj, et al. Tumour microvesicles contain retrotransposon elements and amplified oncogene sequences. *Nature Communications*, 2:180, February 2011. 24

-
- [15] Christoph Kahlert, et al. Identification of Double Stranded Genomic DNA Spanning all Chromosomes with Mutated KRAS and p53 DNA in the Serum Exosomes of Patients with Pancreatic Cancer. *Journal of Biological Chemistry*, page jbc.C113.532267, January 2014. [24](#)
- [16] Marina Colombo, et al. Biogenesis, secretion, and intercellular interactions of exosomes and other extracellular vesicles. *Annual Review of Cell and Developmental Biology*, 30:255–289, 2014. [25](#), [28](#)
- [17] Alicia Llorente, et al. Cholesterol regulates prostatesome release from secretory lysosomes in PC-3 human prostate cancer cells. *European Journal of Cell Biology*, 86(7):405–415, July 2007. [25](#)
- [18] Karine Laulagnier, et al. Mast cell- and dendritic cell-derived exosomes display a specific lipid composition and an unusual membrane organization. *Biochemical Journal*, 380(1):161–171, May 2004. [25](#)
- [19] Isabella Parolini, et al. Microenvironmental pH Is a Key Factor for Exosome Traffic in Tumor Cells. *Journal of Biological Chemistry*, 284(49):34211–34222, April 2009. [25](#), [26](#), [28](#)
- [20] Sander A. A. Kooijmans, et al. Exosome mimetics: A novel class of drug delivery systems. *International Journal of Nanomedicine*, 7:1525–1541, 2012. [25](#)
- [21] Tyson J. Smyth, et al. Examination of the specificity of tumor cell derived exosomes with tumor cells in vitro. *Biochimica Et Biophysica Acta*, 1838(11):2954–2965, November 2014. [25](#)
- [22] Dirk Fitzner, et al. Selective transfer of exosomes from oligodendrocytes to microglia by macropinocytosis. *J Cell Sci*, 124(3):447–458, February 2011. [26](#), [50](#)
- [23] James R. Edgar. Q&A: What are exosomes, exactly? *BMC Biology*, 14, June 2016. [26](#), [27](#)
- [24] Hamish W. King, et al. Hypoxic enhancement of exosome release by breast cancer cells. *BMC Cancer*, 12:421, 2012. [26](#)
- [25] Ariel Savina, et al. Exosome Release Is Regulated by a Calcium-dependent Mechanism in K562 Cells. *Journal of Biological Chemistry*, 278(22):20083–20090, May 2003. [26](#), [148](#)
- [26] Elodie Segura, et al. ICAM-1 on exosomes from mature dendritic cells is critical for efficient naive T-cell priming. *Blood*, 106(1):216–223, July 2005. [26](#)
- [27] Lotta Kilpinen, et al. Extracellular membrane vesicles from umbilical cord blood-derived MSC protect against ischemic acute kidney injury, a feature that is lost after inflammatory conditioning. *Journal of Extracellular Vesicles*, 2, December 2013. [26](#)
- [28] Michelle Demory Beckler, et al. Proteomic analysis of exosomes from mutant KRAS colon cancer cells identifies intercellular transfer of mutant KRAS. *Molecular & cellular proteomics: MCP*, 12(2): 343–355, February 2013. [26](#)
- [29] Bow J. Tauro, et al. Oncogenic H-ras reprograms Madin-Darby canine kidney (MDCK) cell-derived exosomal proteins following epithelial-mesenchymal transition. *Molecular & cellular proteomics: MCP*, 12(8):2148–2159, August 2013. [26](#), [27](#)

-
- [30] Olivier G. de Jong, et al. Cellular stress conditions are reflected in the protein and RNA content of endothelial cell-derived exosomes. *Journal of Extracellular Vesicles*, 1, April 2012. 26
- [31] Paulina Kucharzewska, et al. Exosomes reflect the hypoxic status of glioma cells and mediate hypoxia-dependent activation of vascular cells during tumor development. *Proceedings of the National Academy of Sciences*, 110(18):7312–7317, April 2013. 26
- [32] Hina Kalra, et al. Focus on Extracellular Vesicles: Introducing the Next Small Big Thing. *International Journal of Molecular Sciences*, 17(2):170, February 2016. 26, 27, 35, 53
- [33] Clotilde Théry, et al. Membrane vesicles as conveyors of immune responses. *Nature Reviews Immunology*, 9(8):581–593, August 2009. 27, 28, 35
- [34] Edwin van der Pol, et al. Classification, functions, and clinical relevance of extracellular vesicles. *Pharmacological Reviews*, 64(3):676–705, July 2012. 27, 45
- [35] Samir EL Andaloussi, et al. Extracellular vesicles: Biology and emerging therapeutic opportunities. *Nature Reviews. Drug Discovery*, 12(5):347–357, May 2013. 27, 29
- [36] Clotilde Théry, et al. Isolation and characterization of exosomes from cell culture supernatants and biological fluids. *Current Protocols in Cell Biology / Editorial Board, Juan S. Bonifacino ... [et Al.]*, Chapter 3:Unit 3.22, April 2006. 27, 37, 48, 50
- [37] Harry F. G. Heijnen, et al. Activated Platelets Release Two Types of Membrane Vesicles: Microvesicles by Surface Shedding and Exosomes Derived From Exocytosis of Multivesicular Bodies and alpha-Granules. *Blood*, 94(11):3791–3799, December 1999. 27
- [38] Clotilde Théry, et al. Proteomic Analysis of Dendritic Cell-Derived Exosomes: A Secreted Subcellular Compartment Distinct from Apoptotic Vesicles. *The Journal of Immunology*, 166(12):7309–7318, June 2001. 27
- [39] Electron microscopic evidence for externalization of the transferrin receptor in vesicular form in sheep reticulocytes. *The Journal of Cell Biology*, 101(3):942–948, September 1985. 27
- [40] Shivakumar Keerthikumar, et al. Proteogenomic analysis reveals exosomes are more oncogenic than ectosomes. *Oncotarget*, 6(17):15375–15396, June 2015. 27
- [41] Suresh Mathivanan, et al. Exosomes: Extracellular organelles important in intercellular communication. *Journal of Proteomics*, 73(10):1907–1920, September 2010. 27, 29
- [42] Rossella Crescitelli, et al. Distinct RNA profiles in subpopulations of extracellular vesicles: Apoptotic bodies, microvesicles and exosomes. *Journal of Extracellular Vesicles*, 2, 2013. 27
- [43] Joanna Kowal, et al. Proteomic comparison defines novel markers to characterize heterogeneous populations of extracellular vesicle subtypes. *Proceedings of the National Academy of Sciences*, 113(8):E968–E977, February 2016. 28

-
- [44] Clotilde Théry, et al. Isolation and Characterization of Exosomes from Cell Culture Supernatants and Biological Fluids. In *Current Protocols in Cell Biology*. John Wiley & Sons, Inc., 2001. 28
- [45] Michael Paulaitis, et al. Dynamic Scaling of Exosome Sizes. *Langmuir*, March 2018. 28
- [46] E. van der Pol, et al. Recent developments in the nomenclature, presence, isolation, detection and clinical impact of extracellular vesicles. *Journal of Thrombosis and Haemostasis*, 14(1):48–56, January 2016. 28, 46
- [47] Angela Montecalvo, et al. Mechanism of transfer of functional microRNAs between mouse dendritic cells via exosomes. *Blood*, 119(3):756–766, January 2012. 28
- [48] Katrin J. Svensson, et al. Exosome uptake depends on ERK1/2-heat shock protein 27 signalling and lipid raft-mediated endocytosis negatively regulated by caveolin-1. *Journal of Biological Chemistry*, page jbc.M112.445403, May 2013. 28
- [49] Stefano Gatti, et al. Microvesicles derived from human adult mesenchymal stem cells protect against ischaemia–reperfusion-induced acute and chronic kidney injury. *Nephrology Dialysis Transplantation*, 26(5):1474–1483, January 2011. 29
- [50] Ian del Conde, et al. Tissue-factor–bearing microvesicles arise from lipid rafts and fuse with activated platelets to initiate coagulation. *Blood*, 106(5):1604–1611, September 2005. 29
- [51] G. Raposo, et al. B lymphocytes secrete antigen-presenting vesicles. *The Journal of Experimental Medicine*, 183(3):1161–1172, March 1996. 29
- [52] Joseph Wolfers, et al. Tumor-derived exosomes are a source of shared tumor rejection antigens for CTL cross-priming. *Nature Medicine*, 7(3):297, March 2001. 30
- [53] Pramod K. Giri et al. Exosomes Derived from M. Bovis BCG Infected Macrophages Activate Antigen-Specific CD4+ and CD8+ T Cells In Vitro and In Vivo. *PLOS ONE*, 3(6):e2461, June 2008. 30
- [54] Jason D. Walker, et al. Cytomegalovirus-infected human endothelial cells can stimulate allogeneic CD4+ memory T cells by releasing antigenic exosomes. *Journal of immunology (Baltimore, Md. : 1950)*, 182(3):1548–1559, February 2009. 30
- [55] Lea Luketic, et al. Antigen Presentation by Exosomes Released from Peptide-Pulsed Dendritic Cells Is not Suppressed by the Presence of Active CTL. *The Journal of Immunology*, 179(8):5024–5032, October 2007. 31
- [56] Saho Utsugi-Kobukai, et al. MHC class I-mediated exogenous antigen presentation by exosomes secreted from immature and mature bone marrow derived dendritic cells. *Immunology Letters*, 89(2): 125–131, October 2003. 31
- [57] Charlotte Admyre, et al. Direct exosome stimulation of peripheral human T cells detected by ELISPOT. *European Journal of Immunology*, 36(7):1772–1781, July 2006. 31

-
- [58] Nathalie Chaput, et al. Exosomes as Potent Cell-Free Peptide-Based Vaccine. II. Exosomes in CpG Adjuvants Efficiently Prime Naive Tc1 Lymphocytes Leading to Tumor Rejection. *The Journal of Immunology*, 172(4):2137–2146, February 2004. 31
- [59] Clotilde Théry, et al. Indirect activation of naïve CD4⁺ T cells by dendritic cell–derived exosomes. *Nature Immunology*, 3(12):1156, December 2002. 31
- [60] Dimitris Skokos, et al. Mast Cell-Derived Exosomes Induce Phenotypic and Functional Maturation of Dendritic Cells and Elicit Specific Immune Responses In Vivo. *The Journal of Immunology*, 170(6):3037–3045, March 2003. 31
- [61] Jihène Klibi, et al. Blood diffusion and Th1-suppressive effects of galectin-9–containing exosomes released by Epstein-Barr virus–infected nasopharyngeal carcinoma cells. *Blood*, 113(9):1957–1966, February 2009. 31
- [62] Aled Clayton, et al. Human Tumor-Derived Exosomes Selectively Impair Lymphocyte Responses to Interleukin-2. *Cancer Research*, 67(15):7458–7466, August 2007. 31
- [63] Cunren Liu, et al. Murine Mammary Carcinoma Exosomes Promote Tumor Growth by Suppression of NK Cell Function. *The Journal of Immunology*, 176(3):1375–1385, February 2006. 31
- [64] Aled Clayton, et al. Human Tumor-Derived Exosomes Down-Modulate NKG2D Expression. *The Journal of Immunology*, 180(11):7249–7258, June 2008. 31
- [65] Shaohua Yu, et al. Tumor Exosomes Inhibit Differentiation of Bone Marrow Dendritic Cells. *The Journal of Immunology*, 178(11):6867–6875, June 2007. 31
- [66] Xiaoyu Xiang, et al. Induction of myeloid-derived suppressor cells by tumor exosomes. *International journal of cancer. Journal international du cancer*, 124(11):2621–2633, June 2009. 31
- [67] Hélène Pêche, et al. Presentation of donor major histocompatibility complex antigens by bone marrow dendritic cell-derived exosomes modulates allograft rejection1. *Transplantation*, 76(10):1503–1510, November 2003. 31
- [68] Seon Hee Kim, et al. Effective Treatment of Inflammatory Disease Models with Exosomes Derived from Dendritic Cells Genetically Modified to Express IL-4. *The Journal of Immunology*, 179(4):2242–2249, August 2007. 31
- [69] Noela Prado, et al. Exosomes from Bronchoalveolar Fluid of Tolerized Mice Prevent Allergic Reaction. *The Journal of Immunology*, 181(2):1519–1525, July 2008. 31
- [70] Alexander G. Thompson, et al. Extracellular vesicles in neurodegenerative disease — pathogenesis to biomarkers. *Nature Reviews Neurology*, 12(6):346–357, June 2016. 31
- [71] J. Fauré, et al. Exosomes are released by cultured cortical neurones. *Molecular and Cellular Neuroscience*, 31(4):642–648, April 2006. 31

-
- [72] Mathilde Chivet, et al. Emerging role of neuronal exosomes in the central nervous system. *Frontiers in Physiology*, 3:145, 2012. 31
- [73] A.M. Janas, et al. Exosomes and other extracellular vesicles in neural cells and neurodegenerative diseases. *Biochimica et Biophysica Acta - Biomembranes*, 1858(6):1139–1151, 2016. 31
- [74] Bing Zhang, et al. Synaptic Vesicle Size and Number Are Regulated by a Clathrin Adaptor Protein Required for Endocytosis. *Neuron*, 21(6):1465–1475, December 1998. 31
- [75] Reinhard Jahn et al. Molecular machines governing exocytosis of synaptic vesicles. *Nature*, 490(7419): 201–207, October 2012. 31
- [76] Vivian Budnik, et al. Extracellular vesicles round off communication in the nervous system. *Nature reviews. Neuroscience*, 17(3):160–172, March 2016. 31
- [77] Eva-Maria Krämer-Albers, et al. Oligodendrocytes secrete exosomes containing major myelin and stress-protective proteins: Trophic support for axons? *PROTEOMICS – Clinical Applications*, 1(11): 1446–1461, November 2007. 31
- [78] Flavia Antonucci, et al. Microvesicles released from microglia stimulate synaptic activity via enhanced sphingolipid metabolism. *The EMBO Journal*, 31(5):1231–1240, March 2012. 31
- [79] Lydie Morel, et al. Neuronal Exosomal miRNA-dependent Translational Regulation of Astroglial Glutamate Transporter GLT1. *Journal of Biological Chemistry*, 288(10):7105–7116, August 2013. 31
- [80] Claudia A. Escudero, et al. The p75 neurotrophin receptor evades the endolysosomal route in neuronal cells, favouring multivesicular bodies specialised for exosomal release. *Journal of Cell Science*, 127(9):1966–1979, May 2014. 31
- [81] B. Kumar, et al. Acute myeloid leukemia transforms the bone marrow niche into a leukemia-permissive microenvironment through exosome secretion. *Leukemia*, August 2017. 31
- [82] Youngjin Lee, et al. Oligodendroglia metabolically support axons and contribute to neurodegeneration. *Nature*, 487(7408):443–448, July 2012. 31
- [83] Hae Kyung Lee, et al. Mesenchymal Stem Cells Deliver Exogenous miRNAs to Neural Cells and Induce Their Differentiation and Glutamate Transporter Expression. *Stem Cells and Development*, 23 (23):2851–2861, July 2014. 31
- [84] Shayne Anthony Bellingham, et al. Exosomes: Vehicles for the transfer of toxic proteins associated with neurodegenerative diseases? *Membrane Physiology and Membrane Biophysics*, 3:124, 2012. 31
- [85] Xiang-Yang Cao, et al. MicroRNA biomarkers of Parkinson’s disease in serum exosome-like microvesicles. *Neuroscience Letters*, 644:94–99, March 2017. 31
- [86] A.M. Miranda, et al. Neuronal lysosomal dysfunction releases exosomes harboring APP C-terminal fragments and unique lipid signatures. *Nature Communications*, 9(1), 2018. 31

-
- [87] Francesca Fenizia, et al. EGFR mutations in lung cancer: From tissue testing to liquid biopsy. *Future Oncology (London, England)*, 11(11):1611–1623, 2015. 32
- [88] Alexandra R Lewis, et al. Pancreatic cancer: Are "liquid biopsies" ready for prime-time? *World Journal of Gastroenterology*, 22(32):7175–7185, August 2016. 32
- [89] Marco Gerlinger, et al. Intratumor heterogeneity and branched evolution revealed by multiregion sequencing. *The New England Journal of Medicine*, 366(10):883–892, March 2012. 32
- [90] Angeliki Panagiotara, et al. Exosomes: A Cancer Theranostics Road Map. *Public Health Genomics*, 20(2):116–125, 2017. 32
- [91] Thomas Steuber, et al. Serum markers for prostate cancer: A rational approach to the literature. *European Urology*, 54(1):31–40, July 2008. 32
- [92] M. Rohan Fernando, et al. New evidence that a large proportion of human blood plasma cell-free DNA is localized in exosomes. *PLoS ONE*, 12(8), August 2017. 32
- [93] Han Wei Hou, et al. Isolation and retrieval of circulating tumor cells using centrifugal forces. *Scientific Reports*, 3:1259, February 2013. 32
- [94] L. Guo et al. Extracellular vesicles and their diagnostic and prognostic potential in cancer. *Translational Cancer Research*, 6(3):599–612, 2017. 32
- [95] Mercedes Tkach et al. Communication by Extracellular Vesicles: Where We Are and Where We Need to Go. *Cell*, 164(6):1226–1232, March 2016. 32
- [96] Masamitsu Kanada, et al. Signaling by Extracellular Vesicles Advances Cancer Hallmarks. *Trends in Cancer*, 2(2):84–94, February 2016. 32
- [97] Lorraine O’Driscoll. Expanding on Exosomes and Ectosomes in Cancer. *New England Journal of Medicine*, 372(24):2359–2362, June 2015. 32
- [98] Wiktoria M. Suchorska et al. The role of exosomes in tumor progression and metastasis (Review). *Oncology Reports*, 35(3):1237–1244, March 2016. 32
- [99] Honorary CNRS (Centre National de la Recherche Scientifique, Paris, France) and UPMC (Université Pierre et Marie Curie, Paris, France) Research Director, Founder of RevInterCell, a et al. Cell-derived Extracellular Vesicles Open New Perspectives for Cancer Research. *Cancer Research Frontiers*, 1(2): 208–224, April 2015. 32
- [100] Khalid Al-Nedawi, et al. Intercellular transfer of the oncogenic receptor EGFRvIII by microvesicles derived from tumour cells. *Nature Cell Biology*, 10(5):619–624, May 2008. 32
- [101] Héctor Peinado, et al. Melanoma exosomes educate bone marrow progenitor cells toward a pro-metastatic phenotype through MET. *Nature Medicine*, 18(6):883–891, June 2012. 32

-
- [102] Bok S. Hong, et al. Colorectal cancer cell-derived microvesicles are enriched in cell cycle-related mRNAs that promote proliferation of endothelial cells. *BMC Genomics*, 10(1):556, November 2009. 32
- [103] Takayuki Kogure, et al. Intercellular nanovesicle-mediated microRNA transfer: A mechanism of environmental modulation of hepatocellular cancer cell growth. *Hepatology (Baltimore, Md.)*, 54(4): 1237–1248, October 2011. 32
- [104] Wei Zhu, et al. Exosomes derived from human bone marrow mesenchymal stem cells promote tumor growth in vivo. *Cancer Letters*, 315(1):28–37, February 2012. 32
- [105] Hui Xiao, et al. Mast cell exosomes promote lung adenocarcinoma cell proliferation - role of KIT-stem cell factor signaling. *Cell communication and signaling: CCS*, 12:64, October 2014. 32
- [106] Chi Lam Au Yeung, et al. Exosomal transfer of stroma-derived miR21 confers paclitaxel resistance in ovarian cancer cells through targeting APAF1. *Nature Communications*, 7:11150, March 2016. 32
- [107] Zhuochao Zhang, et al. Loss of exosomal miR-320a from cancer-associated fibroblasts contributes to HCC proliferation and metastasis. *Cancer Letters*, 397:33–42, July 2017. 32
- [108] S. Jossen, et al. Stromal fibroblast-derived miR-409 promotes epithelial-to-mesenchymal transition and prostate tumorigenesis. *Oncogene*, 34(21):2690, May 2015. 32
- [109] Luana Lugini, et al. Exosomes from human colorectal cancer induce a tumor-like behavior in colonic mesenchymal stromal cells. *Oncotarget*, 7(31):50086–50098, July 2016. 32
- [110] Dhruv Kumar, et al. Biomolecular characterization of exosomes released from cancer stem cells: Possible implications for biomarker and treatment of cancer. *Oncotarget*, 6(5):3280–3291, February 2015. 32
- [111] Junyi Wu, et al. Role of stem cell-derived exosomes in cancer. *Oncology Letters*, 13(5):2855–2866, May 2017. 32
- [112] A. Sharma. Role of stem cell derived exosomes in tumor biology. *International Journal of Cancer*, 142(6):1086–1092, 2018. 32
- [113] Minh T. N. Le, et al. miR-200-containing extracellular vesicles promote breast cancer cell metastasis. *The Journal of Clinical Investigation*, 124(12):5109–5128, December 2014. 32, 33
- [114] Anoek Zomer, et al. In Vivo Imaging Reveals Extracellular Vesicle-Mediated Phenocopying of Metastatic Behavior. *Cell*, 161(5):1046–1057, May 2015. 32
- [115] J. P. Webber, et al. Differentiation of tumour-promoting stromal myofibroblasts by cancer exosomes. *Oncogene*, 34(3):290–302, January 2015. 32
- [116] Daisuke Hoshino, et al. Exosome secretion is enhanced by invadopodia and drives invasive behavior. *Cell Reports*, 5(5):1159–1168, December 2013. 32

-
- [117] Ikrame Lazar, et al. Adipocyte Exosomes Promote Melanoma Aggressiveness through Fatty Acid Oxidation: A Novel Mechanism Linking Obesity and Cancer. *Cancer Research*, 76(14):4051–4057, 07 15, 2016. 32
- [118] Simona Taverna, et al. Role of exosomes released by chronic myelogenous leukemia cells in angiogenesis. *International Journal of Cancer*, 130(9):2033–2043, May 2012. 32
- [119] Katrin J. Svensson, et al. Hypoxia triggers a proangiogenic pathway involving cancer cell microvesicles and PAR-2-mediated heparin-binding EGF signaling in endothelial cells. *Proceedings of the National Academy of Sciences*, 108(32):13147–13152, August 2011. 32
- [120] Joshua L. Hood, et al. Paracrine induction of endothelium by tumor exosomes. *Laboratory Investigation; a Journal of Technical Methods and Pathology*, 89(11):1317–1328, November 2009. 32
- [121] Danilo Millimaggi, et al. Tumor vesicle-associated CD147 modulates the angiogenic capability of endothelial cells. *Neoplasia (New York, N.Y.)*, 9(4):349–357, April 2007. 32
- [122] Jinheng Wang, et al. Multiple myeloma exosomes establish a favourable bone marrow microenvironment with enhanced angiogenesis and immunosuppression. *The Journal of Pathology*, 239(2):162–173, June 2016. 32
- [123] Nobuyoshi Kosaka, et al. Neutral sphingomyelinase 2 (nSMase2)-dependent exosomal transfer of angiogenic microRNAs regulate cancer cell metastasis. *The Journal of Biological Chemistry*, 288(15):10849–10859, April 2013. 32
- [124] Guo-Chang Fan. Hypoxic exosomes promote angiogenesis. *Blood*, 124(25):3669–3670, December 2014. 32
- [125] Hiroko Tadokoro, et al. Exosomes derived from hypoxic leukemia cells enhance tube formation in endothelial cells. *The Journal of Biological Chemistry*, 288(48):34343–34351, November 2013. 32
- [126] Xiaolei Liang, et al. Exosomes secreted by mesenchymal stem cells promote endothelial cell angiogenesis by transferring miR-125a. *Journal of Cell Science*, 129(11):2182–2189, 06 01, 2016. 32
- [127] Nobuyoshi Kosaka. Decoding the Secret of Cancer by Means of Extracellular Vesicles. *Journal of Clinical Medicine*, 5(2), February 2016. 32
- [128] Wei-xian Chen, et al. Exosomes from Drug-Resistant Breast Cancer Cells Transmit Chemoresistance by a Horizontal Transfer of MicroRNAs. *PLOS ONE*, 9(4):e95240, April 2014. 32
- [129] Yifang Wei, et al. Exosomal miR-221/222 enhances tamoxifen resistance in recipient ER-positive breast cancer cells. *Breast Cancer Research and Treatment*, 147(2):423–431, September 2014. 32
- [130] Le Qu, et al. Exosome-Transmitted lncARSR Promotes Sunitinib Resistance in Renal Cancer by Acting as a Competing Endogenous RNA. *Cancer Cell*, 29(5):653–668, 05 09, 2016. 32

-
- [131] Yun Chen, et al. Breast cancer resistance protein (BCRP)-containing circulating microvesicles contribute to chemoresistance in breast cancer. *Oncology Letters*, 10(6):3742–3748, December 2015. 32
- [132] Thiha Aung, et al. Exosomal evasion of humoral immunotherapy in aggressive B-cell lymphoma modulated by ATP-binding cassette transporter A3. *Proceedings of the National Academy of Sciences of the United States of America*, 108(37):15336–15341, September 2011. 32
- [133] K. E. Richards, et al. Cancer-associated fibroblast exosomes regulate survival and proliferation of pancreatic cancer cells. *Oncogene*, 36(13):1770–1778, March 2017. 32
- [134] Mirjam C. Boelens, et al. Exosome transfer from stromal to breast cancer cells regulates therapy resistance pathways. *Cell*, 159(3):499–513, October 2014. 32
- [135] Kerby Shedden, et al. Expulsion of small molecules in vesicles shed by cancer cells: Association with gene expression and chemosensitivity profiles. *Cancer Research*, 63(15):4331–4337, August 2003. 32
- [136] Valentina Ciravolo, et al. Potential role of HER2-overexpressing exosomes in countering trastuzumab-based therapy. *Journal of Cellular Physiology*, 227(2):658–667, February 2012. 32
- [137] Theresa L. Whiteside. Tumor-Derived Exosomes and Their Role in Cancer Progression. *Advances in Clinical Chemistry*, 74:103–141, 2016. 32
- [138] Morad-Rémy Muhsin-Sharafaldine, et al. Procoagulant and immunogenic properties of melanoma exosomes, microvesicles and apoptotic vesicles. *Oncotarget*, 7(35):56279–56294, August 2016. 32
- [139] M. Iero, et al. Tumour-released exosomes and their implications in cancer immunity. *Cell Death and Differentiation*, 15(1):80–88, January 2008. 32
- [140] Marta Szajnik, et al. Tumor-Derived Microvesicles Induce, Expand and Up-Regulate Biological Activities of Human Regulatory T Cells (Treg). *PLOS ONE*, 5(7):e11469, 22 juil. 2010. 32
- [141] Eva U. Wieckowski, et al. Tumor-derived microvesicles promote regulatory T cell expansion and induce apoptosis in tumor-reactive activated CD8+ T lymphocytes. *Journal of Immunology (Baltimore, Md.: 1950)*, 183(6):3720–3730, September 2009. 32
- [142] Gang Cai, et al. A Regulatory Role for IL-10 Receptor Signaling in Development and B Cell Help of T Follicular Helper Cells in Mice. *The Journal of Immunology*, 189(3):1294–1302, August 2012. 32
- [143] Thomas Condamine et al. Molecular mechanisms regulating myeloid-derived suppressor cell differentiation and function. *Trends in Immunology*, 32(1):19–25, January 2011. 32
- [144] Roberta Valenti, et al. Human tumor-released microvesicles promote the differentiation of myeloid cells with transforming growth factor-beta-mediated suppressive activity on T lymphocytes. *Cancer Research*, 66(18):9290–9298, September 2006. 32
- [145] Muller Fabbri, et al. MicroRNAs bind to Toll-like receptors to induce prometastatic inflammatory response. *Proceedings of the National Academy of Sciences of the United States of America*, 109(31):E2110–2116, July 2012. 32

-
- [146] Xiang Ying, et al. Epithelial ovarian cancer-secreted exosomal miR-222-3p induces polarization of tumor-associated macrophages. *Oncotarget*, 7(28):43076–43087, July 2016. 32
- [147] Sukhvinder S. Sidhu, et al. The microvesicle as a vehicle for EMMPRIN in tumor-stromal interactions. *Oncogene*, 23(4):956–963, January 2004. 32
- [148] M. Aga, et al. Exosomal HIF1 α supports invasive potential of nasopharyngeal carcinoma-associated LMP1-positive exosomes. *Oncogene*, 33(37):4613–4622, September 2014. 32
- [149] Anoeck Zomer, et al. In Vivo Imaging Reveals Extracellular Vesicle-Mediated Phenocopying of Metastatic Behavior. *Cell*, 161(5):1046–1057, May 2015. 32
- [150] Bruno Costa-Silva, et al. Pancreatic cancer exosomes initiate pre-metastatic niche formation in the liver. *Nature Cell Biology*, 17(6):816–826, June 2015. 32
- [151] Miranda Y. Fong, et al. Breast-cancer-secreted miR-122 reprograms glucose metabolism in premetastatic niche to promote metastasis. *Nature Cell Biology*, 17(2):183–194, February 2015. 32
- [152] Yanfang Liu, et al. Tumor Exosomal RNAs Promote Lung Pre-metastatic Niche Formation by Activating Alveolar Epithelial TLR3 to Recruit Neutrophils. *Cancer Cell*, 30(2):243–256, August 2016. 32
- [153] Ayuko Hoshino, et al. Tumour exosome integrins determine organotropic metastasis. *Nature*, 527(7578):329–335, November 2015. 32
- [154] Dionysios Antonopoulos, et al. Cancer’s smart bombs: Tumor-derived exosomes target lung epithelial cells triggering pre-metastatic niche formation. *Journal of Thoracic Disease*, 9(4):969–972, April 2017. 32
- [155] Naoomi Tominaga, et al. Brain metastatic cancer cells release microRNA-181c-containing extracellular vesicles capable of destructing blood-brain barrier. *Nature Communications*, 6:6716, April 2015. 32
- [156] Lin Zhang, et al. Microenvironment-induced PTEN loss by exosomal microRNA primes brain metastasis outgrowth. *Nature*, 527(7576):100–104, November 2015. 32
- [157] Sarah A. Bliss, et al. Mesenchymal Stem Cell-Derived Exosomes Stimulate Cycling Quiescence and Early Breast Cancer Dormancy in Bone Marrow. *Cancer Research*, 76(19):5832–5844, 10 01, 2016. 32
- [158] Dolores Di Vizio, et al. Large oncosomes in human prostate cancer tissues and in the circulation of mice with metastatic disease. *The American Journal of Pathology*, 181(5):1573–1584, November 2012. 32
- [159] Ana C. Leal, et al. Tumor-Derived Exosomes Induce the Formation of Neutrophil Extracellular Traps: Implications For The Establishment of Cancer-Associated Thrombosis. *Scientific Reports*, 7(1):6438, July 2017. 32
- [160] Edit I. Buzas, et al. Emerging role of extracellular vesicles in inflammatory diseases. *Nature Reviews. Rheumatology*, 10(6):356–364, June 2014. 32

-
- [161] Héctor Peinado, et al. Melanoma exosomes educate bone marrow progenitor cells toward a pro-metastatic phenotype through MET. *Nature Medicine*, 18(6):883–891, June 2012. 33, 35
- [162] Johan Skog, et al. Glioblastoma microvesicles transport RNA and proteins that promote tumour growth and provide diagnostic biomarkers. *Nature Cell Biology*, 10(12):1470–1476, December 2008. 33, 35
- [163] R. Bhome, et al. Exosomal microRNAs (exomiRs): Small molecules with a big role in cancer. *Cancer Letters*, 420:228–235, 2018. 33
- [164] Francesco Cappello, et al. Exosome levels in human body fluids: A tumor marker by themselves? *European Journal of Pharmaceutical Sciences*, 96:93–98, January 2017. 33
- [165] Mariantonia Logozzi, et al. High Levels of Exosomes Expressing CD63 and Caveolin-1 in Plasma of Melanoma Patients. *PLOS ONE*, 4(4):e5219, April 2009. 33, 44, 45
- [166] Cristina Federici, et al. Exosome release and low pH belong to a framework of resistance of human melanoma cells to cisplatin. *PloS One*, 9(2):e88193, 2014. 33
- [167] Antonella Caivano, et al. High serum levels of extracellular vesicles expressing malignancy-related markers are released in patients with various types of hematological neoplastic disorders. *Tumour Biology: The Journal of the International Society for Oncodevelopmental Biology and Medicine*, 36(12): 9739–9752, December 2015. 33
- [168] Diederick Duijvesz, et al. Immuno-based detection of extracellular vesicles in urine as diagnostic marker for prostate cancer. *International Journal of Cancer*, 137(12):2869–2878, December 2015. 33
- [169] J. Silva, et al. Analysis of exosome release and its prognostic value in human colorectal cancer. *Genes, Chromosomes & Cancer*, 51(4):409–418, April 2012. 33
- [170] Estibaliz Alegre, et al. Circulating melanoma exosomes as diagnostic and prognosis biomarkers. *Clinica Chimica Acta; International Journal of Clinical Chemistry*, 454:28–32, February 2016. 33
- [171] Yasunori Matsumoto, et al. Quantification of plasma exosome is a potential prognostic marker for esophageal squamous cell carcinoma. *Oncology Reports*, 36(5):2535–2543, November 2016. 33
- [172] Huilin Shao, et al. Chip-based analysis of exosomal mRNA mediating drug resistance in glioblastoma. *Nature Communications*, 6:6999, May 2015. 34
- [173] Davide Zocco, et al. Extracellular Vesicles as Shuttles of Tumor Biomarkers and Anti-Tumor Drugs. *Frontiers in Oncology*, 4, October 2014. 34
- [174] Angela Schwab, et al. Extracellular vesicles from infected cells: Potential for direct pathogenesis. *Frontiers in Microbiology*, 6:1132, 2015. 34
- [175] Antonio Marcilla, et al. Extracellular vesicles in parasitic diseases. *Journal of Extracellular Vesicles*, 3: 25040, 2014. 34

-
- [176] X. Delabranche, et al. Microparticles and infectious diseases. *Medecine Et Maladies Infectieuses*, 42(8): 335–343, August 2012. 34
- [177] Joel Henrique Ellwanger, et al. Exosomes in HIV infection: A review and critical look. *Infection, Genetics and Evolution*, 53:146–154, September 2017. 34
- [178] Marisa N. Madison et al. Exosomes: Implications in HIV-1 Pathogenesis. *Viruses*, 7(7):4093–4118, July 2015. 34
- [179] Sukrutha Chettimada, et al. Exosome markers associated with immune activation and oxidative stress in HIV patients on antiretroviral therapy. *Scientific Reports*, 8(1):7227, May 2018. 34
- [180] Catherine DeMarino, et al. Antiretroviral Drugs Alter the Content of Extracellular Vesicles from HIV-1-Infected Cells. *Scientific Reports*, 8(1):7653, May 2018. 34
- [181] Hetian Lei, et al. Protein kinase A-dependent translocation of Hsp90 alpha impairs endothelial nitric-oxide synthase activity in high glucose and diabetes. *The Journal of Biological Chemistry*, 282(13): 9364–9371, March 2007. 34
- [182] Huiming Sheng, et al. Insulinoma-released exosomes or microparticles are immunostimulatory and can activate autoreactive T cells spontaneously developed in nonobese diabetic mice. *Journal of Immunology (Baltimore, Md.: 1950)*, 187(4):1591–1600, August 2011. 34
- [183] Roman Bashratyan, et al. Insulinoma-released exosomes activate autoreactive marginal zone-like B cells that expand endogenously in prediabetic NOD mice. *European Journal of Immunology*, 43(10): 2588–2597, October 2013. 34
- [184] C.P. Hasilo, et al. Presence of diabetes autoantigens in extracellular vesicles derived from human islets. *Scientific Reports*, 7(1), 2017. 34
- [185] M. Garcia-Contreras, et al. Exosomes as biomarkers and therapeutic tools for type 1 diabetes mellitus. *European Review for Medical and Pharmacological Sciences*, 21(12):2940–2956, June 2017. 34
- [186] Zhong-bin Deng, et al. Adipose tissue exosome-like vesicles mediate activation of macrophage-induced insulin resistance. *Diabetes*, 58(11):2498–2505, November 2009. 34
- [187] Min-Jae Lee, et al. Exosomes as the source of biomarkers of metabolic diseases. *Annals of Pediatric Endocrinology & Metabolism*, 21(3):119–125, September 2016. 34
- [188] Joseph Withrow, et al. Extracellular vesicles in the pathogenesis of rheumatoid arthritis and osteoarthritis. *Arthritis Research & Therapy*, 18, 2016. 35
- [189] Stella Cosenza, et al. Pathogenic or Therapeutic Extracellular Vesicles in Rheumatic Diseases: Role of Mesenchymal Stem Cell-Derived Vesicles. *International Journal of Molecular Sciences*, 18(4), April 2017. 35

-
- [190] K. Skriner, et al. Association of citrullinated proteins with synovial exosomes. *Arthritis and Rheumatism*, 54(12):3809–3814, December 2006. 35
- [191] Eric Boilard, et al. Platelets amplify inflammation in arthritis via collagen-dependent microparticle production. *Science (New York, N.Y.)*, 327(5965):580–583, January 2010. 35
- [192] Mariola Kurowska-Stolarska, et al. MicroRNA-155 as a proinflammatory regulator in clinical and experimental arthritis. *Proceedings of the National Academy of Sciences of the United States of America*, 108(27):11193–11198, July 2011. 35
- [193] Maria Chiara Deregibus, et al. Endothelial progenitor cell derived microvesicles activate an angiogenic program in endothelial cells by a horizontal transfer of mRNA. *Blood*, 110(7):2440–2448, October 2007. 35
- [194] M B Herrera, et al. Human liver stem cell-derived microvesicles accelerate hepatic regeneration in hepatectomized rats. *Journal of Cellular and Molecular Medicine*, 14(6b):1605–1618, June 2010. 35
- [195] G. Raposo, et al. B lymphocytes secrete antigen-presenting vesicles. *The Journal of Experimental Medicine*, 183(3):1161–1172, March 1996. 35
- [196] Ronne Wee Yeh Yeo, et al. Mesenchymal stem cell: An efficient mass producer of exosomes for drug delivery. *Advanced Drug Delivery Reviews*, 65(3):336–341, March 2013. 35
- [197] Henry G. Lamparski, et al. Production and characterization of clinical grade exosomes derived from dendritic cells. *Journal of Immunological Methods*, 270(2):211–226, December 2002. 35
- [198] Samir EL Andaloussi, et al. Extracellular vesicles: Biology and emerging therapeutic opportunities. *Nature Reviews Drug Discovery*, 12(5):347–357, May 2013. 35
- [199] Katarina Trajkovic, et al. Ceramide triggers budding of exosome vesicles into multivesicular endosomes. *Science (New York, N.Y.)*, 319(5867):1244–1247, February 2008. 35
- [200] Angélique Bobrie, et al. Exosome Secretion: Molecular Mechanisms and Roles in Immune Responses. *Traffic*, 12(12):1659–1668, December 2011. 35
- [201] Khalid Al-Nedawi, et al. Endothelial expression of autocrine VEGF upon the uptake of tumor-derived microvesicles containing oncogenic EGFR. *Proceedings of the National Academy of Sciences*, 106(10):3794–3799, March 2009. 35
- [202] Luize G. Lima, et al. Tumor-derived microvesicles modulate the establishment of metastatic melanoma in a phosphatidylserine-dependent manner. *Cancer Letters*, 283(2):168–175, October 2009. 35
- [203] Gang Cai, et al. A Regulatory Role for IL-10 Receptor Signaling in Development and B Cell Help of T Follicular Helper Cells in Mice. *The Journal of Immunology*, 189(3):1294–1302, August 2012. 35
- [204] Monika Baj-Krzyworzeka, et al. Tumour-derived microvesicles carry several surface determinants and mRNA of tumour cells and transfer some of these determinants to monocytes. *Cancer immunology, immunotherapy: CII*, 55(7):808–818, July 2006. 35

-
- [205] Yujing Zhang, et al. Secreted monocytic miR-150 enhances targeted endothelial cell migration. *Molecular Cell*, 39(1):133–144, July 2010. 35
- [206] Lydia Alvarez-Erviti, et al. Delivery of siRNA to the mouse brain by systemic injection of targeted exosomes. *Nature Biotechnology*, 29(4):341–345, April 2011. 35
- [207] Ryosuke Kojima, et al. Designer exosomes produced by implanted cells intracerebrally deliver therapeutic cargo for Parkinson’s disease treatment. *Nature Communications*, 9(1):1305, April 2018. 35
- [208] Federica Collino, et al. Microvesicles derived from adult human bone marrow and tissue specific mesenchymal stem cells shuttle selected pattern of miRNAs. *PloS One*, 5(7):e11803, July 2010. 35
- [209] Derrick J. Gibbins, et al. Multivesicular bodies associate with components of miRNA effector complexes and modulate miRNA activity. *Nature Cell Biology*, 11(9):1143–1149, September 2009. 35
- [210] J. Szebeni. Complement activation-related pseudoallergy caused by liposomes, micellar carriers of intravenous drugs, and radiocontrast agents. *Critical Reviews in Therapeutic Drug Carrier Systems*, 18(6):567–606, 2001. 35
- [211] Janos Szebeni. Complement activation-related pseudoallergy: A new class of drug-induced acute immune toxicity. *Toxicology*, 216(2-3):106–121, December 2005. 35
- [212] Ev-Track Consortium, et al. EV-TRACK: Transparent reporting and centralizing knowledge in extracellular vesicle research. *Nature Methods*, 14(3):228–232, March 2017. 36, 155
- [213] Kenneth W. Witwer, et al. Standardization of sample collection, isolation and analysis methods in extracellular vesicle research. *Journal of Extracellular Vesicles*, 2, May 2013. 36, 148, 149, 155
- [214] Jan Lötvall, et al. Minimal experimental requirements for definition of extracellular vesicles and their functions: A position statement from the International Society for Extracellular Vesicles. *Journal of Extracellular Vesicles*, 3, December 2014. 36
- [215] Kenneth W. Witwer, et al. Updating the MISEV minimal requirements for extracellular vesicle studies: Building bridges to reproducibility. *Journal of Extracellular Vesicles*, 6(1), November 2017. 36
- [216] Shima Gholizadeh, et al. Microfluidic approaches for isolation, detection, and characterization of extracellular vesicles: Current status and future directions. *Biosensors and Bioelectronics*, 91:588–605, May 2017. 37
- [217] Richard J. Lobb, et al. Optimized exosome isolation protocol for cell culture supernatant and human plasma. *Journal of Extracellular Vesicles*, 4, July 2015. 37, 52
- [218] Bence György, et al. Detection and isolation of cell-derived microparticles are compromised by protein complexes resulting from shared biophysical parameters. *Blood*, 117(4):e39–e48, January 2011. 37, 52

-
- [219] Liron Issman, et al. Cryogenic Transmission Electron Microscopy Nanostructural Study of Shed Microparticles. *PLOS ONE*, 8(12):e83680, December 2013. 37, 149
- [220] Sonia A. Melo, et al. Cancer Exosomes Perform Cell-Independent MicroRNA Biogenesis and Promote Tumorigenesis. *Cancer cell*, 26(5):707–721, November 2014. 37
- [221] Y. Yuana, et al. Atomic force microscopy: A novel approach to the detection of nanosized blood microparticles. *Journal of Thrombosis and Haemostasis*, 8(2):315–323, February 2010. 38
- [222] Julie Hardij, et al. Characterisation of tissue factor-bearing extracellular vesicles with AFM: Comparison of air-tapping-mode AFM and liquid Peak Force AFM. *Journal of Extracellular Vesicles*, 2, August 2013. 38
- [223] Bradley Whitehead, et al. Tumour exosomes display differential mechanical and complement activation properties dependent on malignant state: Implications in endothelial leakiness. *Journal of Extracellular Vesicles*, 4(0), December 2015. 38
- [224] Christopher M. Hoo, et al. A comparison of atomic force microscopy (AFM) and dynamic light scattering (DLS) methods to characterize nanoparticle size distributions. *Journal of Nanoparticle Research*, 10(1):89–96, June 2008. 39
- [225] E. Van Der Pol, et al. Optical and non-optical methods for detection and characterization of microparticles and exosomes. *Journal of Thrombosis and Haemostasis*, 8(12):2596–2607, December 2010. 39
- [226] Sybren L.N. Maas, et al. Possibilities and limitations of current technologies for quantification of biological extracellular vesicles and synthetic mimics. *Journal of Controlled Release*, 200:87–96, February 2015. 39, 40
- [227] Takashi Ito, et al. A Carbon Nanotube-Based Coulter Nanoparticle Counter. *Accounts of Chemical Research*, 37(12):937–945, December 2004. 40
- [228] Robert Vogel, et al. Quantitative Sizing of Nano/Microparticles with a Tunable Elastomeric Pore Sensor. *Analytical Chemistry*, 83(9):3499–3506, May 2011. 40
- [229] Will Anderson, et al. Observations of Tunable Resistive Pulse Sensing for Exosome Analysis: Improving System Sensitivity and Stability. *Langmuir*, 31(23):6577–6587, June 2015. 40
- [230] Darby Kozak, et al. Simultaneous Size and ζ -Potential Measurements of Individual Nanoparticles in Dispersion Using Size-Tunable Pore Sensors. *ACS Nano*, 6(8):6990–6997, August 2012. 40
- [231] Johnny C. Akers, et al. Comparative Analysis of Technologies for Quantifying Extracellular Vesicles (EVs) in Clinical Cerebrospinal Fluids (CSF). *PLOS ONE*, 11(2):e0149866, February 2016. 40, 43
- [232] T.P. Burg, et al. Vacuum-Packaged Suspended Microchannel Resonant Mass Sensor for Biomolecular Detection. *Journal of Microelectromechanical Systems*, 15(6):1466–1476, December 2006. 40

-
- [233] Arif E. Cetin, et al. Determining therapeutic susceptibility in multiple myeloma by single-cell mass accumulation. *Nature Communications*, 8(1):1613, November 2017. 40
- [234] Mark M. Stevens, et al. Drug sensitivity of single cancer cells is predicted by changes in mass accumulation rate. *Nature Biotechnology*, advance online publication, October 2016. 40
- [235] Nathan Cermak, et al. High-throughput measurement of single-cell growth rates using serial microfluidic mass sensor arrays. *Nature Biotechnology*, advance online publication, September 2016. 40
- [236] Robert J. Kimmerling, et al. A microfluidic platform enabling single-cell RNA-seq of multigenerational lineages. *Nature Communications*, 7:10220, January 2016. 40
- [237] Josephine Shaw Bagnall, et al. Deformability-based cell selection with downstream immunofluorescence analysis. *Integrative Biology*, March 2016. 41
- [238] Andrea K. Bryan, et al. Measurement of mass, density, and volume during the cell cycle of yeast. *Proceedings of the National Academy of Sciences*, 107(3):999–1004, January 2010. 41
- [239] Selim Olcum, et al. Weighing nanoparticles in solution at the attogram scale. *Proceedings of the National Academy of Sciences*, 111(4):1310–1315, January 2014. 41, 45, 174
- [240] V. Agache, et al. An embedded microchannel in a MEMS plate resonator for ultrasensitive mass sensing in liquid. *Lab on a Chip*, 11(15):2598–2603, July 2011. 41
- [241] C. Hadji, et al. Hollow MEMS mass sensors for real-time particles weighing and sizing from a few 10 nm to the μm scale. In *2015 28th IEEE International Conference on Micro Electro Mechanical Systems (MEMS)*, pages 180–183, January 2015. 41
- [242] Thomas P. Burg, et al. Weighing of biomolecules, single cells and single nanoparticles in fluid. *Nature*, 446(7139):1066–1069, April 2007. 41
- [243] Irène Tatischeff, et al. Fast characterisation of cell-derived extracellular vesicles by nanoparticles tracking analysis, cryo-electron microscopy, and Raman tweezers microspectroscopy. *Journal of Extracellular Vesicles*, 1, 2012. 41
- [244] Alice Gualerzi, et al. Raman spectroscopy uncovers biochemical tissue-related features of extracellular vesicles from mesenchymal stromal cells. *Scientific Reports*, 7(1):9820, August 2017. 41, 45
- [245] Stephan Stremersch, et al. Identification of Individual Exosome-Like Vesicles by Surface Enhanced Raman Spectroscopy. *Small*, 12(24):3292–3301. 41
- [246] Jaena Park, et al. Exosome Classification by Pattern Analysis of Surface-Enhanced Raman Spectroscopy Data for Lung Cancer Diagnosis. *Analytical Chemistry*, 89(12):6695–6701, June 2017. 41
- [247] Christoph Krafft, et al. A specific spectral signature of serum and plasma-derived extracellular vesicles for cancer screening. *Nanomedicine: Nanotechnology, Biology and Medicine*, 13(3):835–841, April 2017. 41

-
- [248] Luigino Grasso, et al. Molecular screening of cancer-derived exosomes by surface plasmon resonance spectroscopy. *Analytical and Bioanalytical Chemistry*, 407(18):5425–5432, April 2015. 41
- [249] Hyungsoon Im, et al. Label-free detection and molecular profiling of exosomes with a nano-plasmonic sensor. *Nature Biotechnology*, 32(5):490–495, May 2014. 41, 45
- [250] Déborah L. M. Rupert, et al. Determination of exosome concentration in solution using surface plasmon resonance spectroscopy. *Analytical Chemistry*, 86(12):5929–5936, June 2014. 41
- [251] Simon Castorph, et al. Structure Parameters of Synaptic Vesicles Quantified by Small-Angle X-Ray Scattering. *Biophysical Journal*, 98(7):1200–1208, April 2010. 42, 45
- [252] Hans Christian D. Aass, et al. Fluorescent particles in the antibody solution result in false TF- and CD14-positive microparticles in flow cytometric analysis. *Cytometry. Part A: The Journal of the International Society for Analytical Cytology*, 79(12):990–999, December 2011. 43
- [253] Samuel A. Stoner, et al. High sensitivity flow cytometry of membrane vesicles. *Cytometry Part A*, 89(2):196–206, February 2016. 43
- [254] E. van der Pol, et al. Particle size distribution of exosomes and microvesicles determined by transmission electron microscopy, flow cytometry, nanoparticle tracking analysis, and resistive pulse sensing. *Journal of Thrombosis and Haemostasis*, 12(7):1182–1192, July 2014. 43
- [255] Els J. van der Vlist, et al. Fluorescent labeling of nano-sized vesicles released by cells and subsequent quantitative and qualitative analysis by high-resolution flow cytometry. *Nature Protocols*, 7(7):1311–1326, July 2012. 43
- [256] E. Van Der POL, et al. Single vs. swarm detection of microparticles and exosomes by flow cytometry. *Journal of Thrombosis and Haemostasis*, 10(5):919–930, May 2012. 43
- [257] Atsushi Suetsugu, et al. Imaging exosome transfer from breast cancer cells to stroma at metastatic sites in orthotopic nude-mouse models. *Advanced Drug Delivery Reviews*, 65(3):383–390, March 2013. 43
- [258] Anoenk Zomer, et al. In Vivo Imaging Reveals Extracellular Vesicle-Mediated Phenocopying of Metastatic Behavior. *Cell*, 161(5):1046–1057, May 2015. 43, 45
- [259] Yusuke Yoshioka, et al. Ultra-sensitive liquid biopsy of circulating extracellular vesicles using ExoScreen. *Nature Communications*, 5:3591, April 2014. 44, 45
- [260] Mei He, et al. Integrated immunoisolation and protein analysis of circulating exosomes using microfluidic technology. *Lab on a Chip*, 14(19):3773–3780, August 2014. 44, 45, 54
- [261] Yuichi Kitai, et al. DNA-Containing Exosomes Derived from Cancer Cells Treated with Topotecan Activate a STING-Dependent Pathway and Reinforce Antitumor Immunity. *The Journal of Immunology*, 198(4):1649–1659, February 2017. 44

-
- [262] Koji Ueda, et al. Antibody-coupled monolithic silica microtips for highthroughput molecular profiling of circulating exosomes. *Scientific Reports*, 4, August 2014. 44
- [263] Emily Zeringer. Methods for the extraction and RNA profiling of exosomes. *World Journal of Methodology*, 3(1):11, 2013. 44
- [264] Kadri Rekker, et al. Comparison of serum exosome isolation methods for microRNA profiling. *Clinical Biochemistry*, 47(1–2):135–138, January 2014. 44
- [265] Walter W Chen, et al. BEAMing and Droplet Digital PCR Analysis of Mutant IDH1 mRNA in Glioma Patient Serum and Cerebrospinal Fluid Extracellular Vesicles. *Molecular Therapy. Nucleic Acids*, 2(7):e109, July 2013. 45
- [266] Shivani Sharma, et al. Structural- mechanical characterization of nanoparticles- Exosomes in human saliva, using correlative AFM, FESEM and force spectroscopy. *ACS nano*, 4(4):1921–1926, April 2010. 45
- [267] Viktoriya Sokolova, et al. Characterisation of exosomes derived from human cells by nanoparticle tracking analysis and scanning electron microscopy. *Colloids and Surfaces B: Biointerfaces*, 87(1):146–150, October 2011. 45
- [268] Rebecca A. Dragovic, et al. Sizing and phenotyping of cellular vesicles using Nanoparticle Tracking Analysis. *Nanomedicine*, 7(6):780–788, December 2011. 45
- [269] Sybren L. N. Maas, et al. Quantification and Size-profiling of Extracellular Vesicles Using Tunable Resistive Pulse Sensing. *Journal of Visualized Experiments : JoVE*, (92), October 2014. 45
- [270] S. Robert, et al. Standardization of platelet-derived microparticle counting using calibrated beads and a Cytomics FC500 routine flow cytometer: A first step towards multicenter studies? *Journal of Thrombosis and Haemostasis*, 7(1):190–197, January 2009. 45
- [271] Mengdi Zhang, et al. Methods and Technologies for Exosome Isolation and Characterization. *Small Methods*, 0(0):1800021. 46
- [272] Fang Yang, et al. Exosome separation using microfluidic systems: Size-based, immunoaffinity-based and dynamic methodologies. *Biotechnology Journal*, pages n/a–n/a, February 2017. 46, 53
- [273] Déborah L. M. Rupert, et al. Methods for the physical characterization and quantification of extracellular vesicles in biological samples. *Biochimica et Biophysica Acta (BBA) - General Subjects*, 1861(1, Part A):3164–3179, January 2017. 46
- [274] Shima Gholizadeh, et al. Microfluidic Approaches for Isolation, Detection, and Characterization of Extracellular Vesicles: Current Status and Future Directions. *Biosensors and Bioelectronics*, January 2017. 46
- [275] Zamila Khatun, et al. Elucidating diversity of exosomes: Biophysical and molecular characterization methods. *Nanomedicine (London, England)*, 11(17):2359–2377, September 2016. 46

-
- [276] Jina Ko, et al. Detection and isolation of circulating exosomes and microvesicles for cancer monitoring and diagnostics using micro-/nano-based devices. *The Analyst*, 141(2):450–460, January 2016. 46
- [277] Vijaya Sunkara, et al. Emerging techniques in the isolation and characterization of extracellular vesicles and their roles in cancer diagnostics and prognostics. *The Analyst*, 141(2):371–381, 2016. 46
- [278] RAFAL SZATANEK, et al. Isolation of extracellular vesicles: Determining the correct approach (Review). *International Journal of Molecular Medicine*, 36(1):11–17, July 2015. 46
- [279] Mikołaj P. Zaborowski, et al. Extracellular Vesicles: Composition, Biological Relevance, and Methods of Study. *BioScience*, 65(8):783–797, August 2015. 46, 48
- [280] Fatemeh Momen-Heravi, et al. Current methods for the isolation of extracellular vesicles. *Biological Chemistry*, 394(10):1253–1262, 2013. 46
- [281] Masatoshi Maeki, et al. Advances in microfluidics for lipid nanoparticles and extracellular vesicles and applications in drug delivery systems. *Advanced Drug Delivery Reviews*, March 2018. 46
- [282] Eloise Pariset, et al. Extracellular Vesicles: Isolation Methods. *Advanced Biosystems*, 1(5):1700040, May 2017. 46, 47
- [283] Fatemeh Momen-Heravi, et al. Impact of Biofluid Viscosity on Size and Sedimentation Efficiency of the Isolated Microvesicles. *Frontiers in Physiology*, 3, May 2012. 48
- [284] Mikhail A. Livshits, et al. Isolation of exosomes by differential centrifugation: Theoretical analysis of a commonly used protocol. *Scientific Reports*, 5:17319, November 2015. 48
- [285] Josselin Caradec, et al. Reproducibility and efficiency of serum-derived exosome extraction methods. *Clinical Biochemistry*, 47(13-14):1286–1292, September 2014. 49
- [286] Réjean Cantin, et al. Discrimination between exosomes and HIV-1: Purification of both vesicles from cell-free supernatants. *Journal of Immunological Methods*, 338(1–2):21–30, September 2008. 49
- [287] Yuana Yuana, et al. Co-isolation of extracellular vesicles and high-density lipoproteins using density gradient ultracentrifugation. *Journal of Extracellular Vesicles*, 3(0), July 2014. 49
- [288] Irene Vanni, et al. Exosomes: A new horizon in lung cancer. *Drug Discovery Today*, 22(6):927–936, June 2017. 49
- [289] Douglas D. Taylor, et al. Exosome Isolation for Proteomic Analyses and RNA Profiling. In Richard J. Simpson et al., editors, *Serum/Plasma Proteomics*, pages 235–246. Humana Press, January 2011. 50
- [290] Jan Van Deun, et al. The impact of disparate isolation methods for extracellular vesicles on downstream RNA profiling. *Journal of Extracellular Vesicles*, 3(0), September 2014. 50
- [291] Tetsuya Yamada, et al. Comparison of Methods for Isolating Exosomes from Bovine Milk. *Journal of Veterinary Medical Science*, 74(11):1523–1525, 2012. 50

-
- [292] Inas Helwa, et al. A Comparative Study of Serum Exosome Isolation Using Differential Ultracentrifugation and Three Commercial Reagents. *PLOS ONE*, 12(1):e0170628, January 2017. 50
- [293] Xavier Gallart-Palau, et al. Extracellular vesicles are rapidly purified from human plasma by Protein Organic Solvent Precipitation (PROSPR). *Scientific Reports*, 5:14664, September 2015. 50
- [294] Bow J. Tauro, et al. Comparison of ultracentrifugation, density gradient separation, and immunoaffinity capture methods for isolating human colon cancer cell line LIM1863-derived exosomes. *Methods*, 56(2):293–304, February 2012. 50
- [295] Stephen J. Gould et al. As we wait: Coping with an imperfect nomenclature for extracellular vesicles. *Journal of Extracellular Vesicles*, 2(0), February 2013. 50
- [296] Chihchen Chen, et al. Microfluidic isolation and transcriptome analysis of serum microvesicles. *Lab on a chip*, 10(4):505–511, February 2010. 51, 53
- [297] Chihchen Chen, et al. Paper-based immunoaffinity devices for accessible isolation and characterization of extracellular vesicles. *Microfluidics and Nanofluidics*, 16(5):849–856, February 2014. 51
- [298] Leonora Balaj, et al. Heparin affinity purification of extracellular vesicles. *Scientific Reports*, 5:10266, May 2015. 51
- [299] Anirban Ghosh, et al. Rapid Isolation of Extracellular Vesicles from Cell Culture and Biological Fluids Using a Synthetic Peptide with Specific Affinity for Heat Shock Proteins. *PLOS ONE*, 9(10): e110443, October 2014. 51
- [300] Jaco C. Knol, et al. Peptide-mediated ‘miniprep’ isolation of extracellular vesicles is suitable for high-throughput proteomics. *EuPA Open Proteomics*, 11:11–15, June 2016. 51
- [301] S. Cho, et al. Isolation of extracellular vesicle from blood plasma using electrophoretic migration through porous membrane. *Sensors and Actuators, B: Chemical*, 233:289–297, 2016. 51, 52
- [302] Ryan T. Davies, et al. Microfluidic filtration system to isolate extracellular vesicles from blood. *Lab on a Chip*, 12(24):5202–5210, November 2012. 51
- [303] Nikki Heath, et al. Rapid isolation and enrichment of extracellular vesicle preparations using anion exchange chromatography. *Scientific Reports*, 8(1):5730, April 2018. 52
- [304] Laurent Muller, et al. Isolation of Biologically-Active Exosomes from Human Plasma. *Journal of immunological methods*, 411:55–65, September 2014. 52
- [305] M. Lucrecia Alvarez, et al. Comparison of protein, microRNA, and mRNA yields using different methods of urinary exosome isolation for the discovery of kidney disease biomarkers. *Kidney International*, 82(9):1024–1032, November 2012. 52
- [306] Ruenn Chai Lai, et al. Exosome secreted by MSC reduces myocardial ischemia/reperfusion injury. *Stem Cell Research*, 4(3):214–222, May 2010. 52

-
- [307] Michael L. Merchant, et al. Microfiltration isolation of human urinary exosomes for characterization by MS. *PROTEOMICS – Clinical Applications*, 4(1):84–96, January 2010. 52
- [308] Ana Gámez-Valero, et al. Size-Exclusion Chromatography-based isolation minimally alters Extracellular Vesicles' characteristics compared to precipitating agents. *Scientific Reports*, 6:33641, September 2016. 52
- [309] Ali Hashemi Gheinani, et al. Improved isolation strategies to increase the yield and purity of human urinary exosomes for biomarker discovery. *Scientific Reports*, 8(1):3945, March 2018. 52
- [310] Matías Sáenz-Cuesta, et al. Methods for Extracellular Vesicles Isolation in a Hospital Setting. *Frontiers in Immunology*, 6, 2015. 53
- [311] David Issadore, et al. Miniature magnetic resonance system for point-of-care diagnostics. *Lab on a Chip*, 11(13):2282–2287, June 2011. 54
- [312] Junsung Rho, et al. Magnetic Nanosensor for Detection and Profiling of Erythrocyte-Derived Microvesicles. *ACS nano*, 7(12):11227–11233, December 2013. 54
- [313] Zheng Zhao, et al. A microfluidic ExoSearch chip for multiplexed exosome detection towards blood-based ovarian cancer diagnosis. *Lab on a Chip*, 16(3):489–496, January 2016. 54
- [314] Sangmoo Jeong, et al. Integrated Magneto-Electrochemical Sensor for Exosome Analysis. *ACS nano*, 10(2):1802–1809, February 2016. 54
- [315] Jaideep S. Dudani, et al. Rapid inertial solution exchange for enrichment and flow cytometric detection of microvesicles. *Biomicrofluidics*, 9(1):014112, January 2015. 54
- [316] Henrik Bruus. Acoustofluidics 7: The acoustic radiation force on small particles. *Lab on a Chip*, 12(6):1014–1021, February 2012. 55
- [317] Kyunghoon Lee, et al. Acoustic Purification of Extracellular Microvesicles. *ACS Nano*, 9(3):2321–2327, March 2015. 55
- [318] Mengxi Wu, et al. Isolation of exosomes from whole blood by integrating acoustics and microfluidics. *Proceedings of the National Academy of Sciences*, page 201709210, September 2017. 56
- [319] Simona Sitar, et al. Size Characterization and Quantification of Exosomes by Asymmetrical-Flow Field-Flow Fractionation. *Analytical Chemistry*, 87(18):9225–9233, September 2015. 56
- [320] David Müller, et al. Nanoparticle separation with a miniaturized asymmetrical flow field-flow fractionation cartridge. *Frontiers in Chemistry*, 3, 2015. 57
- [321] Lotien Richard Huang, et al. Continuous particle separation through deterministic lateral displacement. *Science (New York, N.Y.)*, 304(5673):987–990, May 2004. 57, 58, 59, 61, 62
- [322] Benjamin H. Wunsch, et al. Nanoscale lateral displacement arrays for the separation of exosomes and colloids down to 20 nm. *Nature Nanotechnology*, advance online publication, August 2016. 57, 178

-
- [323] J. McGrath, et al. Deterministic lateral displacement for particle separation: A review. *Lab on a Chip*, 14(21):4139–4158, September 2014. 57
- [324] David W. Inglis, et al. Critical particle size for fractionation by deterministic lateral displacement. *Lab on a Chip*, 6(5):655–658, May 2006. 59, 62, 69, 121, 126, 187
- [325] David W. Inglis, et al. Critical particle size for fractionation by deterministic lateral displacement. *Lab on a Chip*, 6(5):655–658, May 2006. 59, 60
- [326] John Alan Davis. Microfluidic Separation of Blood Components through Deterministic Lateral Displacement. *Dissertation presented to the faculty of Princeton University in Candidacy for the Degree of Doctor of Philosophy*, September 2008. 59, 60, 63, 67, 86, 109, 112, 121, 131, 195
- [327] T. Kulrattanarak, et al. Analysis of mixed motion in deterministic ratchets via experiment and particle simulation. *Microfluidics and Nanofluidics*, 10(4):843–853, October 2010. 60, 61, 121
- [328] B.R. Long, et al. Multidirectional sorting modes in deterministic lateral displacement devices. *Physical Review E (Statistical, Nonlinear, and Soft Matter Physics)*, 78(4):046304, 2008. 61
- [329] Brian M. Dincau, et al. Deterministic lateral displacement (DLD) in the high Reynolds number regime: High-throughput and dynamic separation characteristics. *Microfluidics and Nanofluidics*, 22(6):59, June 2018. 61, 62
- [330] Y. S. Lubbersen, et al. Suspension separation with deterministic ratchets at moderate Reynolds numbers. *Chemical Engineering Science*, 73:314–320, May 2012. 61, 108
- [331] Gaetano D’Avino. Non-Newtonian deterministic lateral displacement separator: Theory and simulations. *Rheologica Acta*, 52(3):221–236, January 2013. 62
- [332] Martin Heller et al. A theoretical analysis of the resolution due to diffusion and size dispersion of particles in deterministic lateral displacement devices. *Journal of Micromechanics and Microengineering*, 18(7):075030, 2008. 62
- [333] Martin Heller et al. A theoretical analysis of the resolution due to diffusion and size-dispersion of particles in deterministic lateral displacement devices. *Journal of Micromechanics and Microengineering*, 18(7):075030, July 2008. 62
- [334] S. Cerbelli. Separation of polydisperse particle mixtures by deterministic lateral displacement. The impact of particle diffusivity on separation efficiency. *Asia-Pacific Journal of Chemical Engineering*, 7: S356–S371, August 2012. 63
- [335] Christopher P. Cheng, et al. Quantification of Wall Shear Stress in Large Blood Vessels Using Lagrangian Interpolation Functions with Cine Phase-Contrast Magnetic Resonance Imaging. *Annals of Biomedical Engineering*, 30(8):1020–1032, September 2002. 63
- [336] Kaushik K. Rangharajan, et al. Effect of Microstructure Geometric Form on Surface Shear Stress. *Journal of Fluids Engineering*, 139(1):011201–011201, September 2016. 63

-
- [337] Dmitry A. Fedosov, et al. Deformation and dynamics of red blood cells in flow through cylindrical microchannels. *10(24):4258–4267*, May 2014. 63
- [338] J. Dupire, et al. Full dynamics of a red blood cell in shear flow. *Proceedings of the National Academy of Sciences*, 109(51):20808–20813, December 2012. 63
- [339] Raymond Quek, et al. Separation of deformable particles in deterministic lateral displacement devices. *Physical Review E*, 83(5), May 2011. 64
- [340] Charles S. Peskin. The immersed boundary method. *Acta Numerica*, 11:479–517, January 2002. 64
- [341] David Holmes Timm Krueger. Deformability-based red blood cell separation in deterministic lateral displacement devices-A simulation study. *Biomicrofluidics*, 8(5), 2014. 64, 65
- [342] Zunmin Zhang, et al. Behavior of rigid and deformable particles in deterministic lateral displacement devices with different post shapes. *The Journal of Chemical Physics*, 143(24):243145, December 2015. 65, 68
- [343] Gokberk Kabacaoglu et al. Optimal design of deterministic lateral displacement device for viscosity contrast based cell sorting. *arXiv:1805.08849 [physics]*, May 2018. 66
- [344] Xiaowu Fu, et al. Numerical investigation of polygonal particle separation in microfluidic channels. *Microfluidics and Nanofluidics*, 20(7):1–14, July 2016. 66
- [345] Shashi Ranjan, et al. DLD pillar shape design for efficient separation of spherical and non-spherical bioparticles. *Lab on a Chip*, 14(21):4250–4262, November 2014. 66, 67, 91
- [346] Sam H. Au, et al. Microfluidic Isolation of Circulating Tumor Cell Clusters by Size and Asymmetry. *Scientific Reports*, 7(1):2433, May 2017. 66, 67, 72, 178
- [347] Jianhui Wei, et al. Numerical Study of Pillar Shapes in Deterministic Lateral Displacement Microfluidic Arrays for Spherical Particle Separation. *IEEE transactions on nanobioscience*, 14(6):660–667, September 2015. 67, 68
- [348] Kevin Loutherbach, et al. Deterministic Microfluidic Ratchet. *Physical Review Letters*, 102(4):045301, January 2009. 68
- [349] Kevin Loutherbach, et al. Improved performance of deterministic lateral displacement arrays with triangular posts. *Microfluidics and Nanofluidics*, 9(6):1143–1149, May 2010. 68, 69, 88
- [350] Ji-chul Hyun, et al. Improved pillar shape for deterministic lateral displacement separation method to maintain separation efficiency over a long period of time. *Separation and Purification Technology*, 172:258–267, January 2017. 70
- [351] Mohamed Al-Fandi, et al. New design for the separation of microorganisms using microfluidic deterministic lateral displacement. *Robotics and Computer-Integrated Manufacturing*, 27(2):237–244, April 2011. 70

-
- [352] J. P. Dijkshoorn, et al. Reducing the critical particle diameter in (highly) asymmetric sieve-based lateral displacement devices. *Scientific Reports*, 7(1):14162, October 2017. 70
- [353] Siqi Du, et al. Liquid-based stationary phase for deterministic lateral displacement separation in microfluidics. *Soft Matter*, 2017. 70
- [354] Shilun Feng, et al. Maximizing particle concentration in deterministic lateral displacement arrays. *Biomicrofluidics*, 11(2):024121, March 2017. 70, 97
- [355] Jason P. Beech, et al. Tipping the balance of deterministic lateral displacement devices using dielectrophoresis. *Lab on a Chip*, 9(18):2698–2706, September 2009. 70
- [356] Kerwin Kwek Zeming, et al. Real-time modulated nanoparticle separation with an ultra-large dynamic range. 16(1):75–85, December 2015. 70, 178
- [357] Timothy J. Bowman, et al. Inertia and scaling in deterministic lateral displacement. *Biomicrofluidics*, 7(6), December 2013. 70
- [358] Siqi Du et al. Gravity driven deterministic lateral displacement for suspended particles in a 3D obstacle array. *Scientific Reports*, 6:31428, August 2016. 70
- [359] David J. Collins, et al. Particle separation using virtual deterministic lateral displacement (vDLD). *Lab on a Chip*, 14(9):1595–1603, April 2014. 70
- [360] John A. Davis, et al. Deterministic hydrodynamics: Taking blood apart. *Proceedings of the National Academy of Sciences of the United States of America*, 103(40):14779–14784, October 2006. 71
- [361] David W. Inglis, et al. Microfluidic device for label-free measurement of platelet activation. *Lab on a Chip*, 8(6):925–931, May 2008. 71, 178
- [362] David W. Inglis, et al. Scaling deterministic lateral displacement arrays for high throughput and dilution-free enrichment of leukocytes. *Journal of Micromechanics and Microengineering*, 21(5):054024, 2011. 71
- [363] Jason P. Beech, et al. Sorting cells by size, shape and deformability. 12(6):1048–1051, February 2012. 71
- [364] Kerwin Kwek Zeming, et al. Rotational separation of non-spherical bioparticles using I-shaped pillar arrays in a microfluidic device. *Nature Communications*, 4:1625, March 2013. 71
- [365] David Holmes, et al. Separation of blood cells with differing deformability using deterministic lateral displacement. *Interface Focus*, 4(6), December 2014. 71, 178
- [366] Jongchan Choi, et al. On-chip Extraction of Intracellular Molecules in White Blood Cells from Whole Blood. *Scientific Reports*, 5:15167, October 2015. 71
- [367] Curt I. Civin, et al. Automated leukocyte processing by microfluidic deterministic lateral displacement. *Cytometry Part A*, 89(12):1073–1083, December 2016. 71

-
- [368] Ewan Henry, et al. Sorting cells by their dynamical properties. *Scientific Reports*, 6:34375, October 2016. [71](#)
- [369] Kerwin Kwek Zeming, et al. Asymmetrical Deterministic Lateral Displacement Gaps for Dual Functions of Enhanced Separation and Throughput of Red Blood Cells. *Scientific Reports*, 6:22934, March 2016. [71](#), [79](#), [91](#)
- [370] Byeongyeon Kim, et al. Deterministic Migration-Based Separation of White Blood Cells. *Small*, 12(37):5159–5168, October 2016. [71](#)
- [371] Masumi Yamada, et al. Slanted, asymmetric microfluidic lattices as size-selective sieves for continuous particle/cell sorting. *Lab on a Chip*, 17(2):304–314, January 2017. [71](#)
- [372] Tengyang Jing, et al. Single Cell Analysis of Leukocyte Protease Activity Using Integrated Continuous-Flow Microfluidics. *Analytical Chemistry*, 88(23):11750–11757, December 2016. [71](#)
- [373] R. Campos-González, et al. Deterministic Lateral Displacement: The Next-Generation CAR T-Cell Processing? 2018. [71](#)
- [374] James V. Green, et al. Deterministic Lateral Displacement as a Means to Enrich Large Cells for Tissue Engineering. *Analytical Chemistry*, 81(21):9178–9182, November 2009. [72](#)
- [375] Kevin Louterback, et al. Deterministic separation of cancer cells from blood at 10 mL/min. *AIP Advances*, 2(4):042107, October 2012. [72](#)
- [376] Zongbin Liu, et al. Rapid isolation of cancer cells using microfluidic deterministic lateral displacement structure. *Biomicrofluidics*, 7(1):011801, January 2013. [72](#)
- [377] Hiromasa Okano, et al. Enrichment of circulating tumor cells in tumor-bearing mouse blood by a deterministic lateral displacement microfluidic device. *Biomedical Microdevices*, 17(3):59, June 2015. [72](#)
- [378] Nezihi Murat Karabacak, et al. Microfluidic, marker-free isolation of circulating tumor cells from blood samples. *Nature Protocols*, 9(3):694–710, March 2014. [72](#)
- [379] Fabio Fachin, et al. Monolithic Chip for High-throughput Blood Cell Depletion to Sort Rare Circulating Tumor Cells. *Scientific Reports*, 7, September 2017. [72](#)
- [380] Xiaocheng Jiang, et al. Microfluidic isolation of platelet-covered circulating tumor cells. *Lab on a Chip*, September 2017. [72](#)
- [381] Stefan H. Holm, et al. Separation of parasites from human blood using deterministic lateral displacement. *Lab on a Chip*, 11(7):1326–1332, April 2011. [72](#)
- [382] David W. Inglis, et al. Highly accurate deterministic lateral displacement device and its application to purification of fungal spores. *Biomicrofluidics*, 4(2):024109, May 2010. [72](#)
- [383] András J. Laki, et al. Separation of Microvesicles from Serological Samples Using Deterministic Lateral Displacement Effect. *BioNanoScience*, 5(1):48–54, November 2014. [72](#)

-
- [384] Jason P. Beech, et al. Separation of pathogenic bacteria by chain length. *Analytica Chimica Acta*, 1000: 223–231, February 2018. 72
- [385] Timothy Bowman, et al. Force driven separation of drops by deterministic lateral displacement. *Lab on a Chip*, 12(16):2903, 2012. 72
- [386] Naotomo Tottori, et al. Separation of main and satellite droplets in a deterministic lateral displacement microfluidic device. *RSC Advances*, 7(56):35516–35524, 2017. 72
- [387] Kerwin Kwek Zeming, et al. Fluorescent label-free quantitative detection of nano-sized bioparticles using a pillar array. *Nature Communications*, 9(1):1254, March 2018. 72, 119
- [388] Benjamin H. Wunsch, et al. Nanoscale lateral displacement arrays for the separation of exosomes and colloids down to 20 nm. *Nature Nanotechnology*, 11(11):936–940, November 2016. 72
- [389] Peter Schwartz et al. A second-order accurate method for solving the signed distance function equation. *Communications in Applied Mathematics and Computational Science*, 5(1):81–97, February 2010. 76
- [390] Zunmin Zhang, et al. Behavior of rigid and deformable particles in deterministic lateral displacement devices with different post shapes. *The Journal of Chemical Physics*, 143(24):243145, December 2015. 79
- [391] Rohan Vernekar, et al. Anisotropic permeability in deterministic lateral displacement arrays. *Lab on a Chip*, 17(19):3318–3330, September 2017. 79, 117, 133
- [392] Eloise Pariset, et al. Anticipating Cutoff Diameters in Deterministic Lateral Displacement (DLD) Microfluidic Devices for an Optimized Particle Separation. *Small*, 13(37):n/a–n/a, October 2017. 110, 121
- [393] David W. Inglis. Efficient microfluidic particle separation arrays. *Applied Physics Letters*, 94(1):013510, January 2009. 117
- [394] T. Kulrattanak, et al. Mixed motion in deterministic ratchets due to anisotropic permeability. *Journal of Colloid and Interface Science*, 354(1):7–14, February 2011. 121
- [395] Jonathan Cohen, et al. Sepsis: A roadmap for future research. *The Lancet Infectious Diseases*, 15(5): 581–614, May 2015. 138
- [396] Peng Zhang, et al. Characterization of Spherulites as a Lipidic Carrier for Low and High Molecular Weight Agents. *Pharmaceutical research*, 30(6):1525–1535, June 2013. 152
- [397] Tamás Baranyai, et al. Isolation of Exosomes from Blood Plasma: Qualitative and Quantitative Comparison of Ultracentrifugation and Size Exclusion Chromatography Methods. *PLoS ONE*, 10(12), December 2015. 159
- [398] Anita N. Böing, et al. Single-step isolation of extracellular vesicles by size-exclusion chromatography. *Journal of Extracellular Vesicles*, 3, September 2014. 159

-
- [399] Jan Lötvall, et al. Minimal experimental requirements for definition of extracellular vesicles and their functions: A position statement from the International Society for Extracellular Vesicles. *Journal of Extracellular Vesicles*, 3, December 2014. 160
- [400] Mustafa Kotmakci et al. *Exosome Isolation: Is There an Optimal Method with Regard to Diagnosis or Treatment?* September 2017. 162
- [401] Nezihi Murat Karabacak, et al. Microfluidic, marker-free isolation of circulating tumor cells from blood samples. *Nature Protocols*, 9(3):694–710, March 2014. 167, 179, 182
- [402] Stefan H. Holm, et al. Separation of parasites from human blood using deterministic lateral displacement. *Lab on a Chip*, 11(7):1326–1332, April 2011. 178
- [403] John A. Davis, et al. Deterministic hydrodynamics: Taking blood apart. *Proceedings of the National Academy of Sciences*, 103(40):14779–14784, March 2006. 178
- [404] András J. Laki, et al. Separation of Microvesicles from Serological Samples Using Deterministic Lateral Displacement Effect. *BioNanoScience*, 5(1):48–54, November 2014. 178
- [405] Xiao-Bin Li, et al. Study on the mechanism of droplet formation in T-junction microchannel. *Chemical Engineering Science*, 69(1):340–351, February 2012. 182
- [406] Leslie Y. Yeo, et al. Microfluidic Devices for Bioapplications. *Small*, 7(1):12–48, January 2011. 182
- [407] Diego Velasco, et al. Microfluidic Encapsulation of Cells in Polymer Microgels. *Small*, 8(11):1633–1642, June 2012. 182
- [408] Dong-Ku Kang, et al. Droplet microfluidics for single-molecule and single-cell analysis in cancer research, diagnosis and therapy. *TrAC Trends in Analytical Chemistry*, 58(Supplement C):145–153, June 2014. 182
- [409] Samaneh Mashaghi, et al. Droplet microfluidics: A tool for biology, chemistry and nanotechnology. *TrAC Trends in Analytical Chemistry*, 82(Supplement C):118–125, September 2016. 182
- [410] Michele Zagnoni et al. Chapter 2 - Droplet Microfluidics for High-throughput Analysis of Cells and Particles. In Zbigniew Darzynkiewicz, et al., editors, *Methods in Cell Biology*, volume 102, pages 23–48. Academic Press, January 2011. 182
- [411] Evgenia Yu Basova et al. Droplet microfluidics in (bio)chemical analysis. *Analyst*, 140(1):22–38, December 2014. 182
- [412] M. Godin, et al. Measuring the mass, density, and size of particles and cells using a suspended microchannel resonator. *Applied Physics Letters*, 91(12), 2007. 182
- [413] Byeong-Ui Moon, et al. Water-in-Water Droplets by Passive Microfluidic Flow Focusing. *Analytical Chemistry*, 88(7):3982–3989, April 2016. 182

-
- [414] Y. Yan, et al. Numerical simulation of junction point pressure during droplet formation in a microfluidic T-junction. *Chemical Engineering Science*, 84:591–601, December 2012. 182, 183
- [415] Piotr Garstecki, et al. Formation of droplets and bubbles in a microfluidic T-junction—scaling and mechanism of break-up. *Lab on a Chip*, 6(3):437–446, February 2006. 183, 189
- [416] Shuheng Zhang, et al. Prediction of sizes and frequencies of nanoliter-sized droplets in cylindrical T-junction microfluidics. *Chemical Engineering Science*, 138:128–139, December 2015. 189
- [417] Amit Gupta, et al. Droplet formation and stability of flows in a microfluidic T-junction. *Applied Physics Letters*, 94(16):164107, April 2009. 192
- [418] Florian Pineda, et al. Using Electrofluidic Devices As Hyper-elastic Strain Sensors. *Microelectron. Eng.*, 144(C):27–31, August 2015. 193
- [419] C. Parent, et al. Quantitative biological assays with on-chip calibration using versatile architecture and collapsible chambers. *Sensors and Actuators B: Chemical*, 261:106–114, May 2018. 195

Appendix

A.1 Appendix 1: Exosomal functions for different biofluids

Body Fluid	Emitting Cells	Biomarkers
Blood	Cells in blood and at the surface of blood vessels, mostly platelets (25% of blood EVs are positive for platelet specific markers)	Markers specific to platelets: CD41a, CD61, GPIb
Urine	Cells from kidney, bladder, prostate and urethra	CD24
Saliva	Epithelial cells and granulocytes	Epithelial cell markers and granulocyte marker CD66b
Seminal fluid/semen	Prostate and epididymal epithelial cells	Proteins, lipids and RNA molecules specific to the secreting organ of the male reproductive tract
Bile	Cells from liver and gallbladder	CD63 and Tsg101
Bronchoalveolar fluid	Lung cells	MHCI, MHCII, CD54, CD63, CD86
Nasal fluid	Epithelial and dendritic cells lining the epithelium	CD63, CD9, CD81 and Tsg101
Amniotic fluid	Cells from fetal kidney and mother's blood	Markers specific to foetal urine: AQP2, CD24 and annexin-I Markers specific to mother's blood: annexin-I, HSP70
Uterine fluid	Cells from uterus, fallopian tube and ovary	Unknown
Breast milk	Cells in breast milk and blood circulation, epithelial breast cells	Unknown
Faeces	Commensal bacteria	Unknown
Synovial fluid	Macrophages	Unknown
Cerebrospinal fluid	Cells from brain and spine	Unknown

Body Fluid	Functions
Blood	- Physiological functions of platelets - Transmission of pathological states, for example by tumour-derived EVs
Urine	- Increase of water permeability across the nephron thanks to Na ⁺ transporter proteins - Water balance in kidney thanks to an EV angiotensin-converting enzyme in the renal tubule lumen - Immune defense of the urinary track thanks to innate immune proteins enriched in EVs - Coagulation and haemostasis through EV tissue factors
Saliva	- Cleavage of substance P and chemokines with the CD26 protein - Blood coagulation initiation (participate in wound healing after animal licking)
Seminal fluid/semen	- Acquisition of sperm motility and reduction of oxidative stress
Bile	- Interactions with primary cilia for the regulation and proliferation of cholangiocytes
Bronchoalveolar fluid	- Immune defense against external stimuli (nanoparticles, pathogens, allergens, bacteria)
Nasal fluid	- Strong potential for drug delivery towards the brain, lungs and intestines
Amniotic fluid	- Immune defense of the foetus through modulation of intra-amniotic cytokine production by HSP72
Uterine fluid	- Sperm viability, capacitation and fertilization through EV protein transport (plasma membrane calcium-transporting ATPase 4 and sperm adhesion molecule 1) - Embryo implantation process thanks to EV miRNAs and proteins
Breast milk	- Development of the infant immune system through important concentrations of EV immune-related miRNAs
Faeces	- Pro-inflammatory effect
Synovial fluid	- Autoimmune mechanisms (citrullinated peptides that are specific autoantigens in rheumatoid arthritis) - Involvement in joint inflammatory processes through a nuclear DEK-phosphoprotein
Cerebrospinal fluid	- Protection against amyloid beta-protein, which disrupt synaptic plasticity

A.2 Appendix 2: Cancer-specific EV biomarkers

Cancer Type	Biomarker Type	Biomarker(s)	Body Fluid	Reference
Bladder cancer	Protein	EDIL-3	Urine	Beckham et al., 2014
		Del1	Urine	Perez et al., 2014
		LASS2		
		GALNT1	Urine	Chen et al., 2012
		ARHGEF39		
		FOXO3		
		TACSTD2		
Brain tumor	RNA	3 specific miRNAs	Cell sup.	Camacho et al., 2013
Breast cancer	Protein	Fibronectin	Plasma	Moon et al., 2016
	Protein & RNA	Developmental Endothelial Locus 1	Plasma	Moon et al., 2016
		CD24	Plasma	Rupp et al., 2011
	RNA	EpCAM	Serum	Hannafon et al., 2016
		miR-200a		
miR-200c				
		miR-205	Plasma	Lowry et al., 2015
		3 specific miRNAs	Serum	Corcoran et al., 2011
		miR-21	Plasma	
		miR-1246	Serum	
		miR34a		
		miR-21		
Chronic kidney disease	RNA	miR-29c	Urine	Lv et al., 2013
Clear-cell renal cell carcinoma (ccRCC)	RNA	miR-210	Serum	Zhang et al., 2016
		miR-1233		
		12 specific miRNAs	Urine	Butz et al., 2016
Colon cancer	Protein	Hsp60	Plasma	Campanella et al., 2015
	RNA	miR-4772-3p	Serum	Liu et al., 2016
		circRNAs	Serum	Li et al., 2015
		7 specific miRNAs	Serum	Ogata-Kawata et al., 2014
Colorectal cancer	Protein	CD147	Serum	Yoshioka et al., 2014
		CD9		
	RNA	Claudin-3	Ascites fluid	Choi et al., 2011
		3 specific miRNAs	Serum	Zhu et al., 2017
		miR-4772-3p	Serum	Liu et al., 2016
		miR-21	Serum	Uratani et al., 2016
		miR-19a	Serum	Matsumura et al., 2015
Specific miRNAs and mRNAs	Cell sup.	Chiba et al., 2012		

Cancer Type	Biomarker Type	Biomarker(s)	Body Fluid	Reference
Acute myeloid leukemia	Protein	TGF-beta1	Plasma	Hong et al., 2014
Esophageal squamous cell carcinoma	RNA	miR-21	Plasma	Tanaka et al., 2013
Gastric cancer	Protein	methyated LINE1	Gastric juice	Yoshida et al., 2014
		SOX17 DNA	Plasma	Baran et al., 2010
	RNA	CCR6 HER-2/neu	Plasma	Li et al., 2015
		Long intergenic non-protein-coding RNA 152 miR-21 miR1225-5p	Peritoneal lavage fluid	Tokuhisa et al., 2015
Glioma	RNA	miR-21	Cerebrospinal fluid	Shi et al., 2015
		Non-coding RNA	Plasma	Li et al., 2013
Glioblastoma multiforme	RNA	3 specific miRNAs	Serum	Manterola et al., 2014
Glioblastoma	Protein	EGFRvIII	Serum	Shao et al., 2012
		CD63	Serum	Skog et al., 2008
	RNA	EGFRvIII miR-21	Cerebrospinal fluid	Akers et al., 2013
		IDH1 mRNA	Cerebrospinal fluid, Serum	Chen et al., 2013
Hematological cancer	Protein	121 downregulated mRNA	Serum	Noerholm et al., 2012
		CD9	Serum	Caivano et al., 2015
		CD13		
		CD19		
Hepatoblastoma	Protein	CD30		
		CD38		
		CD63		
Hepatoblastoma	RNA	miRNA-24s panel	Whole blood	Jiao et al., 2017
Laryngeal squamous cell carcinoma (LSCC)	RNA	miR-21 HOTAIR	Serum	Wang et al., 2014

Cancer Type	Biomarker Type	Biomarker(s)	Body Fluid	Reference
Liver cancer	RNA	miR-1247-3p	Cell sup.	Fang et al., 2018
Lung cancer	RNA	miR-126	Serum	Grimolizzi et al., 2017
		3 specific miRNAs	Plasma	Liu et al., 2017
		10 marker model	Plasma	Sandfeld-Paulsen et al., 2016
		miR-21	Tumors and serum	Munagala et al., 2016
		miR-155	Serum	Tang et al., 2016
		miR-208a	Plasma	Dinh et al., 2016
		miR-29a	Plasma	Dinh et al., 2016
		miR-150	Plasma	Jacobsen et al., 2015
		30 marker model	Culture medium	Xiao et al., 2014
		6 specific miRNAs	Plasma	Cazzoli et al., 2013
Lung cancer	Protein	5 specific miRNAs	Plasma	Aushev et al., 2013
		4 specific miRNAs	Plasma	Silva et al., 2011
		12 specific miRNAs	Plasma	Rabinowits et al., 2009
		EGFR	Serum	Yamashita et al., 2013
		hsa-mir-155	Plasma	Yanaihara et al., 2006
		hsa-let-7a-2	Plasma	Yanaihara et al., 2006
		MIA	Serum	Alegre et al., 2016
		S100B	Plasma	Peinado et al., 2012
Melanoma	Protein	TYP-2	Plasma	Peinado et al., 2012
		VLA-4	Plasma	Peinado et al., 2012
		HSP70	Plasma	Logozzi et al., 2009
		HSP90	Plasma	Logozzi et al., 2009
Multiple myeloma	Protein & RNA	CD63	Plasma	Logozzi et al., 2009
		caveolin-1	Plasma	Logozzi et al., 2009
Multiple myeloma	Protein & RNA	Let-7b miRNA-18a	Serum	Manier et al., 2017
Nasopharyngeal carcinoma cell	carci- RNA	BART-viral miRNA	Plasma	Gourzones et al., 2010
Ovarian cancer	Protein	Phosphatidylserine	Plasma	Lea et al., 2017
		CD24	Plasma	Zhao et al., 2016
		EpCAM	Plasma	Szajnik et al., 2013
		CA-125	Plasma	Szajnik et al., 2013
		TGFB1	Plasma	Szajnik et al., 2013
Ovarian cancer	Protein	MAGE3/6	Plasma	Szajnik et al., 2013
		EpCAM	Ascites fluid	Runz et al., 2007
		CD24	Ascites fluid	Runz et al., 2007
Ovarian cancer	RNA	8 specific miRNAs	Serum	Taylor et al., 2008

Appendix

Cancer Type	Biomarker Type	Biomarker(s)	Body Fluid	Reference
Pancreatic cancer	Protein	Glypican 1	Serum	Melo et al., 2015
		Macrophage migration inhibition factor (MIF)	Pancreatic cancer cell lines	Costa-Silva et al., 2015
		Combination of 5 proteins and 4 miRNAs	Serum	Madhavan et al., 2015
	RNA	KRAS	Serum	Kahlert et al., 2014
		8 specific miRNAs miR-17-5p, miR-21 RNA PDE8A	Plasma Serum Plasma	Lai et al., 2017 Que et al., 2013 Li et al., 2018
Pancreaticobiliary	DNA	Mutations in the tumor DNA	Plasma	San Lucas et al., 2016
	RNA	miR-1246 miR-4644	Saliva	Machida et al., 2016
Prostate cancer	Protein	PSA	Plasma	Logozzi et al., 2017
		EGFR	Serum	Kharmate et al., 2016
		PCA3	Urine	McKiernan et al., 2016
		ERG		
		PCA3	Urine	Donovan et al., 2015
		ERG		
		CD9	Urine	Duijvesz et al., 2015
		CD63		
		TM256	Urine	Overbye et al., 2015
		ADIRF		
		LAMTOR1		
		PSMA	Plasma	Mizutani et al., 2014
		CD9		
	AGR2 splice variants	Urine	Neeb et al., 2014	
	ITGA3	Urine	Bijnsdorp et al., 2013	
	ITGB1			
	N-linked glycans	Prostatic secretions	Nyalwidhe et al., 2013	
	PTEN	Plasma	Gabriel et al., 2013	
	Survivin	Plasma	Khan et al., 2012	
	Prostasome number	Plasma	Taavosidana et al., 2011	
PSA	Urine	Mitchell et al., 2009		
PCA-3	Urine	Nilsson et al., 2009		
TMPRSS2:ERG				
delta-catenin	Urine	Lu et al., 2009		
RNA	Isoforms of miR-21	Urine	Koppers-Lalic et al., 2016	
	miR-204			
	miR-375			
	miR-1290	Plasma	Huang et al., 2015	
	miR-375			
	miR-141	Serum	Li et al., 2015	
	miR-34a	Urine	Corcoran et al., 2014	
	miR-141 miR-375	Serum, Plasma	Bryant et al., 2012	
Renal cell carc.	Protein	MMP-9 DKP4 EMMPRIN PODXL	Urine	Raimondo et al., 2013

A.3 Appendix 3: Overview of clinical trials for EV-based therapies

Adapted from Ohno et al., International Journal of Molecular Sciences, 2016

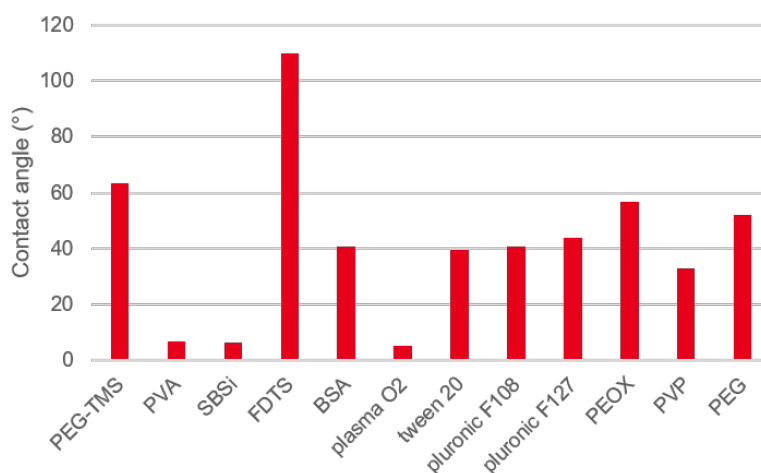
Disease	Drug	EV source	Administration	Reference
Metastatic melanoma	Melanoma peptide anti-gens	DCs	intradermal and subcutaneous	Escudier et al., 2005
Non-small cell lung cancer	MAGE peptide	DCs	intradermal and subcutaneous	Morse et al., 2005
Colorectal cancer	GM-CSF	Ascites fluid	subcutaneous	Dai et al., 2008
Malignant glioma	AS-ODN	Glioma	implanted biodiffusion chamber	Thomas Jefferson University Hospital, 2000
Type 1 diabete	EVs	MSCs	intravenous	Sahel Teaching Hospital, 2000
Graft-versus host disease	EVs	MSCs	intravenous	Kordelas et al., 2014
Meningitis	Vaccine	Cell strains	intramuscular	Sandbu et al., 2007
Meningitis	Vaccine	Cell strains	intramuscular	Marsay et al., 2015
Colon cancer	Curcumin	Fruit	oral	James Graham Brown Cancer Center, 2000
Mucositis	Curcumin	Fruit	oral	James Graham Brown Cancer Center, 2000
Non-small cell lung cancer	IFN-gama, MAGE peptides	DCs	intradermal and subcutaneous	Viaud et al., 2011
Meningitis	rMenB vaccine	Cell strains	intramuscular	Findlow et al., 2010

A.4 Appendix 4: DLD chip surface treatments

12 different surface treatments were tested on samples of oxidized silicon chips in order to reduce bead adhesion to DLD walls:

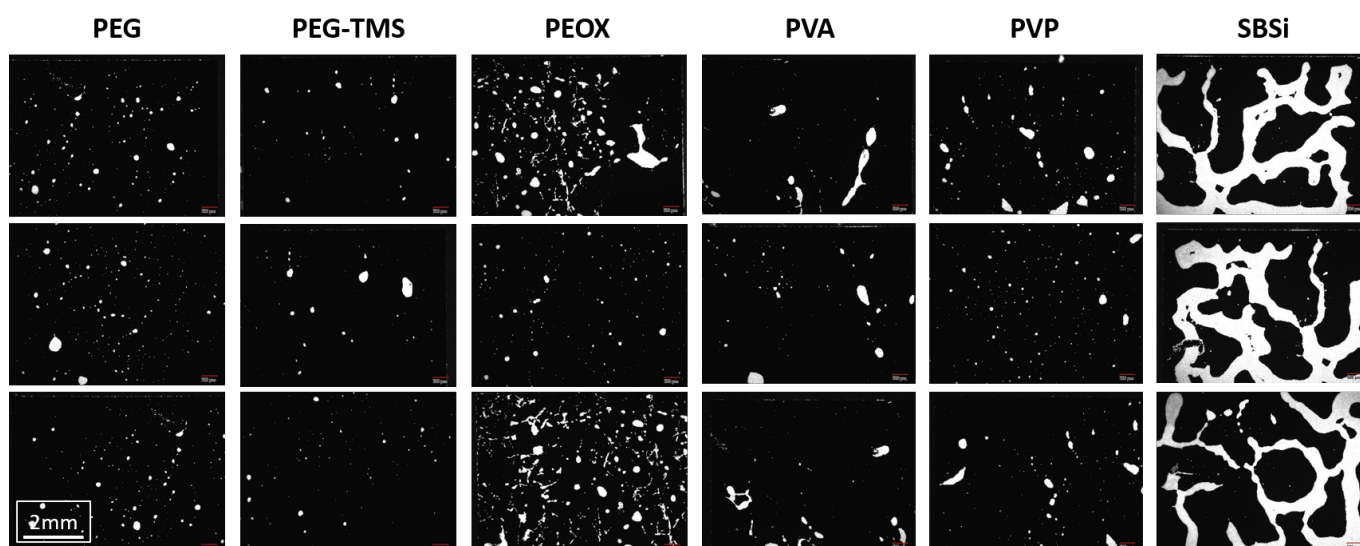
- Polyethyleneglycol-trimethylsulfoxide (PEG-TMS)
- Polyvinylalcohol (PVA)
- Sulfbetaine (SBSi)
- O2 Plasma + Bovine serum albumin (BSA)
- O2 Plasma
- Tween 20 (5 % in water)
- Pluronic F-108 (1 % in water)
- Pluronic F-127 (1 % in water)
- Polyethyleneoxide 50000 MW (1 % in water) (PEOX)
- Polyvinylpyrrolidone 10000 MW (1 % in water) (PVP)
- Polyethyleneglycol 35000 MW (1 % in water) (PEG)

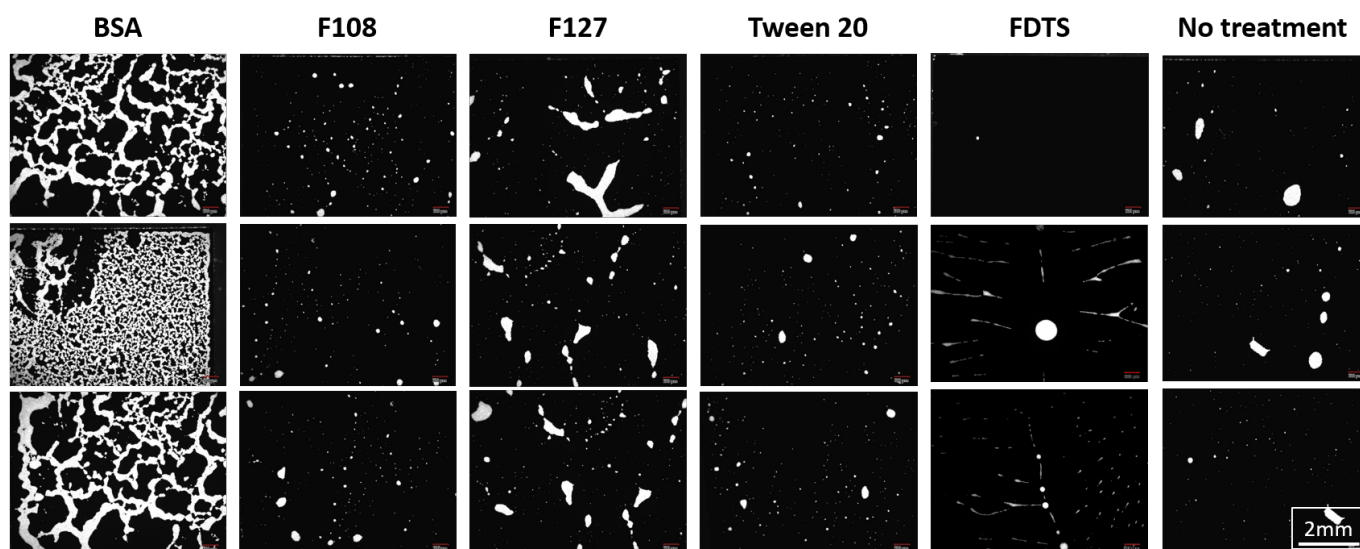
The contact angles are given below for each surface treatment:



Value of contact angle for the 12 tested surface treatments.

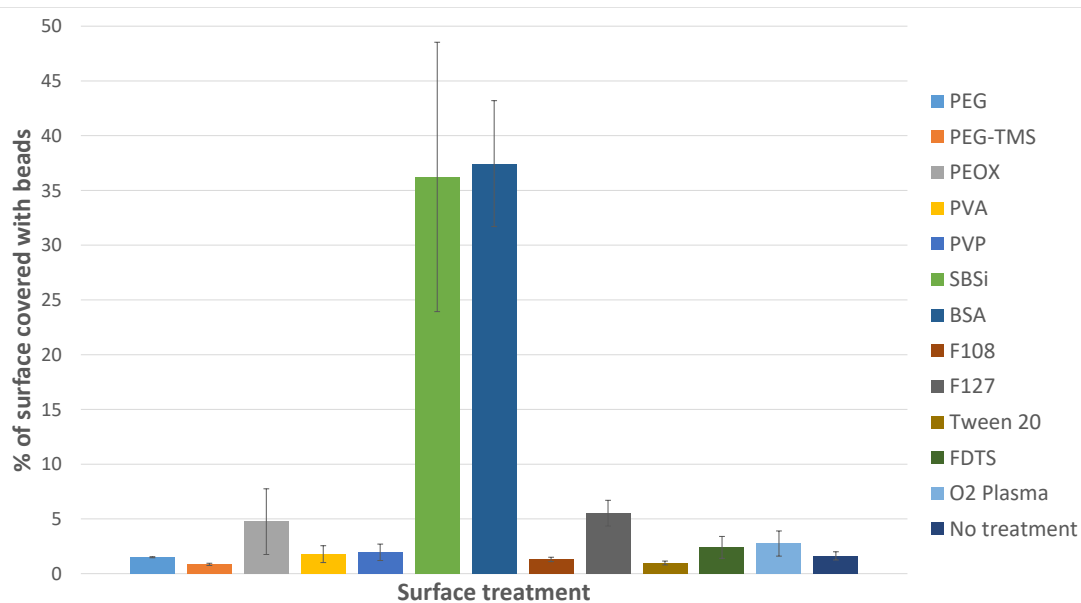
The chips were tested five days after surface treatment with 15 μm fluorescent beads (ThermoFisher Scientific, Fluoro-Max Dyed Green Aqueous Fluorescent Particles) suspended in a 1 % surfactant solution (Tween 20, Sigma-Aldrich) in filtered DPBS (Life Technologies, 14190144), as recommended by the manufacturer. The chips were incubated at room temperature for one hour with the same amount of bead solution before observation under the microscope. According to the surface treatment, different levels of bead aggregation were observed (appendix A.4). Three images were taken for each surface treatment and automatic quantification of the percentage of covered surface was performed with ImageJ software (appendix A.4).





Images of the chips for each surface treatment, after incubation with beads (3 images for each sample) on model samples of oxidized silicon chips.

None of the 12 tested surface treatments shows significant reduction of bead adhesion compared to the control sample without any surface treatment. This is why we have decided not to use surface modification with the bead experiments, which also simplifies the chip preparation process.

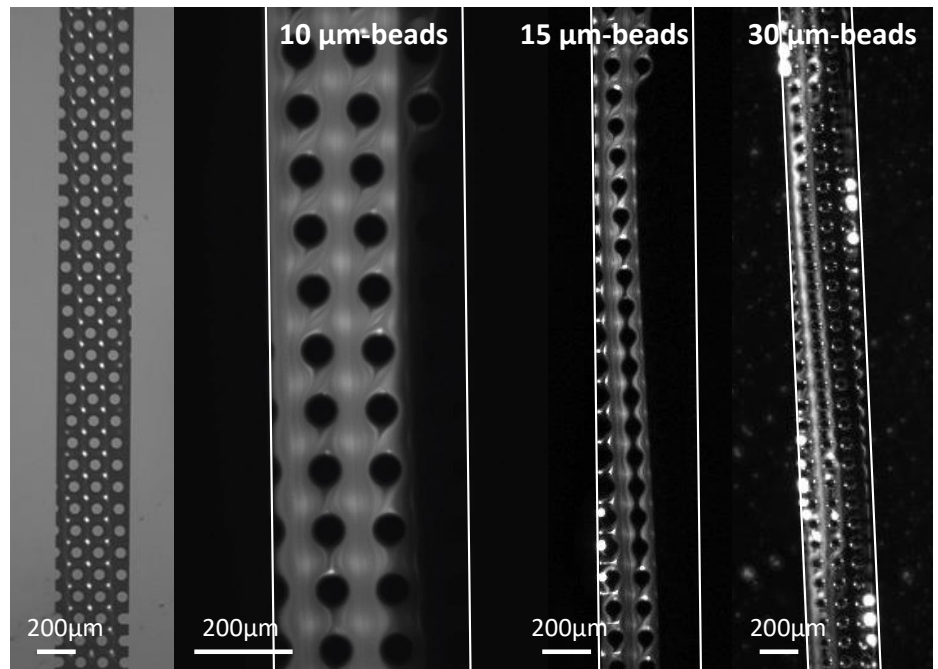


Percentage of surface covered with beads for each surface treatment.

A.5 Appendix 5: DLD trajectory of fluorescent beads

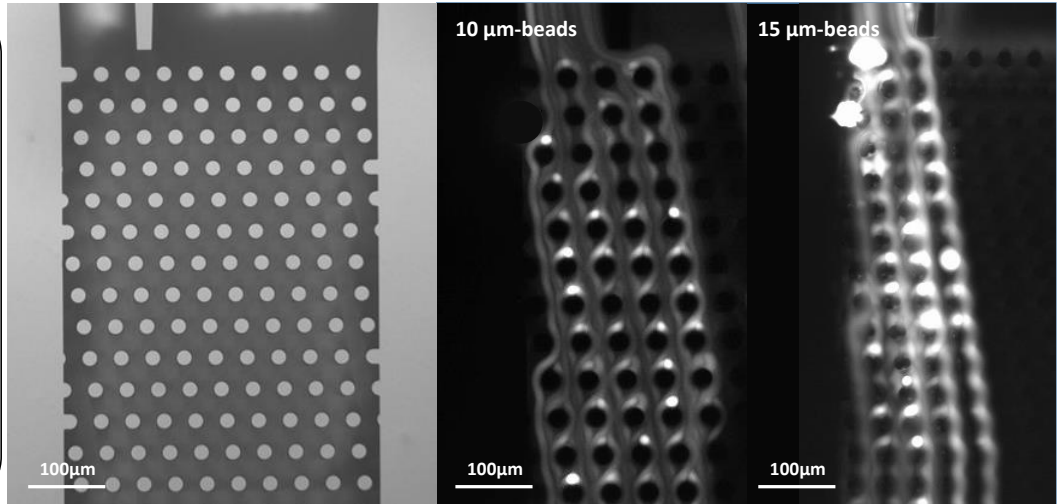
Version 1, Design 1

Pillar shape: Circles
Pillar Diameter: 60 μm
Lateral Gap: 60 μm
Downstream Gap: 60 μm
Periodicity N: 22
Predicted D_c (Davis): 19 μm
Experimental $D_c \sim 30 \mu\text{m}$

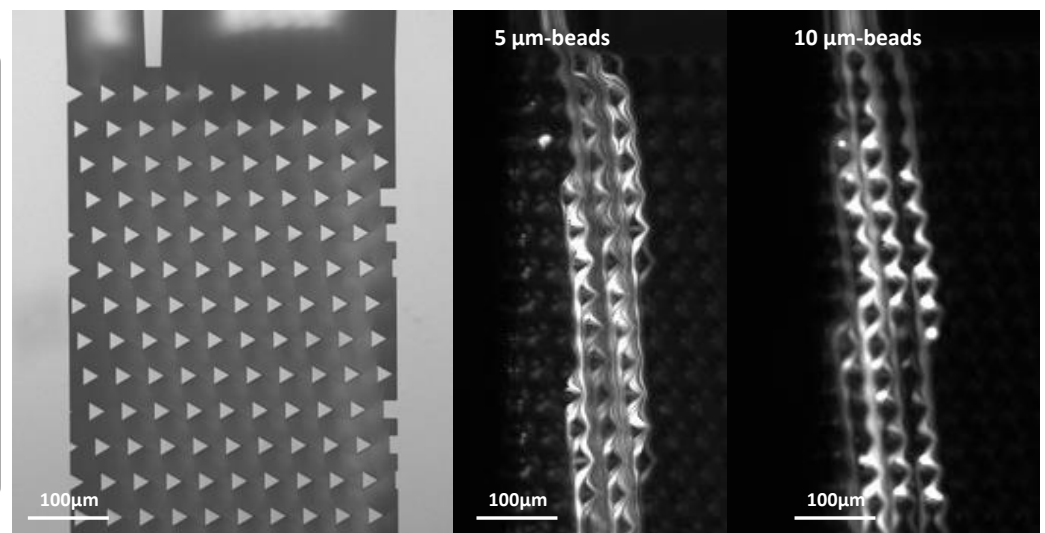


**Version 1, Design 2,
Section 1**

Pillar shape: Circles
Pillar Diameter: 20 μm
Lateral Gap: 20 μm
Downstream Gap: 20 μm
Periodicity N: 5.7
Predicted D_c (Davis): 12 μm
Experimental $D_c \sim 15 \mu\text{m}$

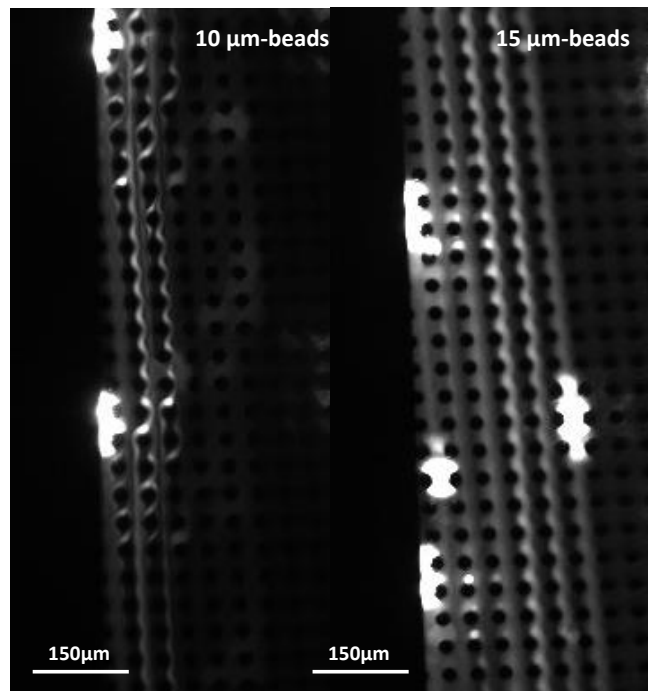
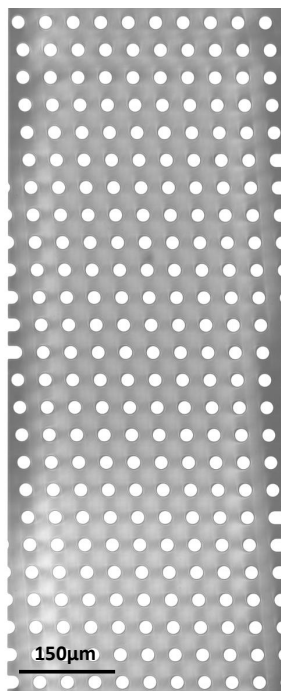
**Version 1, Design 2,
Section 1**

Pillar shape: Triangles
Pillar Diameter: 20 μm
Lateral Gap: 20 μm
Downstream Gap: 20 μm
Periodicity N: 5.7
Experimental $D_c \sim 10 \mu\text{m}$



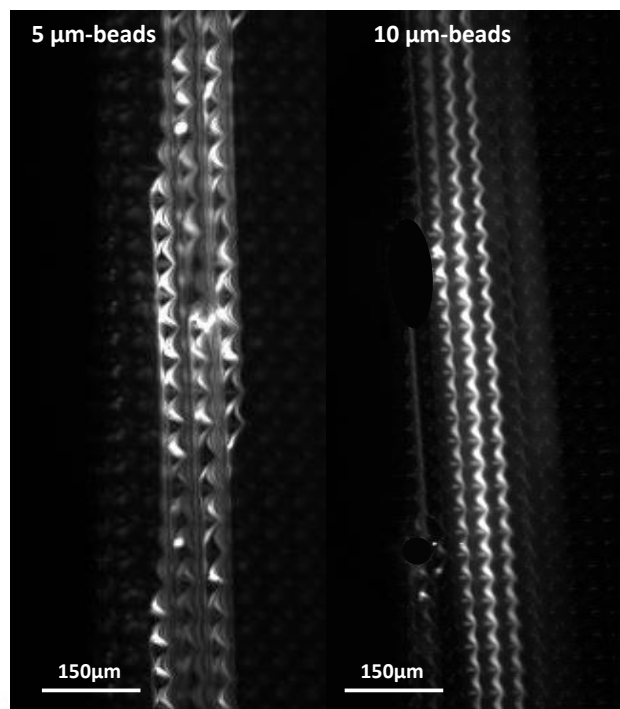
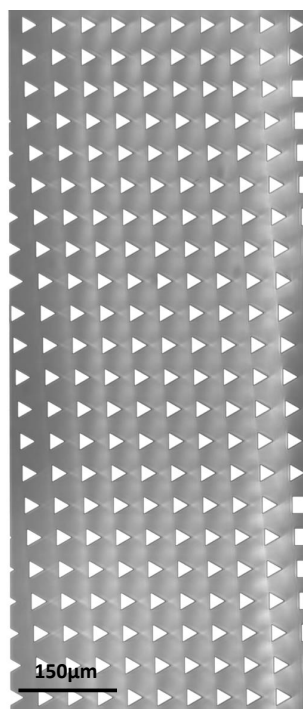
**Version 1, Design 2,
Section 2**

Pillar shape: Circles
 Pillar Diameter: 20 μm
 Lateral Gap: 20 μm
 Downstream Gap: 20 μm
 Periodicity N: 13.3
 Predicted D_c (Davis): 8 μm
 Experimental $D_c \in [10;15]$ μm



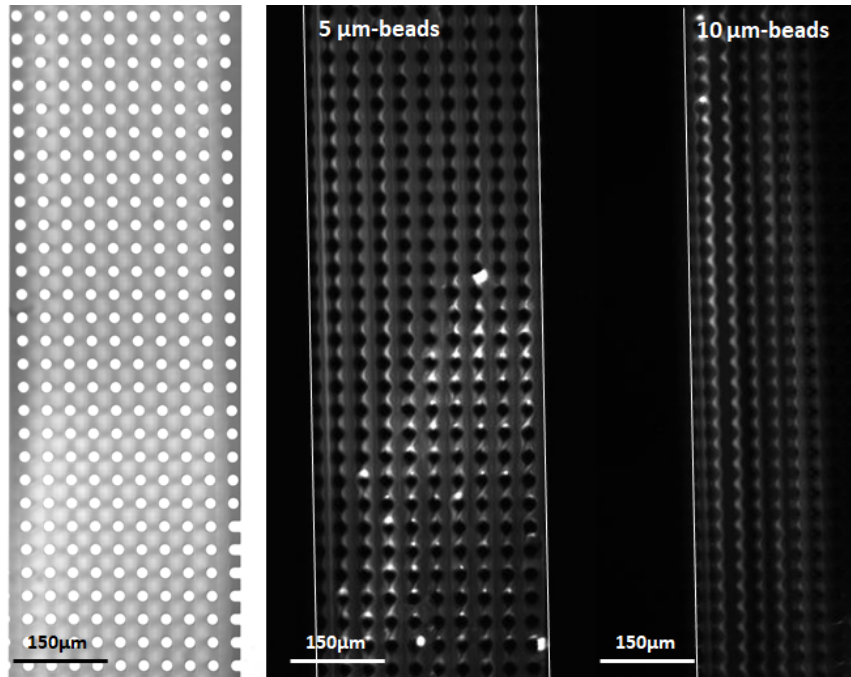
**Version 1, Design 2,
Section 2**

Pillar shape: Triangles
 Pillar Diameter: 20 μm
 Lateral Gap: 20 μm
 Downstream Gap: 20 μm
 Periodicity N: 13.3
 Experimental $D_c \in [5;10]$ μm



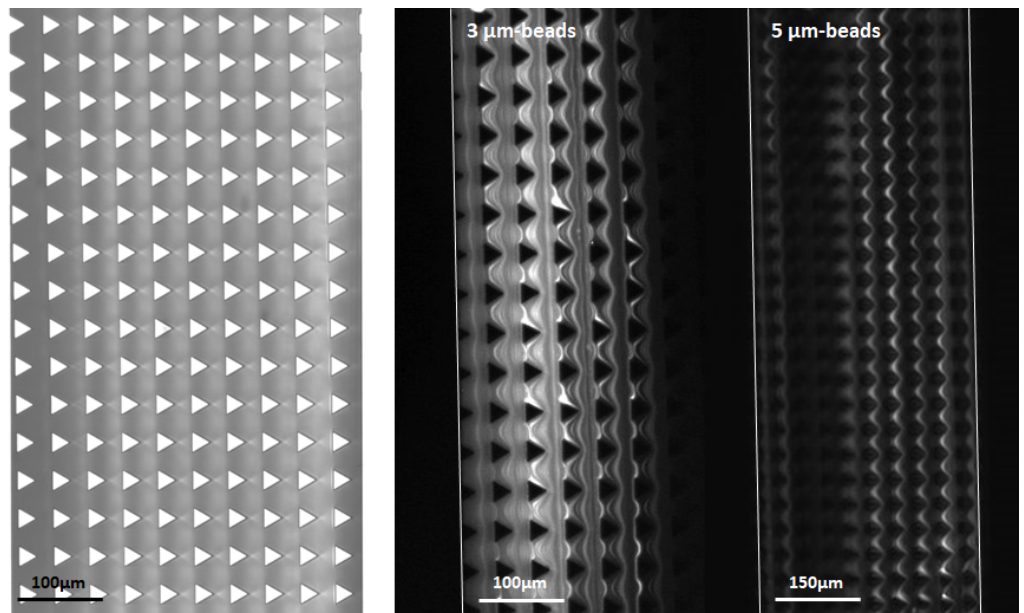
**Version 1, Design 2,
Section 3**

Pillar shape: Circles
 Pillar Diameter: $20\ \mu\text{m}$
 Lateral Gap: $20\ \mu\text{m}$
 Downstream Gap: $20\ \mu\text{m}$
 Periodicity N: 50
 Predicted D_c (Davis): $4\ \mu\text{m}$
 Experimental $D_c \in [5;10]\ \mu\text{m}$



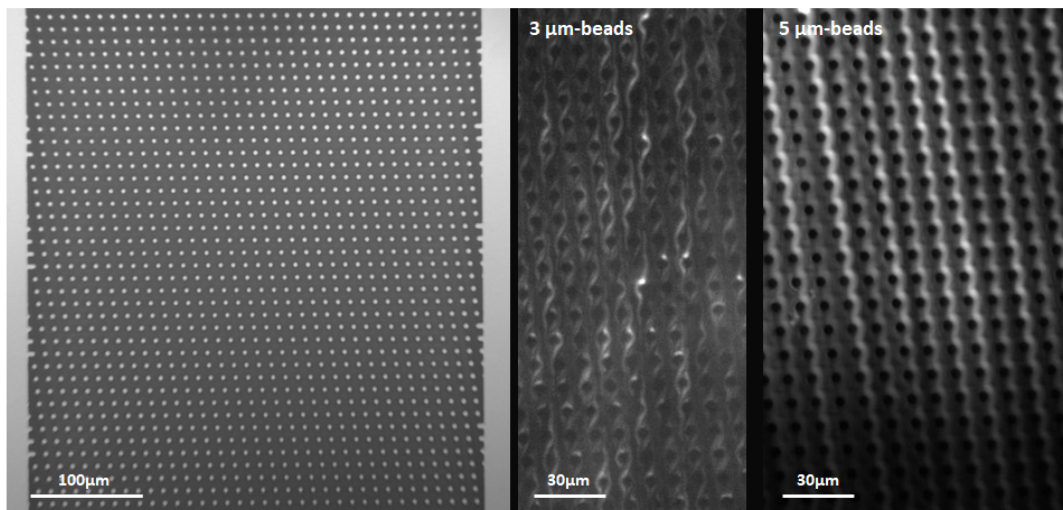
**Version 1, Design 2,
Section 3**

Pillar shape: Triangles
 Pillar Diameter: $20\ \mu\text{m}$
 Lateral Gap: $20\ \mu\text{m}$
 Downstream Gap: $20\ \mu\text{m}$
 Periodicity N: 50
 Experimental $D_c \in [3;5]\ \mu\text{m}$



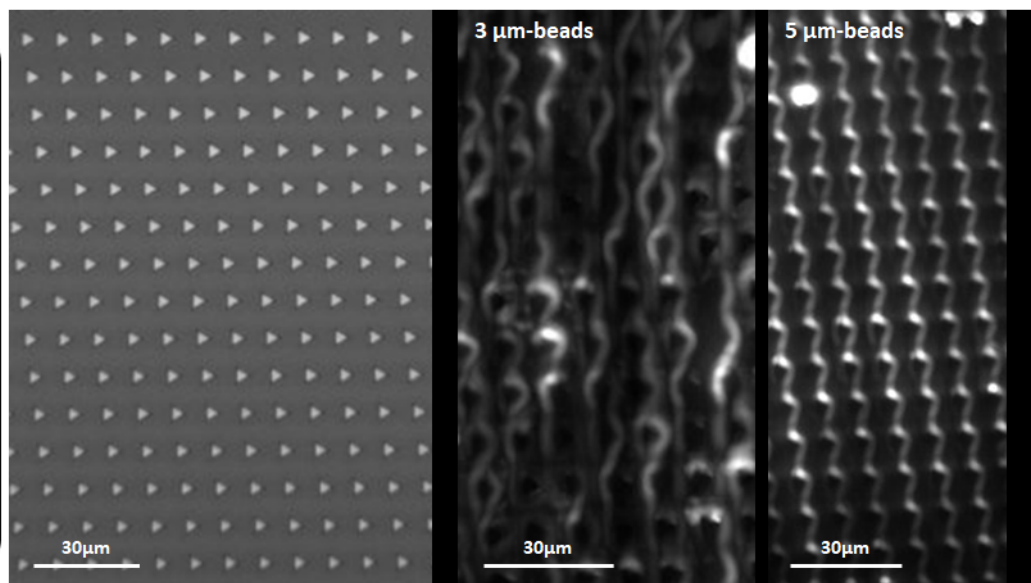
**Version 1, Design 3,
Section 1**

Pillar shape: Circles
Pillar Diameter: 5.5 μm
Lateral Gap: 5.5 μm
Downstream Gap: 5.5 μm
Periodicity N: 7.9
Predicted D_c (Davis): 2.9 μm
Experimental $D_c \in [3;5] \mu\text{m}$



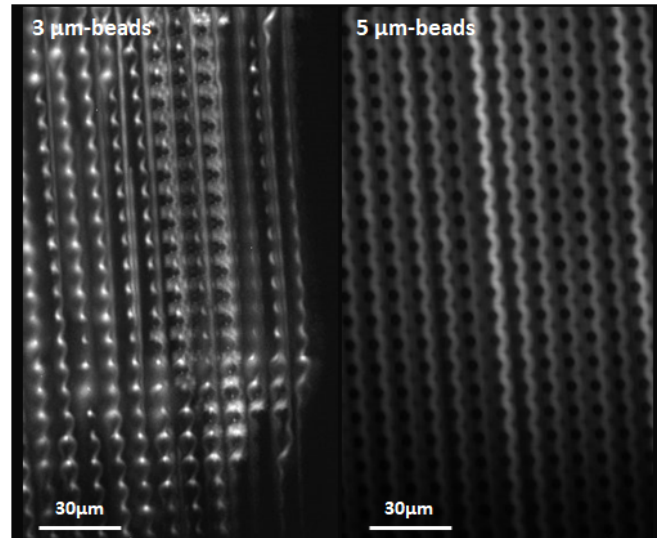
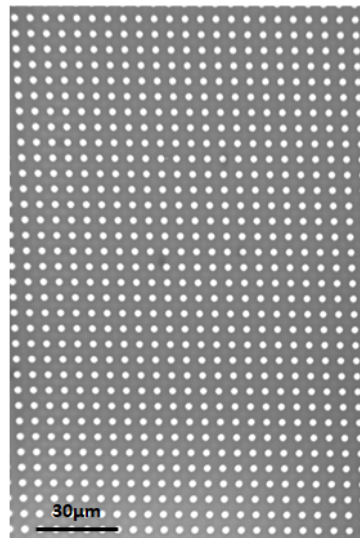
**Version 1, Design 3,
Section 1**

Pillar shape: Triangles
Pillar Diameter: 5.5 μm
Lateral Gap: 5.5 μm
Downstream Gap: 5.5 μm
Periodicity N: 7.9
Experimental $D_c \in [3;5] \mu\text{m}$

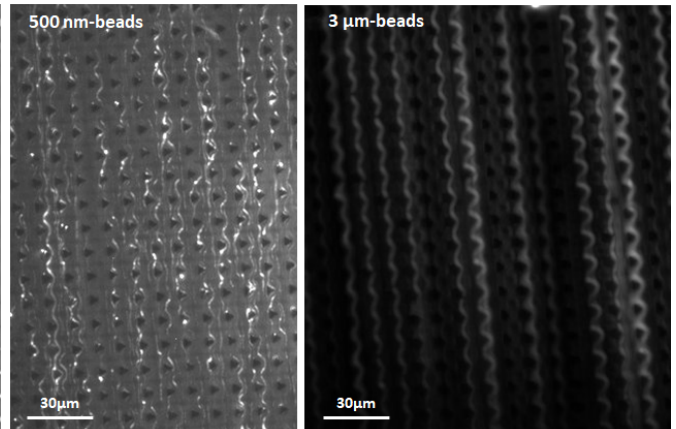
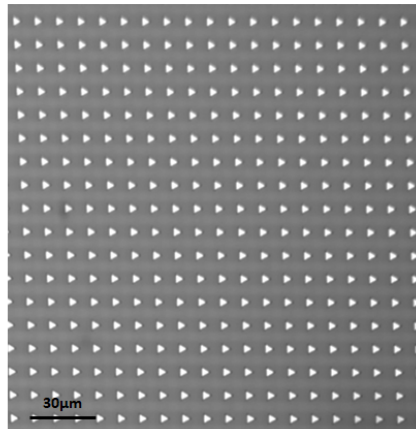


**Version 1, Design 3,
Section 2**

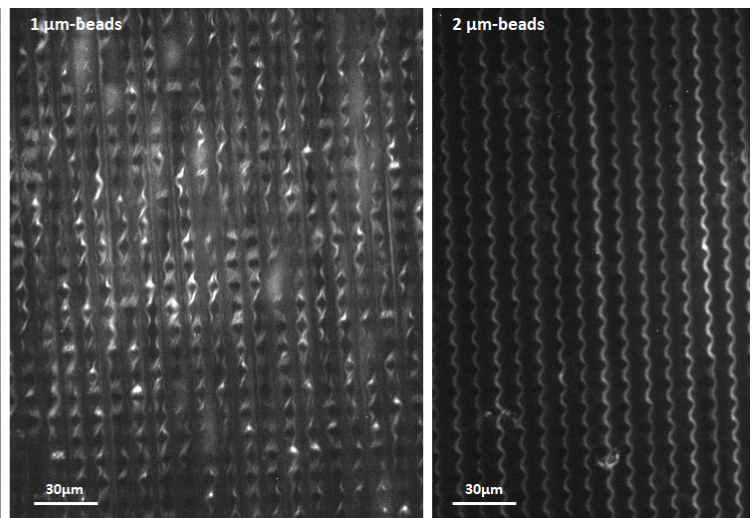
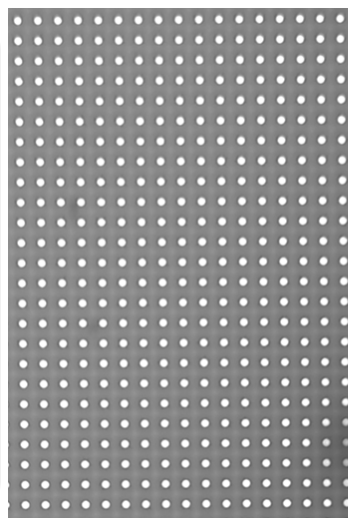
Pillar shape: Circles
 Pillar Diameter: $5.5\ \mu\text{m}$
 Lateral Gap: $5.5\ \mu\text{m}$
 Downstream Gap: $5.5\ \mu\text{m}$
 Periodicity N: 18.3
 Predicted D_c (Davis): $1.9\ \mu\text{m}$
 Experimental $D_c \sim 3\ \mu\text{m}$

**Version 1, Design 3,
Section 2**

Pillar shape: Triangles
 Pillar Diameter: $5.5\ \mu\text{m}$
 Lateral Gap: $5.5\ \mu\text{m}$
 Downstream Gap: $5.5\ \mu\text{m}$
 Periodicity N: 18.3
 Experimental $D_c < 3\ \mu\text{m}$

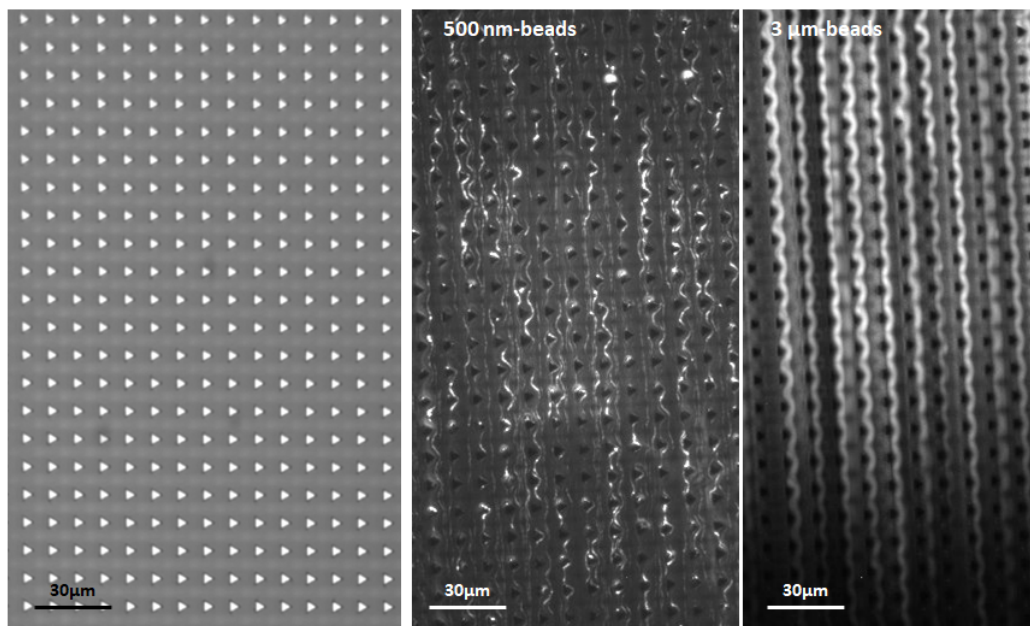
**Version 1, Design 3,
Section 3**

Pillar shape: Circles
 Pillar Diameter: $5.5\ \mu\text{m}$
 Lateral Gap: $5.5\ \mu\text{m}$
 Downstream Gap: $5.5\ \mu\text{m}$
 Periodicity N: 110
 Predicted D_c (Davis): $0.8\ \mu\text{m}$
 Experimental $D_c \in [1;2]\ \mu\text{m}$



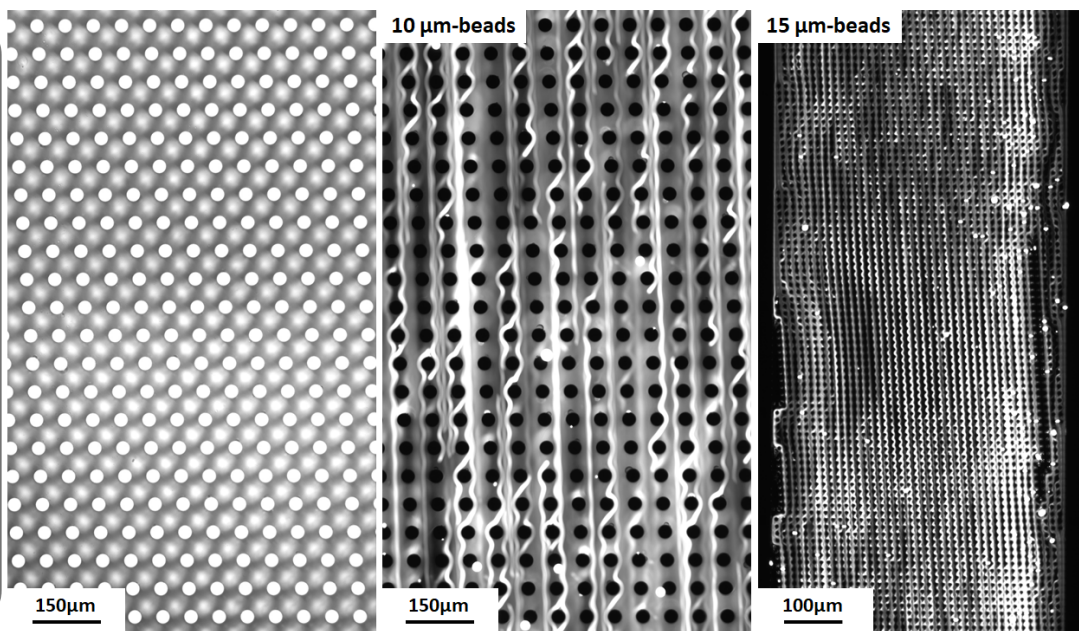
**Version 1, Design 3,
Section 3**

Pillar shape: Triangles
 Pillar Diameter: 5.5 μm
 Lateral Gap: 5.5 μm
 Downstream Gap: 5.5 μm
 Periodicity N: 110
 Experimental $D_c < 3 \mu\text{m}$



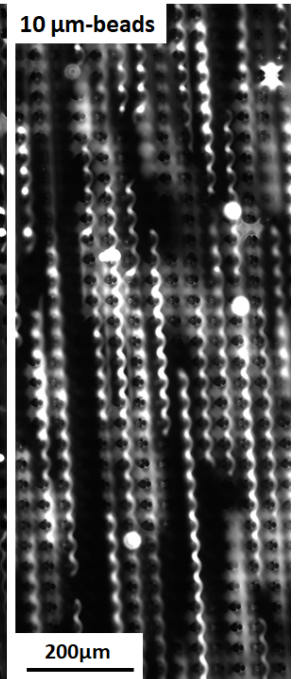
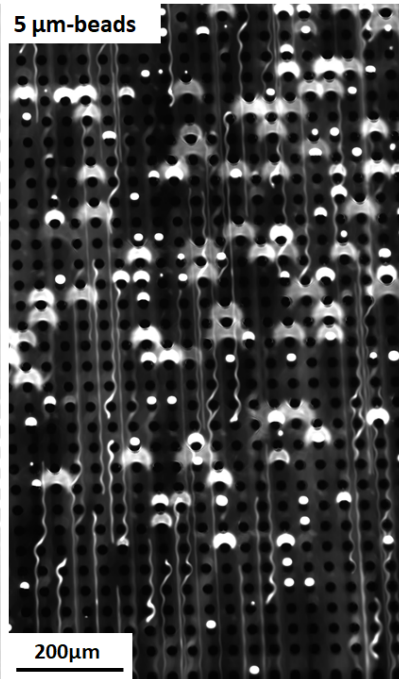
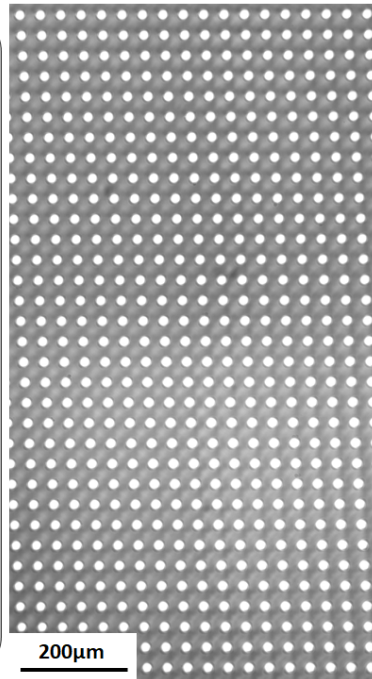
**Version 2, Group 3,
Design 4**

Pillar shape: Circles
 Pillar Diameter: 30 μm
 Lateral Gap: 30 μm
 Downstream Gap: 30 μm
 Periodicity N: 15
 Predicted D_c (Davis): 11 μm
 Experimental $D_c \sim 15 \mu\text{m}$



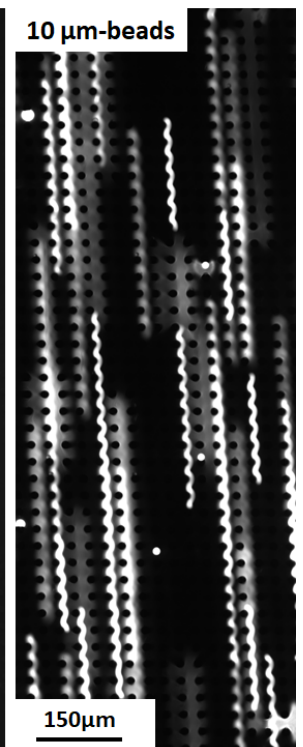
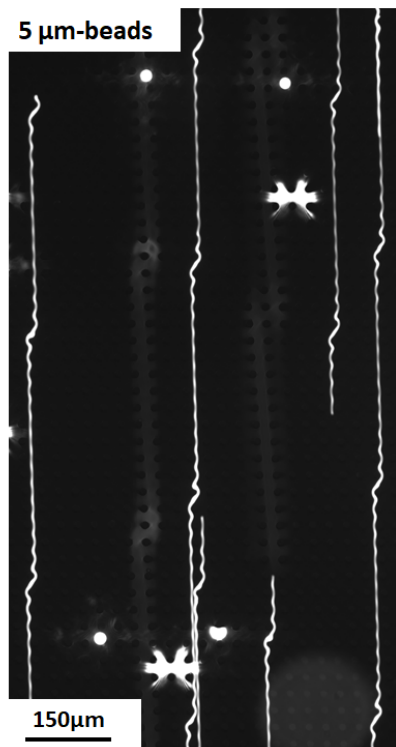
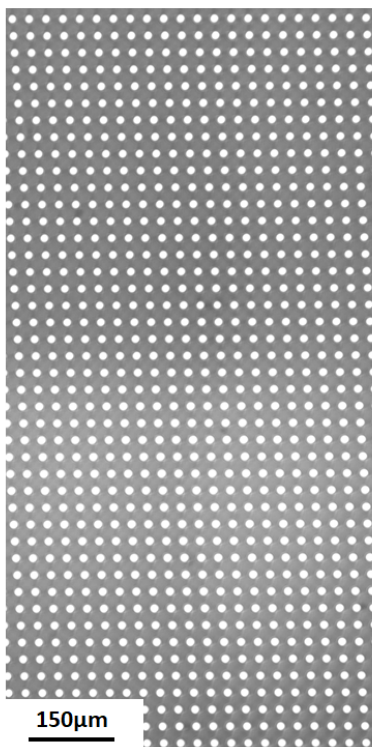
**Version 2, Group 3,
Design 3**

Pillar shape: Circles
 Pillar Diameter: 20 μm
 Lateral Gap: 20 μm
 Downstream Gap: 20 μm
 Periodicity N: 15
 Predicted D_c (Davis): 8 μm
 Experimental $D_c \in [5;10]$ μm



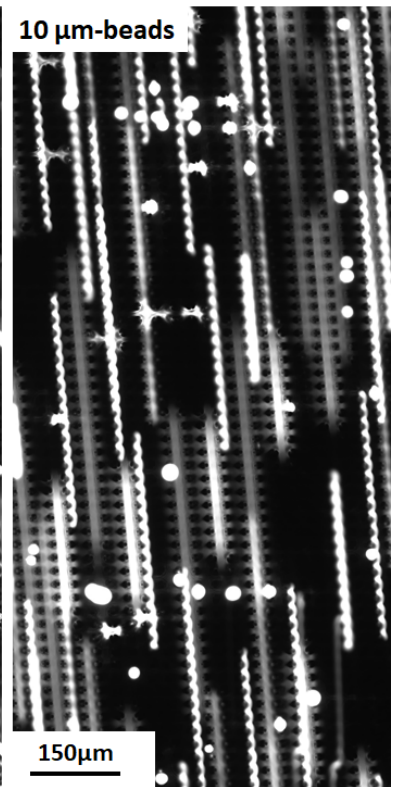
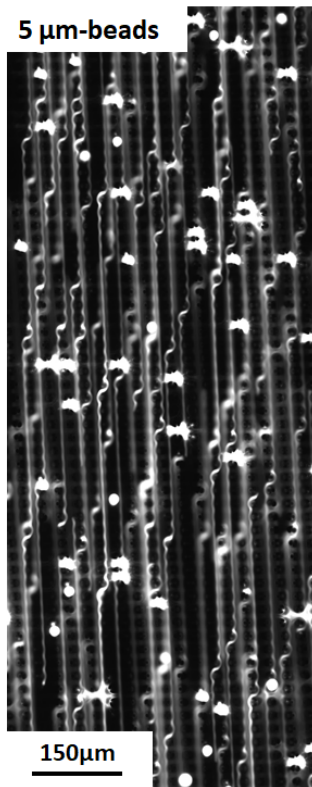
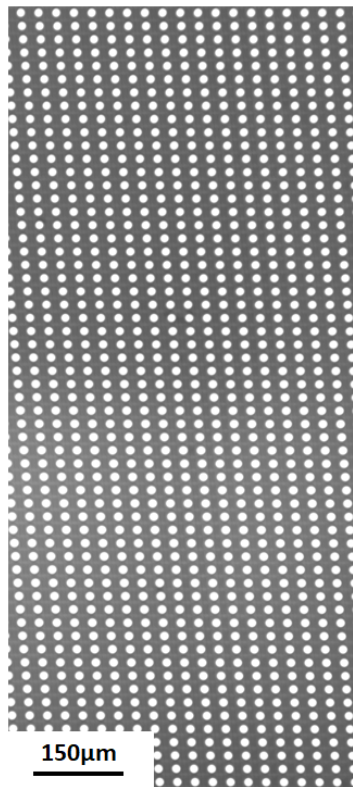
**Version 2, Group 3,
Design 2**

Pillar shape: Circles
 Pillar Diameter: 15 μm
 Lateral Gap: 15 μm
 Downstream Gap: 15 μm
 Periodicity N: 15
 Predicted D_c (Davis): 6 μm
 Experimental $D_c \in [5;10]$ μm



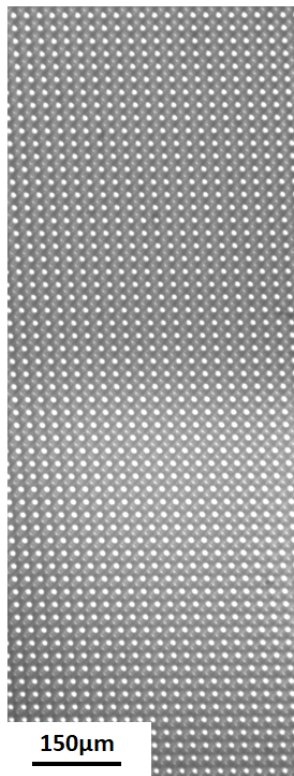
**Version 2, Group 3,
Design 6**

Pillar shape: Circles
Pillar Diameter: 15 μm
Lateral Gap: 15 μm
Downstream Gap: 7.5 μm
Periodicity N: 15
Experimental $D_c \in [5;10]$ μm



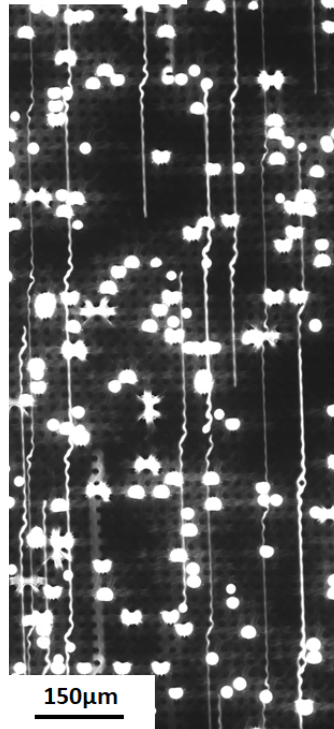
**Version 2, Group 3,
Design 1**

Pillar shape: Circles
 Pillar Diameter: 11 μm
 Lateral Gap: 11 μm
 Downstream Gap: 11 μm
 Periodicity N: 15
 Predicted D_c (Davis): 4 μm
 Experimental $D_c \in [5;10]$ μm



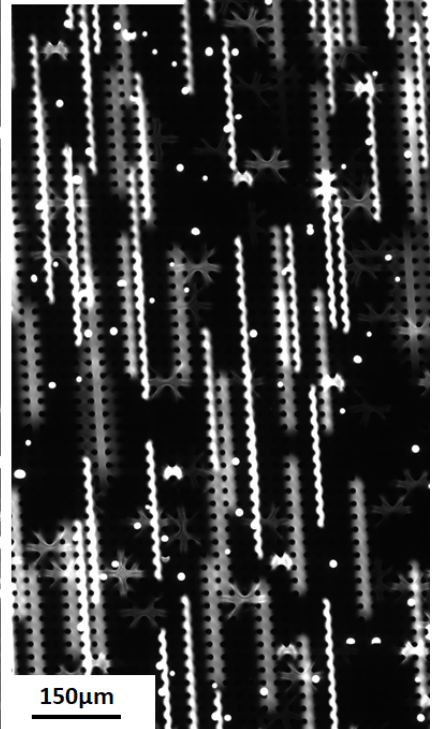
150 μm

5 μm -beads

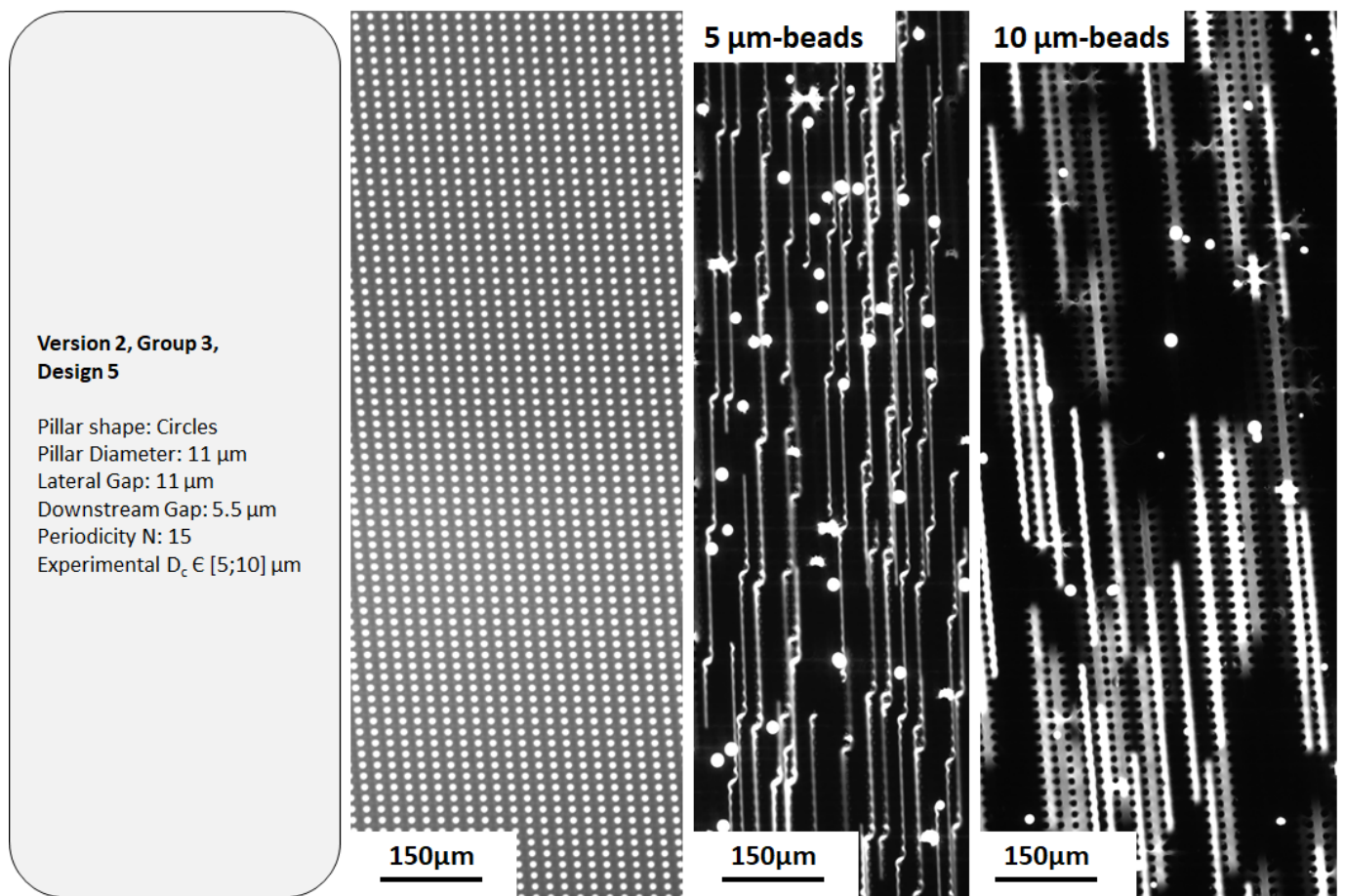


150 μm

10 μm -beads

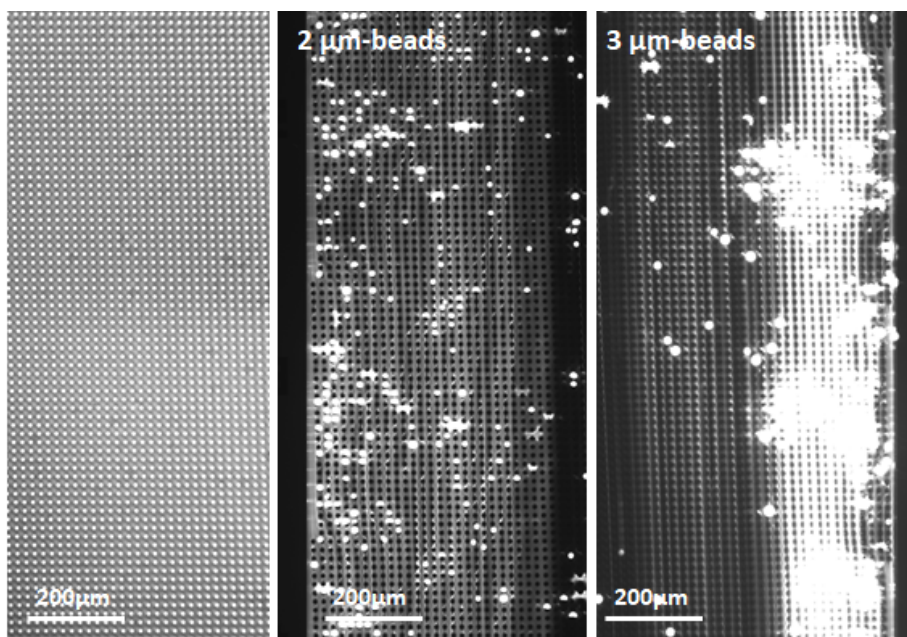


150 μm

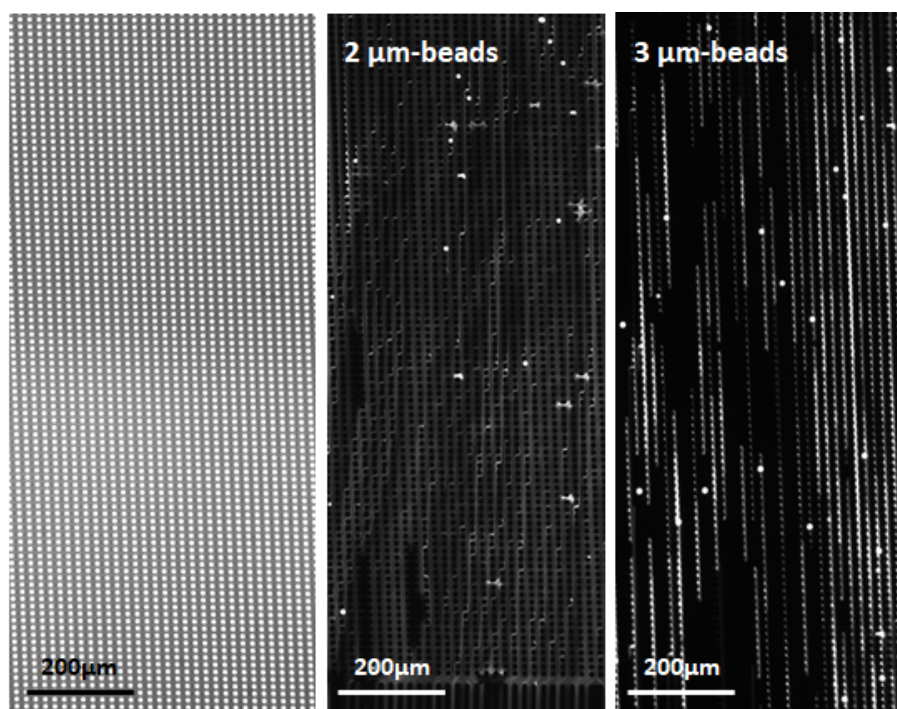


**Version 2, Group 2,
Design 2**

Pillar shape: Circles
Pillar Diameter: $9\ \mu\text{m}$
Lateral Gap: $9\ \mu\text{m}$
Downstream Gap: $9\ \mu\text{m}$
Periodicity N: 30
Predicted D_c (Davis): $2.5\ \mu\text{m}$
Experimental $D_c \in [2;3]\ \mu\text{m}$

**Version 2, Group 2,
Design 3**

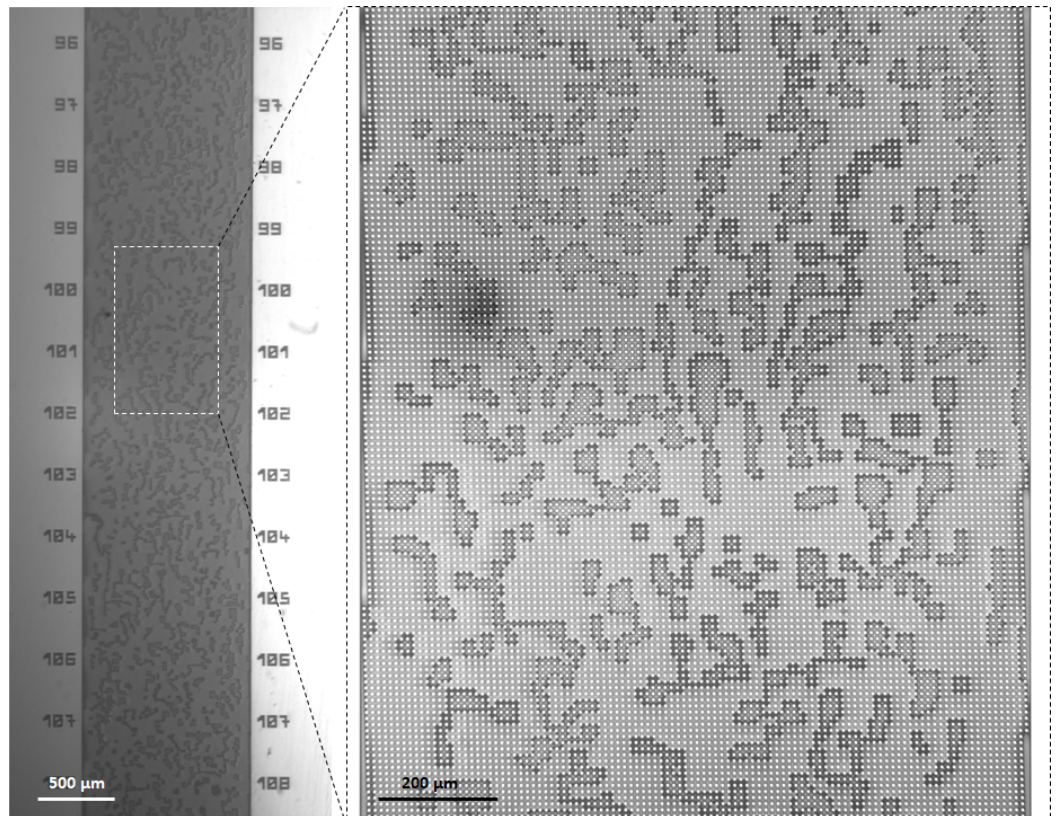
Pillar shape: Circles
Pillar Diameter: $9\ \mu\text{m}$
Lateral Gap: $9\ \mu\text{m}$
Downstream Gap: $4.5\ \mu\text{m}$
Periodicity N: 30
Experimental $D_c \in [2;3]\ \mu\text{m}$

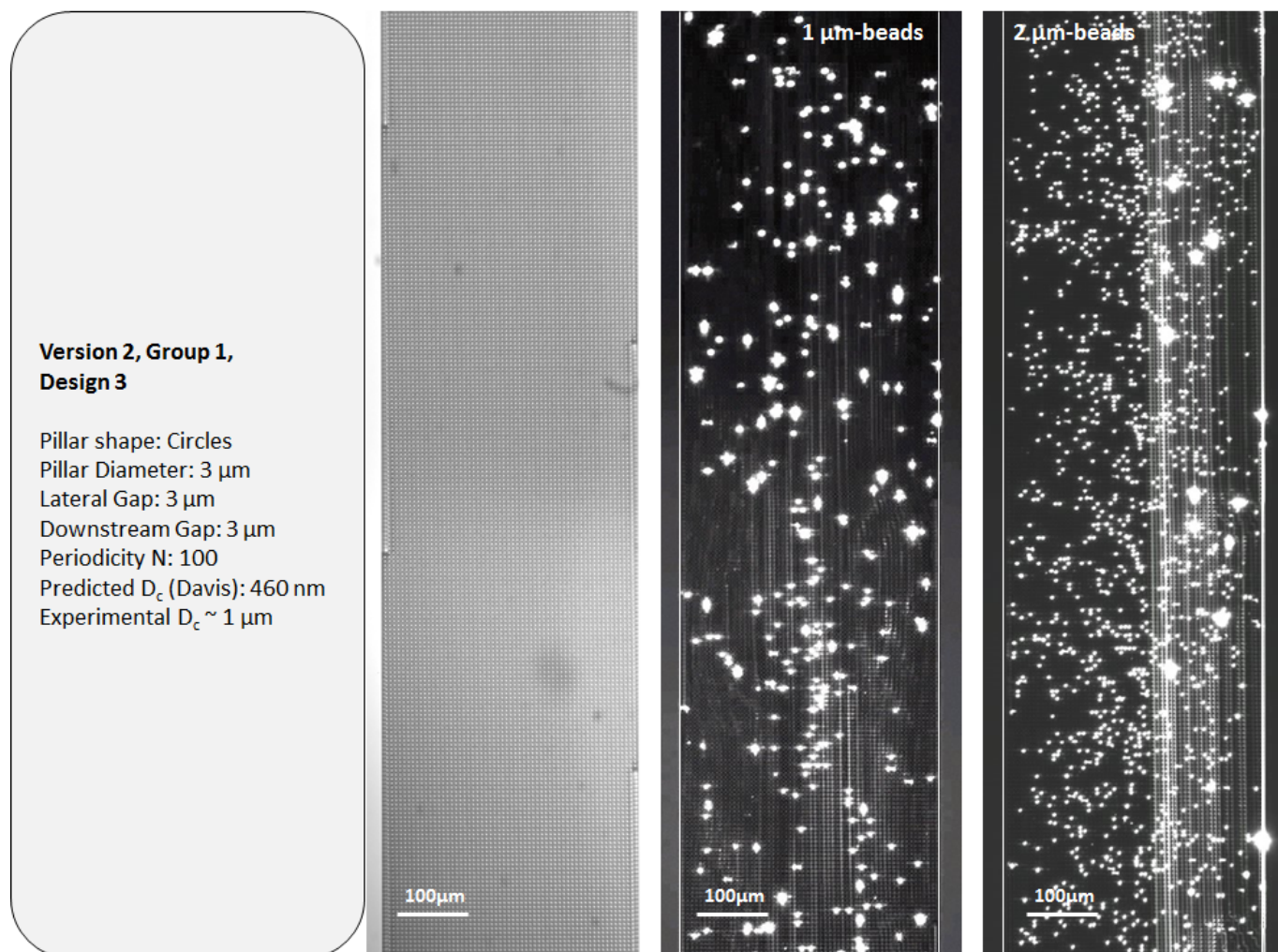


**Version 2, Group 2,
Design 1**

Pillar shape: Circles
Pillar Diameter: 5 μm
Lateral Gap: 5 μm
Downstream Gap: 5 μm
Periodicity N: 40
Predicted D_c (Davis): 1.2 μm

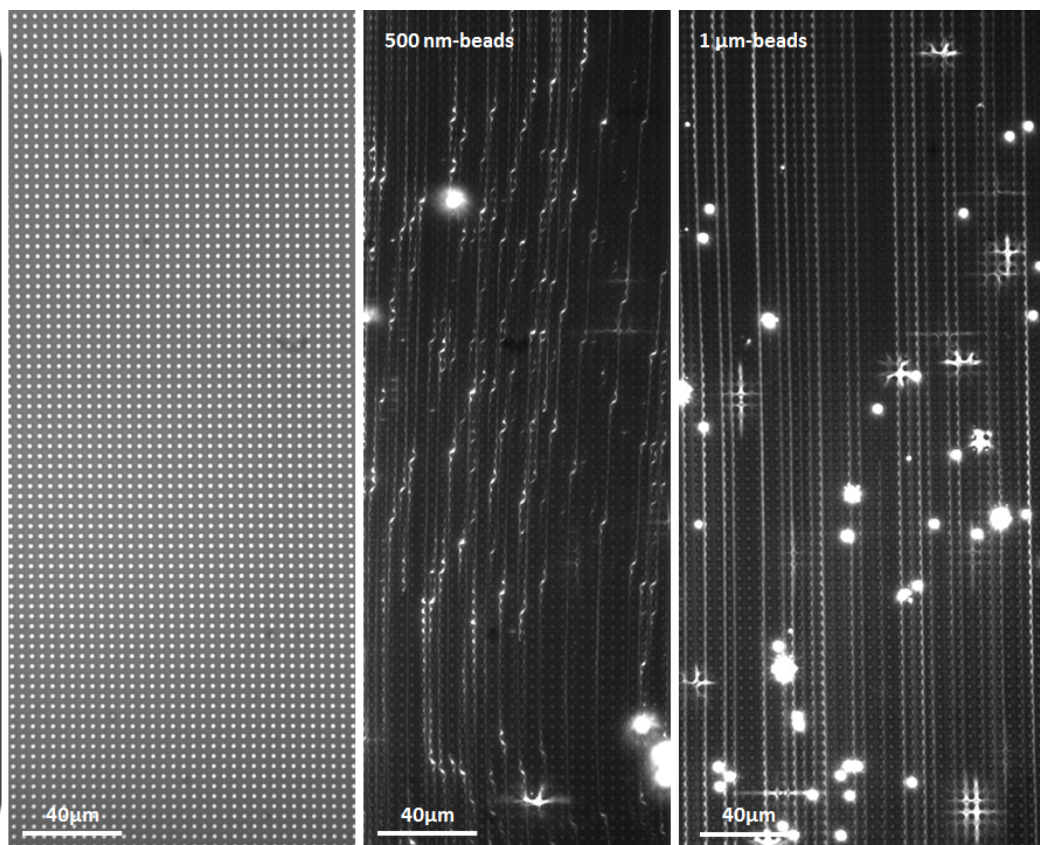
Experimental D_c : could not
be determined because of
bubble issues

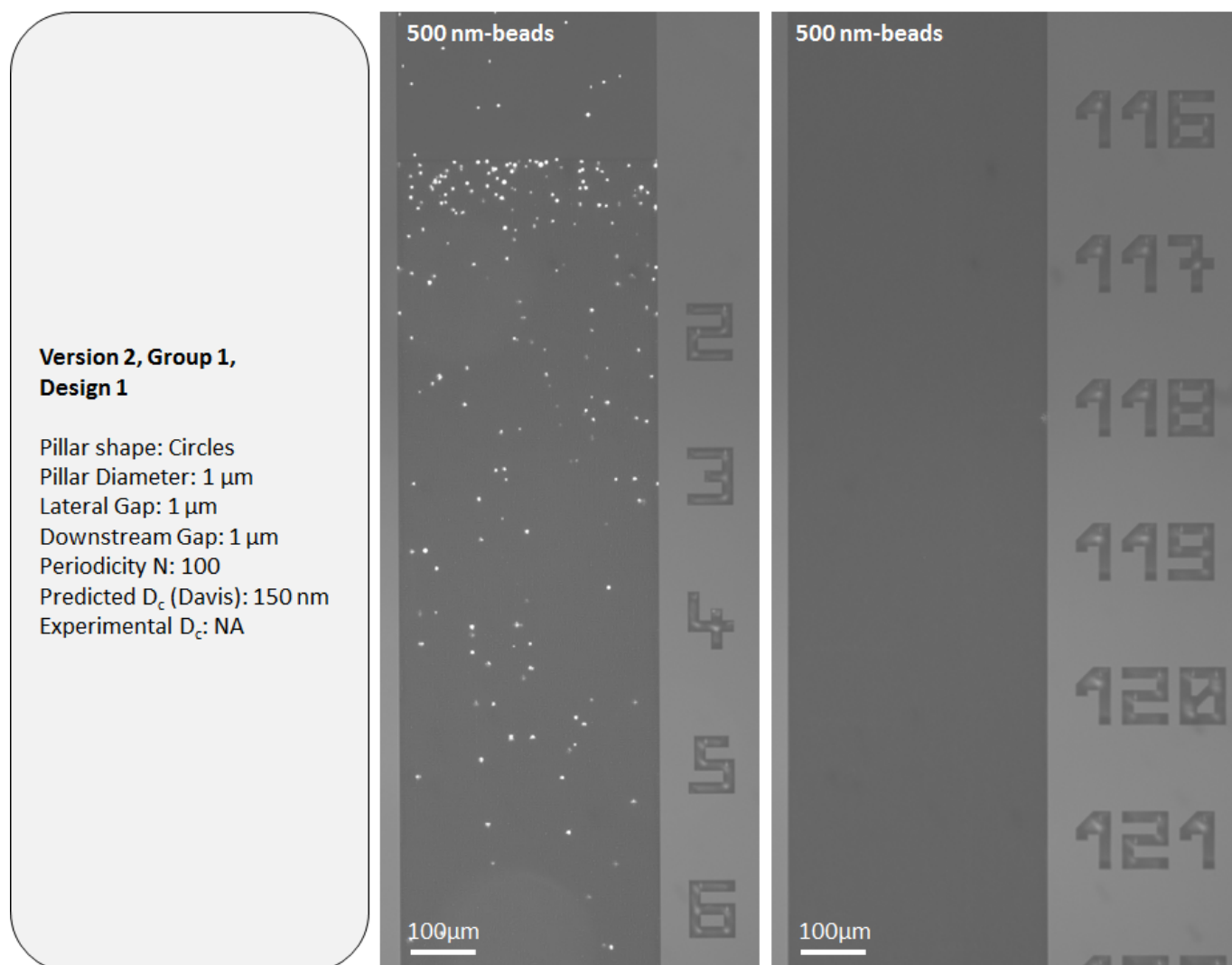




**Version 2, Group 1,
Design 2**

Pillar shape: Circles
Pillar Diameter: $2\ \mu\text{m}$
Lateral Gap: $2\ \mu\text{m}$
Downstream Gap: $2\ \mu\text{m}$
Periodicity N: 100
Predicted D_c (Davis): 310 nm
Experimental $D_c \in [0.5; 1]\ \mu\text{m}$





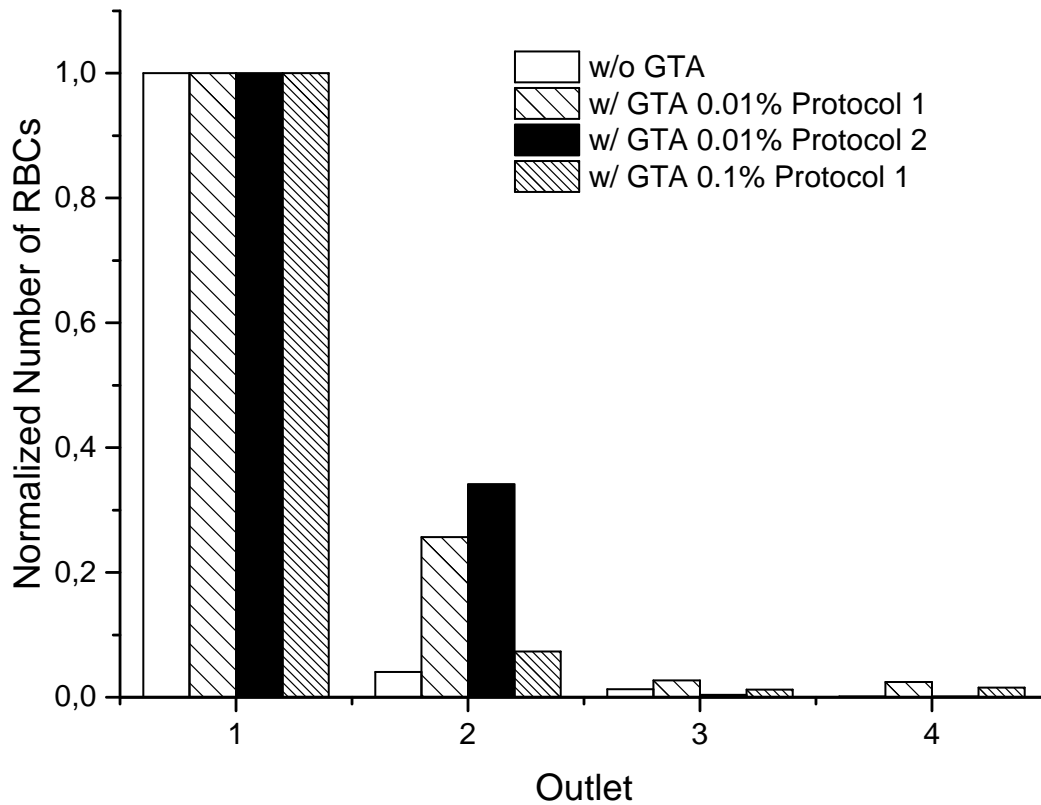
A.6 Appendix 6: Protocol for RBC fixation with glutaraldehyde

Efficient deviation of RBCs could not be performed by version 1 DLD devices with 20 μm triangular pillars from untreated 10x-diluted blood samples. In order to increase RBC deviation, one possible strategy is to increase their stiffness in order to avoid RBC squeezing in the fluidic flow and reduction of their effective size. Glutaraldehyde (GTA) was reported to increase the DLD deviation of RBCs (Holmes et al., *Interface Focus*, 2014) by increasing their stiffness through protein cross-linking. Thanks to two aldehyde groups separated by a flexible chain, GTA can create cross-links of variable distances.

Two GTA-based fixation protocols were tested and the fraction of RBCs flowing out from each of the four DLD outlets was optically quantified with the cell counting chambers. The fixation protocols are described below:

- “Protocol 1” (from *Holmes et al., Interface Focus, 2014*): Blood cells are resuspended at haematocrit of 2.5 % by volume in a DPBS solution containing 0.01 % v/v of GTA (Fluka Biochemika, 49628) (1 mL of whole blood is centrifuged at 2,000 g for 10 minutes and resuspended in 20 mL of the GTA solution). The sample is incubated at room temperature for 45 minutes. After washing three times in DPBS, the pellet is collected in 1 mL of DPBS.
- “Protocol 2” : 10 μL of a DPBS solution with 1 % v/v of GTA (Fluka Biochemika, 49628) is directly added to 1 mL of whole blood. The sample is incubated at room temperature for 45 minutes. After washing three times in DPBS, the pellet is collected in 1 mL of DPBS.
- “Protocol 1” with higher GTA concentration: Blood cells are resuspended at haematocrit of 2.5 % by volume in a DPBS solution containing 0.1 % v/v of GTA (Fluka Biochemika, 49628) (1 mL of whole blood is centrifuged at 2,000 g for 10 minutes and resuspended in 20 mL of the GTA solution). The sample is incubated at room temperature for 45 minutes. After washing three times in DPBS, the pellet is collected in 1 mL of DPBS.

Results are presented in appendix A.6 for these three protocols in addition to a control blood sample without GTA treatment. An increase of the number of deviated RBCs is observed with all three protocols compared to the control blood sample. This confirms that GTA enables to increase the stiffness of RBCs and thus their deviation in DLD arrays. **Protocol 2 - with addition of the GTA solution in whole blood, without preliminary centrifugation - seems to be the most efficient way to maximize RBC deviation with this device.** Unexpectedly, protocol 1 with 0.1 % GTA leads to a lower deviation of RBCs than the same protocol with 0.01 % GTA, which suggests the existence of an optimal GTA concentration to increase the stiffness of RBCs. However, even with the selected protocol 2, **this strategy does not enable to efficiently purify 10x-diluted blood samples** since most RBCs flow out of the device through the non-deviated outlet n°1.



Quantification of RBCs in each of the four DLD outlets for four injected blood samples: without GTA treatment (w/o GTA), treated with GTA at 0.01 % according to the protocol 1 (w/ GTA 0.01% Protocol 1), treated with GTA at 0.01 % according to the protocol 2 (w/ GTA 0.01% Protocol 2) and treated with GTA at 0.1 % according to the protocol 1 (w/ GTA 0.1% Protocol 1). The DLD outlets are numbered from 1 (not deviated) to 4 (completely deviated).

A.7 Appendix 7: THP-1 cell differentiation protocol

For experiments with macrophages, a phorbol myristate acetate (PMA)-induced differentiation of the THP-1 cells to a macrophage-like phenotype is performed, through a 48 h culture with 100 nM PMA in RPMI 1640 media (1 million cells per well). Macrophages are washed 3 times in DPBS. They are then polarized to M1 (pro-inflammatory) and M2 (anti-inflammatory) macrophages. M1 activation is induced by incubation for 24 h at 37 °C with IFN gamma at 20 ng mL⁻¹ and LPS 0111B7 at 1 ng mL⁻¹ and M2 activation is induced by incubation for 24 h at 37 °C with IL4 at 20 ng mL⁻¹ and IL13 at 20 ng mL⁻¹. Non-polarized M0 macrophages are also studied. The supernatant is then replaced by 1 mL of DMEM media with 10 μmol L⁻¹ Calcium Ionophore A23187. Cells are incubated for 20 min at 37 °C. The supernatant is collected and centrifuged twice at 1,500 g for 15 min. Both ultracentrifugation steps (20,000 g for 60 min and 100,000 g for 60 min at 4 °C) are then performed and the pellet is collected in DPBS.

A.8 Appendix 8: Transmission electron microscopy sample preparation

Samples were deposited on a plasma cleaned (Solarus, Gatan) EM grid with lacey carbon (S166-3, Ted Pella) through two successive deposits of 1 μL of sample and a 10 second waiting time between both deposits. Better efficiency was obtained when the sample deposit was performed with specific pipette tips (TipOne, Star lab) on horizontally-oriented grids. Automated vitrification was ensured by a Vitrobot instrument (FEI Company) to perform cryo-fixation at a controlled 20.5 °C temperature, 100 % relative humidity, blotting conditions and freezing velocity. Excess sample was removed with filter paper with the following blotting parameters: blot time: 3 s, relative blot force: -5, wait time: 1 s, drain time: 0, blot total: 1. The grids were then plunged into liquid ethane in equilibrium with solid ethane at about - 185 °C. The grids were stored in liquid nitrogen before mounting in a Gatan 626 cryo-holder for imaging with an FEI Technai Osiris transmission electron microscope operated at 200 kV. Images were recorded on a US1000XP camera (Gatan) with 2048 x 2048 pixels.

List of Publications and Patents

Articles Published in Peer-Reviewed Journals

E. Pariset, C. Parent, Y. Fouillet, F. Boizot, N. Verplanck, F. Revol-Cavalier, A. Thuaiere, V. Agache, "Separation of Biological Particles in a Modular Platform of Cascaded Deterministic Lateral Displacement Modules", *Scientific Reports*, **2018**, 8:17762, doi: 10.1038/s41598-018-34958-8.

E. Pariset, C. Pudda, F. Boizot, N. Verplanck, F. Revol-Cavalier, J. Berthier, A. Thuaiere, V. Agache, "Purification of complex samples: implementation of a modular and reconfigurable droplet-based microfluidic platform with cascaded deterministic lateral displacement separation modules", *PLOS ONE*, **2018**, 13 (5), 1-18, doi: journal.pone.0197629.

E. Pariset, C. Pudda, F. Boizot, N. Verplanck, J. Berthier, A. Thuaiere, V. Agache, "Anticipating Cutoff Diameters in Deterministic Lateral Displacement (DLD) Microfluidic Devices for an Optimized Particle Separation", *Small*, **2017**, 13 (37), 1-11, doi: 10.1002/smll.201701901. **Back Cover of Issue 37**.

E. Pariset, V. Agache, A. Millet, "Extracellular Vesicles: Isolation Methods", *Advanced Biosystems*, **2017**, 1 (5), 1-12, doi: 10.1002/adbi.201700040.

Patents

N° E.N: 18 52121, **E. Pariset**, J. Berthier, A. Thuaiere, V. Agache, "Système de tri de particules par gamme de tailles", Filing Date: March 12 2018

N° E.N: 17 61263, **E. Pariset**, C. Parent, F. Boizot, Y. Fouillet, "Dispositif d'injection d'un échantillon fluïdique", Filing Date: November 28 2017

N° E.N: 18 52121, **E. Pariset**, F. Revol-Cavalier, V. Agache, "Équipement de tri de particules présentes dans un échantillon fluïdique", Filing Date: November 7 2016

International Conferences

E. Pariset, F. Revol-Cavalier, F. Boizot, C. Pudda, A. Thuaiere, F. Navarro, B. Icard, V. Agache, "Droplet platform for integration of deterministic particle separation in a multi-stage modular and reconfigurable cartridge", *µTAS 2017*, October 22-26 2017, Savannah (USA). Oral Presentation

E. Pariset, J. Berthier, C. Pudda, F. Navarro, B. Icard, V. Agache, "Particle separation with Deterministic Lateral Displacement (DLD): The Anisotropy Effect", *Euroensors 2017*, September 3-6 2017, Paris. Oral Presentation

E. Pariset, J. Berthier, F. Revol-Cavalier, C. Pudda, D. Gosselin, F. Navarro, B. Icard, V. Agache, "Deterministic Lateral Displacement: Finite element modeling and experimental validation for particle trajectory and separation", *Nanotech 2017*, May 14-17 2017, Washington, DC. Oral Presentation

E. Pariset, J. Berthier, F. Navarro, B. Icard, V. Agache, "Deterministic Lateral Displacement: Finite element modeling and experimental validation for particle trajectory and separation", *Flow 17*, July 3-5 2017, Paris. Poster Presentation

National Conferences

E. Pariset, D. Gosselin, V. Agache, J. Berthier, "Modeling the steric effect in COMSOL for Deterministic Lateral Displacement based separation", *GDR Micro et Nanofluidique 2016*, June 23-24 2016, Paris. Poster Presentation

E. Pariset, C. Hadji, L. Viro, A. Millet, B. Icard, V. Agache, "Suspended microchannel plate resonator for mass sensing of cells and exosomes", *Workshop on BioMEMS and Cancer*, December 17 2015, Lille. Poster Presentation

Awards

L'Oréal-UNESCO French Fellowship for Women in Science, 2017 session

Travel Grant for the 20th International Conference on Miniaturized Systems for Chemistry and Life Sciences (μ TAS 2017), Chemical and Biological Microsystems Society, Savannah (Ga, USA)

IDEX Travel Grant from Grenoble Alpes University to conduct research at MIT (Koch Institute for Integrative Cancer Research, Manalis Laboratory), 2017

Développement d'un dispositif microfluidique de Déplacement Latéral Déterministe (DLD) pour la préparation d'échantillons biologiques, en vue de l'extraction de vésicules extracellulaires

Les vésicules extracellulaires (EVs) apparaissent depuis une dizaine d'années comme de nouveaux biomarqueurs à fort potentiel pour des applications de biopsie liquide. En effet, les EVs portent la signature de leurs cellules émettrices, par le transport de matériel génétique et protéique cellulaire, qui peut être exploité comme outil de diagnostic précoce. L'une des principales limitations actuelles à l'utilisation clinique des EVs est la difficulté à extraire ces nano-objets à partir de biofluides complexes et à standardiser les protocoles de préparation d'échantillon. En effet, de nouvelles technologies sont requises pour effectuer un isolement efficace, bas coût et rapide de sous-populations d'EVs, sans altérer leur intégrité et à partir de faibles volumes d'échantillon. La technique microfluidique de Déplacement Latéral Déterministe (DLD) apparaît comme une des technologies prometteuses pour atteindre ces performances grâce à une purification passive et sans marquage. Les dispositifs de DLD mettent en oeuvre un réseau de piliers générant un tri en taille des particules, et dont les paramètres géométriques permettent de contrôler précisément le diamètre de séparation. Parmi les nombreuses applications de cette technologie dans le secteur biomédical, aucune ne permet pour le moment de réaliser l'extraction complète d'EVs directement à partir du biofluide d'intérêt, sans étapes de purification intermédiaires par centrifugation par exemple. Dans cette perspective, nos développements technologiques ont pour but d'améliorer la fiabilité, l'efficacité et l'intégration des dispositifs de DLD. A partir d'études numériques et expérimentales, nous proposons ici de nouveaux modèles pour anticiper au mieux le comportement des particules lors de la conception de réseaux de DLD. Par ailleurs, dans une approche orientée système, nous proposons également un packaging fluide des dispositifs de DLD. Plusieurs étapes de tri étant généralement requises pour la purification d'échantillons biologiques, nos développements portent également sur la façon d'interconnecter ces modules au sein d'une configuration en série. Deux applications biologiques sont adressées et démontrent la versatilité de la technologie de DLD : l'isolement de bactéries *E. coli* à partir de prélèvements sanguins humains - en vue du diagnostic du sepsis - et l'extraction d'EVs dans des milieux de culture cellulaires - avec en perspective la détection d'EVs spécifiques par biopsie liquide. L'étape de préparation d'échantillon ne peut être dissociée de l'étape de caractérisation. C'est pourquoi, l'isolement des EVs devra dans un second temps être couplé à leur analyse au sein d'un dispositif intégré, portable et autonome, ce qui pourrait ouvrir de nouvelles perspectives vers l'application clinique des recherches actuelles sur les EVs.

Development of a microfluidic device based on Deterministic Lateral Displacement (DLD) for biological sample preparation, towards the extraction of extracellular vesicles

Over the past decades, Extracellular Vesicles (EVs) have demonstrated strong potential as new biomarkers for liquid biopsy. Indeed, since EVs are fingerprints of parent cells, they can be exploited as early diagnostic tools. However, owing to their small size and high heterogeneity, EVs are challenging to extract from biofluids. In particular, reproducible and standardized protocols are required to perform fast, efficient, and cost-effective preparation of undamaged EV subpopulations from limited sample volumes. Deterministic Lateral Displacement (DLD) appears to be a promising microfluidic technology for this preparation by means of passive and label-free separation. DLD performs size-based separation of particles around a critical diameter that can be fine-tuned according to design parameters in an array of micropillars. Across the numerous biotechnological applications of DLD, none has yet successfully performed the complete extraction of EVs from unprocessed biofluids. This is the underlying motivation of this thesis, which outlines technological enhancements that make DLD separation more predictable, efficient, and easy-to-integrate. Based on both numerical and experimental developments, predictive models are proposed in order to anticipate particle behavior and to help in the design of efficient DLD devices. In addition to the optimization of single DLD devices, this thesis also addresses the issue of system integration. An innovative approach of serial connection between DLD modules is proposed to address the sequential sorting of particles from a complex biofluid and ensure that there is no loss of function of individual DLD devices when operated alone or in series. Two biological applications illustrate the potential of DLD-based sample preparation systems: the isolation of *E. coli* bacteria from human blood samples for sepsis diagnostics and the extraction of EVs from cell culture media with the perspective of liquid biopsy applications. And as sample preparation cannot be dissociated from detection or characterization, this thesis moreover highlights the potential integration of DLD in an all-in-one microfluidic device for both sample preparation and analysis of extracted EVs. Such a portable and autonomous device could overcome some of the current limitations with regard to the clinical use of EVs.